ELECTRON MICROINSTABILITIES IN AN ECRH, MIRROR-CONFINED PLASMA

Garner, R.C.[*]

September 1986

Plasma Fusion Center
Massachusetts Institute of Technology
Cambridge, Massachusetts 02139 USA

[*]present address: Photometrics, Inc., Woburn, MA

Electron Microinstabilities in an ECRH, Mirror-Confined Plasma

by

Richard Charles Garner

B.A. Carleton College
(1980)

Submitted to the Department of Physics
in partial fulfillment of the requirements for
the degree of

Doctor of Philosophy

at the
Massachusetts Institute of Technology
August 8, 1986

Signature of Author _____

<div align="right">

Department of Physics
August 8, 1986

</div>

Certified by _____

<div align="right">

Richard S. Post
Thesis Supervisor

</div>

Accepted by _____

<div align="right">

George F. Koster
Chairman, Ph.D. Committee

</div>

Electron Microinstabilities in an ECRH Mirror-Confined Plasma

by

Richard C. Garner

Abstract

The ECRH, mirror–confined plasma of the Constance B experiment is whistler unstable. Two types of rf emission, referred to as whistler B (bursting) and whistler C (continuous), are observed. The whistler B emission bursts at a fairly regular rate and correlates with electron and ion endloss bursts, and diamagnetism and potential fluctuations. The burst rate increases for increasing electron heating rate. The whistler C emission comes continously in time and is associated with continous enhanced endloss. The whistler C emission is associated with off–axis plasma where the heating rate is expected to be higher than on–axis due to low field line gradients at resonance.

The Constance B plasma is characterized by three electron components: cold (100 eV), warm (2 keV), and hot (400 keV). The whistler instability is studied over a wide range of machine operating conditions to determine 1) its effect on the electron velocity space distribution function and 2) the enhanced particle and power loss it induces. It is found that the warm component drives the microinstability while the hot component is microstable. Warm electron endloss is due almost entirely to microinstability. Its measured loss time is more than 10 times less than the collisional loss time. Although microstable, the hot electrons are also driven into the loss cone when microinstability exists. The loss rate of the hot electrons due to microinstability can be as high as 1/3 the loss rate due to the applied ECRH waves. The two mechanisms together induce endloss which is 100 times greater than the collisional endloss.

Power loss due to microinstability is primarily in the form of unstable rf emission (40 W) and induced warm and hot electron endloss (80 W and 90 W, respectively). These numbers correspond to an ECRH input power of 1000 W.

Relativistic Vlasov dispersion relation calculations with a new distribution function (ECRH distribution) are performed. The ECRH distribution function models a population of ECRH, mirror–confined electrons. Theoretically calculated unstable whistler frequencies match the experimentally measured frequencies when the ECRH distribution is used to model the *warm electrons*.

Acknowledgements

I would like to thank my thesis advisor, Dr. Richard Post, for overseeing the work performed for this thesis. His guidance and support are greatly appreciated, as is his seemingly infinite source of new ideas and enthusiasm.

I am deeply grateful to Mike Mauel for his guidance, support, and advice in conjunction with this thesis. Mike has been a constant source of unbounded enthusiasm and new ideas which I have been witness to from my first day as a graduate student at M.I.T. He has been a friend, a colleague, a teacher, and an advisor. He has been an integral part of my education at M.I.T. His dedication as a scientist and his general world outlook are to be admired.

I would like to thank Donna Smatlak. Donna's advice on performing experiments and analyzing data has been invaluable. She is the most immediate overseer of Constance B and is responsible for its excellent operation as a plasma physics experiment. I would also like to thank her for her support while performing this work.

Thanks also to the rest of the members of the Constance group. They have been good colleagues and good friends and it has been a pleasure working with them. Special thanks to Sam Hokin, who has built an excellent x-ray detection system and has become an expert at analyzing x-ray data, and to Xing Chen, who is responsible for the proper operation of the diamagnetic loop. Thanks also to Dan Goodman, Craig Petty, Dilys Liu, Phil Goodrich, and Tom Farish. These people have made the graduate student ghetto an enjoyable place.

I would like to thank Ken Retman for keeping the Constance machine running smoothly. Thanks also to the Tara scientists for support, especially Jim Irby, who has offered support and advice since my arrival at M.I.T., and Don Smith, who is responsible for the Constance B ECRH transmitter.

I would like to thank Jennifer Melcher for her help and support during the final stages of this thesis–always the most difficult time.

Finally, I would like to express my appreciation to Professor Ron Davidson and to Professor George Bekefi for serving on the thesis committee.

Contents

List of Figures

9

Chapter 1

Introduction

1.1 Statement of Problem

Plasma microinstability refers to the unstable state of a non-Maxwellian plasma in which electromagnetic or electrostatic waves may grow at the expense of particle free energy. Unlike MHD instabilities, which depend on unfavorable spatial configurations, microinstabilities depend on unfavorable velocity space configurations of the plasma. There is a particular class of microinstability which may occur if the number of particles with some energy E_1 is greater than the number of particles with some other energy $E_2 < E_1$. If such a situation exists then a transfer of particles from higher energy to lower energy is possible due to the action of an intermediary—a plasma wave which acquires the energy. The wave can also lose energy by the reverse process (i.e. it can be absorbed) through interaction with some other portion of the distribution function, the strength of the interaction varying according to velocity space location. Therefore the occurence of microinstability depends on the entire velocity space distribution function. Microinstability may be driven either by non-Maxwellian ions or non-Maxwellian electrons, the latter being associated with with higher frequencies and shorter wavelengths.

This thesis presents a study of the electron microinstability of an electron cyclotron resonance heated (ECRH), mirror-confined plasma. Some examples of electron microinstabilities which have been the subject of previous experimental and theoretical investigations are the whistler instability and the upper hybrid loss cone

instability, which are driven by temperature anisotropy, and the cyclotron maser instability, which is driven by a population inversion. The electrons of an ECRH, mirror-confined plasma are susceptible to both temperature anisotropy and population inversion. Since ECRH heats the electrons along characteristic paths in velocity space it induces temperature anisotropy as long as it can overcome collisions that tend to isotropize the temperature. If the electrons can be heated enough so that they are magnetically confined and not simply electrostatically confined by the plasma potential, then a loss cone in velocity space exists which leads to population inversion.

The Constance B mirror experiment is a single cell, quadrupole magnetic mirror in which a hydrogen plasma is produced and the electrons are heated by ECRH. Electron microinstability occurs within 1 msec after gas breakdown and persists during the entire heating phase and a few milliseconds after the heating phase ends. Microinstability is observed due to the emission of electromagnetic waves in the electron cyclotron range of frequencies and the enhanced electron endloss which correlates with these waves.

Two types of rf emission, referred to as whistler B (bursting) emission and whistler C (constinuous) emission, are observed in the Constance B experiment. Both types of emission are identified by dispersion relation calculations (Chapter 4) as the whistler instability. Experiments show that the whistler C emission is associated with off-axis magnetic field lines (Chapter 3) where the heating rate is expected to be higher. The whistler B emission occurs in fairly regular bursts and correlates with bursts of electron and ion endloss, and diamagnetism and potential fluctuations (see Fig. 1.1). It has frequencies in the range of 6.7–8.7 GHz when the midplane magnetic field is 3 kG, although the range is fairly insensitive to changes in the magnetic field. The whistler C emission has frequencies in a range which has a lower bound at approximately the upper bound of whistler B emission and an upper bound at the ECRH frequency of 10.5 GHz. The whistler C emission is

DIAMAGNETIC LOOP

RF EMISSION
    AT 8.575 Gc

RF EMISSION
    AT 8.575 Gc

NORTH ELECTRON ENDLOSS

RF EMISSION
    > 7.8 Gc

RF EMISSION
    AT 8.575 Gc

SOUTH ION ENDLOSS (mA)
    (AND ELECTRONS > 5 keV)

NORTH ELECTRON ENDLOSS (mA)
    (E > 100 eV)

NORTH ELECTRON ENDLOSS
    (E > 100 keV)

DIAMAGNETIC LOOP
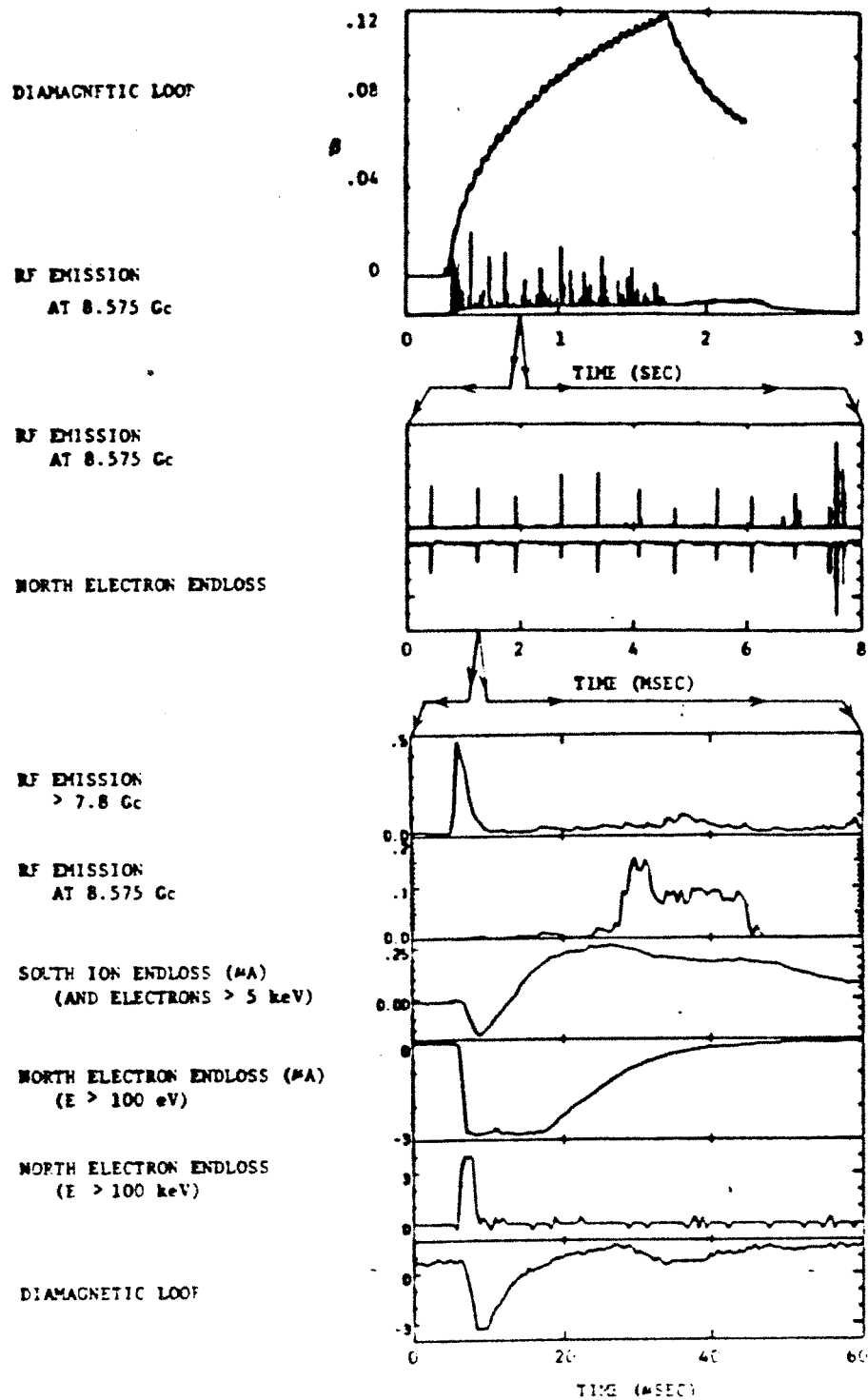
Figure 1.1: The whistler B rf emission and some other diagnostics which have correlating bursts. The three blocks of plots show data on different time scales.

14

seen continuously and is associated with continous enhanced electron endloss (see Fig. 1.2).

The goal of this thesis has been to understand the electron microinstability exhibited by the Constance B plasma. Particular emphasis has been placed on relating microinstability to different parts of the electron velocity space distribution of that plasma. This problem is of interest for several reasons. Among them are the following:

1) The Constance B plasma provides an excellent medium for studying the general problem of microinstability, which occurs in a wide variety of systems that are characterized by a non-Maxwellian velocity space distribution function. Some examples are laboratory fusion plasmas, electron beam devices used to generate microwaves, and atmospheric and space plasmas.

2) ECRH, mirror-confined plasmas are employed as endcells of tandem mirrors. These plasmas must be tailored correctly to produce both a plug potential and a thermal barrier. It is therefore important to understand the role microinstability plays in power loss, in degrading electron confinement, and in altering the velocity space distribution if the tandem mirror concept is to be used as the basis of a fusion reactor.

1.2   Previous Work

Research on electron microinstability has been motivated primarily by work in three areas:

1) Electron beam microwave devices: Early work in the 1950's lead to the developement of the gyrotron, which uses the cyclotron maser instability as a driving mechanism.

2) Ionspheric and magnetospheric plasmas: The auroral kilometric radiation is intense bursts of radio emission ($\lambda \approx 1$ km) coming from the earth's auroral zones. A
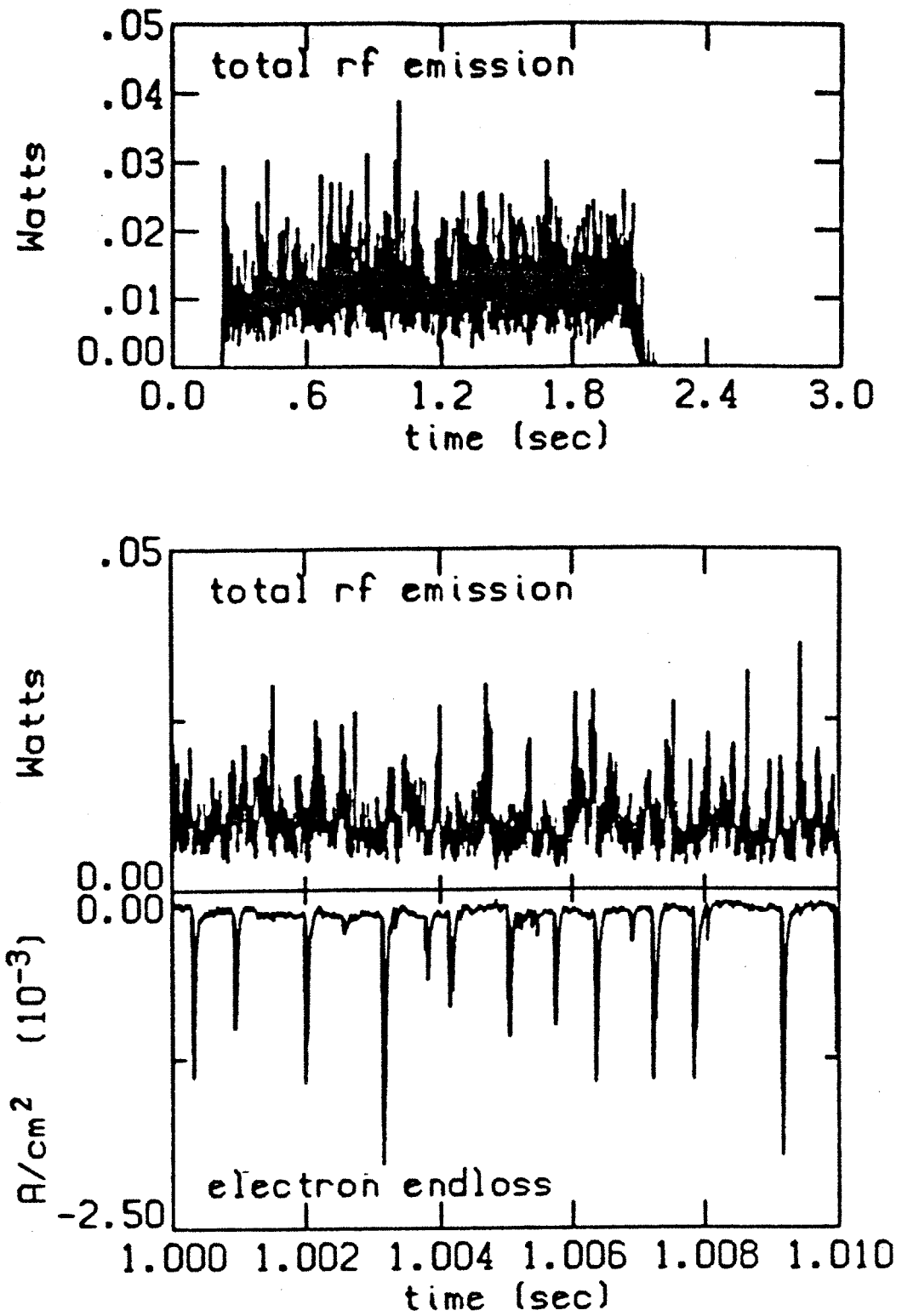
Figure 1.2: The whistler C rf emission and the axial electron endloss. It will be shown in Chapter 3 that the whistler C emission correlates with off axis endloss.

possible souce of this emission, and similar emission on the planet Jupiter (Jovian decametric radiation with $\lambda \approx 10$ m), is electron microinstability.

3) Magnetically confined laboratory plasmas: Microinstabilities have been found to occur in many different magnetic mirror experiments and dispersion relation calculations with mirror-like distribution functions predict microinstability.

1.2.1 Theoretical

Most of the previous theoretical work has involved solving the linearized Vlasov equation together with Maxwell equations for a variety of different distribution functions. Two mechanisms exist within the framework of this type of calculation which may lead to instability: the coupling of negative and positive energy waves, and the transfer of energy from resonant particles to waves. In general, the two mechanisms exist simultaneouly, however calculations can be done such that only one of the mechanisms exists in the model. For example, the distribution function which is typically used for modeling gyrotrons is a beam distribution: $\delta(p_\perp - p_{\perp o})\delta(p_{\parallel})/2\pi p_{\perp o}$. There are generally no resonant particles for this distribution function (except for special choices of $p_\perp$ and $p_{\parallel}$). The method of calculation done in this thesis (see Chapter 4) only considers resonant particle effects by approximating the Hermitian part of the relativistc Vlasov dispersion tensor with the cold fluid dispersion tensor. Instabilities derived using only the anti-Hermitian part of the Vlasov dispersion tensor are resonant particle driven instabilities.

Landau (1946) first showed that a transfer of energy from waves to particles is theoretically possible within the framework of a linear Vlasov–Maxwell formulation. His analysis has since been referred to as Landau damping. The inverse of Landau damping, or Landau growth, is the mechanism responsible for the instabilities considered in this thesis.

Sudan (1963) did one of the earliest analyses showing that temperature anisotropy could drive the whistler instability. His analysis used a bi-Maxwellian distribution

function and considered the case of $\mathbf{k} = k_\parallel \hat{z}$. It was initially nonrelativistic but he later extended his analysis (Sudan. 1965) using the relativistic Vlasov equation.

Subsequent analyses have involved the use of bi-Maxwellian distributions and loss cone distributions to primarily study the whistler instability and the upper hybrid loss cone instability. Lau and Chu (1983) showed that a loss cone distribution will drive the cyclotron maser instability, which previously was reserved for nonkinetic types of analyses with beam distributions. His analysis considered $\mathbf{k} = k_\perp \hat{z}$.

Lee and Wu (1980) performed a more general analysis than had been done in the past. They calculated ω_i using the anti-Hermitian part of the (weakly) relativistic[1] Vlasov dispersion relation, using a loss cone distribution and considering all directions of propagation. The normal modes of the plasma (ω_k) were calculated using the cold plasma dispersion relation. Their analysis was one of the first to treat several of the different instabilities in a unified way. It considered the whistler instability, and instabilities associated with the two fast wave branches (the fast wave X-mode, for 90°, and the fast wave R-mode, for 0° propagation, are sometimes called the cyclotron maser instability since the modes of propagation are similar to the same instability derived from a beam distribution). The motivation for their work was the study of the auroral kilometric radiation. The theoretical analysis presented in Chapter 4 of this thesis is done in a similar way except it is fully relativistic and uses a distribution function more suitable to describing the Constance B plasma.

Wong et al. (1982) studied the X-mode fast wave instability using a weakly relativistic Vlasov dispersion relation and considered all propagation directions. The improvement over earlier analysis by Lee and Wu (1980) was that they calculated the normal modes using the Vlasov dispersion relation as well.

Smith et al. (1983) studied the cyclotron maser and whistler instabilities with the relativistic Vlasov dispersion relation with $\mathbf{k} = k_\parallel \hat{z}$. He used a distribution function of the form $f(E, \theta) = f_1(E) f_2(\theta)$ where f_1 was typically taken to be a

---

[1]Weakly relativistic means that the following expansion was made: $\gamma^{-1} \approx 1 - v^2/2c^2$

18

Maxwellian and f_2 was chosen to model a loss cone. He studied the absolute versus convective properties of the instabilities. The motivation of the investigation was to understand the microinstabilities in the TMX-U endplug.

Gladd (1983) recently investigated the role relativity plays in the behavior of the whistler instability. He compared the relativistic and nonrelativistic Vlasov dispersion relations with a bi-Maxwellian distribution and considered $\mathbf{k} = k_{||}\hat{z}$. He showed that the relativistic formulation predicts smaller whistler wave growth rates than the nonrelativistic formulation but that it can never lead to stabilization of the wave. He also showed that relativity causes the whistler instability to be less susceptible to temporal growth (absolute instability) and more susceptible to spatial growth (convective instability).

Tsang (1984) recently investigated the whistler and cyclotron maser instabilities within the context of the same analysis so that a comparison could be made. He used the relativistic Vlasov dispersion relation with a bi-Maxwellian distribution that was set to zero in the loss cone, and with $\mathbf{k} = k_{||}\hat{z}$. He showed that the growth rates of both instabilties increase as the hot electron temperature is increased. He showed that the cyclotron maser instability is most severe for $k_{|} = 0$, is insensitive to $T_\perp/T_{||}$, and becomes more severe as the loss cone angle increases. His work on the whistler instability showed results similar to Gladd.

Chu and Hirschfield (1978) compared the whistler and cyclotron maser instabilities, both relavistic and nonrelativistic, in a unified treatment in which they solved the Vlasov dispersion relation with a beam distribution function and with $\mathbf{k} = k_{||}\hat{z}$. The cyclotron maser instability only appears in the relativistic treatment in this situation. They described a physical mechanism whereby the the whistler instability is driven by axial bunching and the cyclotron maser instability is driven by azimuthal bunching of electrons in response to a wave.

Bers and Ram solved the relativistic Vlasov equation with a beam distribution considering first (Bers and Ram, 1982) $\mathbf{k} = k_{||}\hat{z}$ and then (Bers *et al.*, 1983) $\mathbf{k} = k_\perp\hat{r}$.

Their analyses included the study of the absolute and convective nature of the instabilities.

The work of Bespalov (1982) is one of the few to address the issue of the bursting nature of the whistler instability. He showed that bursting is predicted by a quasilinear formulation whereby the electrons diffuse in the pitch angle direction in response to the whistler wave (a good approximation when ω is small compared to ω_{ce}), and the whistler wave grows due to positive density gradient of the distribution in the pitch angle direction. The diffusion and wave growth rate terms were approximations, but they contained the underlying physics of quasilinear theory. His model considered a constant particle source with a velocity space distribution function that was critical in determining whether or not instability would exist. The loss cone was a particle sink, to balance the particle source. A linear wave absorption term was included as well.

The quasilinear theory of Bespalov is a good first approximation to a quasilinear theory. It is successful because it predicts bursting. It suggests that the strength of the particle source is related to the burst rate (this is suggested in Constance B as well). It also suggests that a wave must have a minimum positive growth rate before it is viewed as an instability because absorption mechanisms may damp it out before it is observed outside the plasma. The theory is limited for ECRH plasmas because of its lack of an ECRH diffusion term. The inclusion of such a term would cause the theory to lose its simplicity of being a one dimensional (in velocity space) theory.

1.2.2 Experimental

Observations of the earth's auroral kilometric radiation have been made with the ISIS 1 satellite (Calvert, 1981) and the Hawkeye satellite (Gurnett and Green, 1978). These observations indicate bursts of fast electromagnetic waves polarized in the X-mode. The electron distribution function on an auroral flux tube has been measured (Omidi and Gurnett, 1982) with instruments on the S3-3 satellite and

indicate a loss cone type distribution, suggesting that the emission may be due to microinstability.

Single-cell magnetic mirrors were first built in the late 1950's. In the early years most attention was given to the MHD instability, which was the dominant effect leading to loss of plasma confinement. When this problem was solved with the introduction of the minimum-B configuration, particle confinement times were still much shorter than the classically expected confinement times and it was soon realized that microinstabilities were responsible. At first ion microinstabilities received more attention, but with the advent of the tandem mirror and various schemes for electron heating which lead to anisotropic electron distribution functions, electron microinstability became an important issue to understand.

Perkins and Barr (1968) investigated an electron microinstability which occured in a quadrupole, magnetic mirror in which the electrons were heated by adiabatic magnetic compression. They observed radiation at the electron cyclotron frequency and corresponding electron endloss. They measured the electron energy distribution both before and after the occurence of instability in order to assist in theoretical modeling. They found that before the instability the distribution function contained both a cold and hot component. After the instability there was a decrease in the hot density and an increase in the cold density. The hot component was measured to be a loss cone distribution. They did theoretical calculations with the electrostatic Vlasov dispersion relation, using a two component distribution function and concluded that the instability is what is now referred to as the upper hybrid loss cone instability. The basis of this identification was comparisons of instability thresholds with respect to hot particle fraction in both the theory and the experiment (i.e. they did not use the frequency arguments that are used in this thesis to identify instability).

Schwartz and Lichtenberg (1972) also performed an experimental and theoretical investigation of electron microinstabilities which occur in a mirror-confined plasma

in which the electrons were heated by adiabatic magnetic compression. They concluded. with the aid of theoretical calculations of the dispersion relation, that they observed an electrostatic microinstability (upper hybrid loss cone) early in the compression cycle, and an electromagnetic instability (whistler) later in the compression cycle. The early instability occured at frequencies at or slightly above the cyclotron frequency and the other instability occured at frequencies well below the cyclotron frequency. There theoretical analysis consisted of solving the three dimensional nonrelativistic Vlasov dispersion relation. The identification was based on matching experimentally measured frequencies of unstable emission to those occuring theoretically.

Ikegami *et al.* (1968) investigated the electron microinstability of an ECRH, mirror-confined plasma (maximum-B). They observed narrow band emission at 2.1 GHz and its harmonics for a midplane cyclotron frequency of 3.36 GHz and an ECRH frequency of 6.4 GHz. They observed corresponding electron endloss with average energy of 200 keV, the same as the hot electron component in the plasma. They used a scintillator probe to measure this, so they did not detect low energy electrons. They identified the instability as the whistler instability because the fundamental harmonic frequency of the instability satisfied the well known condition $\omega_i/\omega_{ce} \leq 1 - T_{\parallel}/T_{\perp}$, which gives an upper frequency bound of the whistler instability using a bi-Maxwellian distribution and for $k_{\perp} = 0$.

Blanken and Lazar (1971) investigated the instability of the ECRH, mirror-confined plasma (minimum-B) which served as a model for the design of Constance B. They observed bursts of narrow-band unstable rf emission at frequencies slightly above the midplane cyclotron fequency. They identified the instability as the upper hybrid loss cone instability, because the frequency occured above the midplane cyclotron frquency. Calculations done in conjunction with this thesis would identify it as the whistler instability. The failure to recognize the fact that the instability frequency was really associated with a higher cyclotron frequency off the midplane lead to their erroneous identification. They also observed corresponding bursts of

electron endloss with an average endloss energy of 1.1 keV, close to the average energy of the endloss bursts observed in Constance B (2 keV).

James and Ellis (1984) have studied the electron microinstability of the TMX–U endplug, in which the plasma is heated by ECRH and the magnetic field is a minimum-B configuration. They observe three types of rf emission which they identify as the whistler, cyclotron maser, and upper hybrid loss cone instabilities. They have measured the power of the unstable rf emission and conclude that it is negligible compared to the ECRH input power. They do not observe particle endloss. The whistler instability of TMX–U is similar in character to the whistler instability in Constance B. The rf emission identified as cyclotron maser and upper hybrid loss cone instability in TMX–U is not observed in Constance B. A possible explanation for this be that the ECRH power density is typically five times greater in the TMX–U endplug than in Constance B.

Booske *et al.* (1985) have studied the microinstability of an ECRH, mirror confined plasma (maximum-B). Before the plasma goes MHD unstable and loses confinement after a few milliseconds, it gives off one burst of radiation in the cyclotron range of frequencies. They identify the microinstability as the whistler instability by comparing the measured frequency spectrum to the theoretically calculated ones for a bi-Maxwellian distribution. The one burst that they observe is consistent with the observations of the Constance B whistler instability, which typically bursts once every millisecond (depending on pressure, power, and magnetic field).

1.2.3 Comparison to this Thesis

The experimental anaysis of this thesis has provided a detailed description of the whistler instability of an ECRH, mirror-confined plasma. Such a description has never before encompassed such a broad range of machine operating conditions (defined by ECRH power, magnetic field, and pressure). This detailed description has lead to the other major experimental discoveries about the whistler instability:

1) The warm electrons drive microinstability while the hot electrons are stable.

2) Differences in the electron heating characteristics at different radii lead to different whistler instability characteristics. On axis the electron endloss bursts at a fairly regular rate and correlates with the whistler B emission. Off axis the electron endloss occurs either continuously in time or at a very high, irregular burst rate. It correlates with the whistler C emission.

3) Although the hot electrons do not drive microinstability, they are nonetheless diffused into the loss cone when microinstability exists. For conditions of maximum microinstability the experimentally measured confinement time is 0.2 sec, which is 100 times less than the experimentally determined collision time. The microunstable waves and the applied ECRH waves are responsible for approximately the same amount of endloss for these conditions.

The theoretical analysis of this thesis has involved solving the linearized, relativistic Vlasov equation together with Maxwell's equations using a new distribution function (referred to as the ECRH distribution) that models an ECRH, mirror-confined plasma. The assumptions of the model are *a priori* justified by the calculated results for Constance B. The work is new because of its choice of a distribution function which describes the velocity space diffusion that electrons undergo in response to ECRH. The results, unlike past theoretical analyses, unambiguously identify the whislter instability of ECRH, mirror-confined plasmas. The extensive experimental investigation of frequency range as a function of magnetic field has made this identification with theory possible.

1.3   Organization

The organization of the thesis is as follows:

Chapter 2 describes the Constance B experiment. The first three sections describe the machine, some of the diagnostics used for this thesis, and the rf cavity effects of the vacuum chamber. The last section describes the plasma. It identifies three electron components and discusses the confinement properties of each.

Chapter 3 experimentally characterizes the microinstability through discussion of the unstable rf emission and the microinstability induced particle endloss. The first section presents the frequency spectrum for different magnetic fields, which is used, in conjunction with the calculations of Chapter 4, to identify the unstable rf emission as whistler instability. It then presents the power of the total unstable rf emission as a function of machine operating conditions. The next section presents the evidence which shows that the warm electron component drives microinstability while the hot component is microstable. The last section discusses the power and particle loss associated with the microinstability induced particle endloss.

Chapter 4 presents a theoretical model to describe microinstability. A dispersion relation is used that is derived from the linearized, relativistic Vlasov equation together with Maxwell's equations. Arguments are presented which indicate the necessity of choosing a warm electron distribution function which describes the velocity space diffusion that such electrons undergo in response to ECRH. A new distribution function, referred to as the ECRH distribution, is introduced which has this property. The model is successful in identifying and describing the microinstability of the warm electrons. The results of theoretical calculations are related to the experimental results of Chapter 3.

Chapter 5 provides a summary of the results of the experimental and theoretical analyses of microinstability, briefly discusses it implications on tandem mirror physics, and provides suggestions for future work.

Chapter 2

The Constance B Experiment

This chapter presents an overall description of the Constance B experiment. Section 2.1 gives a general description of the Constance B machine. Section 2.2 describes the diagnostics used in this thesis. Section 2.3 discusses the behavior of the vacuum chamber as an rf cavity. This is needed to relate the rf power detected by the rf detection system to the rf power emitted by the plasma. Section 2.4 gives a description of the events during a typical shot. Section 2.5.1 provides a description of the Constance B plasma. The first part identifies and describes the three electron components: the cold, warm, and hot components. The second part discusses the experimentally measured confinement times of each component and relates them to the respective collisional loss times. It is found that the warm and hot component collision times are respectively 10 times and 100 times less than the collisional loss times for those components (for the pressure at which endloss is the greatest). This is in part due to microinstability, which is discussed in Chapter 3.

2.1 General Description

Constance B is a single-cell, minimum-B magnetic mirror in which the plasma is created and the electrons are resonantly heated by microwaves. A picture of Constance B appears in Fig. 2.1 and a schematic diagram showing some diagnostics appears in Fig. 2.2.
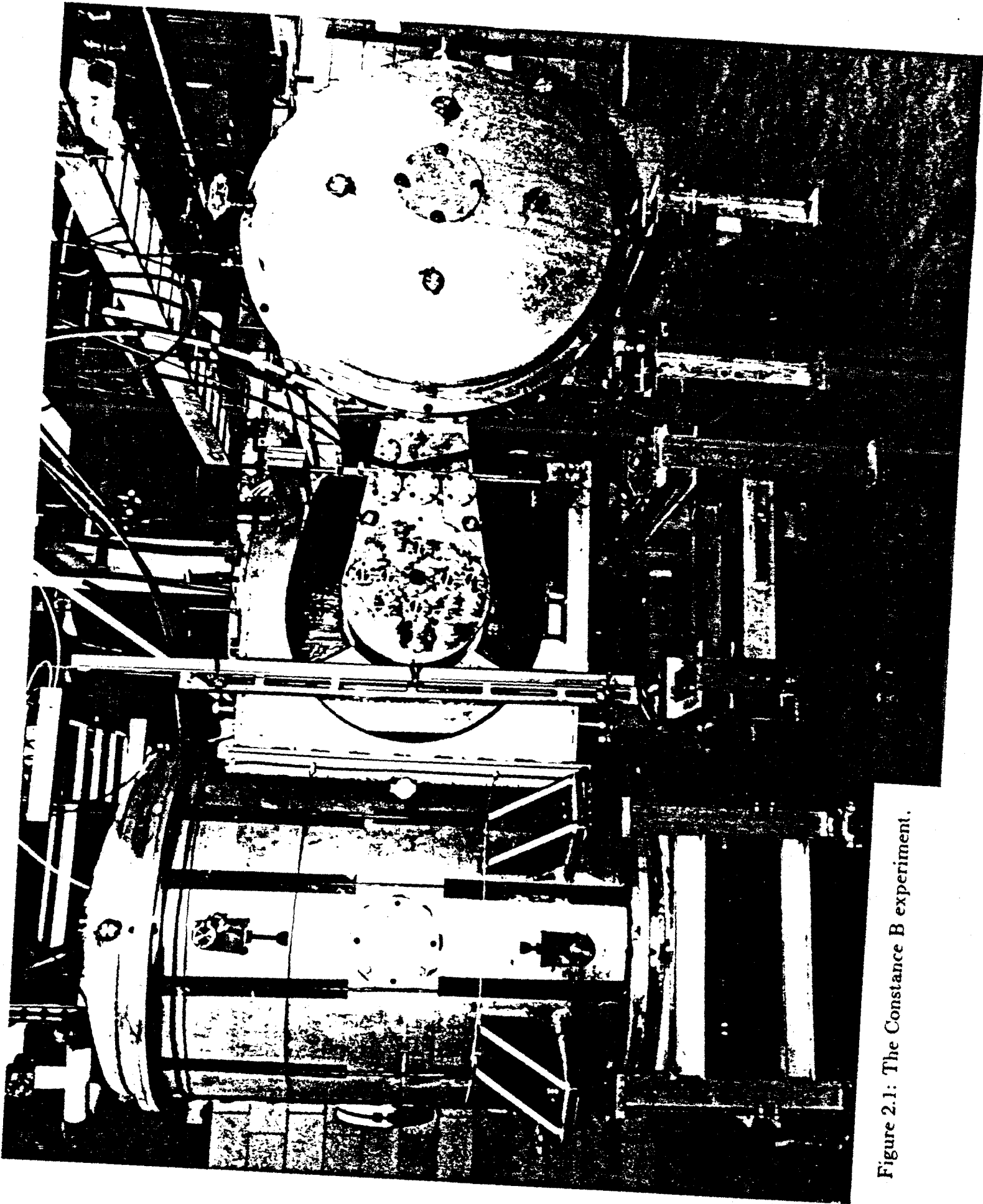
Figure 2.1: The Constance B experiment.
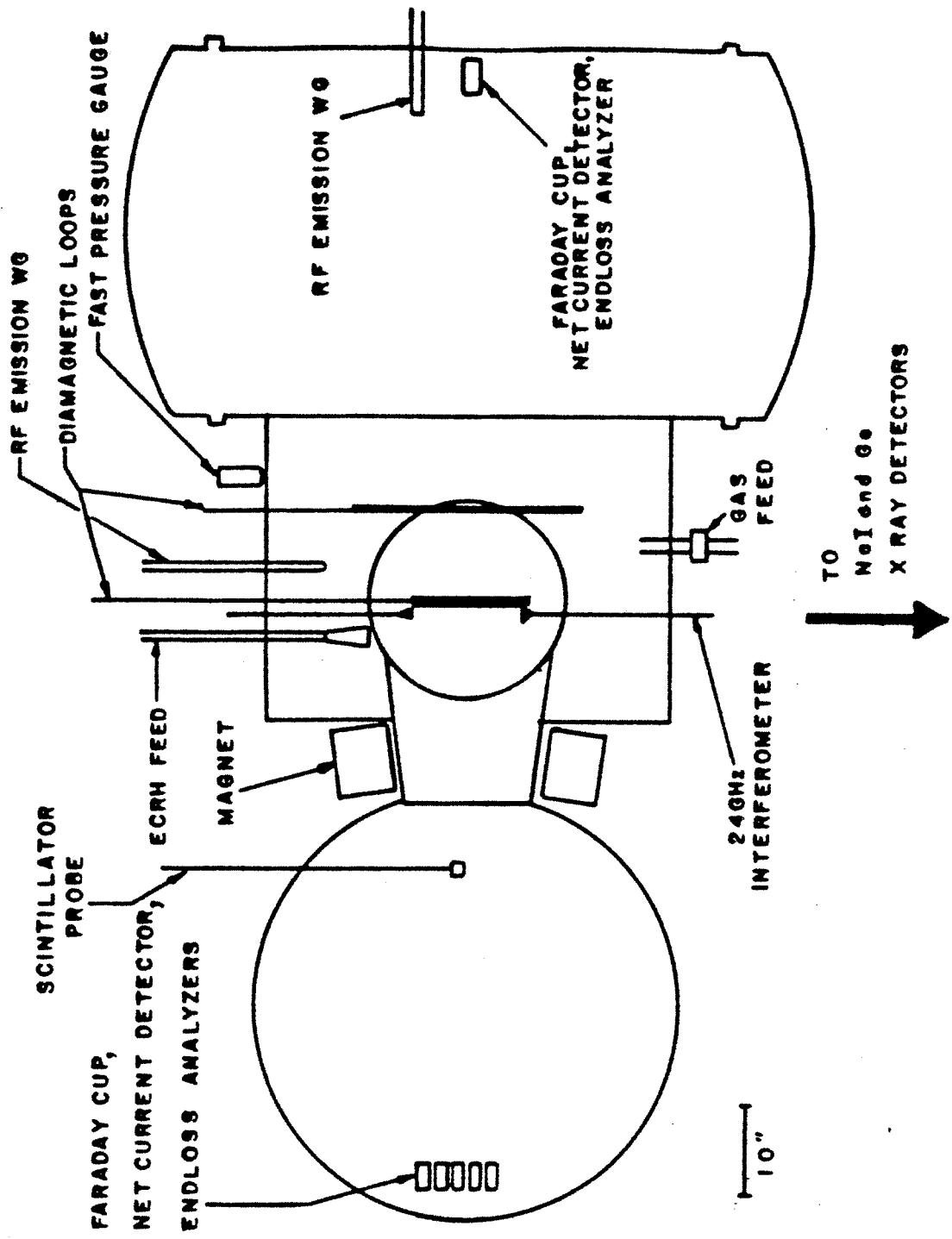
Figure 2.2: The Constance B experiment with diagnostics.

Microwaves are produced by a Gunn diode and amplified by a klystron (Varian model VA-1911) which delivers up to 3 kW at 10.5 GHz with a bandwidth of 1 MHz. XL band waveguide is used to direct the microwaves from the output of the klystron to the inside of the vacuum chamber. A 17 db horn is located at the waveguide termination inside the vacuum chamber approximately 50 cm from the axis and is directed perpendicularly at the axis 10 cm north of the midplane. The waves are lauched primarily in the O-mode (electric field parallel to z axis).

The magnetic field is produced by a coil shaped like the seam of a baseball. Fig. 2.3 shows some field lines and $|B|$ contours in the vertical plane. Each field line is a magnetic mirror with its own mirror ratio and resonance location. The resonance surface, defined by $f_{ce} = f_h$ (f_h is the ECRH frequency), is egg-shaped with a 30 cm length and a 10 cm radius when the midplane field on axis is 3 kG. The circular flux surfaces at the midplane map to approximately elliptical flux surfaces at the endwall with a major radius to minor radius ratio of 40. The mirror ratio on axis is 1.8. The ratio of the magnetic field at the midplane on axis to the magnetic field at the endwall on axis is approximately 37.[1]

The baseball coil is located outside of the vacuum chamber, electrically isolated from it, and braced to prevent any movement during operation. The midplane magnetic field on axis is typically 3000 Gauss. For this field the magnet is capable of operating for as long as 10 sec. This time limit is set by the maximum flow of the cooling water throught the conductor.

The 5000 liter aluminum vacuum chamber consists of three sections and is specifically designed for the magnetic field geometry of the baseball magnet. The center chamber consists of two welded pieces which fit within the baseball magnet. The resonance zone and therefore the hot electrons are within the center chamber. Plasma that escapes as endloss flows into either of the two fan tanks located on both sides of the central chamber. The fan tank walls are relatively far away from the center

---

[1] All magnetic field calculations were done with the computer code EFFI which is available to users of the MFE-LLL computer system. EFFI was written by S. Sackett and can be referenced in LLL report no. UCRL-52402.
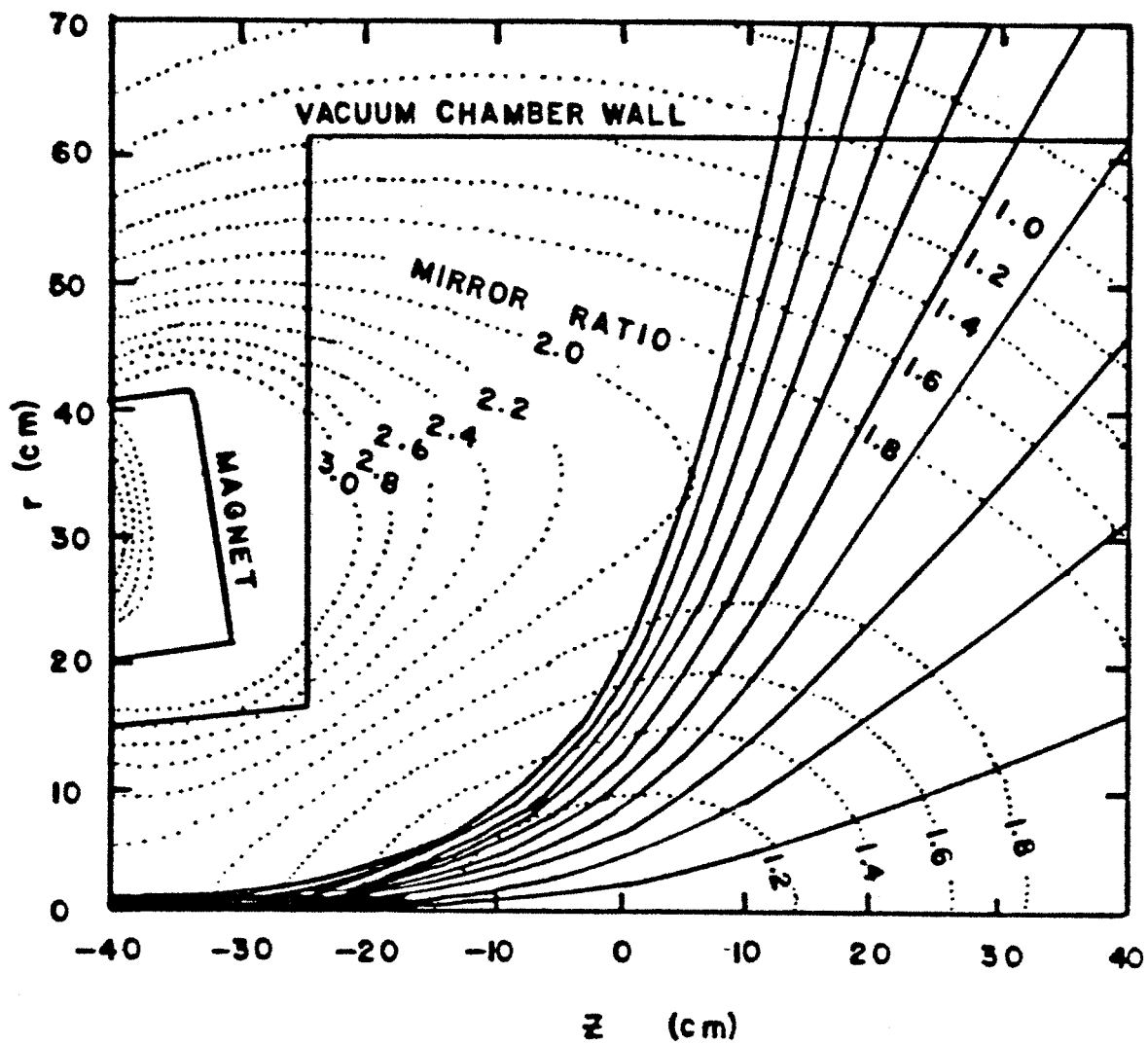
Figure 2.3: Constance B magnetic geometry.

so that interactions between wall and endloss plasma have a relatively minor effect on the core plasma. All access ports are covered by either metal flanges or by glass flanges with wire mesh in front so that the inside of the chamber constitutes a high Q ($\sim 10^4$) rf cavity resonator (additional discussion of this and its relevance to interpreting data occurs in Section 2.3). The vacuum chamber is behind a concrete wall to shield the operators from x-rays that are produced due to the presence of hot electrons.

The vacuum is maintained by a single turbomolecular pump (Airco model 514), which provides 265 liter/sec of pumping speed, and four titanium getters. The base pressure is typically in the range of 1×10^{-8} to 5×10^{-8} Torr. A base pressure higher than this may impede experimentation. In producing plasma the pressure of hydrogen gas puffed into the chamber is typically 1×10^{-6} torr but can be as low as 2×10^{-7} Torr.

A process controller (pc) (Gould model 484) controls the timing sequence of the experiment as well as the magnetic field strength and various safety interlocks. A shot is initiated by the pc which then sends triggers to various locations (e.g. magnet controller, klystron, and data acquisition system) at the desired times. The operator has direct control over the magnetic field amplitude, the pressure of the hydrogen gas puff, the ECRH power, and the start and end times of each of these.

2.2 Diagnostics

The principle diagnostics used in this thesis are the gridded, electrostatic endloss analyzers, the rf detection system, diamagnetic loop, hard and soft xray detectors, a scintillator probe, Faraday cups, and an interferometer (see Fig. 2.2). A CAMAC-based data acquisition collects data and sends it to a VAX 11/750 computer for processing between shots.

Endloss Analyzers

The endloss analyzers, located on the ends of both fan tanks. measure the endloss current. This is comprised primarily of particles which, for one of several reasons, are kicked into the loss cone of velocity space. These reasons include pitch angle scattering due to collisions and scattering due to interaction with ECRH or unstable waves (discussed in later chapters). The endloss analyzers are used in this thesis to study the short bursts of electron endloss ($\sim$ 5-10 μsec in duration) induced by the microinstability and for determining the cold electron endloss temperature.

The north fan tank contains one endloss analyzer located on the machine axis. The south fan tan contains five identical endloss analyzers lined up symmetrically about the axis along the thin dimension of the elliptical flux surface (the fan). The north endloss analyzer was designed by Mauel (1982) and was originally used for the Constance 2 experiment. The south endloss analyzers are modified versions of the ones designed by Klinkowstein (1983) for the Tara tandem mirror experiment. The two major issues involved in the design of the endloss analyzers are 1) the spacing between the grids must small enough so that expected endloss current does not exceed the space charge limited current and 2) a particle which get through the analyzer opening must not hit the wall (because of its nonzero Larmor radius) before hitting the collector.

The endloss analyzers can measure the total endloss current. as well as the ion and electron endloss current separately. The current is determined by measuring the voltage V_{el} across a resistor R placed from the collector to ground. The steady state endloss current is given by

$$I_{el} = T_{el} A_{el} \frac{V_{el}}{R} \frac{B_{wall}}{B_{mid}} J_{mid} \qquad (2.1)$$

where T_{el} is the grid transmission coefficient, A_{el} is the area of the collector, B_{wall} is the magnetic field amplitude at the fan tank, B_{mid} is the midplane magnetic field. and J_{mid} is the effective endloss current density at the midplane.

A measurement of current from an endloss burst induced by whistler instability is affected by the capacitance of the cables between the analyzers and the diagnostic racks. Fig. 2.4 shows the equivalent circuit. R is typically chosen to be 50 kΩ and the measured value of C is approximately 100 pF, making RC approximately 5 μsec. This is comparable to the endloss burst time, which is typically 5−10 μsec. It is not necessary to know the capacitance if the desired quantities are the total number of particles and the total energy per burst. The total number of particles in a burst is computed from the total charge in a burst, which is given by

$$Q_{el} = \int_0^{\tau_b} I_{el}(t')dt'$$

$$= \int_0^{\tau_b} \left(C\frac{dV_s}{dt'} + \frac{V_s}{R} \right) dt'$$

$$= \frac{1}{R} \int_0^{\tau_b} V_s(t')dt' \tag{2.2}$$

where V_s is the measured voltage signal, τ_b is the duration of a burst, and it has been recognized that $V_s(0) = V_s(\tau_b) = 0$. The total energy in a burst is then the product of the average particle energy in a burst (determined by the analyzers) and the total number of particles in a burst.

The endloss analyzers can measure the energy distribution of the endloss of each species by appropriate biasing of the repeller grids. The upper limit for this measurement is 5 keV which is determined by the breakdown voltage of the grids. A lower limit for this measurement for electrons is 30 eV because there must be at least −30 volts on the grid nearest the collector to turn back secondary electrons coming off and traveling away from the collector.

Rf Detection System

Fig. 2.5 shows a diagram of the rf detection system. An open-ended, XL band rectangular waveguide (low cutoff of 5.4 GHz), oriented in a direction facing the plasma from one of several locations in the vacuum chamber wall, detects rf emission from the plasma. It is coupled to an elliptical waveguide (low cutoff frequency of
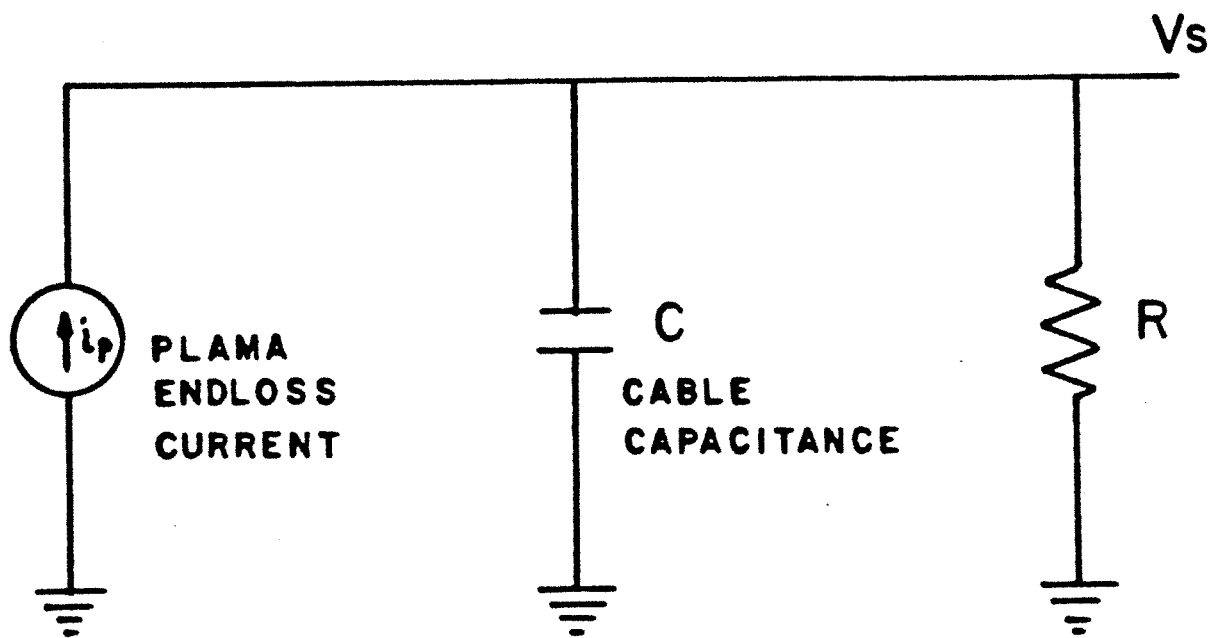
Figure 2.4: Equivalent endloss analyzer circuit.

RF EMISSION FROM PLASMA

OPEN ENDED XL BAND WG

VACUUM CHAMBER WALL

30 ft. ELLIPTICAL WAVE GUIDE

40 dB COUPLER

RF DETECTOR

A/D (1 kHz)

HP 8441A YIG FILTER

HP 8551B SPECTRUM ANALYZER

3 dB COUPLER

ATTENUATOR

HP 851 DISPLAY SECTION

VAX 11-750

10.5 GHZ NOTCH FILTER

RF DETECTOR

x1

x10

A/D (1kHz)

A/D (400 kHz)

A/D (1kHz)

A/D (400 kHz)
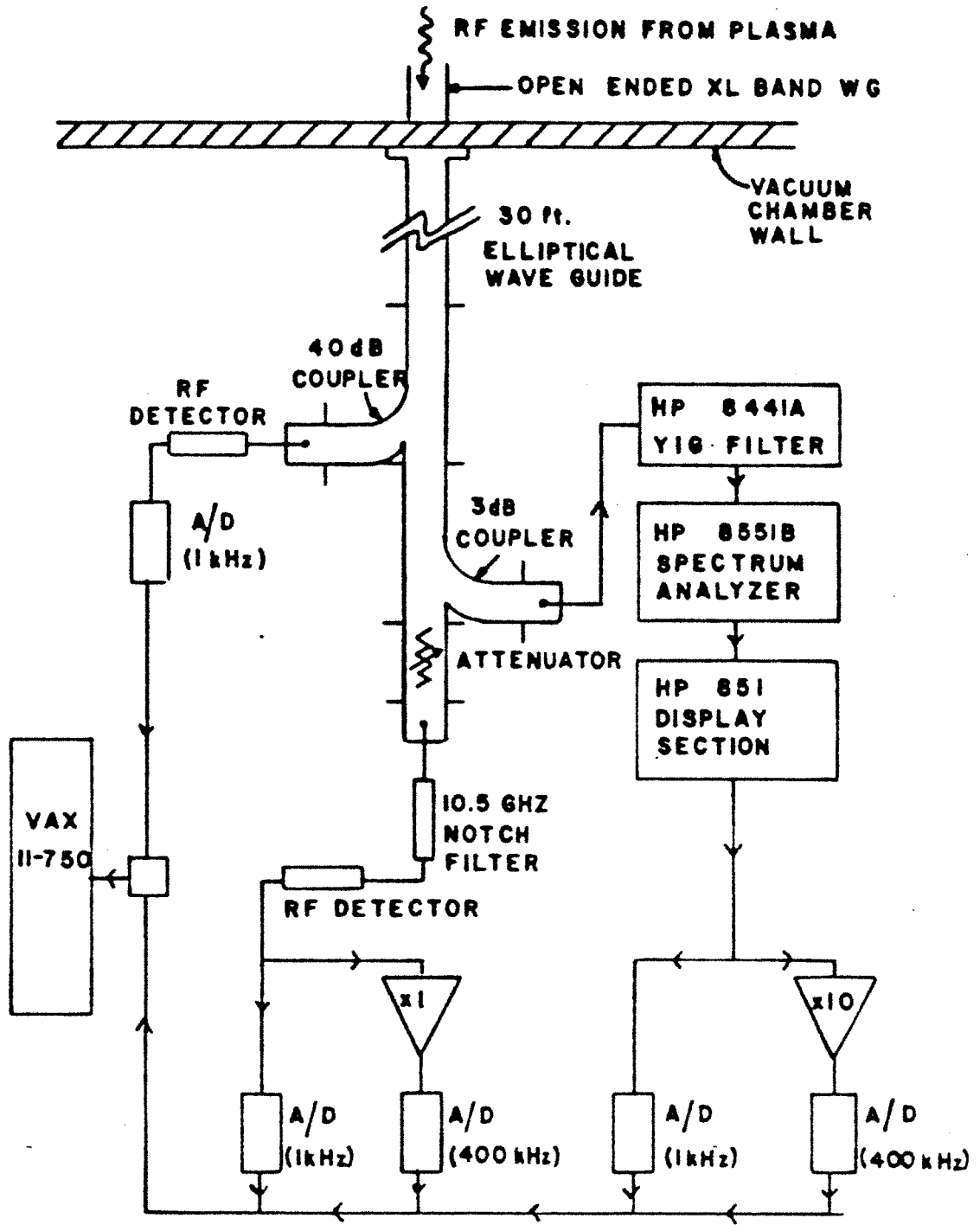
Figure 2.5: The rf detection system.

5.25 GHz) which directs the rf to the diagnostic racks. A coupling back to XL band waveguide follows and two directional couplers split the rf along three paths. The rf in each path is analyzed in a different way and three types of information are determined: 1) the total power, 2) the total power minus the power at 10.5 GHz, and 3) the power in a 1 MHz wide band about some specified frequency (> 5.25 GHz). These powers refer to the power detected and directed through the rf detection system. The relationship between this and the power emitted by the plasma, which is dependent on the cavity effects of the vacuum chamber, will be discussed in Section 2.3

1) The total power is determined with a high frequency diode (Omni Spectra model 20760). The power in this path is primarily the ECRH cavity power, however a burst of whistler emission is usually greater than this. The voltage across the diode is related to the microwave power incident on the diode by a power law, experimentally determined to be $P_{rf} = 4.17 \times 10^{-3} V^{1.51}$, with V in volts and P in Watts. This relation is valid for frequencies in the range of $1-15$ GHz. There is a 100 nsec delay between the beginning of a test pulse sent into the diode and the beginning of the response. This same delay exists when the test pulse goes off. There is a 2 μsec rise time and decay time in the response. Thus, the diode does not perform an accurate instantaneous power measurement on a $5-10$ μsec burst. Since the area under a pulse is preserved by the electronic distortions, a burst of rf emission is analyzed by integrating the pulse to obtain the total rf energy in a burst. The diode will accurately determine the average power of the continuous whistler C emission.

2) The total power minus the power at 10.5 GHz is referred to in Chapter 3 as the total rf emission. A 50 db notch filter (custom made by Daden Associates, Inc.), centered at 10.5 GHz with a full width at half maximum of 15 MHz, filters out the 10.5 GHz power. The remaining power is then measured with another high frequency diode of the same type mentioned above, which has the experimentally determined transfer function $P = 1.57 \times 10^{-3} V^{1.17}$, with V in volts and P in Watts.

3) The final signal is referred to in Chapter 3 as single frequency emission. The rf first goes to a preselector (HP model 8441A) which uses a YIG (yttrium-iron-garnet) filter to select a 15 MHz wide band about some specified frequency ($<$ 12 GHz). The signal is then routed to a spectrum analyzer (HP model 8551B with the HP model 851 spectrum analyzer display section). The spectrum analyzer determines the amount of power in a 1 MHz wide band about the specified frequency.

In determining the frequency of the rf emission the preselector is necessary to ensure that only the desired frequency is detected by the spectrum analyzer. The frequency select knob of the HP Model 8551B spectrum analyzer controls the frequency of the local oscillator (LO) of a mixer inside the unit. The LO is $2n$ GHz less than the frequency which is being measured, where n is an integer dependent on the frequency range selected for the spectrum analyzer. The incoming rf signal which is being analyzed enters the RF port of the mixer, is mixed to $2n$ GHz, and appears on the IF port of the mixer. The power of the $2n$ GHz wave is determined by the spectrum analyzer. The problem inherent in using a mixer is that an incoming rf wave may mix with any harmonic of the LO (although the IF associated with the upper harmonics contain less power than the IF associated with the fundamental harmonic):

$$f_{if} = f_{rf} \pm m f_{lo} \qquad (2.3)$$

where m is any integer. The undesirable result is that either a single frequency incoming rf wave will be detected at many different frequencies, or many different frequencies will be detected at the same frequency. The first effect can be accounted for by proper calibration of the system. However, the second effect can only be eliminated by using a filter on the input of the spectrum analyzer to ensure that only the desired frequency enters.

The HP 8441A/8551B/851B rf detection system has been calibrated for the 2–10 GHz range (mixing with the $n = 2$ harmonic of the LO) and for the 4–12.4 GHz range (mixing with the $n = 3$ harmonic of the LO) of the 8551B spectrum analyzer (and for some additional settings given below). For these two ranges the

37

output voltage V_s of the model 851B display section (the signal recorded by the data system) is related to the power input to the model 8441A preselector by the following relationships:

$$2\text{-}10 \text{ GHz range:} \quad P_{rf} = 10^{(-1.5V_s - 7.5)}$$
$$4\text{-}12 \text{ GHz range:} \quad P_{rf} = 10^{(-1.5V_s - 5.3)}$$

where V_s is in volts and P_{rf} is in Watts. This pertains to the following setup for the spectrum analyzer and display sections:

IF gain:	68 dB
IF bandwidth:	1 MHz
spectrum width:	1 MHz (no sweep)
vertical display:	logarithmic

Diamagnetic Loop [2]

A circular diamagnetic is located 2.5 cm off the midplane, centered on the axis, and measures the change in magnetic field due to plasma currents. The integrated diamagnetic loop signal provides a number which is proportional to the perpendicular energy density $nT_\perp$, as is shown below. The constant of proportionality is dependent on the plasma geometry. The voltage induced across the loop is related to the flux in the loop by

$$V_l = -n_t \frac{d\phi}{dt} \tag{2.4}$$

where n_t is the number of windings in the loop. The signal is actively integrated (Evans Electronics Model 4130A Gated Integrator Module) so that $\phi(t)$ is ascertained. The flux is related to the plasma currents by

$$\begin{aligned} \phi &= \int_{loop} \mathbf{B} \cdot d\mathbf{S} \\ &= \oint_{loop} \mathbf{A} \cdot d\mathbf{l} \\ &= \oint_{loop} d\mathbf{l} \cdot \left(\frac{\mu_o}{4\pi} \int \frac{\mathbf{J}(\mathbf{r}')}{|\mathbf{r}' - \mathbf{r}|} d^3\mathbf{r}' \right) \end{aligned} \tag{2.5}$$

---

[2] The diamagnetic loop was set up and software to interpret the integrated signal was written by Xing Chen.

38

Therefore, ϕ is some complicated function of the plasma geometry. If a fluid-like equilibrium is assumed then

$$\mathbf{J}_\perp = \frac{\mathbf{B} \times \nabla \cdot \mathbf{P}}{|\mathbf{B}|^2} \qquad (2.6)$$

where $\mathbf{P}$ is the pressure tensor, $\mathbf{J}_\perp$ is the current density perpendicular to the magnetic field, and the gradient operator is with respect to flux coordinates defined by the magnetic field direction. For Constance B it is assumed that $\mathbf{J} \approx \mathbf{J}_\perp$ and that $\dot{\mathbf{J}}_{\parallel}$ is a second order quantity which is induced by parallel electric fields that buildup as the plasma attempts to maintain $\nabla \cdot \mathbf{J} = 0$. For a mirror $P_{\parallel}$ and $P_\perp$ are related by

$$P_\perp = P_{\parallel} + B \frac{\partial P_{\parallel}}{\partial B} \qquad (2.7)$$

If $P_\perp$ is written as $nT_\perp$, where n is the density, then Eqs. 2.5 and 2.6 imply that $\phi \propto nT_\perp/B$, or simply $nT_\perp$ if B is approximated by the time independent vacuum magnetic field.

X-ray Detection[3]

The x-ray detection system detects and discriminates the energies of bremsstrahlung x-rays with energies greater than 2 keV. A NaI crystal detector is used for energies above approximately 100 keV and a germanium detector complements this measurement and is used for energies down to 2 keV. An x-ray entering the NaI crystal interacts with the crystal by creating visible light photons with a characteristic wavelength of the crystal. The number of photons, or scintillations, equals the energy of the x-ray divided by the scintillation photon energy, multiplied by an efficiency which is a function of x-ray energy and the geometry of the NaI crystal. The light is detected with a photomultiplier tube. An x-ray entering the germanium detector creates electron-hole pairs in the semiconductor. The number of electron-hole pairs equals the energy of the x-ray divided by the characteristic transistion

---

[3]The x-ray detection system was built and most of the x-ray data was analyzed by Sam Hokin.

energy needed by the electron to get to the conduction band, multiplied by an efficiency which is a function of x-ray energy. The germanium acts as a current source in an RC circuit and electrical pulses are generated as the x-rays are detected. For both detectors a preamplifier is placed on the output and the pulses are sent to a spectroscopy amplifier (Canberra Model 2010) which smooths out pulses into a Gaussian shape. In order that a single pulse corresponds to a single x-ray the x-ray count rate must be attenuated until it is below 75 kHz, the maximum rate at which the spectroscopy amplifier can detect and smooth pulses. The pulses are then collected and discriminated by the CAMAC-based data acquisition system. The information is stored and processed with a VAX 11/750 computer.

The intensity of x-rays with frequencies in the interval between ω and $\omega - d\omega$ at position z along the axis is given by

$$I(\omega, z) = \underbrace{\int dy R(0, z) \eta(y_o(y, z)) n_t(y, z)}_{radial\ effects} \int_0^1 d\lambda \int_\omega^\infty d\epsilon \sqrt{\epsilon} G(\epsilon, \omega) f(\epsilon, \lambda_o) \qquad (2.8)$$

where $R(y = 0, z)$ is the local mirror ratio, $y_o(y, z)$ is the midplane y position to which the local (y, z) position maps, $\eta(y_o)$ is the fractional electron density at the radial y_o position normalized to 1 at $y_0 = 0$, $n_t(y, z) = \sum_s Z_s^2 n_s(y, z)$ is the total Z^2 weighted target density, $\lambda = \cos\theta$, $G(\epsilon, \omega)$ is the bremsstrahlung cross-section, and $f(\epsilon, \lambda_o)$ is the electron distribution function at the midplane normalized to 1. Eq. 2.8 assumes that the distribution maps to different magnetic field locations along a given field line by the free particle orbits. It is a difficult task to determine the electron distribution from a knowledge of $I(\omega, z)$ in the manner given by Eq. 2.8. This thesis is concerned with the behavior of the electron microinstability with respect to different portions of the electron velocity space distribution function. Therefore, the information needed to be deduced from the x-rays is the number of different electron components there are (which differ according to their pitch-angle integrated temperature) and how the temperatures of each component vary in time and with respect to machine operating conditions. If there are no radial

temperature variations then it suffices to neglect radial profile variations, variations in target density and species, and to concentrate on the x-ray spectrum at the midplane. The distribution function is assumed to be of a certain form, the integral of Eq. 2.8 is performed, and the shape is compared to the shape of the experimentally determined $I(\omega, z = 0)$.

Scintillator Probe[4]

A small, cylindrically-shaped piece of plastic NE102 is used as a scintillator probe to detect hot electron endloss. Its cross section is square with a length of 4 mm. It is epoxied onto a stalk so that it can be moved inside the vacuum chamber between shots. A photo-diode detects the light signal it produces in response to the hot electrons. It is relatively insensitive to x-rays because of its small size and the relatively low x-ray flux. Windows of particular thickness are put in front to discriminate electron energies. The thinnest window allows for detection of electrons with energies greater than 50 keV.

There is a conversion factor which relates the current out of the photo-diode to the power of hot electrons incident on the scintillator. The scintillator theoretically converts 3% of the incident power into light energy at 420 nm. The photodiode produces 4 mA for every 5 mW/cm^2 of light energy incident on it at the wavelength for which it peaks. At 420 nm this efficiency is reduced by 20%. The photo-diode area is 0.16 cm^2 and the scintillator area is 0.1 cm^2. The conversion factor is then

$$\frac{\text{photo-diode current (mA)}}{\text{incident electron power (mW)}} = \frac{4\text{mA}}{5\frac{\text{mW}}{\text{cm}^2} \times 0.1\text{cm}^2} \times 0.03 \times 0.16\text{cm}^2 \times 0.2 = 3.8 \times 10^{-3}$$

(2.9)

This conversion factor does not take into account the light that is reflected at the interface between the photo-diode and the scintillator. Light that is reflected back at the interface may undergo additional reflections at the other scintillator boundaries and eventually get collected by the photo-diode. In addition, when an

---

[4]Built by Sam Hokin.

electron causes a scintillation half of the light is radiated in the backward direction which, again, may be reflected off the scintillator boundaries and eventually be collected by the photo-diode. Since it is not known how much of an effect the scintillator boundaries, and the interface with the photo-diode have, the conversion factor is uncertain by a factor of 2. The hot electron endloss power deduced is thus a lower bound to within a factor of 2.

Interferometer[5]

A 24 GHz microwave interferometer is used to measure the line averaged electron density. Waves polarized with their electric fields parallel to the z axis pass through the plasma at the midplane. The dielectric for these O-mode waves in cgs units is

$$\epsilon = 1 - \frac{\omega_p^2}{\omega^2} \left\langle \frac{1}{\gamma} \right\rangle \tag{2.10}$$

where

$$\left\langle \frac{1}{\gamma} \right\rangle = \left\langle \left(1 - \frac{v^2}{c^2} \right)^{1/2} \right\rangle \tag{2.11}$$

is an approximate relativistic correction (Mauel, 1985). The phase shift between waves traveling an equal distance l through plasma and through air (approximately a vacuum for 24 Ghz) is

$$\Delta\phi = \int_0^l dr \frac{\omega}{c} \left(\sqrt{1 - \frac{\omega_p^2(r)}{\omega^2} \left\langle \frac{1}{\gamma} \right\rangle} - 1 \right) \tag{2.12}$$

where $\omega_p^2(r) = 4\pi n_e(r) e^2/m_e$. Assuming $\omega_p^2 \ll \omega^2$ (which turns out to be approximately .03 after performing the measurement) Eq. 2.12 can be written

$$\Delta\phi \approx \int_0^l dr \frac{\omega_p^2(r)}{2\omega c} \left\langle \frac{1}{\gamma} \right\rangle \implies \frac{1}{l} \int_0^l n_e l dr \equiv \langle n_e l \rangle = \frac{m_e^2 \omega c \Delta\varphi}{2\pi e} \left\langle \frac{1}{\gamma} \right\rangle^{-1} \tag{2.13}$$

---

[5]The interferometer hardware was set up by Donna Smatlak and software to interpret the data was written by Evelio Sevillano

42

Therefore, the line averaged density across the plasma radius can be determined from the phase shift and an approximation for $\left\langle \frac{1}{\gamma} \right\rangle$. The relativistic correction implies that hot electrons are more transparent to waves than cold electrons because they cause a smaller phase shift.

Data Acquisition

Data acquisition is performed with a CAMAC-based data acquisition system (LeCroy) in conjunction with a VAX 11/750 computer (Digital Equipment Corporation). There are two types of data with respect to the data acquisition system : 1) slow time scale data collected during the entire shot with a LeCroy model 8212A analog-to-digital converter set at a 1 kHz digitization rate and 2) fast time scale data collected in a 40 msec time span during the shot with a LeCroy model 2264 analog-to-digital converter set at a 400 kHz digitization rate. For the slow time scale data 4196 samples can be stored per shot. This defines the "entire shot" to be approximately 4 sec long. The fast time scale data is typically collected to allow 16784 samples to be stored per shot.

Signals relevant to the study of microinstability must collected in the fast time scale fashion since they fluctuate on the order of several microseconds and the time between these fluctuations is on the order of 1 msec. These signals include the signals from the rf detection system, the endloss analyzers, and the diamagnetic loop. The signals are split up and collected in the slow time scale fashion as well. Amplifiers with 1 MΩ input impedance (Tektronix model AM-502) are employed as buffer amplifiers. The rest of the signals are collected in the slow time scale fashion.

To determine the x-ray energy spectrum the signals from the x-ray detectors are also collected by a LeCroy model 3512 analog-to-digital converter in conjunction with a LeCroy model 3587 data router and a LeCroy model 3588 histogramming memory module. The data router takes the pulses produced by the x-ray detectors and places them in the correct memory bin of the histogramming memory module

43

which then adds up the pulses according to their size. A spectrum is typically taken every 100 msec and 30 spectra are taken during the entire shot.

Miscellaneous Diagnostics

Five Faraday cups and five net current detectors are at the end of the south fan tank parallel to the south endloss analyzers. A Faraday cup and a net current detector are at the end of the north fan tank and are on stalks which can move across the thin dimension of the plasma fan. The Faraday cups can measure total ion or total electron endloss current. A photo diode with a H_α filter in front is used to monitor the H_α light. Emissive probes for local plasma potential measurements, Langmuir probes, and skimmer probes are available.

2.3 Vacuum Chamber as an Rf Cavity

The relationship between the power detected by the rf detectors and the power emitted by the plasma is dependent on the cavity effects of the vacuum chamber. The Constance B vacuum chamber is an rf cavity with an extremely complicated modal pattern due to the irregular shape of the walls, the ports in the walls, and various diagnostics and other pieces of metal inside the chamber. The chamber has a measured Q of approximately 10^4 ($\delta f \approx 1$ MHz for $f = 10.5$ GHz). Waves emitted by the plasma are expected to settle into a steady state chamber mode in the time it takes a wave to make several bounces around the vacuum chamber at the speed of light. For example, considering 10 bounces and 3 meters per bounce (both high estimates) gives a time of 0.1 μsec, much shorter than the several microsecond burst time of the whistler instability.

Experimental justification of the cavity-like nature of the vacuum chamber is shown by the response of an rf detector to a test wave put into the chamber. A short waveguide section was placed at several different locations on the vacuum chamber wall. One end was left open-ended looking into the chamber. The other end had a diode detector placed across its output (see Section 2.2 for a description

44

of the diode). The waveguide section was movable along its axis so that the position of its open end could be varied. Approximately 100 W of rf power from the ECRH transmitter was put into the chamber from the standard ECRH waveguide location (see Fig. 2.2).[6]

The power received by the detector can be classified as either direct power or cavity power. The direct power is the power that the detector picks up directly from the source. Without the detector the waves would reflect from the wall (or be partially absorbed by it) to become part of the cavity power. The cavity power is the electromagnetic radiation that has undergone several bounces and forms the cavity mode. A receiver detects power according to its gain characteristics:

$$P_r = \int d\theta d\phi \sum_k S_k(\theta, \phi) \times \underbrace{\frac{\pi}{k^2} G(\theta, \phi)}_{(antenna\ area)} \qquad (2.14)$$

where P_r is the received power, S_k is the flux of waves with wave vector $\mathbf{k}$, and $G(\theta, \phi)$ is the antenna gain. The flux of waves from the direct power should decrease with distance, as long as the receiving antenna remains in the path of the directed power. The flux of waves from cavity power should oscillate according to the cavity mode structure.

Figure 2.6 shows the voltage across the diode as the position of the waveguide was moved by hand, for each of the different sampled locations on the vacuum chamber wall. In the figure O-mode orientation means that the short dimension of the waveguide (direction of $\mathbf{E}$ for TE_{10} mode) is parallel to the z-axis and X-mode orientation means that the short dimension is perpendicular to the z-axis. Two characteristics of these signals reveal the cavity-like nature of the vacuum chamber: 1) The signals oscillate as the position of the waveguide is varied. The distance between adjacent peaks is approximately 1 cm on the average. The variation from a purely sinusoidal dependence on position reveals the highly complicated geometrical structure of a chamber cavity mode.

---

[6]This was done while the chamber was at atmospheric pressure—no plasma was produced.
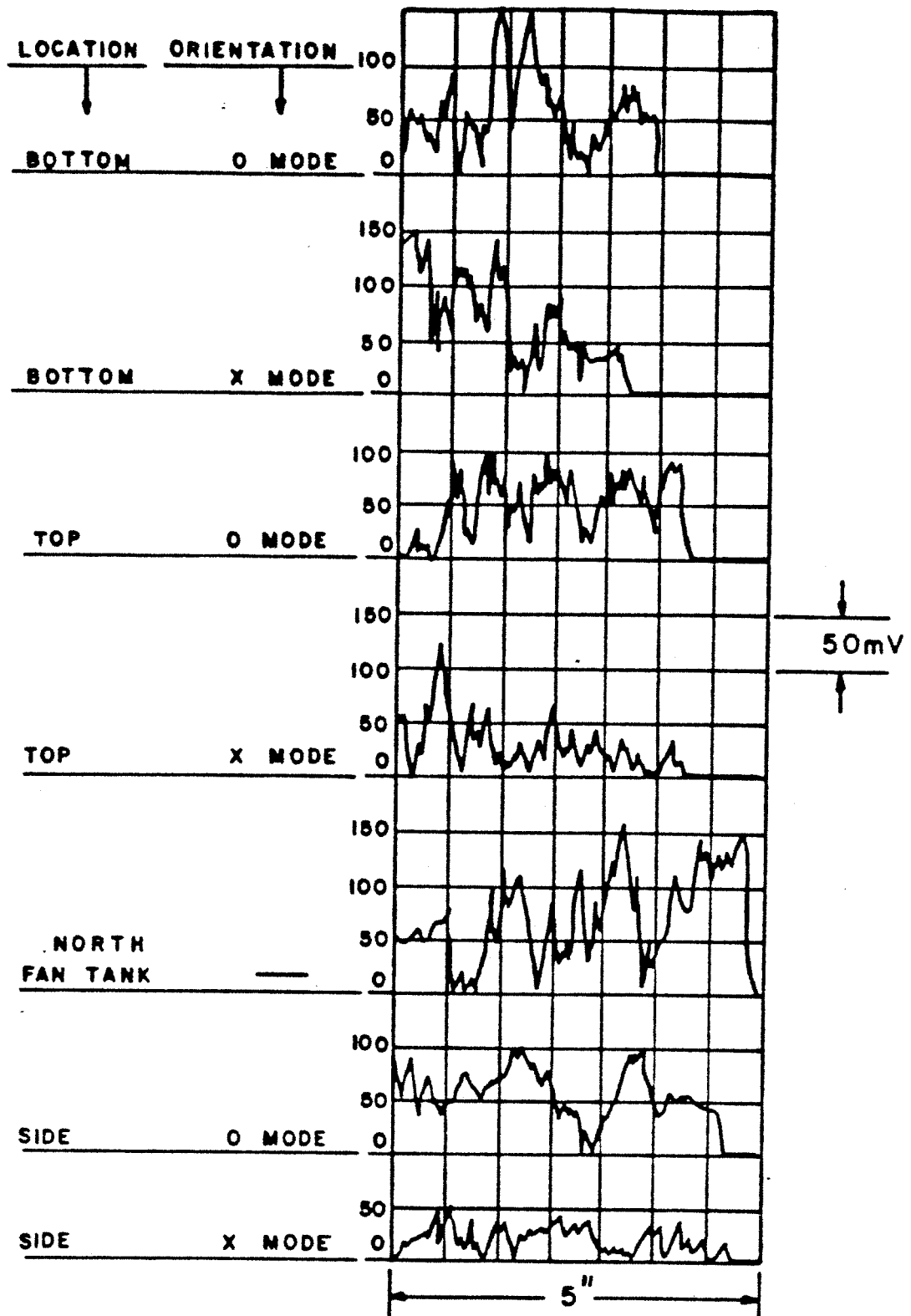
Figure 2.6: The response of a diode to ECRH waves in the chamber as the waveguide is moved approximately 5 inches. Each picture refers to a particular vacuum chamber location and waveguide orientation.

2) The amplitudes of the signals at widely differing chamber locations are of the same order of magnitude. This indicates that the entire chamber is filled up with electromagnetic energy as would be expected for a cavity. Since the detected signal from a diode at the bottom of the vacuum chamber, pointed directly at the ECRH waveguide at the top of the chamber, is approximately the same as the detected signal at the fan tank wall, then the directed electromagnetic energy before a bounce is negligible compared to the electromagnetic energy in the cavity mode. This is the situation for the open-ended waveguide, which was specifically chosen because of its broad antenna pattern which makes it insensitive to the directed power.

Additional evidence of the cavity-like nature of the chamber is revealed when the waveguide is left stationary and a piece of metal anywhere in the chamber (e.g. a probe) is moved. When this is done the diode signal goes through the same type of oscillations as in the moving waveguide case.

The ECRH source is a narrow band, spatially localized source. The plasma is a wide band (unstable rf emission in the range of 6.5 to 10.5 GHz), non-spatially localized (scale length greater than 1 cm) source. In addition, the plasma in the chamber partially defines the structure of the cavity modes. Since plasma currents are constantly fluctuating in time in some complicated fashion, the cavity modes are constantly changing as well. However, due to the wide band, non-local nature of the emission, all the bumps and wiggles associated with the various modes should superpose so that the electromagnetic energy in the cavity is distributed uniformly. This is verified experimentally. For constant machine operating conditions the detected unstable rf power is approximately constant, on the time average (this is discussed in Chapter 3). For different shots in which the machine operating conditions are the same but the detector location is different the detected power is the same. In addition, the detected power does not change from shot to shot between which probes or other objects inside the chamber are moved.

The directed power of the unstable rf emission is much smaller than the cavity power. This is verified by moving a metallic flap 10 cm in front of the receiving

waveguide so that the waveguide is not looking directly at the plasma. The amount of detected power is the same as without the flap.

Since the detection of rf is strongly influenced by the cavity nature of the vacuum chamber an approximate calibration factor relating the detected power to the power emitted by the plasma can be ascertained. The stored energy U in a cavity is related to the source power P_s in steady-state by

$$U = \frac{Q_\omega P_s}{\omega} \qquad (2.15)$$

where Q_ω is the "Q" of the cavity for that particular mode. If a small "hole" is made so that the Q is not affected then the amount of additional power that gets out (the detected power) is proportional to the stored energy, which is proportional to the power of the source. The small hole is effectively the waveguide which is used in the chamber to detect the cavity power. The total detected power is a sum over powers for each mode. Different modes of the Constance B vacuum chamber cavity have different Q's, which is reflected by the fact that the amplitudes of the various oscillations in Fig. 2.6 are widely different. In order to estimate the total cavity power the average of a number of local maxima of a cavity mode (like the ones in Fig. 2.6) is considered. The ratio of this average to the power of the ECRH input is then used as a calibration factor in relating cavity power to source power. That is, it is assumed that this ratio is the same when the source power is the unstable rf emission from the plasma. Using several different ECRH input powers this calibration factor is 1400 ± 700. In Chapter 3 experimental data concerning the power of the rf emission is usually given in terms of detected power. When total power emitted is quoted in Chapter 3 it refers to the total detected power times 1400.

2.4 Machine Operation

The operation of Constance B is described in terms of the machine operating condition which is defined by the ECRH power level, the neutral gas pressure, and the magnetic field amplitude. The ECRH power refers to output of a thermistor which is connected to the output of the klystron by a 40 dB directional coupler. The pressure refers to the output of an ionization gauge controller (Varian model 842) which is connected to an ionization gauge located at the top of the center chamber. This number refers to the pressure of N_2, if it were the gas in the chamber. This will be the number used in this thesis. Multiplication by 2.1 gives the H_2 pressure.[7] The magnetic field amplitude refers to the value on the axis at the midplane. The standard operating condition will refer to an ECRH power level of 1 kW, a pressure of 1×10^{-6} torr, and a magnetic field of 3 kG.

Fig. 2.7 shows the events of a typical shot for the standard machine operating condition. Several seconds before the CAMAC trigger time at $t=0$ the magnetic field is turned on. By $t=0$ it reaches the steady state value desired for the shot. Beginning at $t=-0.2$ sec hydrogen enters the vacuum chamber through a valve located at the bottom of the center chamber. At $t=0.2$ sec 1 kW of ECRH power enters the vacuum chamber and plasma begins to form less than 1 msec later. Until ECRH ends at $t=2$ sec, the electrons are heated, as indicated by the rising diamagnetic loop. The plasma is unstable during the entire ECRH phase of the shot, as indicated by the total rf emission signal. The electron endloss also shows the negative bursts associated with microinstability, in addition to an average level associated primarily with collisions. The 10.5 GHz cavity power signal is the result of tuning the spectrum analyzer to 10.5 GHz. It is seen that it is on the time average approximately 1/3 of the value it takes on when there is no plasma (indicated by the initial spike at $t=0.2$ sec). This indicates that approximately 2/3 of the ECRH power is absorbed by the plasma. However, this varies from shot to shot. When

---

[7]This number is given in the ionization gauge controller manual.
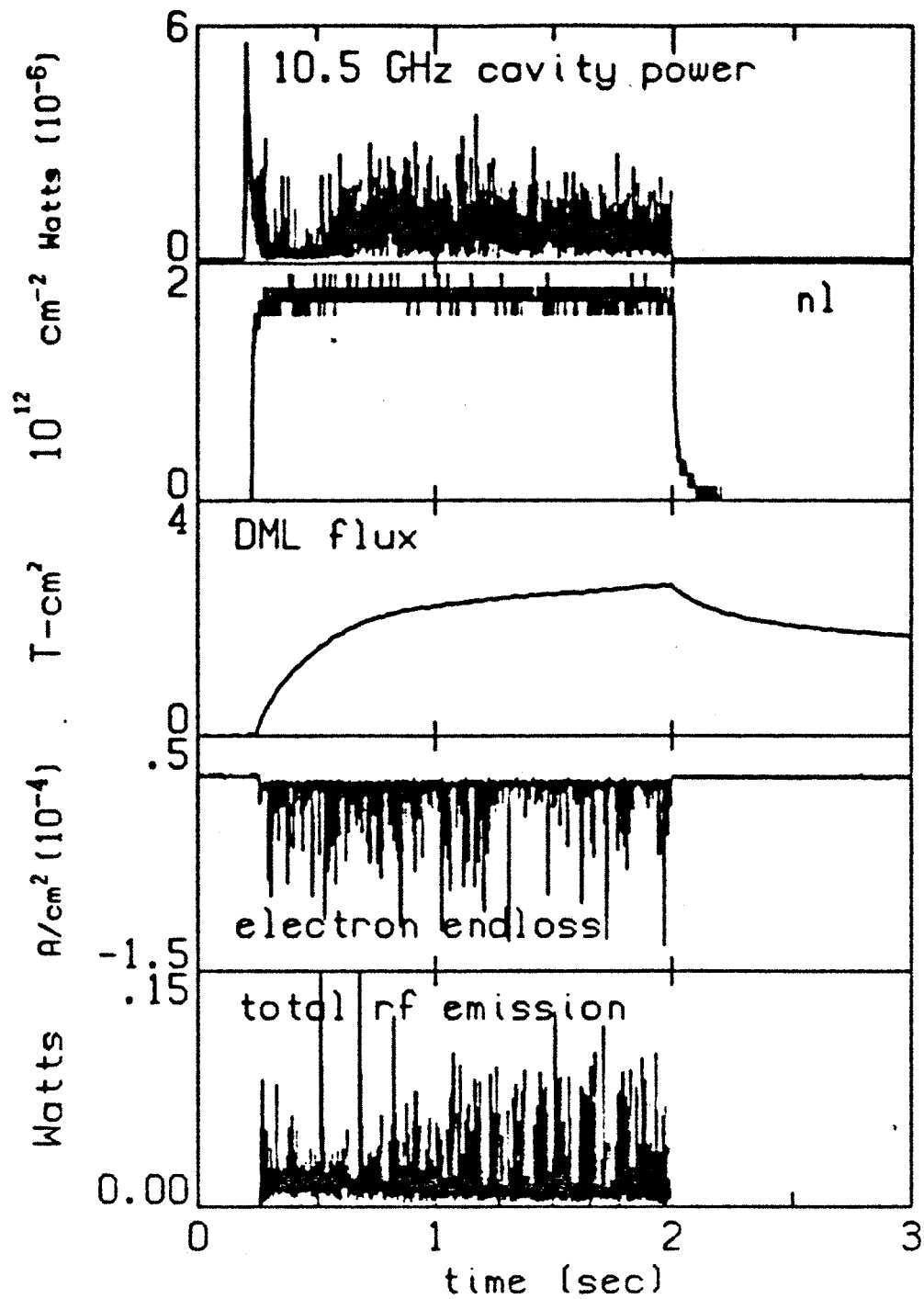
Figure 2.7: A typical shot for the standard machine operating condition.

T_i	30 eV
ϕ_p	100 volts
T_{ec} (endloss)	250 eV
T_{ec} (plasma)	100 eV
T_{eh}	400 keV
electron line density	2×10^{12} cm^{-2}
hot electron line density	1×10^{12} cm^{-2}
β	.15
plasma diameter	20 cm
plasma length	30 cm

Table 2.1: The plasma parameters for the standard machine operating condition.

ECRH ends the plasma decays. A population of hot electrons remains confined for several seconds due to their long collision time. At t=3 sec the magnetic field begins to decay.

2.5 Description of Plasma

2.5.1 Plasma Components

The Constance B plasma consists of a cold ion component and three electron components referred to as cold, warm, and hot. Table 2.1 summarizes their parameters for the standard machine operating condition. Each component can be identified experimentally.

The endloss analyzers identify the ion component. The 30 eV ion temperature and the 100 Volt plasma potential are determined by sweeping the ion repeller grid of the endloss analyzers through a range of values during a single shot. These values are fairly uniform across the plasma radius.

The endloss analyzers identify both the cold and warm electron components. Fig. 2.8 shows the electron endloss current on axis as a function of repeller grid voltage. The two slopes are indicative of two components. Each slope corresponds to a Maxwellian distribution of energies *along the loss cone boundary* and the reciprocals of the slopes correspond to the respective temperatures. Each temperature
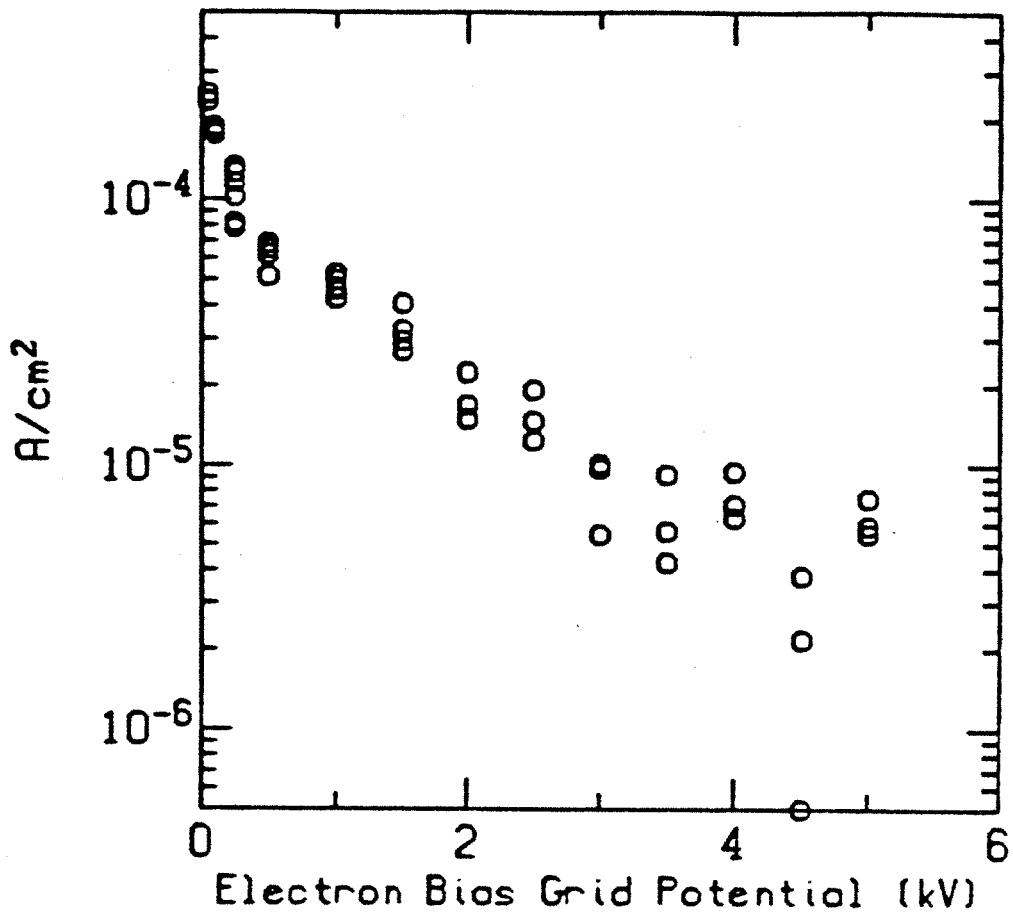
Figure 2.8: Electron endloss current as a function of repeller grid voltage. Each point is for a different shot.

is twice the average energy of each component (Chapter 4 models each component with a distribution function that is Maxwellian along the loss cone boundary). The endloss temperatures are not the true temperatures of the components within the plasma; to detemine the true temperatures it is necessary to know how the electrons got to the loss cone boundary. This is discussed in more detail in the next section for each component. For brevity the endloss temperatures will be referred to as the temperatures. The cold electron temperature of Fig. 2.8 is 250 eV. This temperature is fairly steady during the entire heating phase of the shot. Endloss analysis as early as 1 msec after the gas breakdown indicates a 250 eV cold electron temperature as well.

The cold electron line density of 2×10^{12} cm^{-2} is determined by subtracting the interferometer signal approximately 1 msec after ECRH goes off from the interferometer signal during ECRH. Fig. 2.7 shows that when the ECRH is turned off the interferometer signal first abruptly drops and then decays more slowly. This first abrupt drop is due to the cold electrons collisionally decaying when the cold electron source function (i.e. ionization of gas) is removed. The slower drop is due to hot electrons collisionally decaying away at their characterisically slower rate. Assuming a constant cold electron radial density profile and a 20 cm diameter gives a cold electron density of 1×10^{11} cm^{-3}.

The warm electron temperature of Fig. 2.8 is 2 keV. The electron endloss associated with the warm component is primarily in the form of short bursts. It is shown in Section 3.4 that the warm electron endloss is due primarily to the interaction between these electrons and the unstable waves.

The hot electron component is identified by the x-ray detectors. Fig. 2.9 shows the average x-ray spectrum for many identical shots, along with the theoretically expected spectra for a 467 keV Maxwellian distribution. The lower solid curve is the theoretical detector modified curve. Fig. 3.21 shows the hot electron temperature as a function of time during the shot. It indicates a heating rate of 450 keV/sec until a 400 keV steady state temperature is attained.

Maxwellian Electron Distribution

Upper Curve - True Spectrum

Lower Curve - Detector Modified

Points - Dotol NRI12570

T = 467 keV

EBAR   (15,1500)= 114

EBARmod (15,1500)= 132

EBARdotol(15,1500)= 168

Shot 1200- 120C. Spectrum 25-25

Bethe-Heitler Rel. X-S 6/11/85   3"x3" NoI, 86" Air, .020" Al
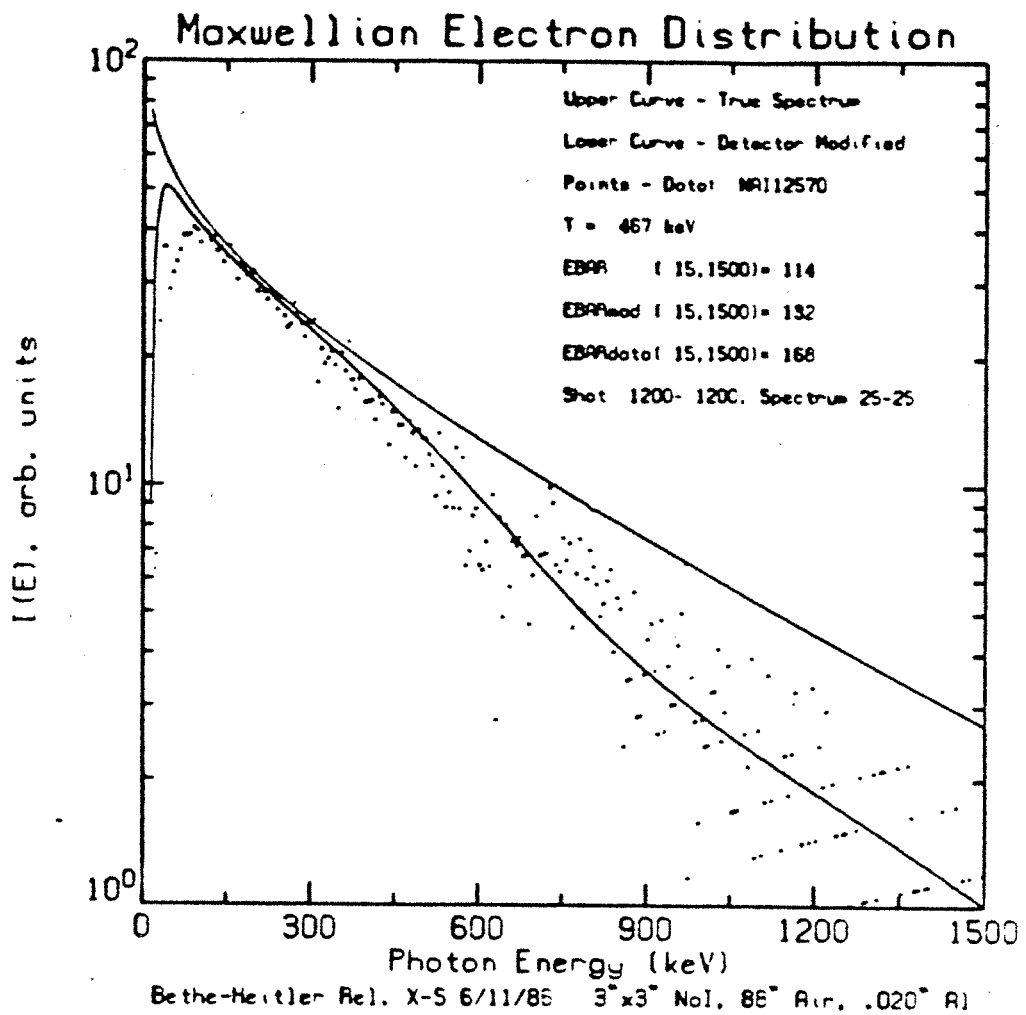
Figure 2.9: X-ray spectrum for many identical shots.

54

The density of the hot electron component can be deduced in two ways: 1) The drop in the interferometer signal at the end of ECRH (see Fig. 2.7) indicates that the hot component contributes approximately half of the total line density of 3.5×10^{12} cm^{-2}. 2) If an assumption about the electron radial pressure profile is made then the diamagnetic loop provides a value for the perpendicular energy density $nT_\perp$. The perpendicular energy density is almost completely due to the hot component, given the parameters of the components as stated above.[6] Therefore, the diamagnetic loop value of $nT_\perp$ divided by the x-ray temperature is approximately the hot component density. Experimental evidence suggests that the hot electron pressure profile is hollow (Smatlak *et al.*, 1986). Assuming a volume of 8 liters (the volume of the region enclosed by the resonance surface) and a suitable analytic form for a hollow pressure profile gives $\beta \approx 0.15$ (Chen *et al.*, 1986) and $n_{eh} \approx 2 \times 10^{11}$ cm^{-3}. Other choices of pressure profile will give different values of β but all values usually lie in the range from 0.1 (for a Fermi distribution type profile) to 0.3 (for a Gaussian profile) (Chen *et al.*, 1986).

2.5.2 Particle Confinement

General Discussion

The classical particle loss time is the collisional loss time, the time it takes an electron to scatter into the loss cone as a result of a collision (with modifications due to the condition that the ion and electron loss times are equal and that a plasma potential develops as a result). A figure of merit is therefore the deviation of the particle loss time from the classical loss time. It is of interest to know if electron microinstability, which also causes electrons to get kicked into the loss cone, is responsible for such a deviation. The issue of the electron endloss which is induced specifically as a result of microinstability is addressed in in Section 3.4. This section

---

[6]This assumes that the (unknown) warm component density is not several orders of magnitude greater than the hot component density. This is a reasonable assumption since such a density would almost certainly be identified by the x-ray detectors and the interferometer.

is devoted to a short discussion of particle loss in general. and the experimentally determined loss time values for each of the components of the plasma is presented.

In steady state the loss rate of electrons must balance the production rate, regardless of the loss mechanism. This is expressed as

$$\frac{\partial n_\epsilon}{\partial t} = 0 = n_o n_\epsilon \langle \sigma v \rangle - \frac{n_\epsilon}{\tau_{loss}(n_\epsilon)} \qquad (2.16)$$

where n_o is the neutral gas density, τ_{loss} is an average loss rate due to all processes inducing loss, and σ is the cross section for ionization of neutral gas where the result is a free electron. The equilibrium density depends on what loss rate is actually taken on by the plasma, and this depends on the mechanisms inducing loss. If a particular mechanism causes a loss time much greater than the classical loss time then, without that mechanism, the density would much greater. Assuming that the electrons only leave axially as endloss, the endloss current density J_{loss} can be related to the loss time by:

$$J_{loss} = -\frac{n_\epsilon \epsilon L_p}{\tau_{loss}} \qquad (2.17)$$

where L_p is the plasma length. Eqs. 2.16 and 2.17 then give the condition

$$J_{loss} = -e n_\epsilon n_o \langle \sigma v \rangle L_p \qquad (2.18)$$

which can be used to give a rough estimate for n_ϵ if the other quantities are estimated. This can then be compared to the interferometer measurements of line density. Using the experimentally determined value of -3×10^{-4} A/cm^2 for J_{loss} from Fig. 2.8. a value of 5×10^{-8} cm^3/sec for $\langle \sigma v \rangle$ (a 250 eV Maxwellian ionizing hydrogen molecules (Freeman and Jones, 1977)). $L_p = 80$ cm (the distance between the mirror peaks). and $n_o = 3.5 \times 10^{10}$ cm^{-3} (density of particles at 1×10^{-6} torr). Eq. 2.18 gives a density of 3×10^{10} cm^{-3}. Assuming a flat profile the interferometer gives a density of 1×10^{11} cm^{-3}. although this value is probably lower on axis since the profile is hollow.

With an experimental value of J_{loss} for each component, Eq. 2.17 can be used to compare each component's actual loss time to its classical loss time. It is shown below that the measured cold electron loss time is nearly the same as the Pastukhov time which, for simplicity, is considered to be the classical loss time for this component. However, the warm and hot component confinement times are much less then their respective classical loss times, which are taken to be the electron-electron collision times. Chapter 3 shows that the warm electron confinement time is degraded by microinstability induced endloss and the hot electron confinement time is degraded by both microinstability and ECRH induce endloss.

Cold Electrons

Fig. 2.8 gives a cold electron endloss current density of 3×10^{-4} amps/cm^2. Using $L_p = 80$ cm (the distance between mirror peaks on axis), and $n_e = 1 \times 10^{11}$ cm^{-3} Eq. 2.17 gives a cold electron loss time of 0.4 msec.

For simplicity the classical loss time of the cold electrons is taken to be the Pastukhov time. The Pastukhov time (Pastukhov, 1974) takes into account the modification due to the plasma potential, although it does not take into account the effects of ECRH (which causes an additional "loss" of cold electrons to the warm electron component. The Pastukhov loss time for electrons (with a factor of 2 correction due to Cohen *et al.* (1978) is

$$\frac{1}{\tau_{past}} = \frac{2}{\sqrt{\pi}} \frac{1}{\tau_{ee}} \frac{2R}{(2R+1)} \frac{\epsilon^{-x}}{\ln(4R+2)} \frac{1}{x}$$

$$\times \underbrace{\int_0^\infty \epsilon^{-\xi} \sqrt{1 + \frac{\xi}{x}} d\xi}_{1 + \frac{\sqrt{\pi}}{2} \frac{\epsilon^x}{\sqrt{x}} [1 + erf(\sqrt{x})]} \qquad (2.19)$$

where $x = \phi/\hat{T}_e$, $\hat{T}_e$ is the actual temperature of the electrons inside the plasma, to distinguish it from the endloss temperature T_e. R is the mirror ratio. and τ_{ee} is the electron–electron collison time (Schmidt, 1979):

$$\tau_{ee} = 3.44 \times 10^5 \frac{\left[\hat{T}_e \, (\text{eV})\right]^{3/2}}{n_e \ln \Lambda} \qquad (2.20)$$

The Pastukhov loss time for electrons must equal the ion loss time. which is taken to be the collisional loss time in a mirror with mirror ratio R:

$$\tau_i = 2.09 \times 10^7 \frac{\left[T_i \, (eV)\right]^{3/2}}{n_i \ln \Lambda} \log(R) \qquad (2.21)$$

For $T_i = 30$ eV, $n_i = 2 \times 10^{11}$ cm^{-3}, $R = 2$, and $\ln\Lambda = 15$, Eq. 2.21 gives $\tau_i = 0.3$ msec, close to the experimentally determined cold electron loss time of 0.3 msec. [9] Eq. 2.19 can be solved for $\hat{T}_e$ if τ_{past} and ϕ are known. Taking the value of τ_{past} just derived, and the experimentally determined value of 100 volts for ϕ, Eq. 2.19, which has been calculated numerically, gives $\hat{T}_e \approx 80$ eV. The Pastukhov formulation also gives the theoretical average value of the energy of the electron endloss, given the true electron temperature and the potential. This has been calculated numerically for the above parameters and is approximately 150 eV. Therefore, the endloss temperature predicted by the Pastukhov formulation is 300 eV (twice the average energy), which is to be compared to the 250 eV experimentally determined endloss temperature.

Warm Electrons

The particle loss time of the warm component is not known experimentally because the density of the warm component is not known. The germanium x-ray detector provides a photon spectrum down to energies of 2 keV, however the detector response and the beryllium window energy cutoff make the detector too insensitive

---

[9]The total ion density is taken to be equal to the total electron density. not just the cold electron density.

to photon energies below approximately 5 keV. Also, the x-ray spectrum for the hot component diverges at low temperatures[10] and thus has a tendency to mask a warm component spectrum even for warm component densities on the order of the hot component density. must be taken into account for low energies when there is a large exchange of momentum between an incoming electron and a photon. An upper limit for the warm electron density can be taken to be the hot electron density of approximately 1×10^{11} cm^{-3}. An upper limit for n_{ew} combined with a warm electron endloss current of 2×10^{-4} amps/cm^2 (see Figure 2.8) gives an upper limit for the warm electron particle loss time:

$$\tau_{loss,warm} < 2 \times 10^{-3} \text{sec.}$$

where L_p for the warm electron is taken to be 30 cm, the approximate length of the field line between resonance zones, on axis. Chapter 4 will show (see Fig. 4.7) that this is the appropriate length if the warm electron distribution function is similar to the distributions predicted by Fokker-Planck simulations of ECRH, mirror-confined plasmas.

Since the 2 keV warm component is not affected by the 100 volt plasma potential significantly the classical loss is given by the electron–electron collision time (Eq. 2.20), with the warm electron density colliding with the total electron density. Since the warm electrons collide with the entire plasma the classical loss time is

$$\tau_{loss,classical} > 2 \times 10^{-2} \text{sec.}$$

This is a factor of 10 greater than the lower limit of the measured loss time. Microinstability is primarily responsible for this deviation.

---

[10]This divergences occurs in the cross section which. for higher electron energies is derived using the Born approximation. This is not valid when there is a large transfer of momentum between the initial electron and final photon (Heitler 1954).

Hot Electrons

The hot particle endloss current and hence the loss time can be determined with the scintillator probe. The scintillator probe is only sensitive to electrons above approximately 50 keV. Figure 3.44 on page 126 shows scintillator probe data from a shot which consists of three parts. The first part is similar to a typical shot in which gas and ECRH power are held constant. In the second part the gas and ECRH are stopped and the plasma consequently decays primarily due to collisions. The warm and cold components decay on the order of a few milliseconds while the hot component decays on the order of a few seconds. In the third part the ECRH is turned on, but the gas is kept off. In the first part the hot electron endloss is caused by collisions, ECRH, and microinstability. In the second part it is caused by collisions only. In the third part it is caused by ECRH and collisions because the hot electrons are microstable (which is discussed in Chapter 3. Shots like the one depicted in Fig. 3.44 directly give the ratio of the actual loss time to the classical loss time, since the endlosses due to collisions alone can be separated out. The ratios of the loss times due to the three mechanisms are the ratios of the endloss currents, or the endloss powers, which is what the scintillator probe provides. Referenced to the loss time due to collisions, these ratios are

$$
\begin{aligned}
\text{collisions:} &\quad 1 \\
\text{microinstability:} &\quad \tfrac{1}{25} - -\tfrac{1}{50} \\
\text{ECRH:} &\quad \tfrac{1}{50}
\end{aligned}
$$

The calibration factor determined in Section 2.2 can be used to determine the actual endloss power (low to within a factor of 2) which, with a knowledge of the hot electron density from the interferometer, provides the hot electron loss time. A plot of endloss power as a function of pressure is shown in Fig. 3.45 on page 128, at the end of Chapter 3. The hot electron endloss is described in more detail in that section. For the purposes here, all that is needed is the total endloss current. The maximum endloss power shown in that figure, which is the total due to both microinstability and ECRH (the power due to collisions is negligible, as determined

60

above) is approximately 1 W/cm^2 on axis. With a 400 keV temperature the hot electron endloss current density is then 2.5×10^{-6} A/cm^2. With a density of 1×10^{11} cm^{-3} the loss time is therefore

$$\tau_{loss,hot} = 0.2 \text{sec}$$

The collisional loss time is experimentally determined to be 100 times longer, or 20 sec. The theoretically expected collision time, as given by Eq. 2.20, is 29 sec ($T_{eh} = 400$ keV, $n_e = 2 \times 10^{11}$ cm^{-3}, and $\ln \Lambda = 15$).

Chapter 3

Experimental Analysis of Microinstability

This chapter presents the results of the experimental investigation of microunstable rf emission and microinstability induced endloss. Section 3.1 summarizes the experimental observations and provides qualitative ideas as to how microinstability behaves. This behavior is sensitive to neutral gas pressure, which is used as a common reference to relate microinstability to other plasma characteristics. This is done since the neutral pressure is one of the controllable parameters of the experiment. Section 3.2 describes the unstable rf emission. The first part presents the experimental determination of the frequency spectrum as a function of magnetic field. This is used to identify both types of rf emission as the whistler instability (in conjunction with the theory of Chapter 4), and to show that the whistler C emission is associated with off axis magnetic field lines. The second part presents the experimental determination of total unstable rf emission power loss. It characterizes the total unstable rf emission with respect to the machine operating condition. Section 3.3 uses some of the experimental results of Section 3.2 and presents additional evidence to show that the warm electrons drive microinstability while the hot electrons are stable and have little effect. Section 3.4 describes the microinstability induced particle endloss. It discusses the power losses associated with both the warm and the hot electron components.

3.1   General Description of Observations

Microinstability manifests itself through the emission of electromagnetic waves in the electron cyclotron range of frequencies and through electron endloss which is induced by the microinstability. Chapter 1 briefly described the two different types of unstable rf emission from the Constance B plasma. The first type, referred to as the whistler B emission, occurs in bursts and usually correlates with bursts of electron and ion endloss, and diamagnetism and potential fluctuations (see Fig. 1.1). The burst rate is fairly regular and the time between bursts is usually much greater than the duration of the burst. Its frequencies are in the range of 6.7–8.7 GHz, when the magnetic field is 3 kG, although this range is not sensitive to changes in magnetic field. The second type, referred to as the whistler C emission, is seen continuously and is associated with enhanced continuous electron endloss (see Fig. 1.2). Single frequencies ($\delta\omega \sim 1$ MHz) which make up this emission come in bursts under some conditions, but the time between bursts is on the order of, or less than, the duration of a burst. It has frequencies in the range with lower bound at approximately the upper bound of the whistler B emission and upper bound at the ECRH frequency of 10.5 GHz. The theoretical calculations of Chapter 4, in conjunction with the experimentally determined frequency spectrum shown in this chapter, identify both types of rf emission as the whistler instability. Both types of emission will be referred to collectively as the unstable rf emission.

In general, for a constant machine operating condition and one in which gas breakdown can occur, the plasma which is produced is unstable, during ECRH, as long as the pressure is not too high. The value of this pressure threshold is dependent on the magnetic field and ECRH power. Higher powers allow for wider pressure ranges of instability. Lower magnetic fields allow for more narrow pressure ranges of instability. For the standard shot (1 kW ECRH power, 3 kG magnetic field, 1×10^{-6} torr neutral gas pressure) the whistler B emission begins less than 1 msec, and the whistler C emission begins less than 10 msec. after a non-zero endloss

current is observed with the endloss analyzers (a reliable indication of the existence of plasma in the mirror).

It is worthwhile to distinguish between three different pressure regimes for a given ECRH power and a given magnetic field. These regimes are characterized according to the behavior of the unstable emission that occurs in them. The whistler B emission is prevalent at low and high pressures while the whistler C emission is prevalent at intermediate pressures. At very low pressures there is no whistler C emission. The following description pertains to an ECRH power of 1 kW and a magnetic field of 3 kG.

The low pressure regime is the range 8×10^{-8} torr to 5×10^{-7} torr. Fig. 3.1 shows representative data for this regime. Plasma cannot be produced at pressures below 8×10^{-8} torr. Only the whistler B emission exists in this regime. The bursts of unstable rf emission are clearly distinct from each other because the time between bursts, when the plasma is stable because no rf emission is observed, is much longer than the duration of a burst. At the lower end of this regime the rf bursts occur at a fairly regular rate and there is 100% correlation with bursts of endloss. At the higher end of this regime the burst rate is less regular, and there is less than 100% correlation with endloss bursts. Figure 3.2 shows the fraction of rf bursts which correlate with endloss bursts as a function of pressure.

The medium pressure regime is the range 5×10^{-7} torr to 2×10^{-6} torr. Fig. 3.3 shows representative data for this regime. Both types of unstable emission exist together in this regime, although the whistler C emission occurs at higher frequencies. as will be shown in Section 3.2.1. Individual bursts of whistler B emission are difficult to separate and analyze because of the non-zero, nonsteady whistler C emission that is present all the time. The electron endloss exhibits bursts and has a non-zero average current between bursts. This current is associated with the whistler C emission, as will be shown in Section 3.4.2.

The high pressure regime is the range 2×10^{-6} torr to 5×10^{-6} torr. In this regime the whistler C emission is relatively low and individual bursts are. once

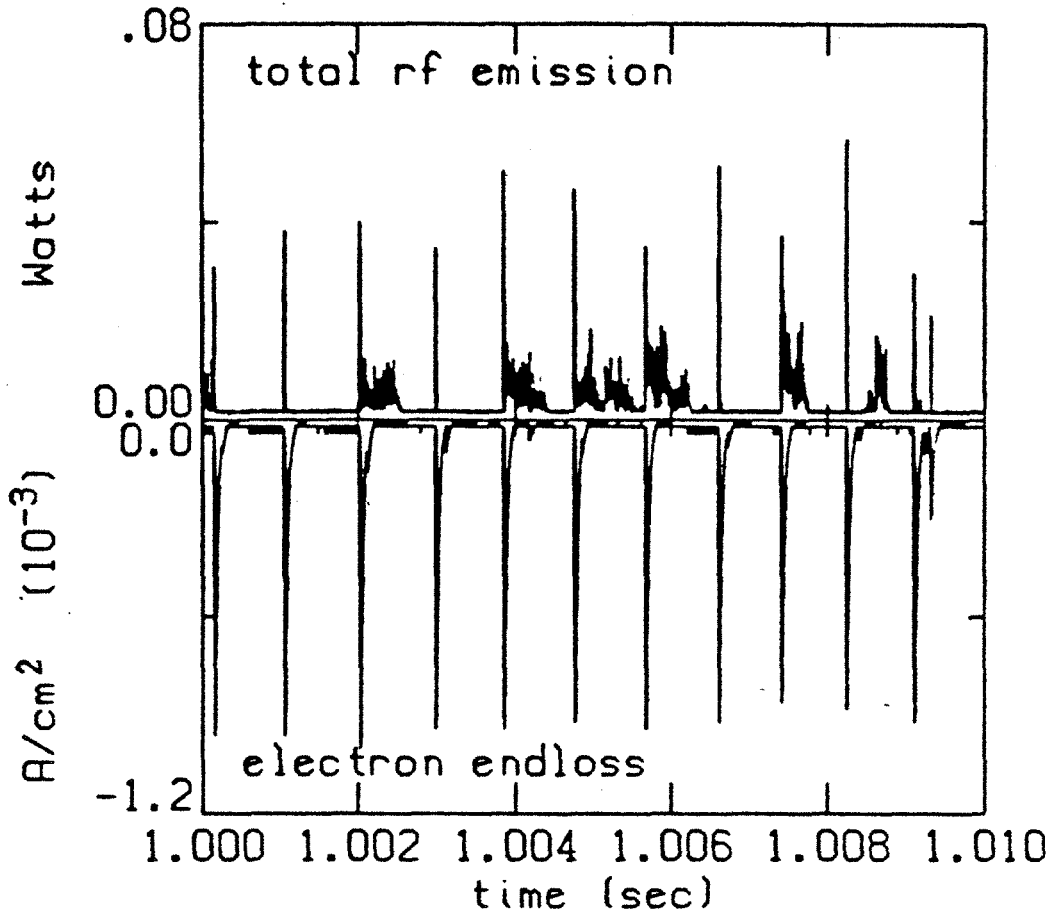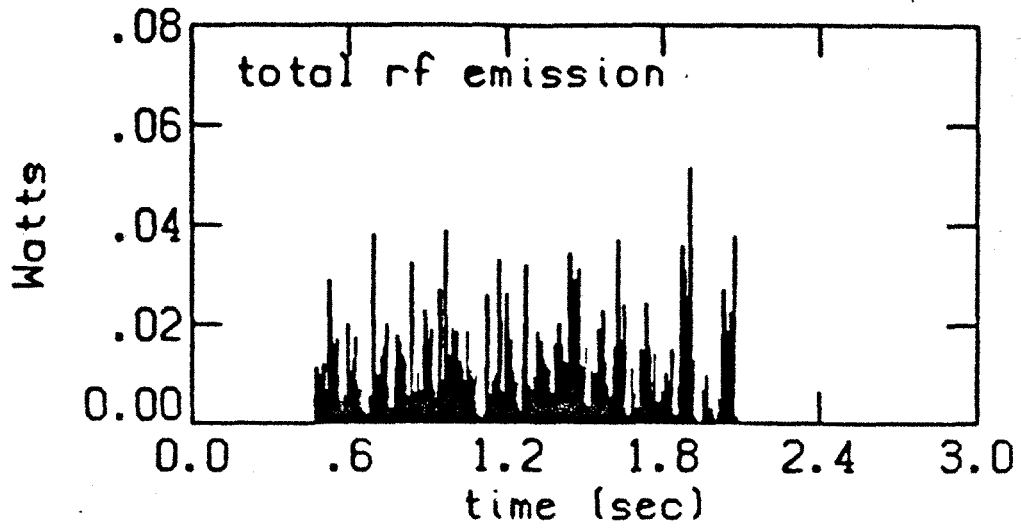Figure 3.1: Rf emission in the low pressure regime. Data from the lower set of plots were digitized at 400 kHz. Data from the upper plot were digitized at 1 kHz.
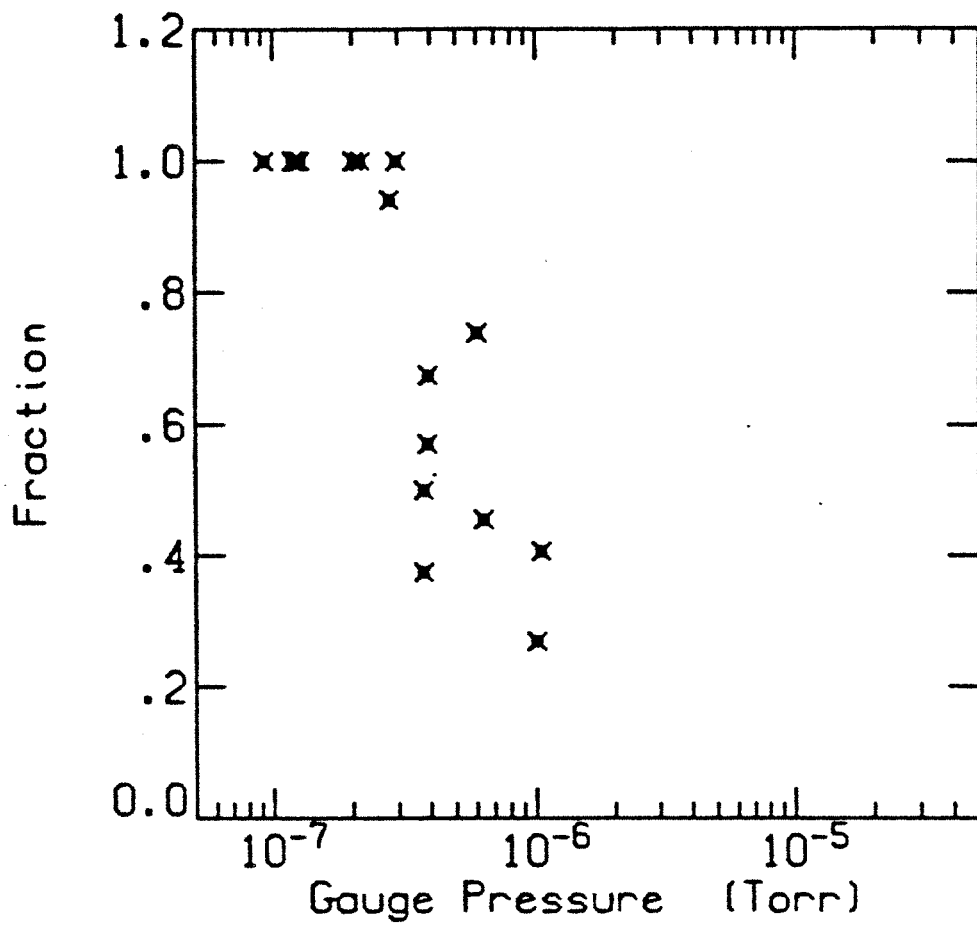
Figure 3.2: Fraction of rf bursts which correlate with endloss bursts
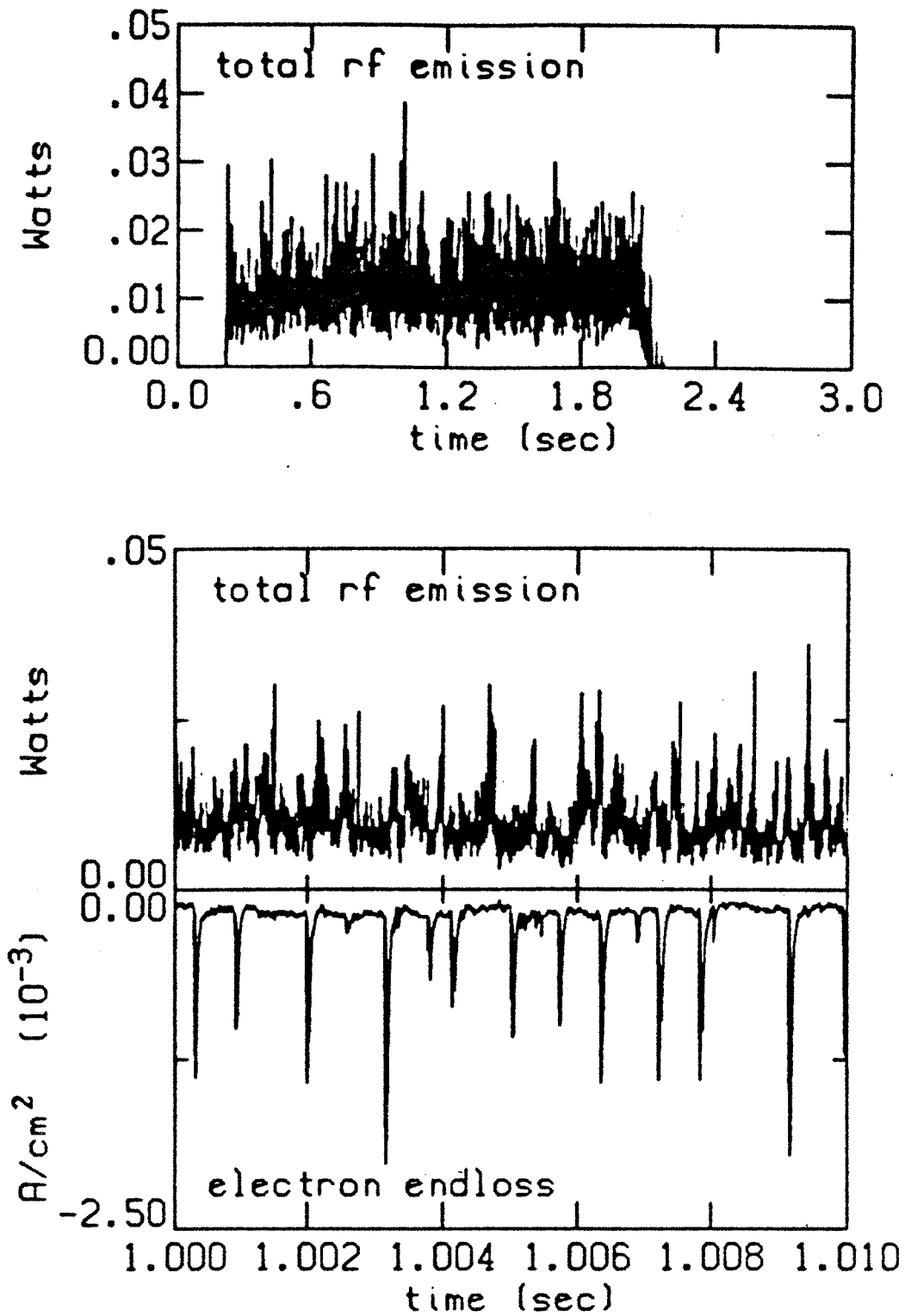
Figure 3.3: Rf emission in the medium pressure regime. Data from the lower set of plots were digitized at 400 kHz. Data from the upper plot were digitized at 1 kHz.

again, discernable. Although the endloss bursts are well defined, there is very little correlation with rf bursts. For pressures above approximately 5×10^{-6} torr the plasma is microstable.

The general scenario described is qualitatively the same for other the ECRH powers and the other magnetic fields considered. The borders between the various pressure regimes may be altered. There are some instances of high power and high enough magnetic field (e.g. ECRH power > 2 kW for magnetic fields > 2.4 kG) for which there is no low pressure regime, defined by the absence of whistler C emission. The general description presented here is relevant for the the ranges of parameters explored in this thesis:

pressure: 2×10^{-8}–5×10^{-5} Torr
magnetic field: 2.2–3.7 kG
power: 100–3000 W

The whistler B emission is identified as an electron microinstability because of the combination of 1) its frequency range, 2) its bursting nature, 3) its association with bursts of endloss, and 4) its power. Linear theory predicts that microinstability exists for the frequencies coincident with the frequencies of the bursting emission and it identifies it as the whistler instability (Chapter 4). Bursting is a phenomenon which can be explained as an instability by a quasilinear solution of the Vlasov equation together with Maxwell's equations (Bespalov, 1982). This was discussed briefly in Chapter 1. Diffusion of electrons due to their interaction with plasma waves is also explained by quasilinear theory, as discussed in Chapter 4. This would explain the bursts of endloss, electrons which diffuse into the loss cone of velocity space through interaction with unstable waves. The instantaneous power of a burst is 10–1000 times the cyclotron emission, as will be shown in the next section. Only an instability can emit at levels higher than the thermal level.

The whistler C emission is identified as an electron microinstability because 1) it has frequencies in the neighborhood of electron cyclotron frequency, 2) it is emitted at power levels greater than the cyclotron emission, as will be shown in

Section 3.2.1, and 3) it is not a parametric instability caused by the wave–wave coupling of the ECRH waves and natural modes of the plasma. The possibility that the whistler C emission is a parametric instability has been ruled out[1] because waves with frequencies equal to difference between the whistler C emission frequencies and the ECRH frequency would have to exist. These waves would have to have virtually all frequencies below approximately 2 GHz. However, emission in the range of 0.5–2 GHz has not been observed when the whistler C emission is present.

3.2 Characteristics of Rf Emission

Information about the rf emission comes in two forms, as discussed in Chapter 2: 1) the power of rf contained in a 1 MHz wide band about some specified frequency determined by a spectrum analyzer (referred to as single frequency emission), and 2) the power contained in all frequencies above 5.25 Ghz with the 10.5 GHz ECRH power filtered out (referred to as total emission). 5.25 GHz is the cutoff frequency of the waveguide used to guide the detected rf from the plasma to the diagnostic racks. Earlier experiments using C band waveguide (cutoff frequency of 2.6 GHz) indicated no rf emission corresponding to electron microinstability at, or below, 5.25 GHz and above 2.6 GHz, for magnetic fields above 2.4 kG. If such emission exists then its power is less than the threshold sensitivity of the detector, which is approximately 10^{-12} W, or 6 orders of magnitude less than a typical burst of whistler B emission. A single-turn magnetic loop probe has also been used and has indicated no rf emission below 2.4 GHz. It was successfully able to detect the standard whistler B and whistler C emission at higher frequencies, indicating that it would have been capable of detecting lower frequency emission.

A study of the the single frequency emission for different magnetic fields leads to the identification of both types of rf emission as whistler instability. This is done in conjunction with the analytical results of Chapter 4. A study of single frequencies

---

[1] The idenfication of the whistler C emission was essentially made by eliminating all the processes might be responsible for it.

in conjunction with a study of the electron endloss behavior at different radii leads to the conclusion that the whistler C emission is associated with off axis field lines.

A study of the total rf emission as a function of pressure, magnetic field, and ECRH power provides information about the total power emitted in the form of unstable waves. In addition it provides most of the evidence which shows that the microinstability is driven by the warm electrons, while the hot electrons are stable. The total rf emission, in conjuction with the endloss studies, determine that the maximum power loss due to microinstability is approximately 10% of the ECRH input power.

3.2.1 Single Frequency Emission

Whistler B Emission

A frequency spectrum for the whistler B emission can be determined in the low pressure regime in which the whistler C emission does not exist. When the whistler C emission is present it is difficult to separate out the two types of emission. Figure 3.4 shows the upper and lower frequency boundaries of the whistler B emission as a function of magnetic field for an ECRH power of 1 kW and a pressure of 2×10^{-7} torr. Outside of these boundaries bursts of whistler B emission are not detected. Figure 3.4 indicates that the whistler B emission is fairly independent of magnetic field, a characteristic which agrees with the calculations of Chapter 4.

It is difficult to determine the power contained in a burst of single frequency whistler B emission because of the cavity effects of the vacuum chamber (see Section 2.3). Instead, the burst rate is considered. Figure 3.5 shows the burst rate of the whistler B emission as a function of frequency. Each of the four plots of corresponds to a different time in a series of identical shots in which the ECRH power was 1 kW and the magnetic field was 3 kG. Each point corresponds to the average burst rate in a 40 msec time period beginning at the time specified at the top of the respective plot. A burst is counted if the power level, as detected by the spectrum analyzer, is above a certain threshhold. Therefore, a low burst rate may not mean
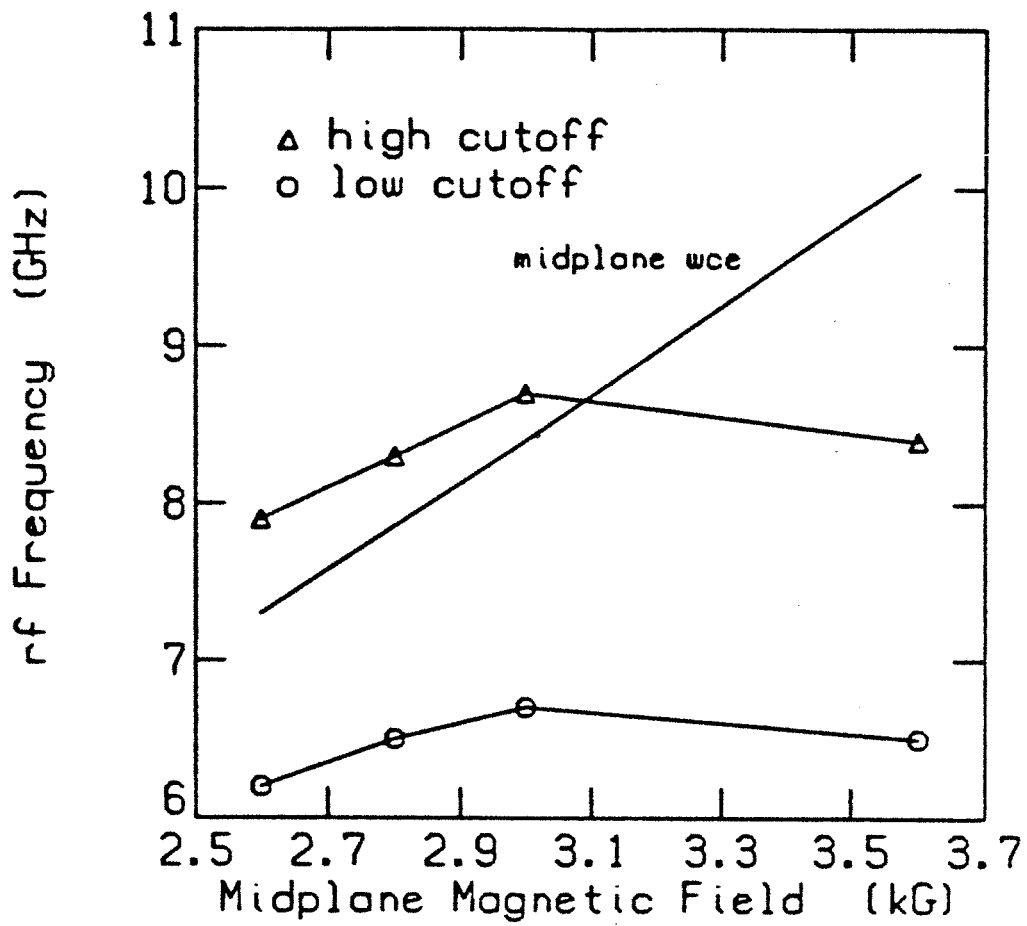
Figure 3.4: Upper and lower cutoff frequencies for the whistler B emission as a function of magnetic field. The points indicate the fields for which data was taken.
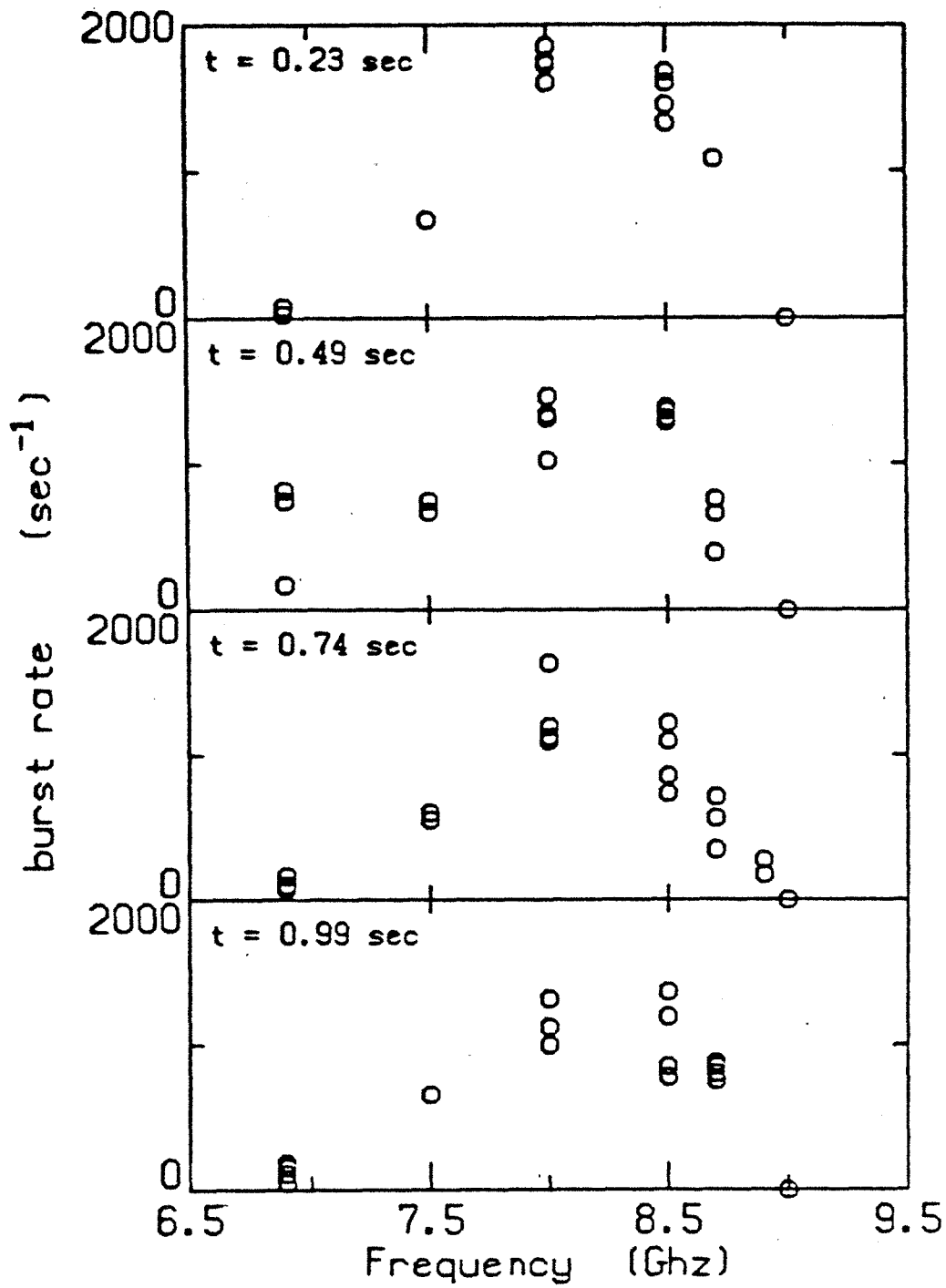
Figure 3.5: Whistler B emission frequency spectra for different times in the shot.

that the burst rate is actually low; a low burst rate may mean that the emission per burst at the specified frequency is very low. This is adequate information for at least providing the frequency range in which the rf emission exists. Figure 3.5 indicates that the spectrum and burst rate remain fairly constant during the entire ECRH portion of the shot.

Figure 3.6 shows information similar to that shown in Figure 3.5 except for a magnetic field of 2.6 kG. A comparison is made here between two different pressures in the low pressure regime. The spectrum is seen to remain the same at the two pressures, although the burst rate increases for the higher pressure, a phenomenon that will be seen more clearly with the total rf emission and endloss data.

Although a burst of whistler B emission is fairly broad band for the duration of the burst, all frequencies composing a burst do not come simultaneously. This is indicated in Figure 3.7(a), which shows a total rf emission burst and the corresponding single frequency emission burst. Single frequency bursts of different frequency may have a different time delay relative to the start of a total rf emission burst.[2] Figure 3.7(b) shows a plot of this time delay as a function of frequency for many different bursts. The figure indicates a general trend of the higher frequencies occuring earlier in time than the lower frequencies.

The whistler B emission starts less than 2.5 μsec after the endloss analyzers start detecting endloss current. Figure 3.8 shows the total rf emission and some other signals at the beginning of a standard shot when ECRH goes on. The well defined bursts at the beginning of the shot occur almost immediately with the rise of the endloss signal. An analysis of the frequencies of these bursts indicates that they are whistler B emission. They begin earlier in time than the whistler C emission and are therefore easy to identify. The whistler C emission for this shot is seen to begin approximately 1 msec after the rise of the endloss signal. An analysis of many shots indicate that it usually does not begin later than 10 msec after the rise of the

---

[2]Since the spectrum analyzer is more sensitive than the diode which detects total rf emission bursts, it may happen that the single frequency emission burst occurs when the total rf emission signal is undetectable.
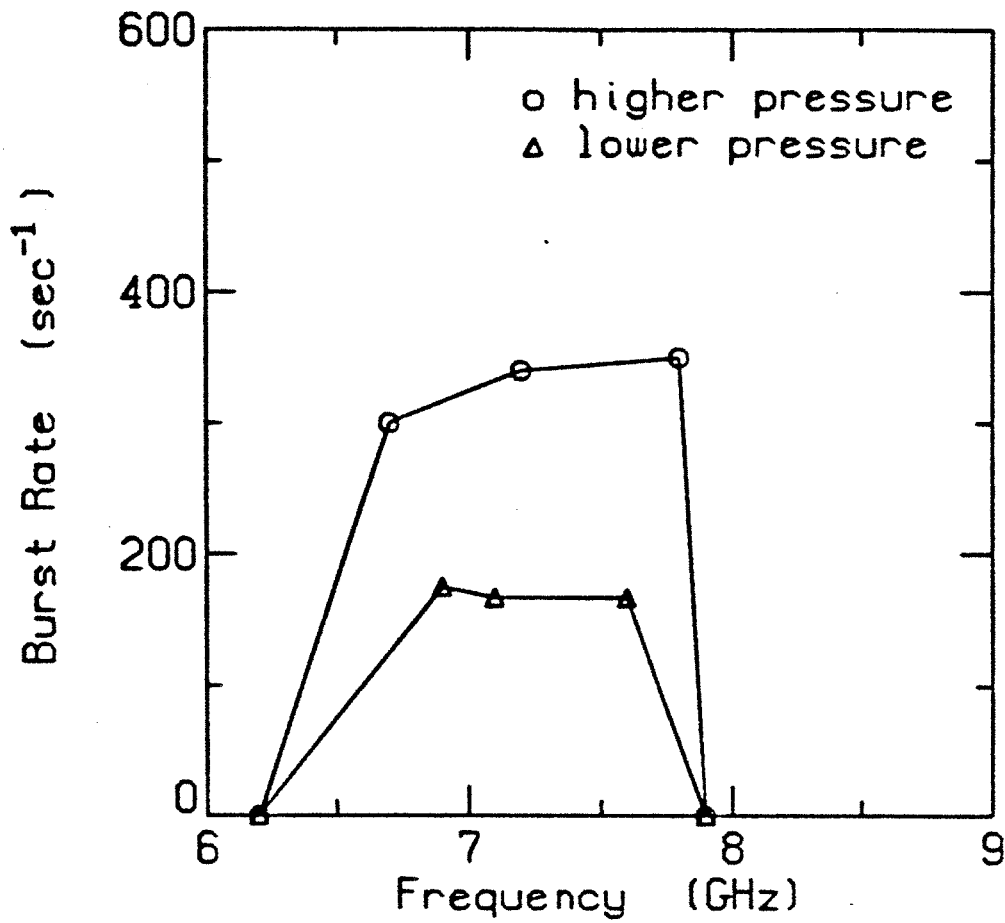
73

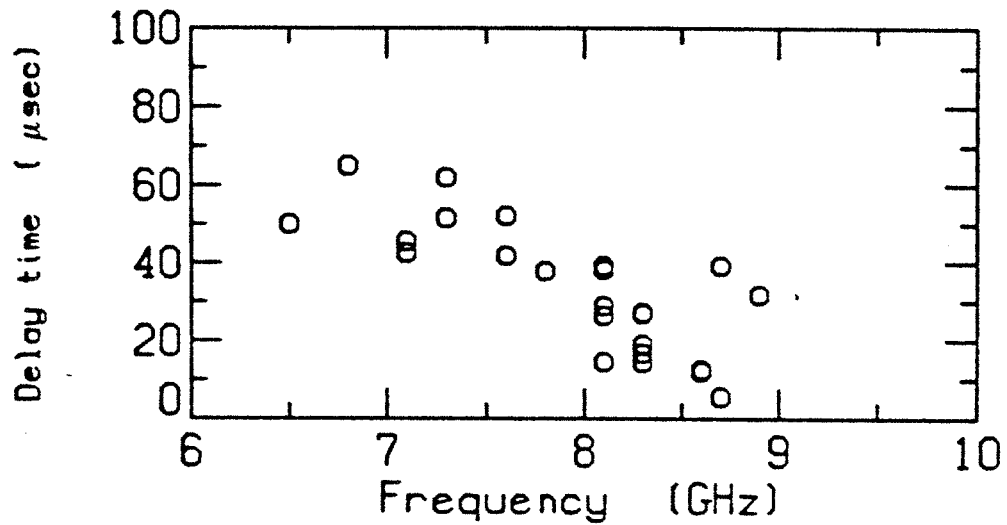Figure 3.6: Whistler B frequency spectra at 2.6 kG for two different pressures in the low pressure regime.
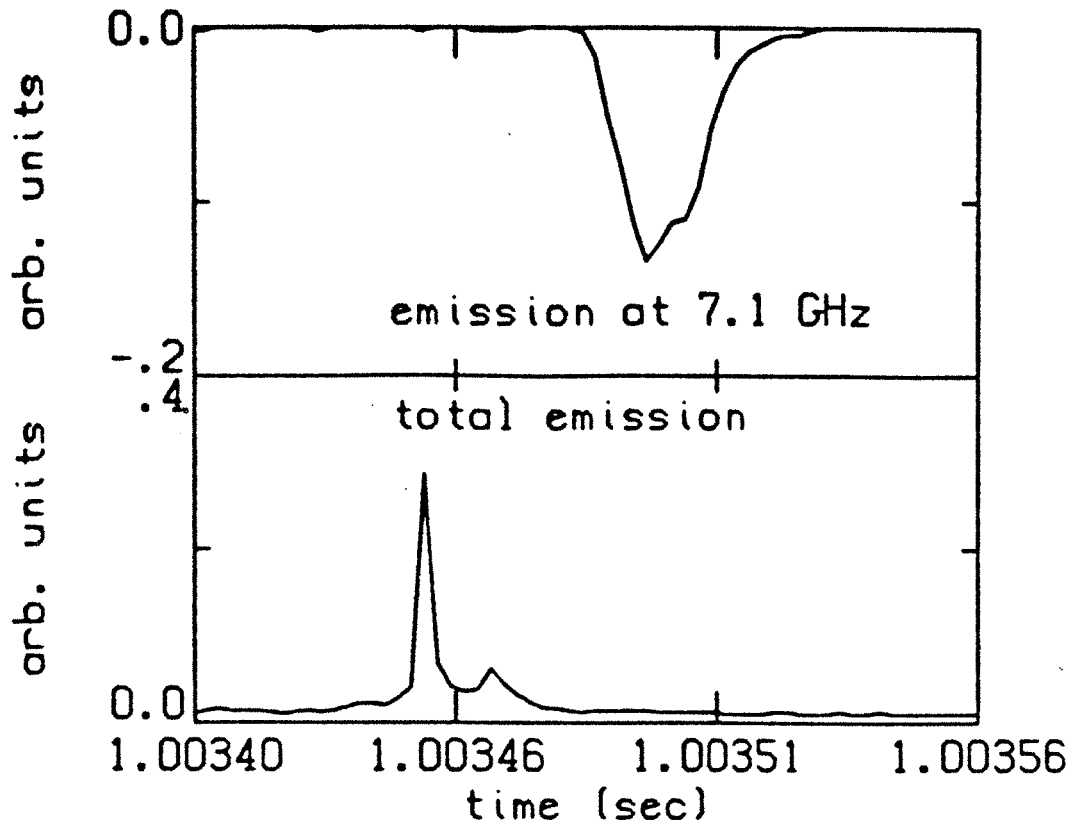
Figure 3.7: a) Total rf emission burst and a corresponding single frequency burst at 7.5 GHz. b) Time delay between single frequency bursts and total rf emission bursts as a function of frequency.
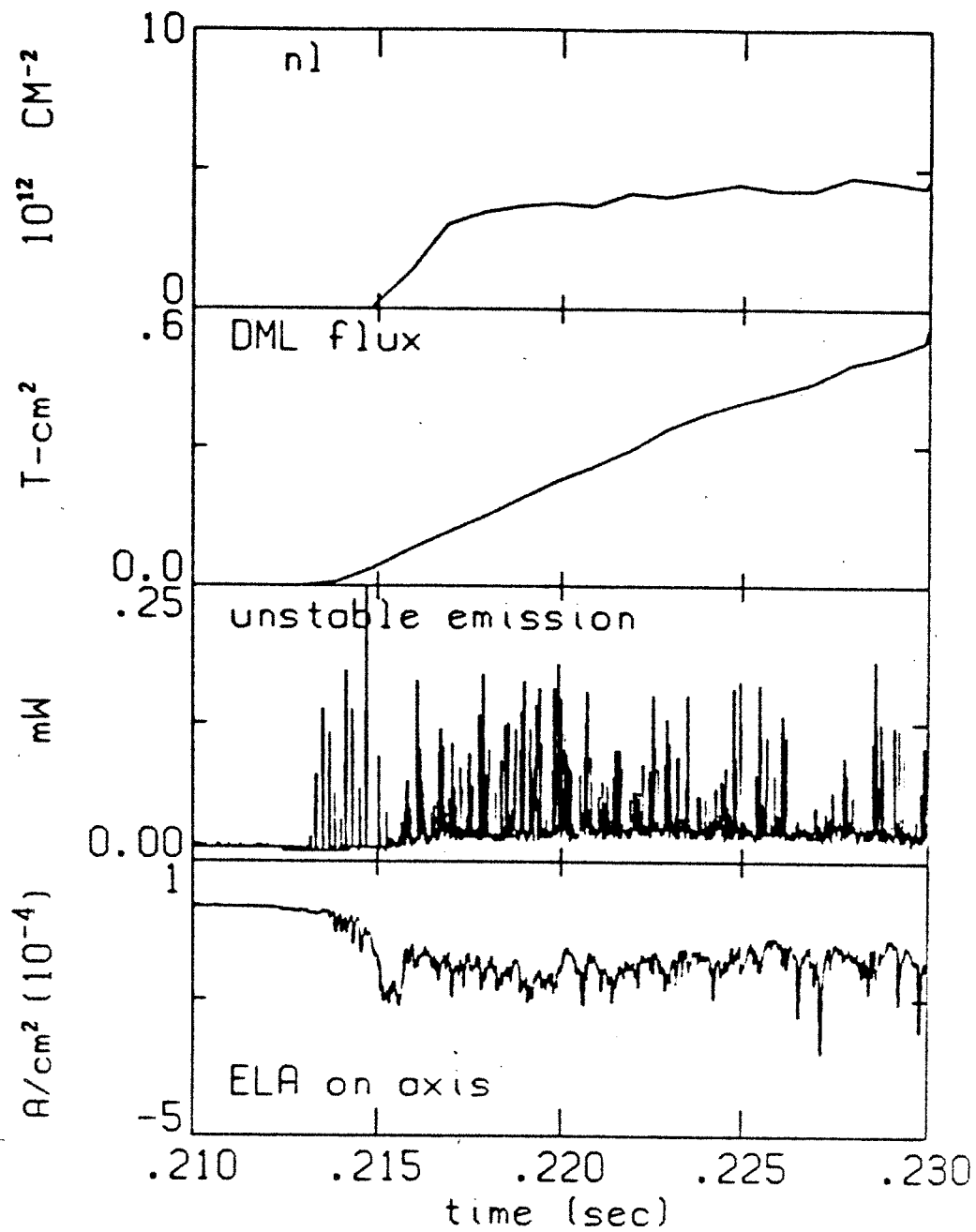
Figure 3.8: The beginning of a standard shot. ECRH goes on at 0.2 ± 0.01 sec.

endloss signal. The endloss analyzer signal is digitized at a rate of 400 kHz, which implies that the whistler B emission begins less than 2.5 μsec after the rise of the endloss analyzer signal. A non-zero endloss current is a reliable indication of the existence of plasma in the mirror. The interferometer signal is digitized at a rate of 1 kHz and is therefore not as accurate an indicator of plasma in the mirror.

The whistler B emission bursts for several milliseconds before completely stopping after the ECRH goes off. Figure 3.9 shows the total rf emission at the end of a standard shot when the ECRH is turned off. A few bursts of rf emission occur sporadically for several milliseconds and correlate with burst of endloss. An analysis of the frequencies of these bursts indicate that they are whistler B emission. The whistler C emission usually ends approximately 5 msec after the ECRH goes off.

Whistler C Emission

As the pressure is raised to medium pressure regime values the bursting nature of the whistler B emission continues to occur in approximately the same frequency range as discussed above, and the whistler C emission appears at higher frequencies. Figure 3.10 shows single frequency emission corresponding to three different frequencies for shots in which the pressure was 5×10^{-7} torr. The 7.1 GHz signal corresponds to the whistler B emission. It continues to come in bursts such that the time between bursts is long compared to the duration of a burst (the defining characteristic of whistler B emission). The 8.4 GHz and the 9.1 GHz signals correspond to the whistler C emission. Although all the frequencies of the whistler C emission come continuously as a whole, it is seen here that 1 MHz wide emission may come in bursts with the time between bursts of the same order or less than the duration of a burst.

The upper frequency bound of the whistler C emission is the ECRH frequency of 10.5 GHz. No emission is observed above 10.5 GHz and below 14 GHz.[3] The lower frequency bound of the whistler C emission is difficult to determine due its merging

---

[3]The issue of higher harmonic emission was not addressed in this thesis.
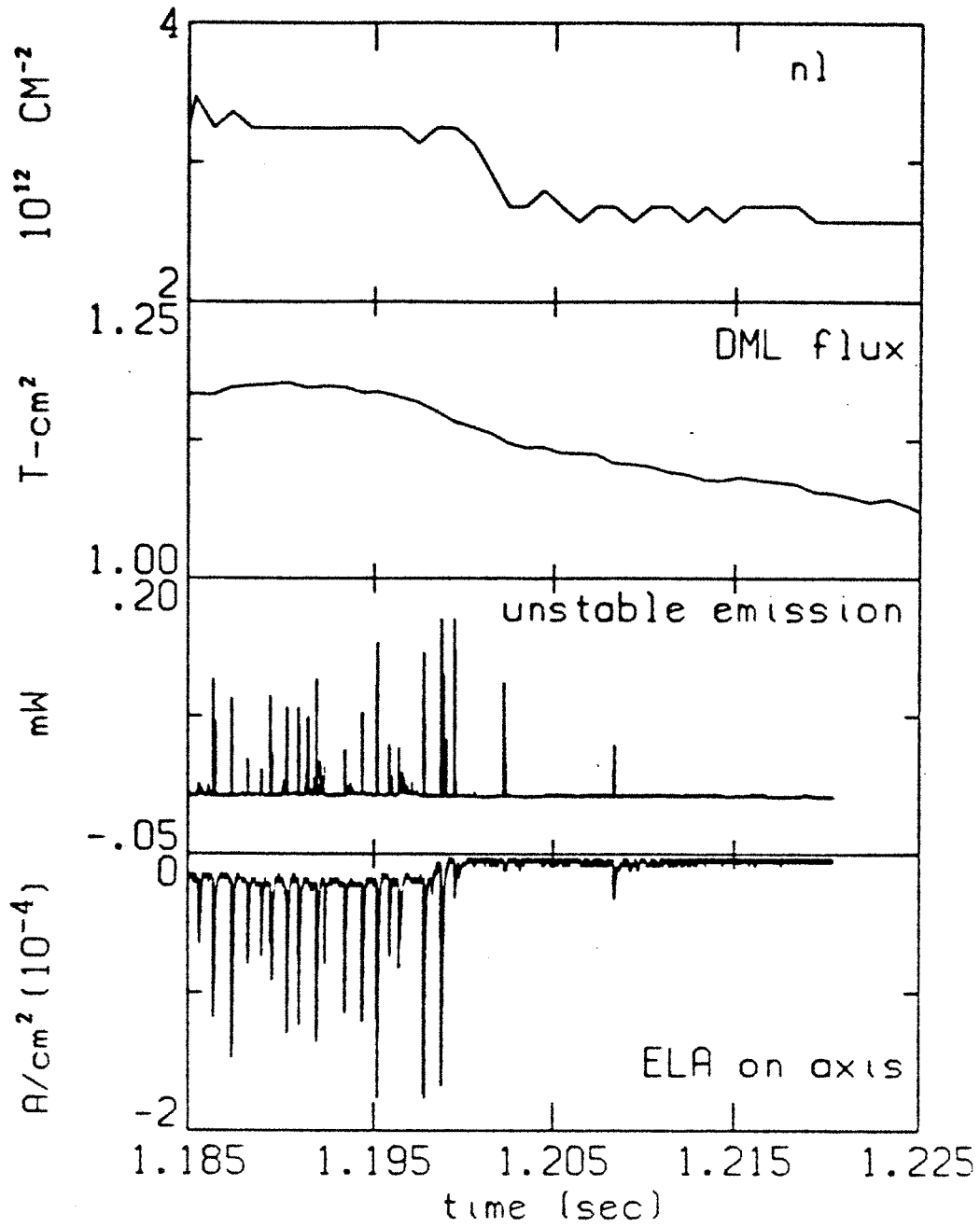
Figure 3.9: The end of a standard shot. The ECRH goes off at approximately 2 sec.
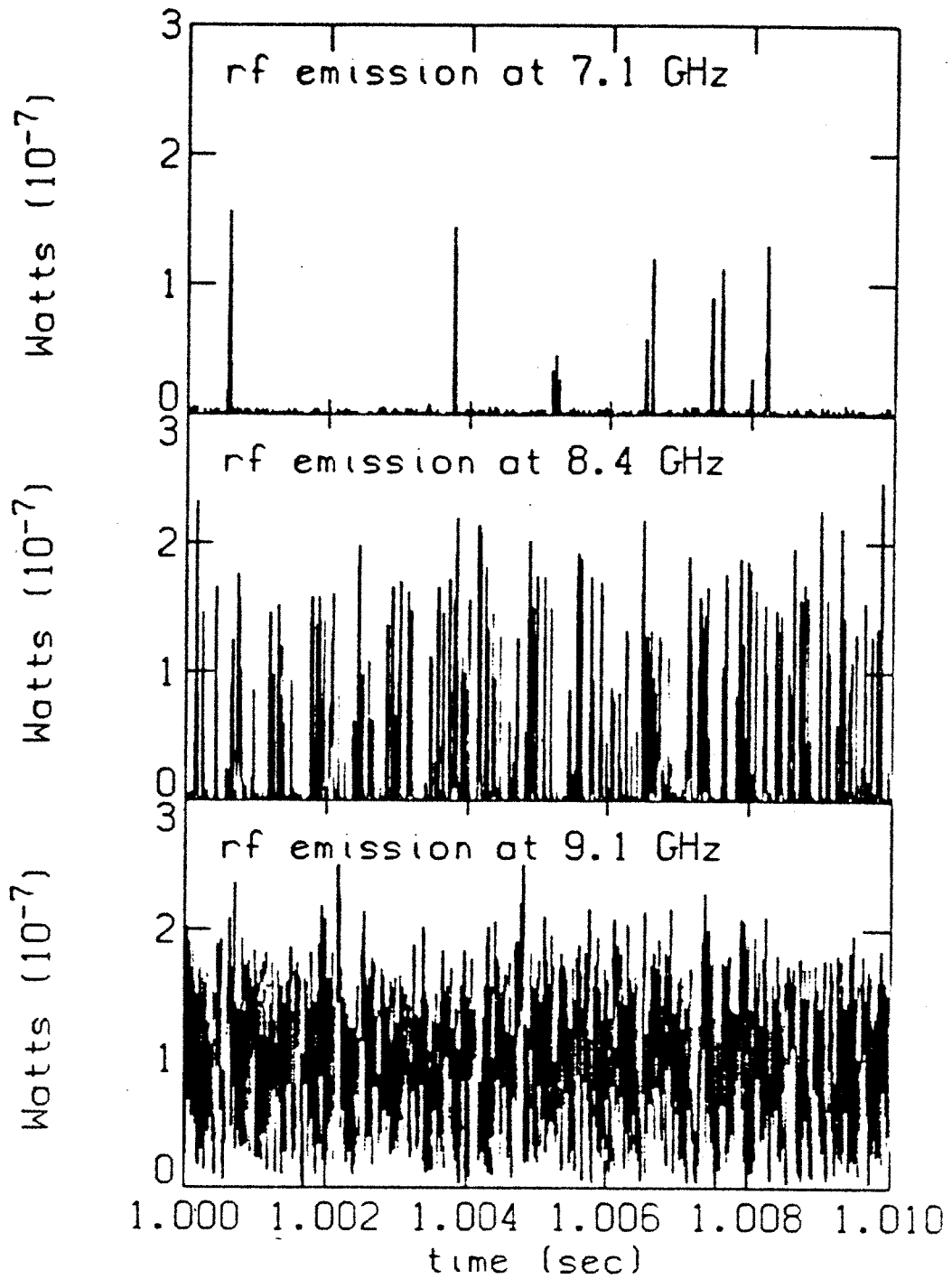
Figure 3.10: Single frequency emission at three different frequencies for a machine operating condition of 3 kW. 3 kG. and 5 > 10^{-7} torr.

into the whistler B emission. It is not even clear that the whistler B emission does not occur at the higher frequencies characteristic of the whistler C emission when the latter is present. It is clear however that the whistler C emission does not occur in the frequency ranges indicated in Fig. 3.4, the frequency range for the whistler B emission when only the whistler B emission is present. Since the single frequency whistler C emission occurs either continously or in bursts with a very high burst rate, the power of this emission for single frequencies is more reliable in depicting a frequency spectrum than for lower burst rate whistler B emission. For the whistler C emission the cavity effects of the vacuum chamber are presumably averaged out in time as the plasma randomly changes the geometrical structure of the cavity modes.

Figure 3.11 shows the frequency spectrum of the whistler C emission for several different magnetic fields. Each plot shows the detected power, averaged over a 40 msec time span at 1 second after ECRH begins, for a series of shots in which the ECRH power was 3 kW. Similar results are obtained when considering other times in the shot. An important fact to note is that the whistler C emission for a magnetic field of 3.6 kG is less than 10.1 GHz, which is the corresponding midplane cyclotron frequency. This rules out the possibility that the whistler C emission corresponds to the upper hybrid loss cone instability (Porkolab, 1984) or a fast electromagnetic wave instability, both of which have frequencies above the cyclotron frequency.

Figure 3.12 shows the power of the whistler C emission at 9.2 GHz as a function of pressure and magnetic field. These are similar to plots of the total rf emission as a function of pressure and magnetic field, which will be shown in the next section.

Qualitative analysis of the electron endloss at different radial positions indicates that the whistler C emission is associated with the plasma of the off-axis magnetic field lines, when the magnetic field is is less than approximately 3.4 kG. Figures 3.13 to 3.16 show data from the five endloss analyzers on the south end of the machine.

Each figure shows data for a magnetic field of 2.4 kG, 2.8 kG, 3 kG, and 3.6 kG, respectively, and for a pressure for which the whistler C emission is present.
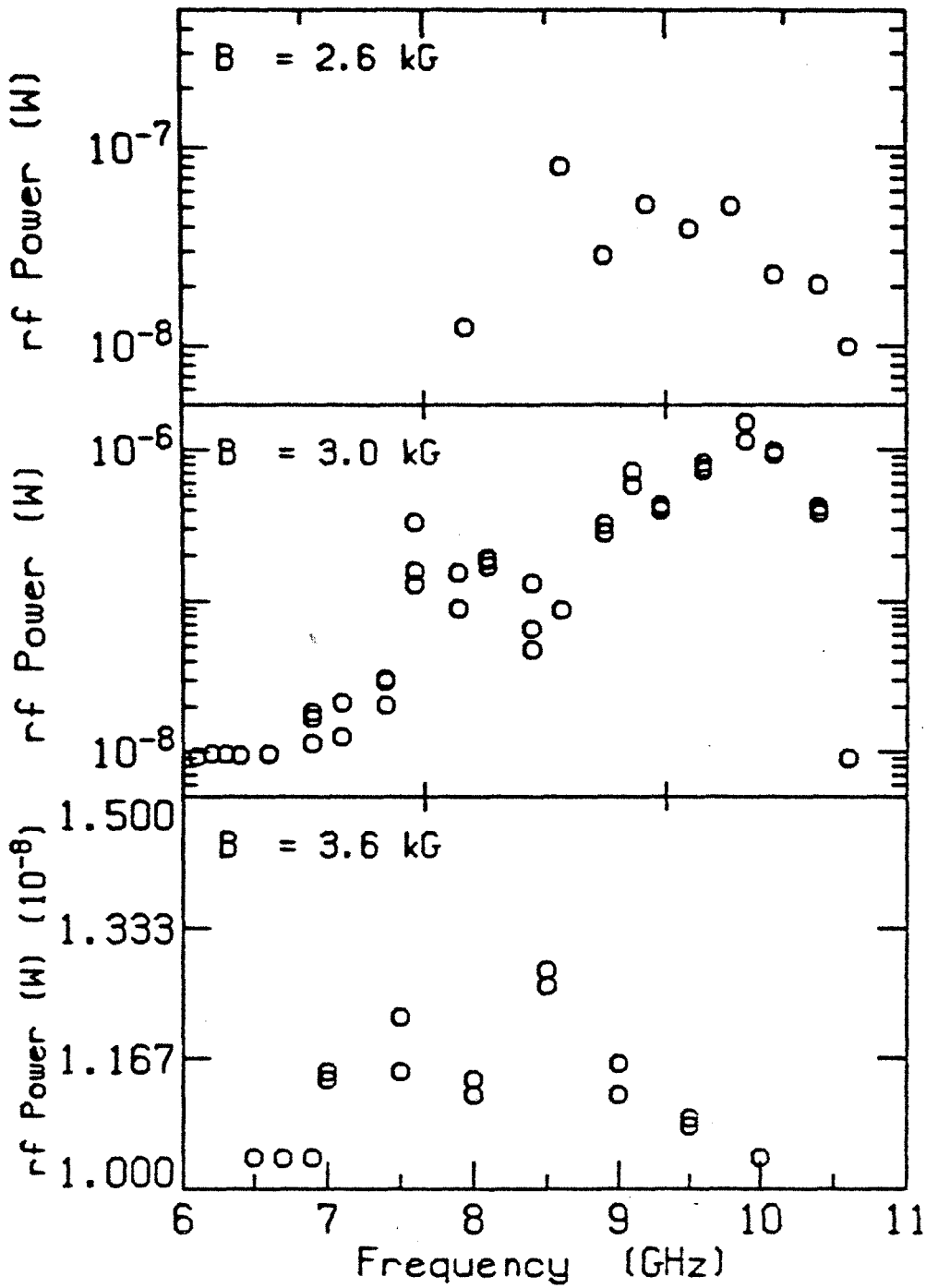
Figure 3.11: Power of emission versus frequency spectrum for different magnetic fields.
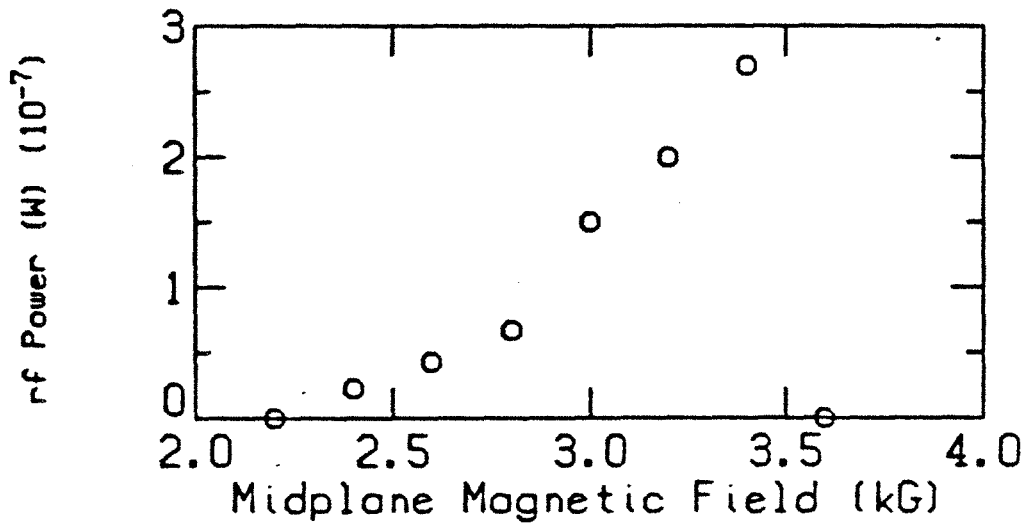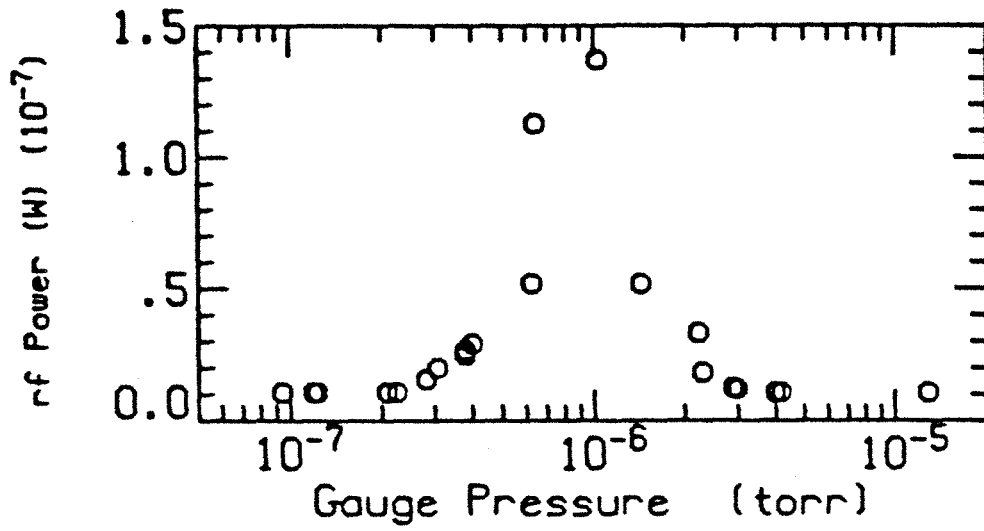
Figure 3.12: Power of emission at 9.2 GHz (a) versus pressure and (b) versus magnetic field.
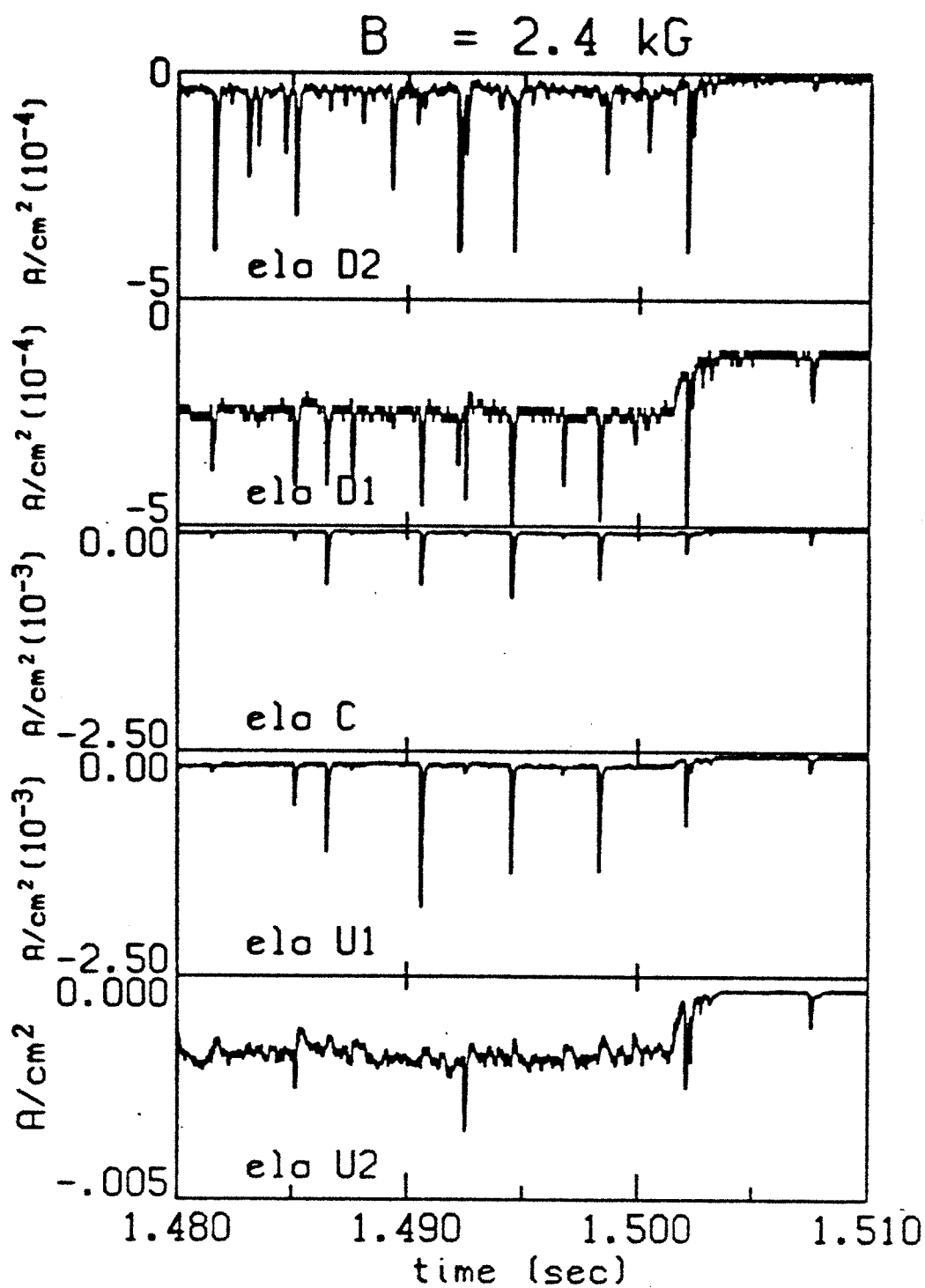
Figure 3.13: Data from the five south endloss analyzers for a magnetic field of 2.4 kG in the medium pressure regime.
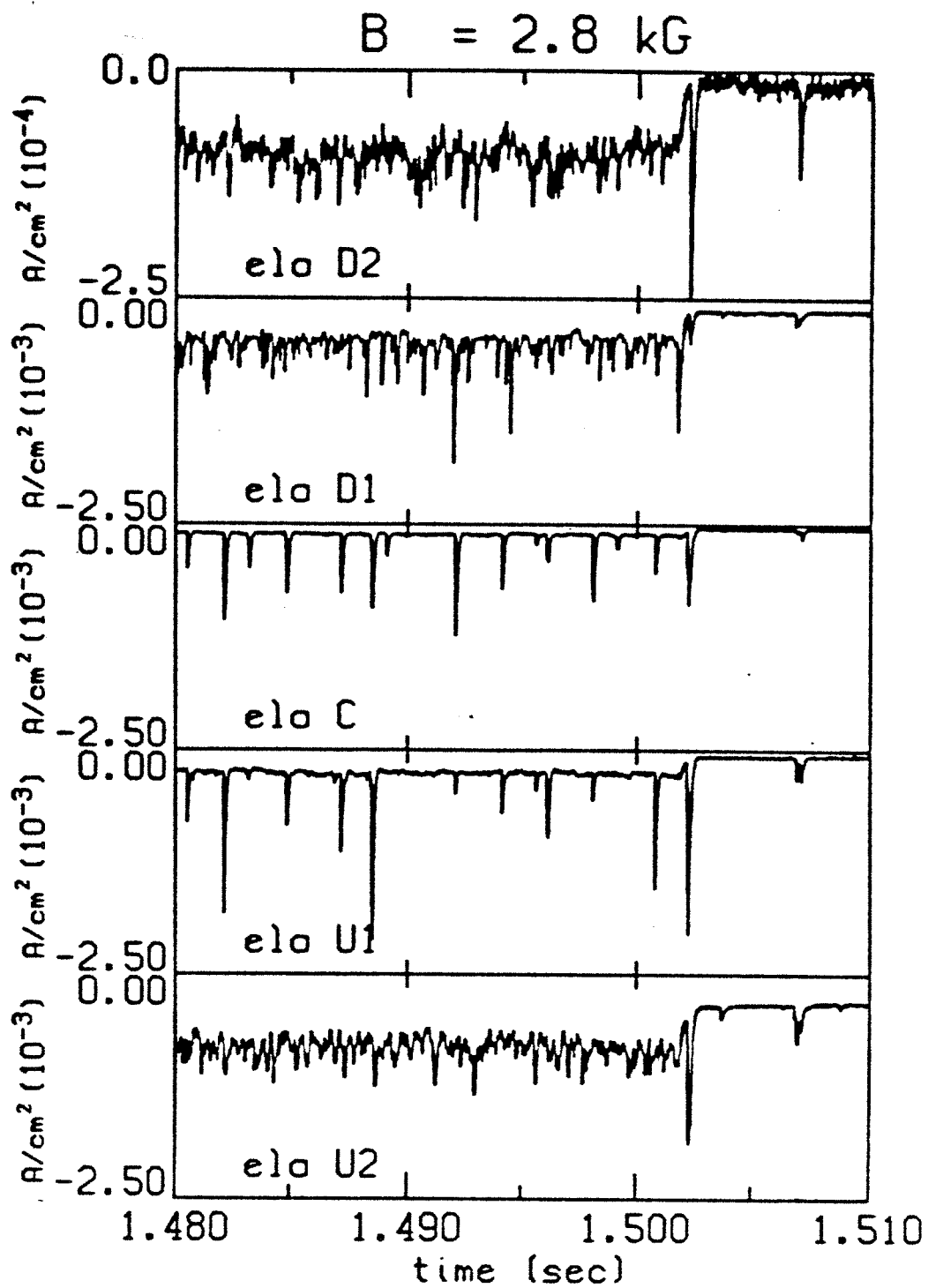
Figure 3.14: Data from the five south endloss analyzers for a magnetic field of 2.8 kG in the medium pressure regime.

B = 3.0 kG
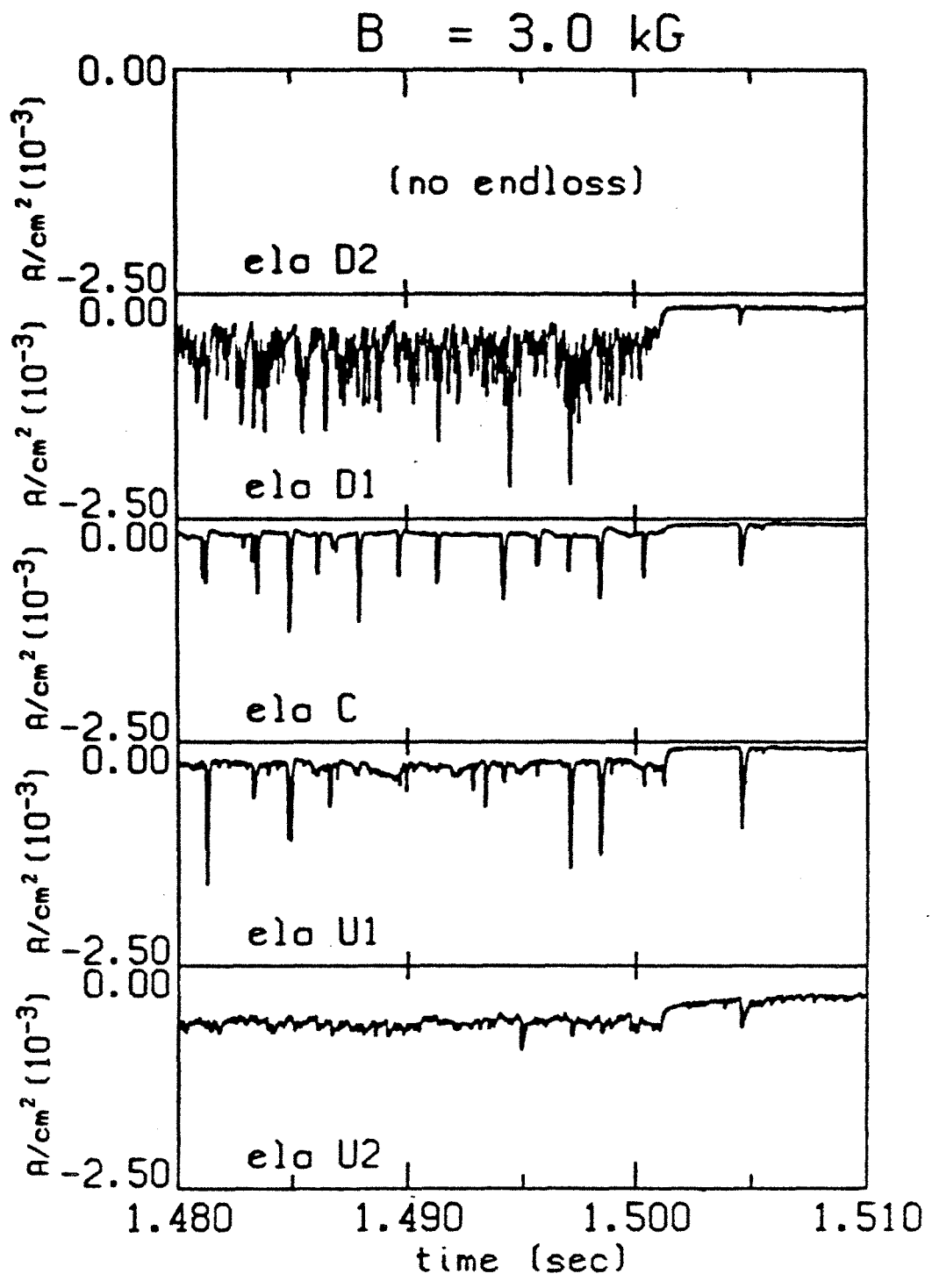
Figure 3.15: Data from the five south endloss analyzers for a magnetic field of 3 kG in the medium pressure regime.
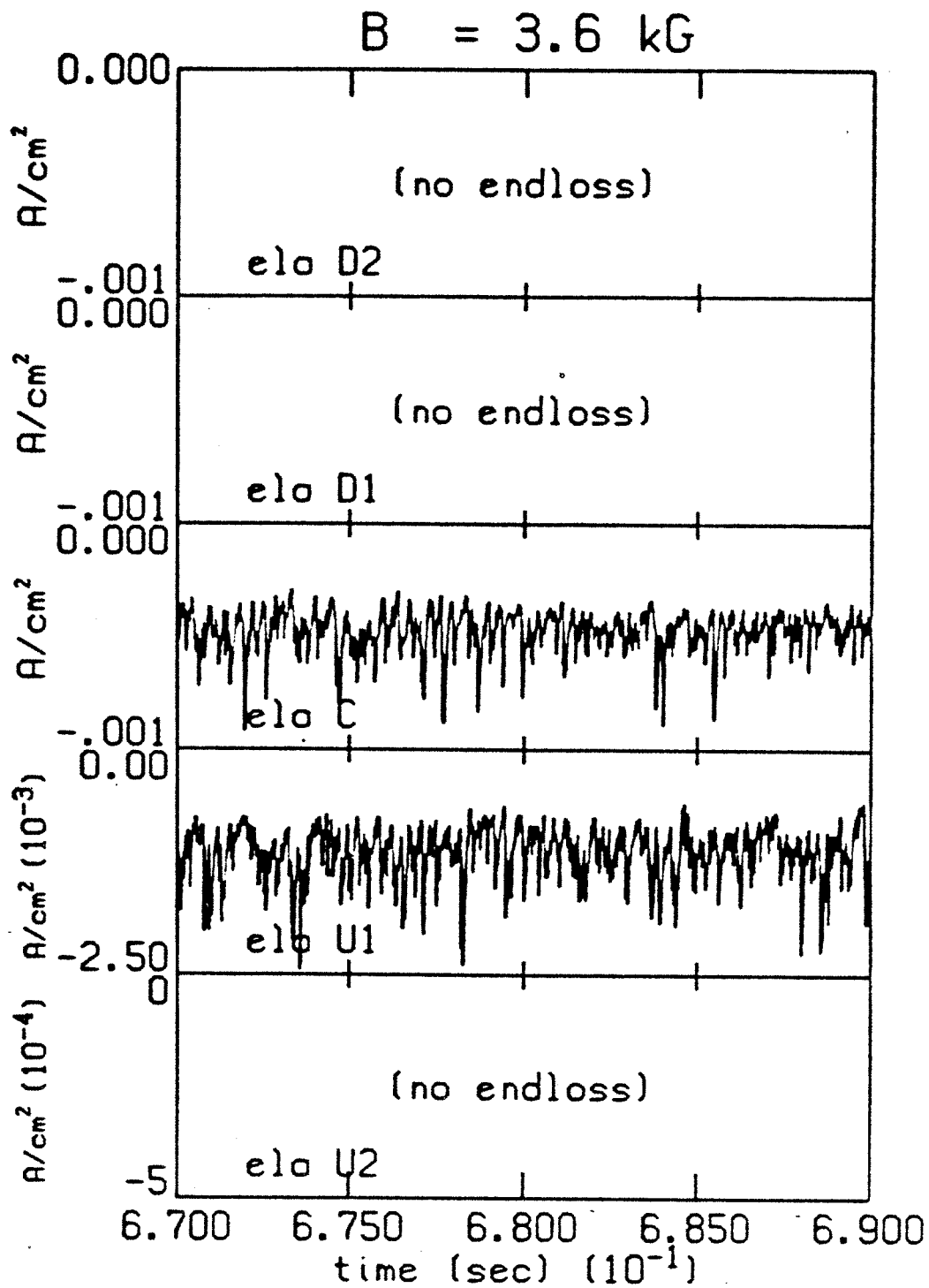
Figure 3.16: Data from the five south endloss analyzers for a magnetic field of 3.6 kG in the medium pressure regime.

The midplane radial positions of the resonance zone for 2.4 kG, 2.8 kG, 3 kG, and 3.6 kG are 15 cm, 12 cm, 10 cm, and 5 cm, respectively. The five analyzers are at different positions along the thin part of the plasma fan at the endwall. These positions map to the following midplane positions, referenced to the machine axis:[4]

endloss analyzer	midplane postions
U2	+11.4 cm
U1	+5.9 cm
C	on machine axis
D1	−5.9 cm
D2	−11.4 cm

where "U" means up, "D" means down, and "C" means center. For 3 kG it is seen that the signal of analyzer D1 is more similar to the whistler C emission, in the sense that the bursts are very irregular and not well defined. This is to be compared to the bursts on analyzers U1 and C, which are more similar to the whistler B emission. When the magnetic field is lowered to 2.4 kG the resonance zone is moved outward and the plasma is larger. For this case the signal on analyzer D1 looks more like the whistler C emission and the signal on analyzer D2 looks like what the signal on analyzer D1 looked like for 3 kG. When the magnetic field is 2.8 kG the signal on analyzer D1 is intermediate between the two types of behavior. When the magnetic field is 3.6 kG the plasma is made smaller. For this case the signal on analyzer C takes on an appearance similar to the signal that analyzer D1 had for the 3 kG case. Figure 3.17 shows data from the five endloss analyzers for a magnetic field of 3 kG and for a pressure in the low pressure regime in which the whistler C emission is absent. It is seen that the bursts on analyzer D1 are very similar now to the whistler B emission, although approximately 10 times smaller than the bursts on analyzers U1 and C.

Speculations can be made as to why the whistler C emission is associated with outer field lines. It will be shown in Section 3.4 that the burst rate of the emission

---

[4]These values were determined analytically with the EFFI code. The actual mapping of the field lines from the midplane is 1-2 cm below the axis at the endwall (Smatlak, 1986).
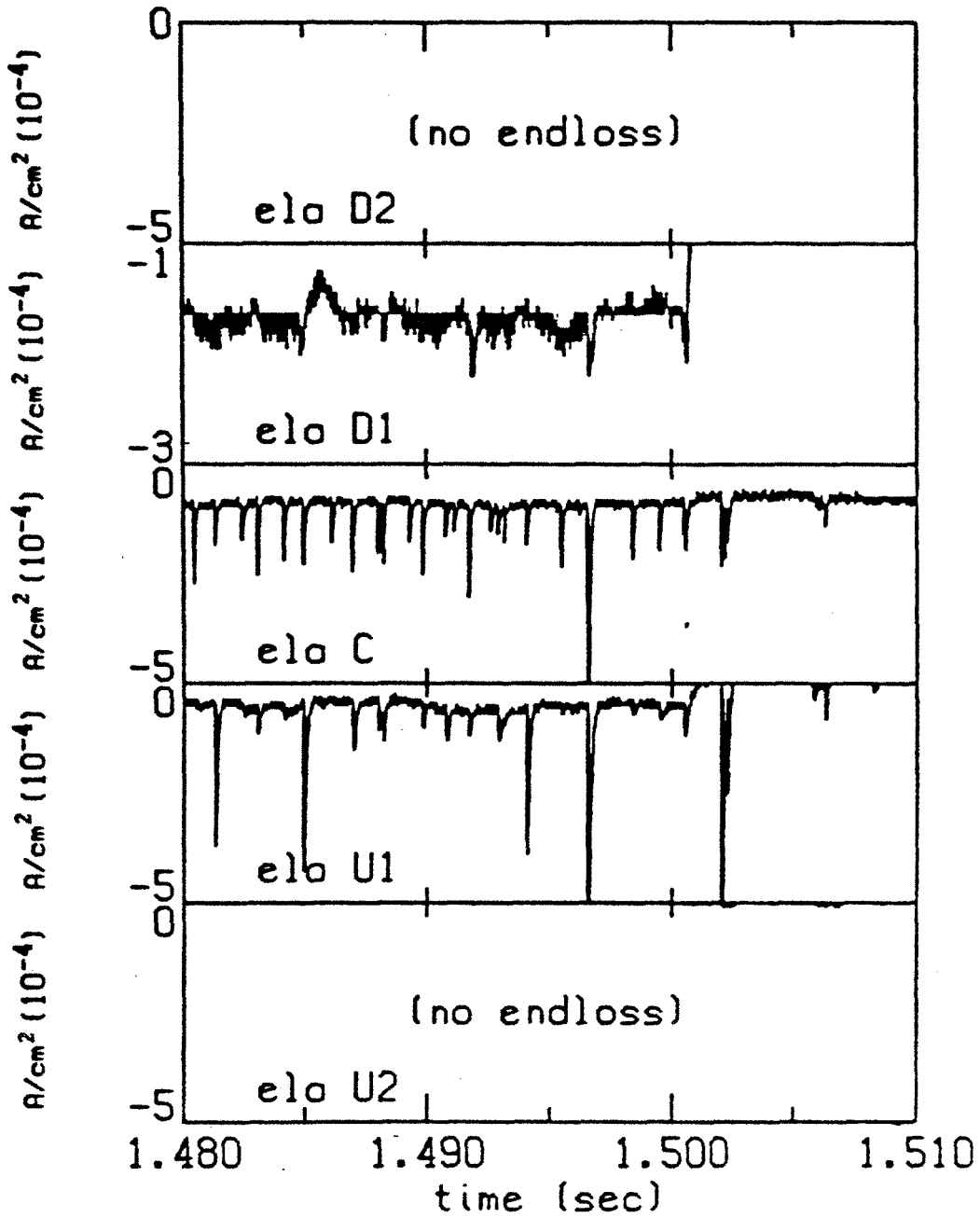
Figure 3.17: Data from the five south endloss analyzers for a magnetic field of 3 kG in the low pressure regime in which the whistler C emission is absent.

increases for increasing ECRH power, indicating that bursting is a heating rate effect. The heating rate, according to quasilinear theory (Lieberman and Lichtenberg, 1973), is proportional to the square of effective time τ_{eff} that a particle stays in resonance, which is inversely proportional to the derivative of the magnetic field along the field line dB/ds at resonance (when the resonance is not at the midplane or a particle turning point):

$$\frac{dW}{dt} \sim D \sim \left(\frac{qE_k\tau_{eff}}{m} \right)^2 \frac{1}{\tau_b}$$

where W is the total particle energy energy, D is the quasilinear diffusion coefficient, and τ_b is the particle bounce time. A field line further from the axis has a smaller dB/ds at resonance than a field line nearer to the axis (assuming it is not so far out that it does not have a resonance) and thus a higher heating rate. The field line with the highest heating rate is the one which is tangent to the resonance zone at its midplane because it has $dB/ds = 0$ at resonance. Therefore, outer field lines should be associated with higher burst rates than inner field lines, if they are unstable. The reason why the whistler C emission is associated with higher frequencies is discussed in Chapter 4. It is based on the fact that the observed plasma density profile is hollow and has a higher density on the off-axis field lines. Theoretical calculations show that higher densities cause higher growth rates for unstable waves with the frequencies characteristic of the whistler C emission (as well as for unstable waves with the frequencies corresponding to the whistler B emission).

3.2.2 Total Rf Emission

The figures in this section show the power of the total rf emission. In these figures the power is displayed as the average power over a 40 msec time span at some time during the shot.[5] In some of the figures the power per burst and the burst rate are displayed in parameter regimes where this is possible (i.e. where individual bursts

---

[5] It is recalled from Chapter 2 that the detected power can be multiplied by 1400 to get an approximate value for the cavity power to within 50%.

are discernilble). The display of average power is more reliable in providing total power information, since the bursts cannot be analyzed for all parameter regimes. The display of burst information shows that the increase in power for different parameters is often a result of both an inrease in energy per burst as well as an increase in burst rate.

Figures 3.18 to 3.20 show the power of the total rf emission, the energy per burst of the total rf emission at low pressures, and the corresponding diamagnetism all as a function of pressure. Each figure corresponds to a different time in a series of identical shots in which the ECRH power was 1 kW and the magnetic field was 3 kG. Each point corresponds to the average value of the particular quantity in a 40 msec time span beginning at the time specified in the figure. These figures show that the power of the rf emission is approximately constant in time during the ECRH phase of the shot. This is to be contrasted with the behavior of the hot electrons, which does change during the shot. This is revealed in Figure 3.21, which shows the temporal evolution of the hot electron temperature, the diamagnetism, and some other parameters for the same series of shots. Figures 3.18 to 3.20 also show that the power of total rf emission does not peak at the same pressure that the diamagnetism peaks, another indication that the hot electrons are independent of hot electron behavior. This is discussed in more detail in the next section. Finally, the figures indicate that a higher power of emission is the result of both a higher burst rate and a higher amount of rf energy per burst.

Figures 3.22 to 3.24 show the power of the total rf emission, the energy per burst and burst rate of the total rf emission at low pressures, and the corresponding diamagnetism all as a function of pressure, for different ECRH powers. Each point corresponds to the average power of the particular quantity in a 40 msec time beginning at 1 sec after ECRH, although the absolute time does not matter, as was shown above. These figures also show that the total rf emission does not peak at the same pressure as the diamagnetism, and that an increase in total rf emission is the result of both an increase in burst rate and an increase in energy per burst. Also,
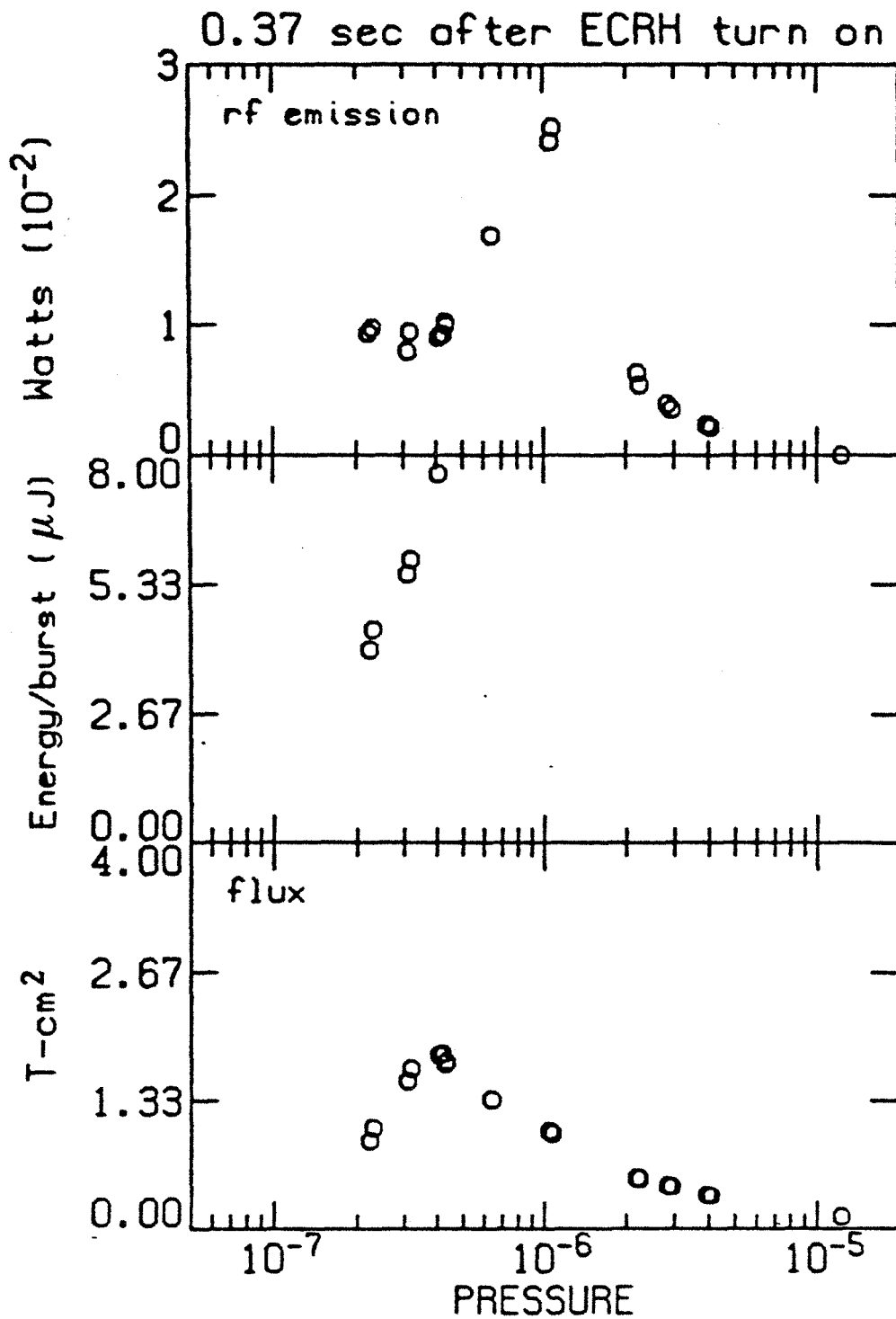
Figure 3.18: .5 sec after ECRH goes on. a) Power and b) energy per burst of total rf emission as seen by the detector. c) Diamagnetism
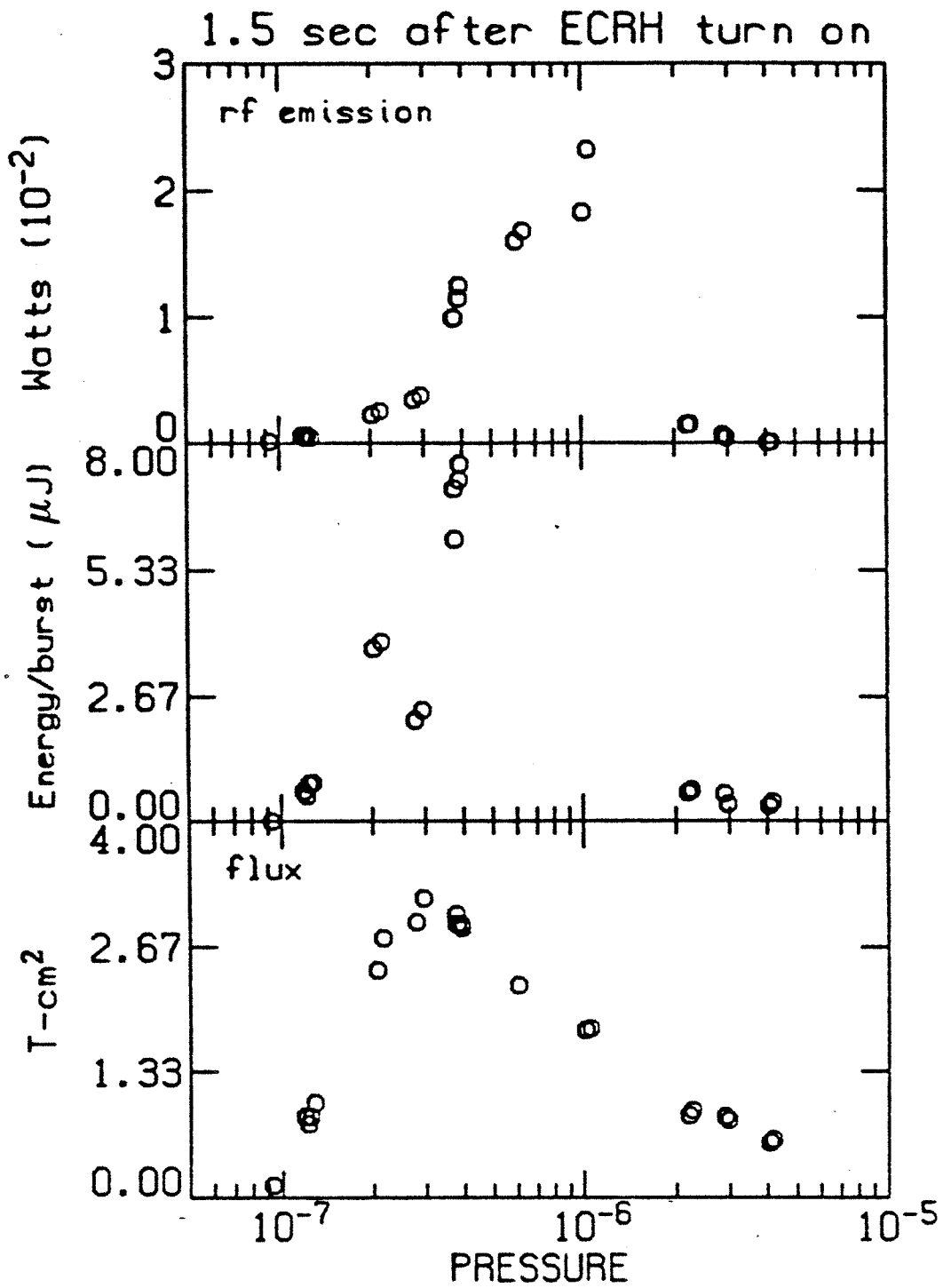
Figure 3.19: 1.5 sec after ECRH goes on. a) Power and b) energy per burst of total rf emission as seen by the detector. c) Diamagnetism
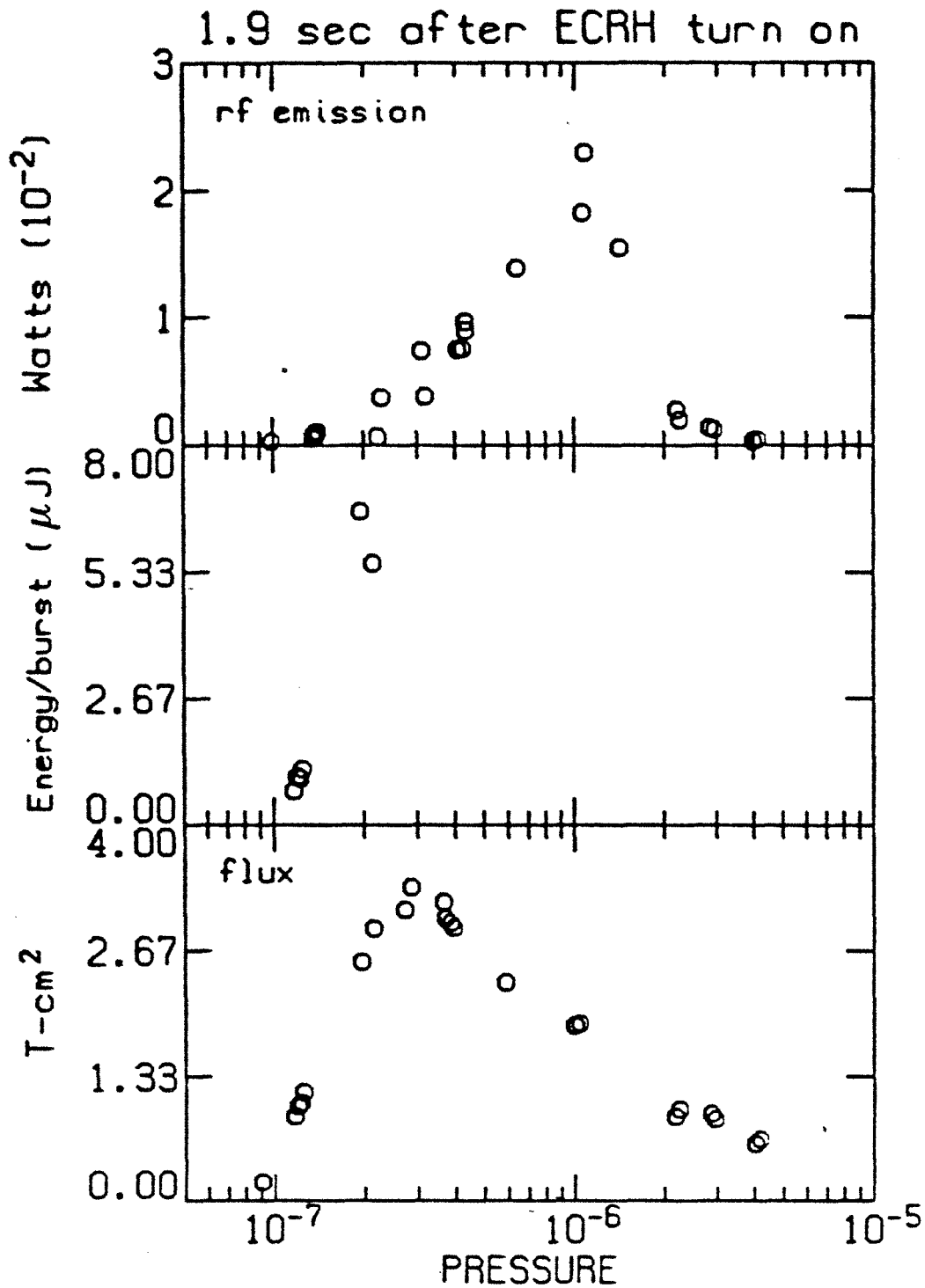
Figure 3.20: 2 sec after ECRH goes on. a) Power and b) energy per burst of total rf emission as seen by the detector. c) Diamagnetism
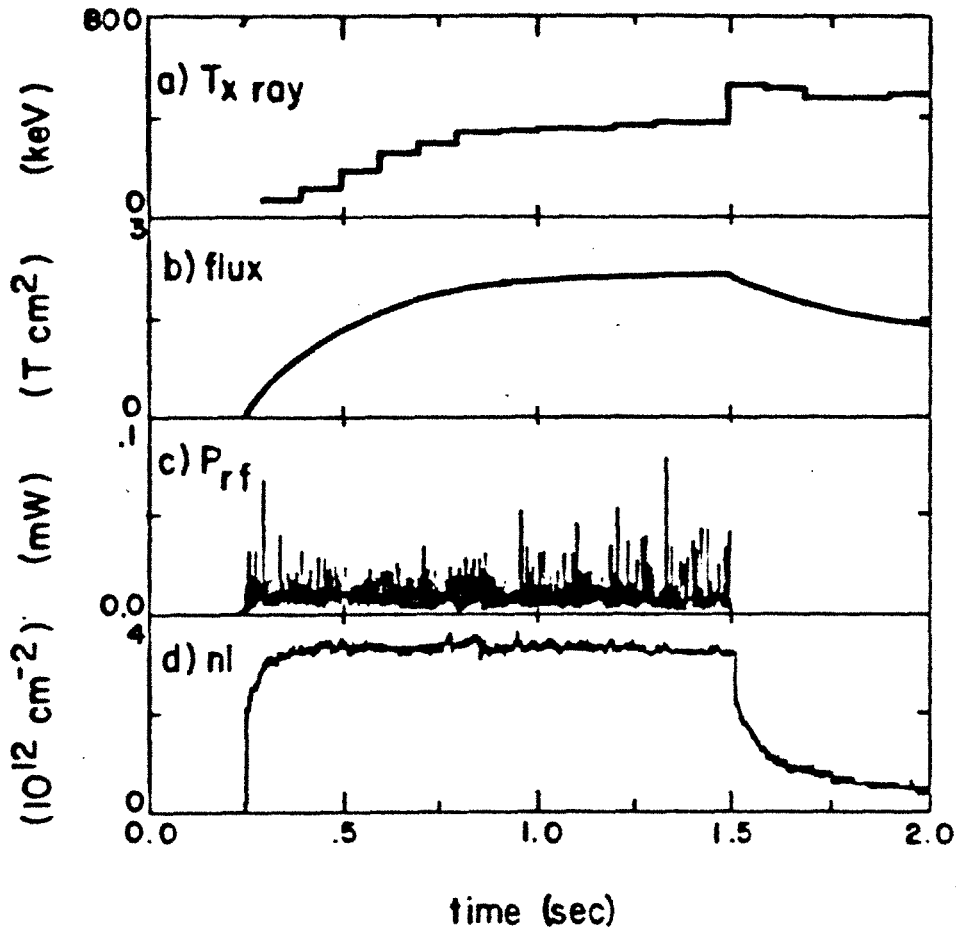
Figure 3.21: a) Hot electron temperature determined with x-rays. b) Diamagnetism. c) Detected power of total rf emission. c) Line density.

the power of the total rf emission increases with ECRH power; the dependence is shown more clearly below.

Figure 3.25 shows the peak total rf emission power (which occurs for a pressure of 1×10^{-6} torr as shown in several of the figures above) as a function of ECRH power. The rf emission is fairly linear up to 1 kW. Above 1 kW the rf emission power increases at a lower rate with ECRH power. A plot of diamagnetism versus ECRH power shows a similar dependence (see Fig. 3.28), indicating that the total plasma energy content is proportionately less above 1 kW as compared to below 1 kW.

Figure 3.26 shows the peak total rf emission power as a function of magnetic field. For this plot data was collected for a pressure which did not necessarily correspond to the pressure which gives the peak total rf emission power. The result was normalized to the known peak values obtained earlier. There is no unstable rf emission at 3.7 kG because plasma cannot be produced for this magnetic field. Plasma can be produced for a magnetic field of 2.2 kG (as shown by the plot of diamagnetism and density versus magnetic field in Fig. 3.27). The plasma is microstable at and below 2.2 kG.

Figures 3.25 and 3.26 indicate (as do the results of endloss analysis shown in the next section) that the amount of power associated with the microinstability is related to the electron heating rate. This is indicated directly by the linear relationship between power of total rf emission and ECRH power (normalized to power absorbed by plasma). It is suggested by the increase in total rf emission power for increasing magnetic field. As the magnetic field increases the volume of the plasma decreases and the power density increases, leading to higher heating rates.
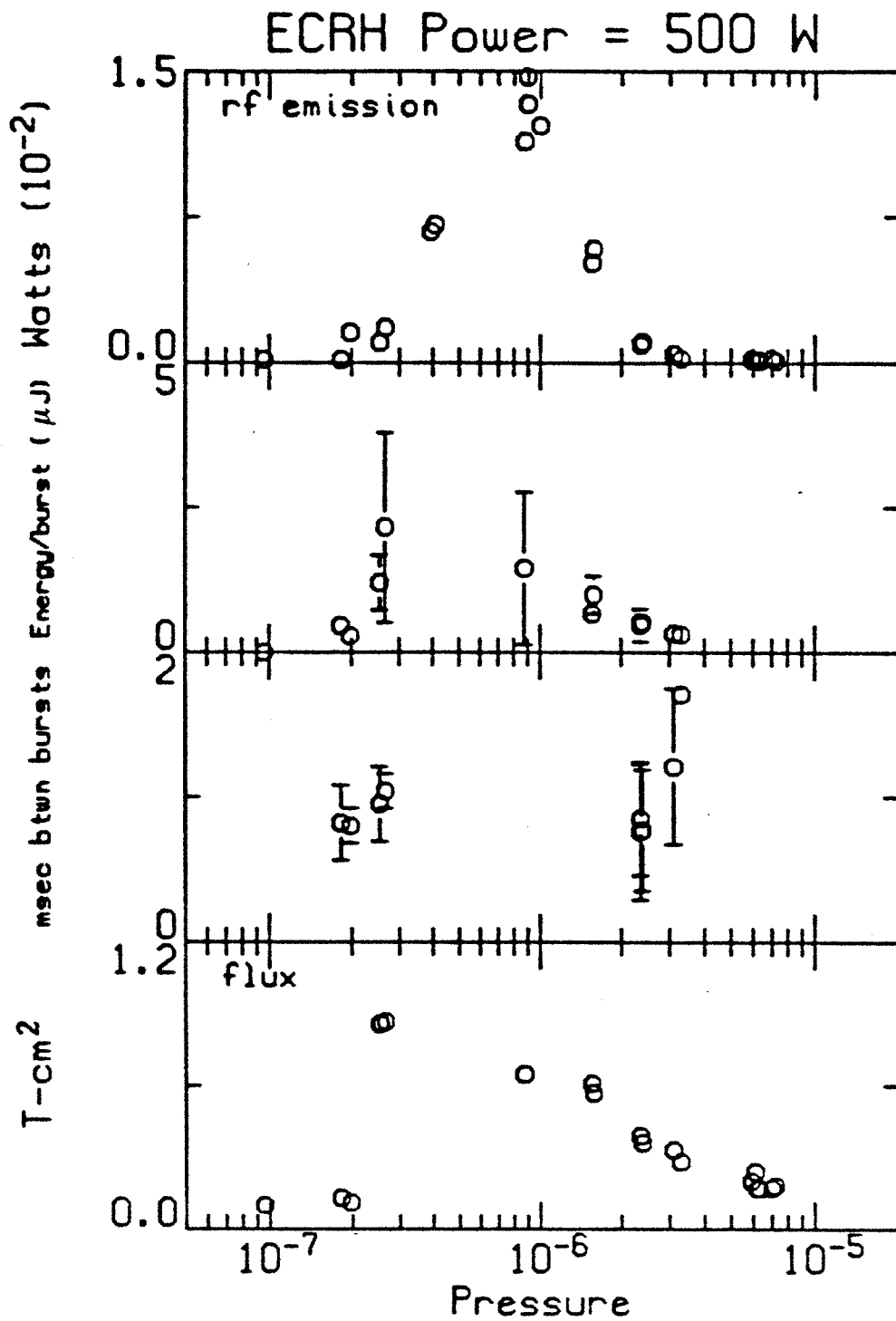
Figure 3.22: 500 W of ECRH power. a) Power. b) energy per burst, and c) time between bursts of total rf emission. d) Diamagnetism
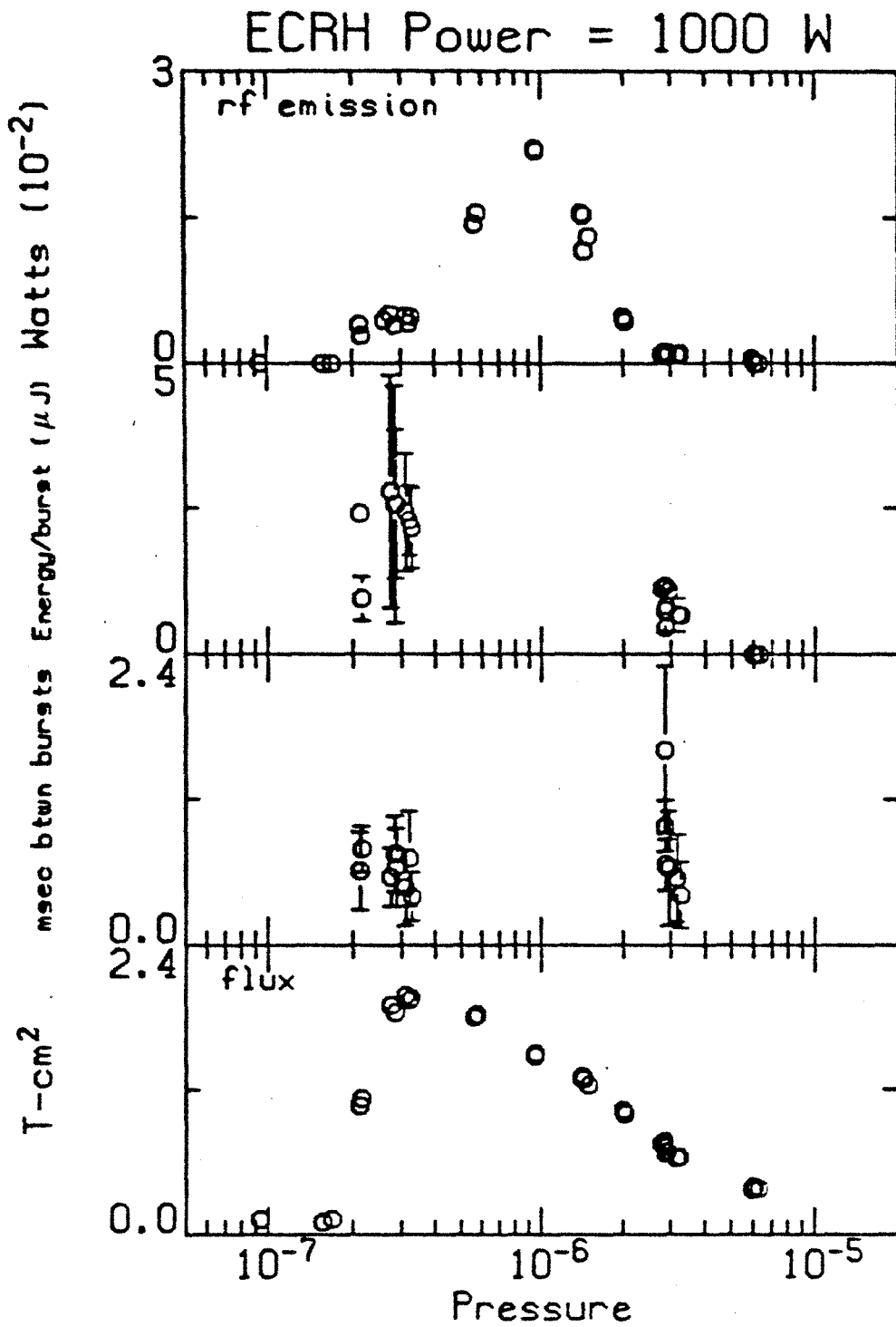
Figure 3.23: 1000 W of ECRH power. a) Power. b) energy per burst. and c) time between bursts of total rf emission. d) Diamagnetism
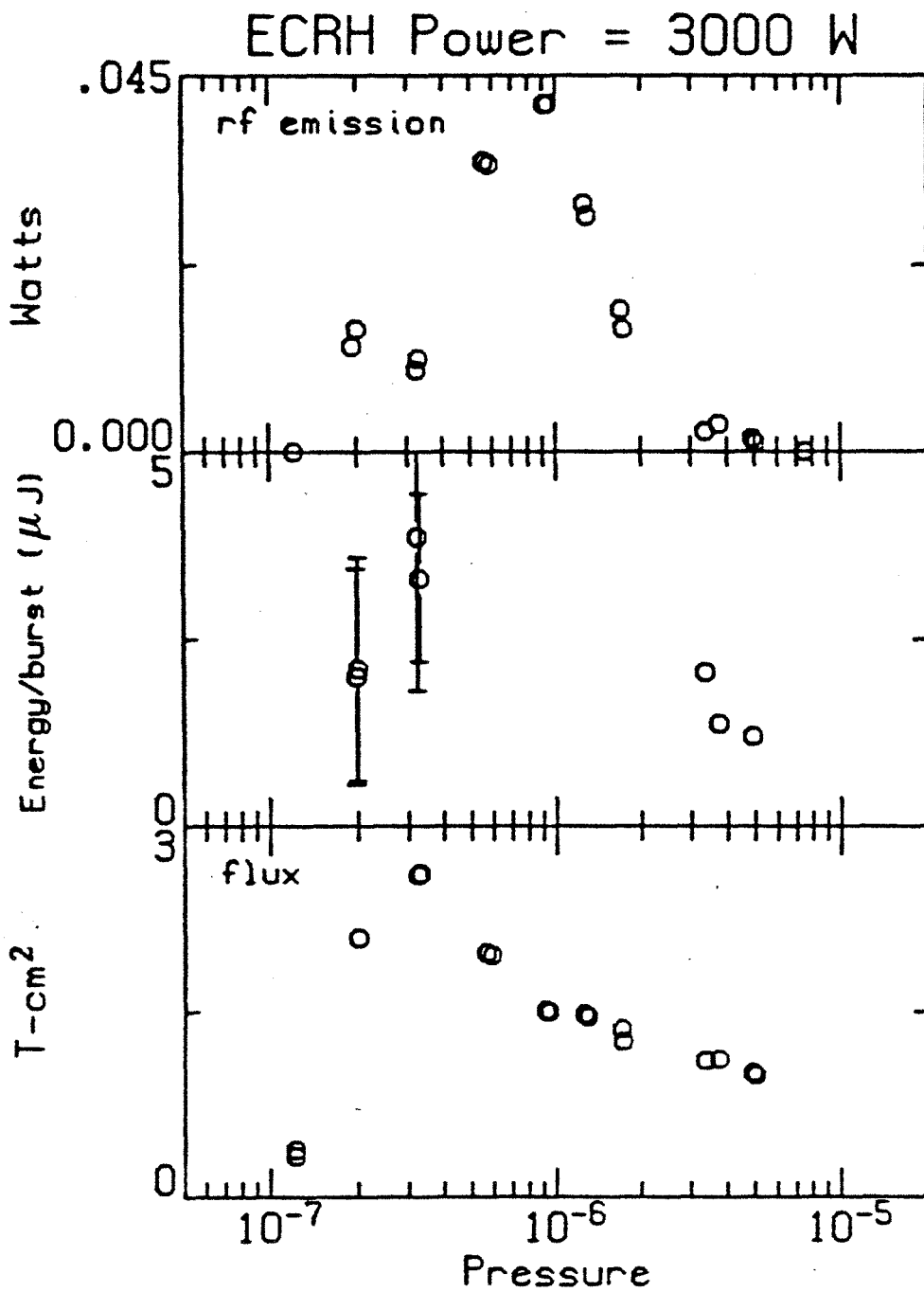
Figure 3.24: 3000 W of ECRH power. a) Power. b) energy per burst. and c) time between bursts of total rf emission. d) Diamagnetism
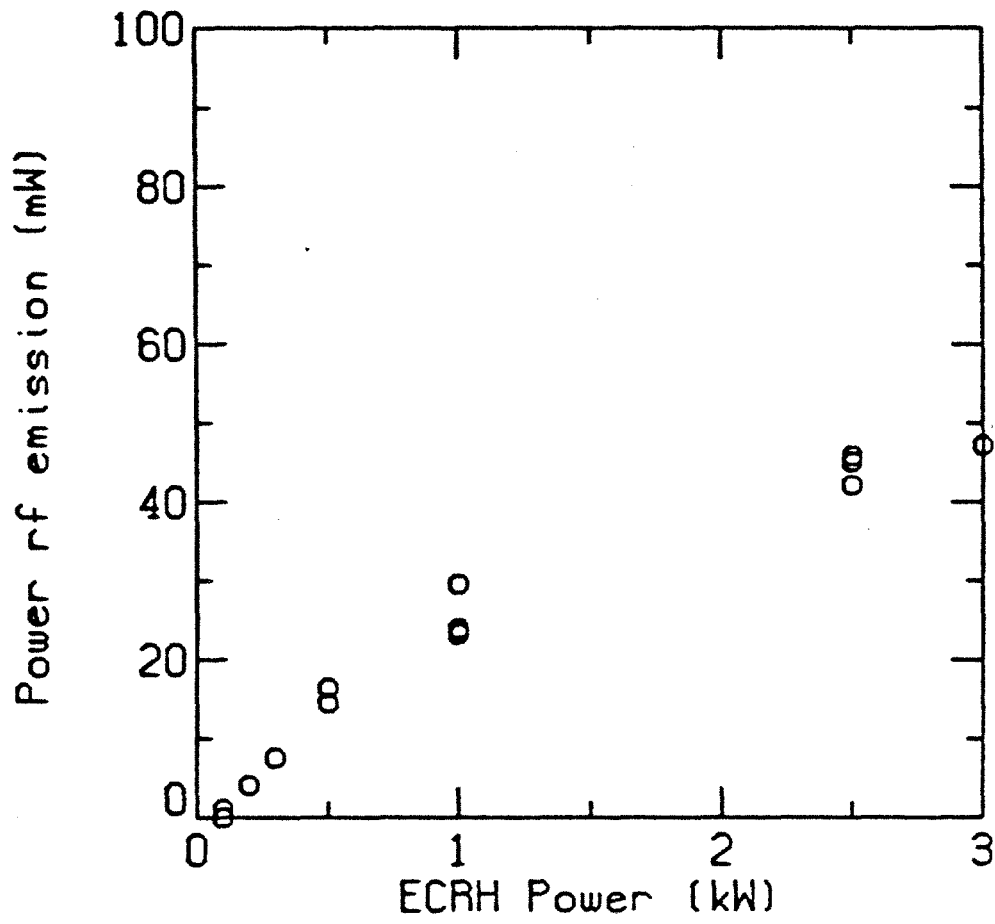
Figure 3.25: Peak power of total rf emission as a function of ECRH power.
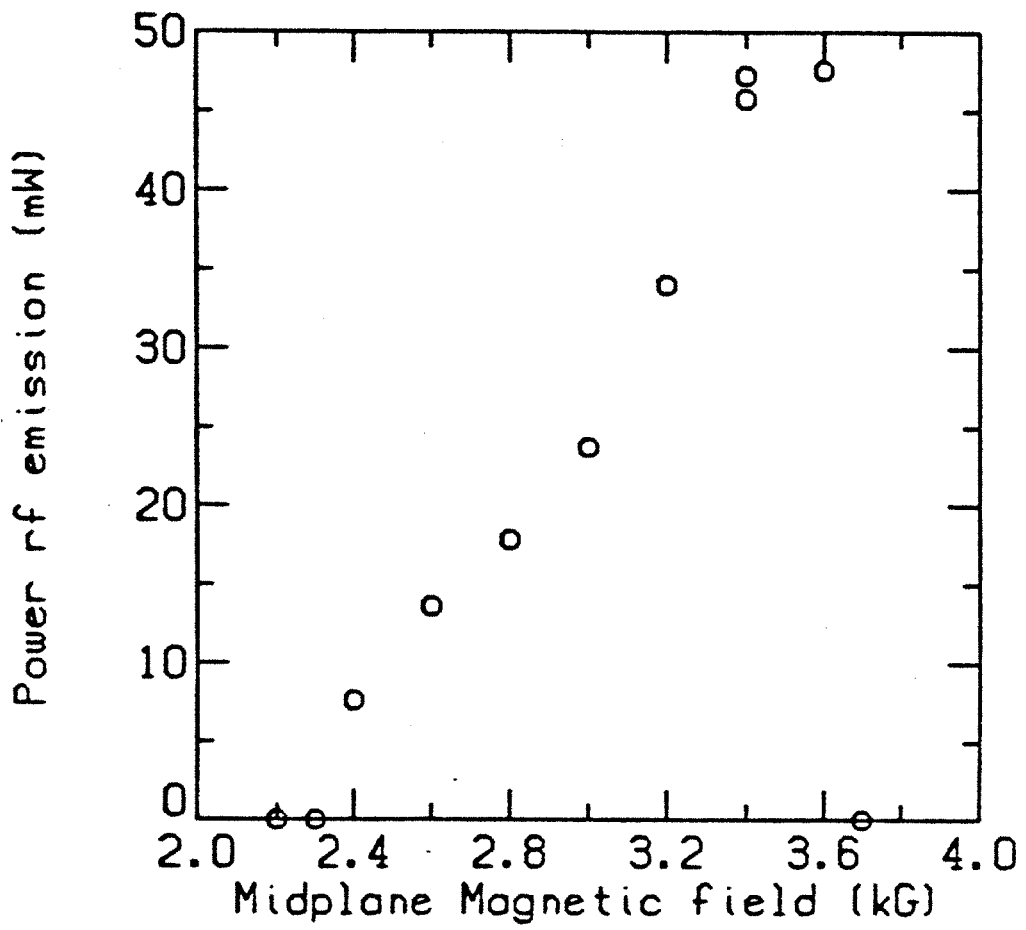
Figure 3 26: Peak power of total rf emission as a function of magnetic field.
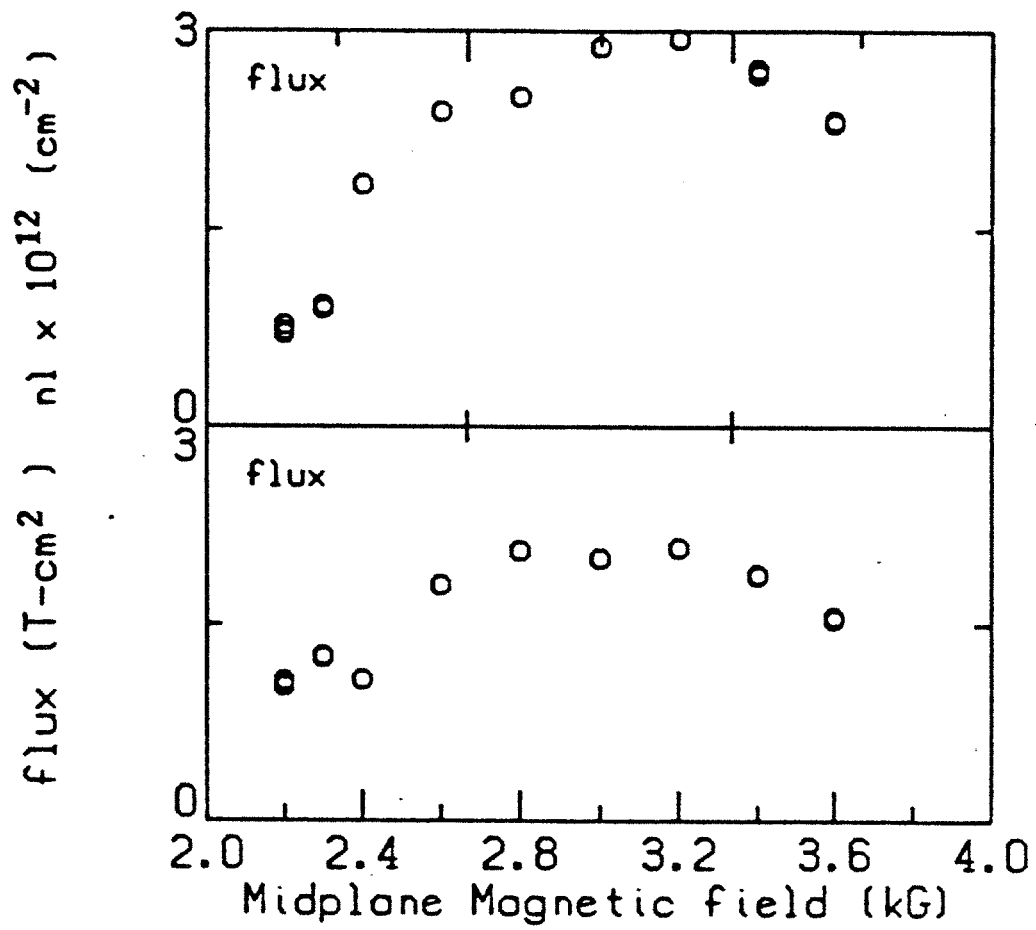
Figure 3.27: Diamagnetism and line density versus magnetic field.
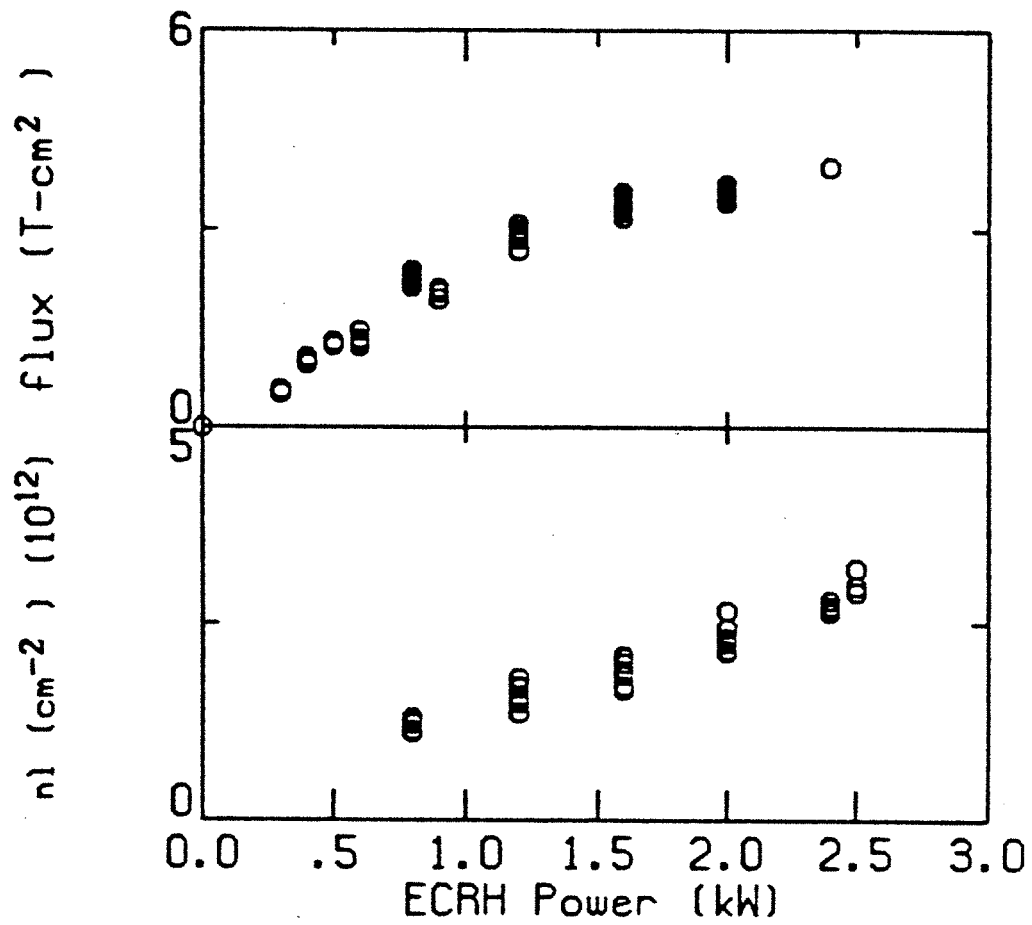
Figure 3.28: Diamagnetism and line density versus ECRH power.

3.3 Warm Electron Microinstability

The following experimental evidence shows that microinstability is driven by the warm electrons while the hot component is stable and has little effect on microinstability:

1) The unstable rf emission power is constant in time during ECRH whereas the hot electron parameters vary in time. Figures 3.18 to 3.20 show that the total unstable rf emission power is approximately the same while the diamagnetism is different at different times in the shot. Figure 3.21(c) also shows qualitatively that the total rf emission power is constant on the time average. Figures 3.21(a) and 3.21(b) show the diamagnetism and the hot electron temperature varying in time during the shot. Figures. 3.18 to 3.20 also show the that the diamagnetism does not peak at the same value of pressure as the power of the unstable rf emission.

2) The whistler B emission begins less than 2.5 μsec after the gas breaks down and the whistler C emission begins less than 10 msec after the gas breaks down (see Fig. 3.8). The temperature determined from the x ray spectrum is only 10 keV 20 msec after the gas breaks down. It was mentioned in Section 2.5.1 and shown in Fig. 3.21 that the x-ray temperature for the standard shot increases at the rate of 450 keV/sec until a steady state temperature of 400 keV is attained. The first accurate spectrum (where there are enough counts for accurate statistics) is approximately 20 msec after plasma is formed.

3) The whistler C emission completely stops approximately 1 msec after ECRH is turned off. The whistler B emission bursts sporadically for several milliseconds after ECRH is turned off and then completely stops (see Fig. 3.9). The endloss analyzers indicate that the electrons with energies less than 5 keV, which are responsible for more than 99% of the total electron endloss current. leave within approximately 1 msec after ECRH is turned off, the same amount of time it would take a 1.2 keV Maxwellian of the same density to collisionally decay (see Fig. 2.8). The x-ray detector indicates that the hot electron temperature does not change after ECRH is

turned off and the diamagnetic loop together with the x-ray detector indicates that hot electron density decays exponentially with a 1 sec time constant (see Fig. 3.21).

4) There is no unstable rf emission from a plasma which contains just a hot electron component and which is being heated by ECRH. Such a plasma can be produced by turning off the neutral gas during the shot while leaving the ECRH on. Figure 3.29 shows data from such a shot. Hydrogen is supplied at a constant level in the beginning of the shot. When a sufficiently hot plasma is produced (400 keV in Fig. 3.29), the hydrogen supply is removed while the ECRH power is kept on. This removes the source of cold electrons which is the source for warm electrons which, in turn, is the source for hot electrons. Since the hot electrons have the longest confinement time, the plasma of this shot contains a very high fraction of hot electrons. The striking observation shown in Fig. 3.29 is that the unstable rf emission stops after the pressure has decayed by a sufficient amount.

5) An ECRH plasma which contains just a hot electron component can also be produced by applying a sufficient amount of ICRF power. Such a plasma is also observed to be microstable. An ICRF heating experiment is being performed on the Constance B mirror experiment (Goodman *et al.*, 1986). Figure 3.30 shows data from a shot in which 5 kW of power at 5 MHz was supplied for 100 msec during a shot in which the ECRH power was 2 kW and the magnetic field was 3.2 kG. The data indicate that only a hot electron component is present during ICRF: the endloss analyzers indicate no endloss current, the interferometer signal is reduced, and the diamagnetic loop shows a decay of the hot component which is typical of experiments in which the gas is removed but the ECRH is left on (see Fig. 3.29). (This decay is associated with the combination of collisional loss and ECRH induced loss of hot electrons.) There is no unstable rf emission during ICRF. Goodman *et al.* (1986) have observed that there is a threshold power, dependent on pressure, above which the cold and warm electron components are completely extinguished.

The conclusion that the warm electrons drive the microinstabilities leads to conclusions about the experimentally measured microinstability induced electron
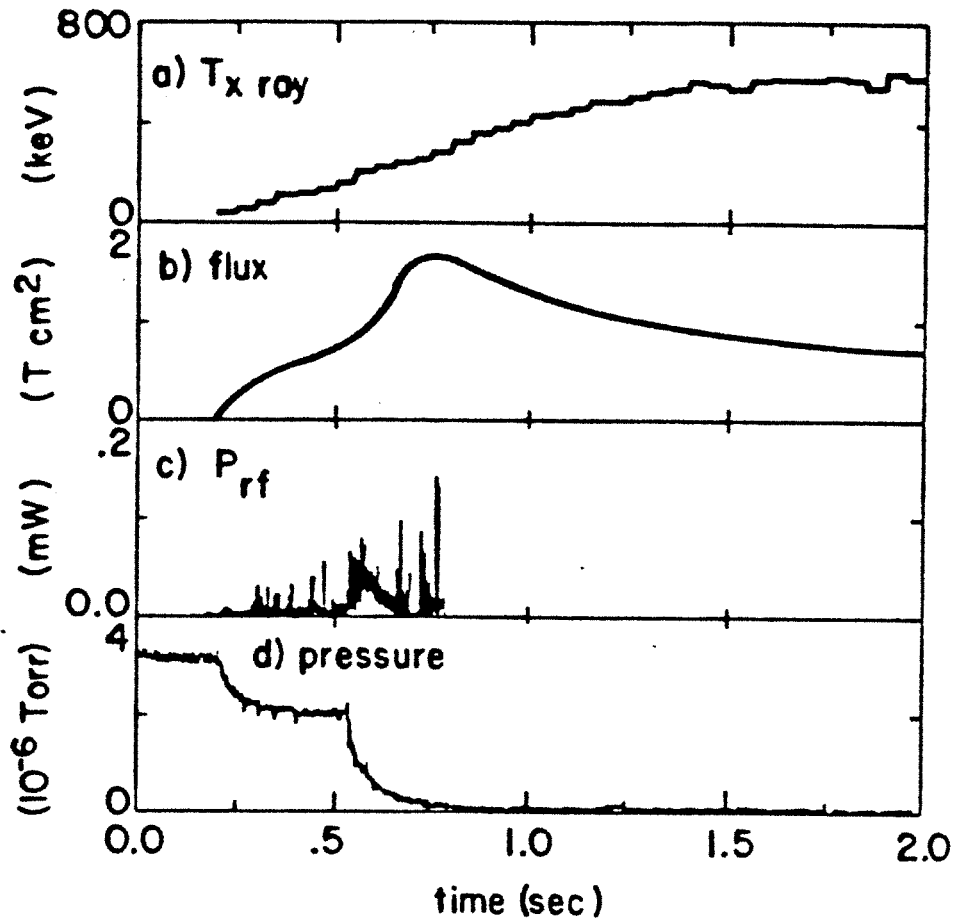
Figure 3.29: Data from a shot in which the gas was turned off and the ECRH left on.
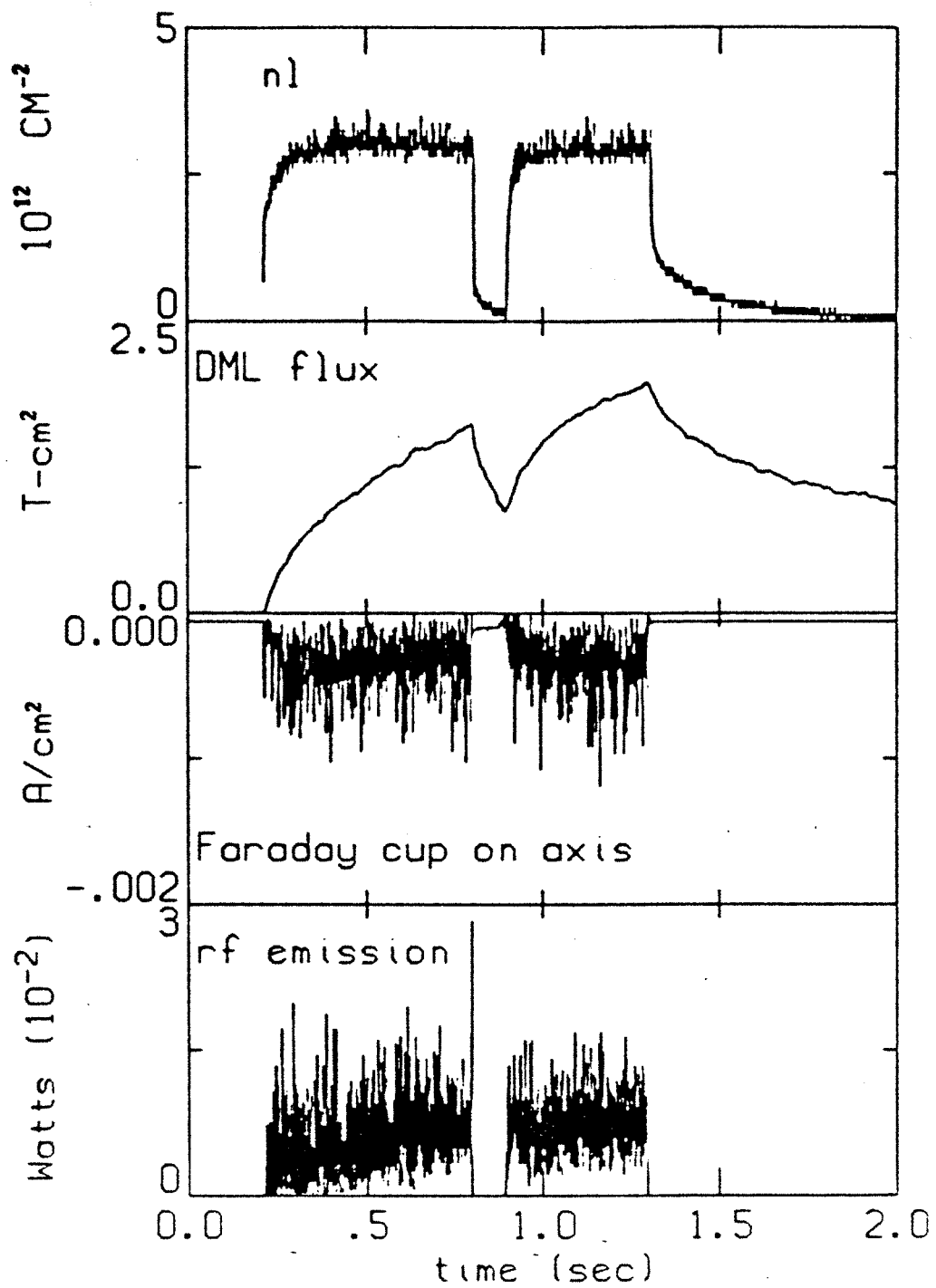
Figure 3.30: Data from a shot in which ICRF is applied to an ECRH plasma for 0.1 sec beginning at 0.8 sec.

endloss (which is discussed in the next section). The endloss analyzers indicate that 99% of the microinstability induced electron endloss consists of particles with energies less than 5 keV and with average energy in the range of 1.5–2.5 keV. The unstable wave energy comes primarily from these particles. The scintillator probe indicates that 25–50% of the hot electron endloss is caused by interactions with the unstable waves (the remainder is caused almost entirely by interactions with the applied ECRH waves (Hokin *et al.*, 1986)). Since the hot electrons do not drive microinstability this implies that hot electrons gain energy from the unstable waves as well. However, there is a net energy loss because the hot electrons which diffuse downward in energy have a chance to enter the loss cone and carry their total energy out of the plasma.

3.4   Induced Particle Endloss

3.4.1   General Description

Section 2.5.2 concluded that microinstability is responsible for particle endloss which exceeds the classically expected endloss due to collisions. Taking the hot electron density as an upper limit for the warm electron density implies that the warm particle loss rate is more than 10 times greater than the classically expected loss rate. Hot electron endloss measurements show directly that the hot electron loss rate is as much as 100 times greater than the classical loss rate. The loss rate due to microinstability is 25–50 times greater and the loss rate due to ECRH diffusion is 50 times greater than the classical loss rate. This section provides a more detailed description of the microinstability induced endloss and justifies the assertion that the warm electron endloss is primarily due to microinstability. First a general description of the endloss is provided in this subsection. It provides information on the electron endloss burst rate and the charge per burst as a function of pressure, ECRH power. and magnetic field. The next two subsections discuss the power loss as a result of microinstability induced warm and hot electron respectively.

Electrons which are scattered out of the plasma axially due to microinstability can have energies up to several hundred keV. Of these electrons, 99% have energies less than 5 keV, with average energies in the range of 1–2 keV, and can be classified as warm electrons. A small fraction in number, but not necessarily in energy, belong to the hot electron component. Figures 3.13 to 3.17 indicate how far out in radius bursts are detected. For example, Fig. 3.15 indicates that bursts are only detected out to 6 cm in radius when the magnetic field is 3 kG.

The axial electron endloss burst rate and charge per burst versus pressure are shown in Figs. 3.31 to 3.33 as a function of pressure for different ECRH powers and for a magnetic field of 3 kG. These figures indicate, as do the analogous ones for the rf bursts (Figs. 3.22 to 3.24), that the burst rate increases and the charge per burst increases with pressure for pressures below 1×10^{-6} torr, where the rf emission is maximum. The endloss burst rate and charge per burst are shown as a function of ECRH power and magnetic field in Figs. 3.34 and 3.35 respectively. Fig. 3.36 shows the average electron endloss current for all electrons greater than 500 eV versus magnetic field. These electrons are primarily the microinstability induced endloss electrons, as will be shown in the next subsection when energy spectra of the total electron endloss up to 5 keV are shown.   In Figs. 3.31 to 3.33 data is left out for intermediate pressures for which individual bursts are too difficult to identify.

Figure 3.34 implies directly that the burst rate is related to the heating rate, for ECRH powers less than 1 kW: the charge per burst tends to remain the same, on average, independent of the ECRH power and the burst rate increases linearly. For ECRH powers greater than 1 kW the heating rate is still probably the determining factor for burst rate and charge per burst, but the heating rate is no longer directly proportional to ECRH power, perhaps because of geometrical effects that do not occur at the lower ECRH powers. Fig. 3.33 supports the heating rate dependence of the burst rate as well. For lower magnetic fields the plasma is larger and the ECRH power density is smaller, making the heating rate smaller and the burst rate smaller. It can then be inferred how the heating rate qualitatively depends on pressure using
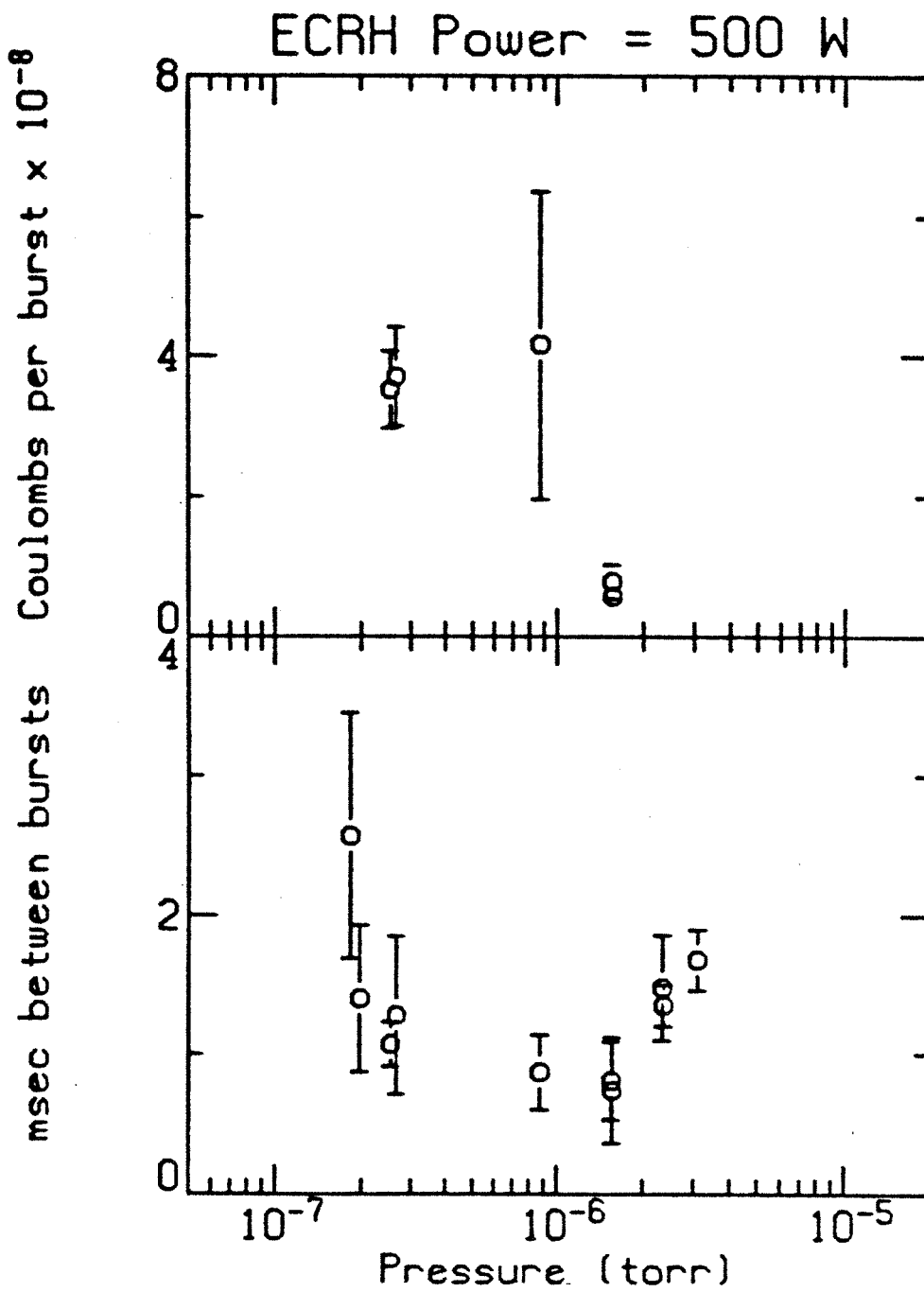
Figure 3.31: Axial endloss burst rate and charge per burst versus pressure for an ECRH power of .5 kW and a magnetic field of 3 kG.
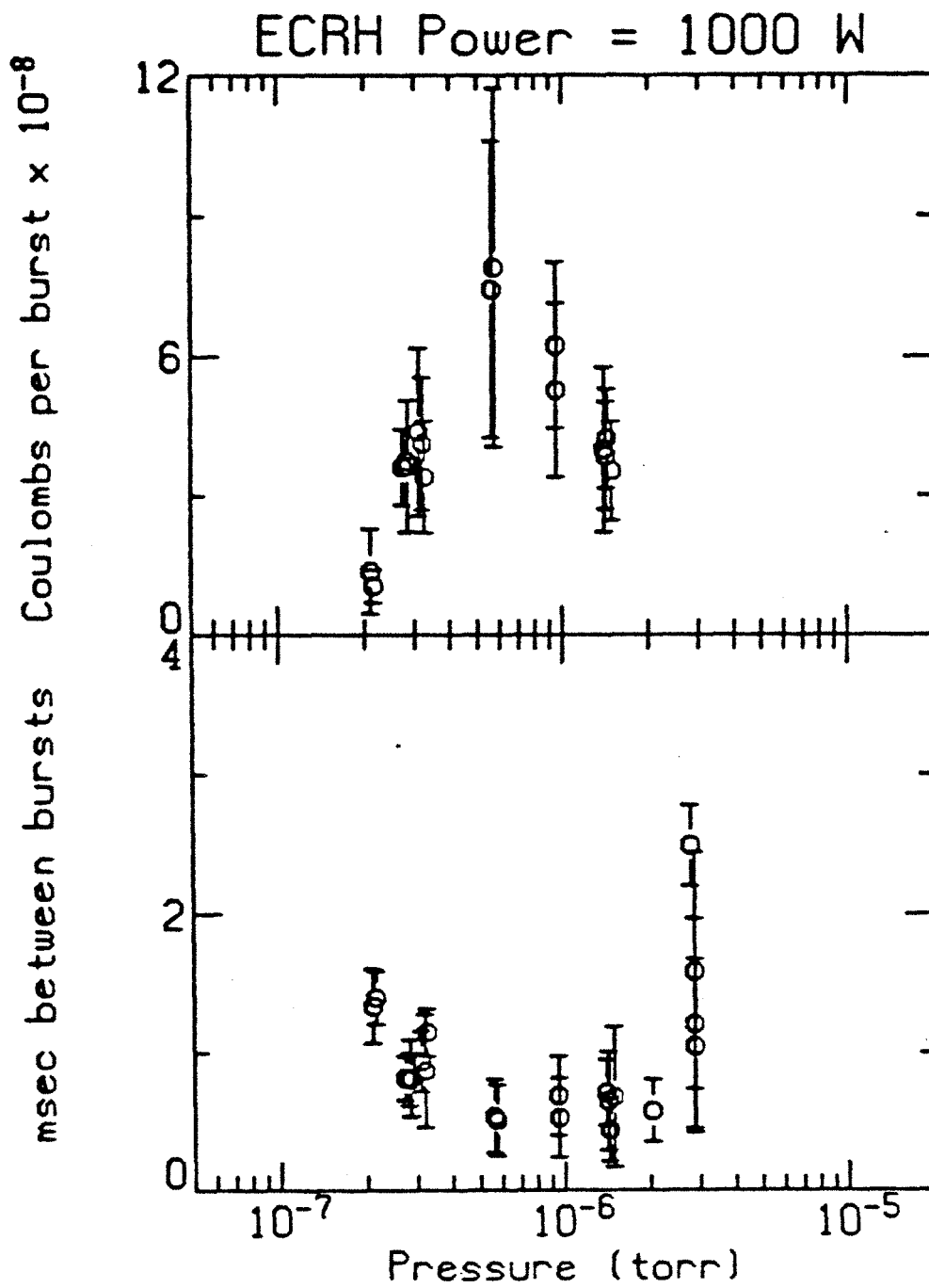
Figure 3.32: Axial endloss burst rate and charge per burst versus pressure for an ECRH power of 1 kW and a magnetic field of 3 kG.
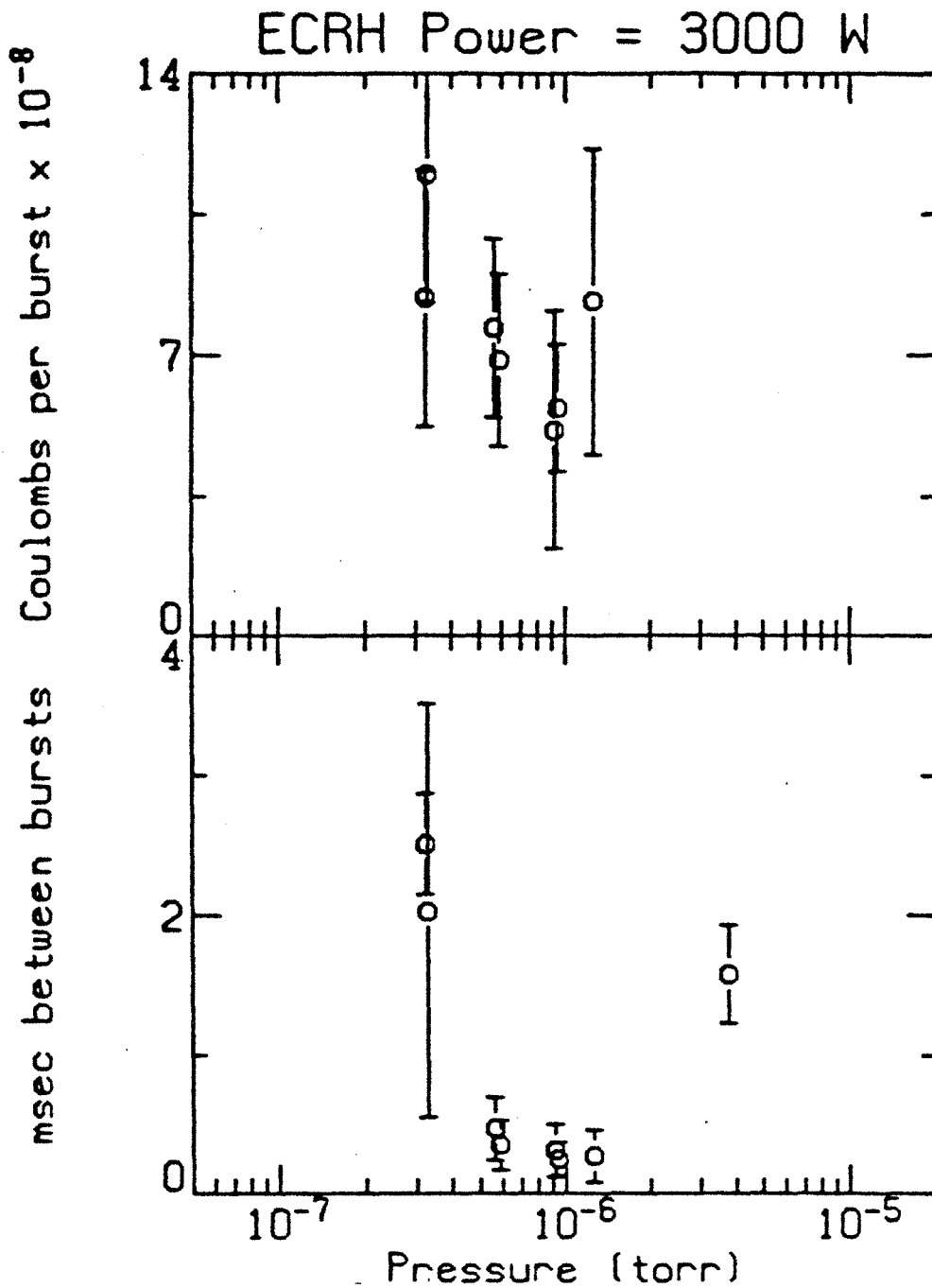
Figure 3.33: Axial endloss burst rate and charge per burst versus pressure for an ECRH power of 3 kW and a magnetic field of 3 kG.
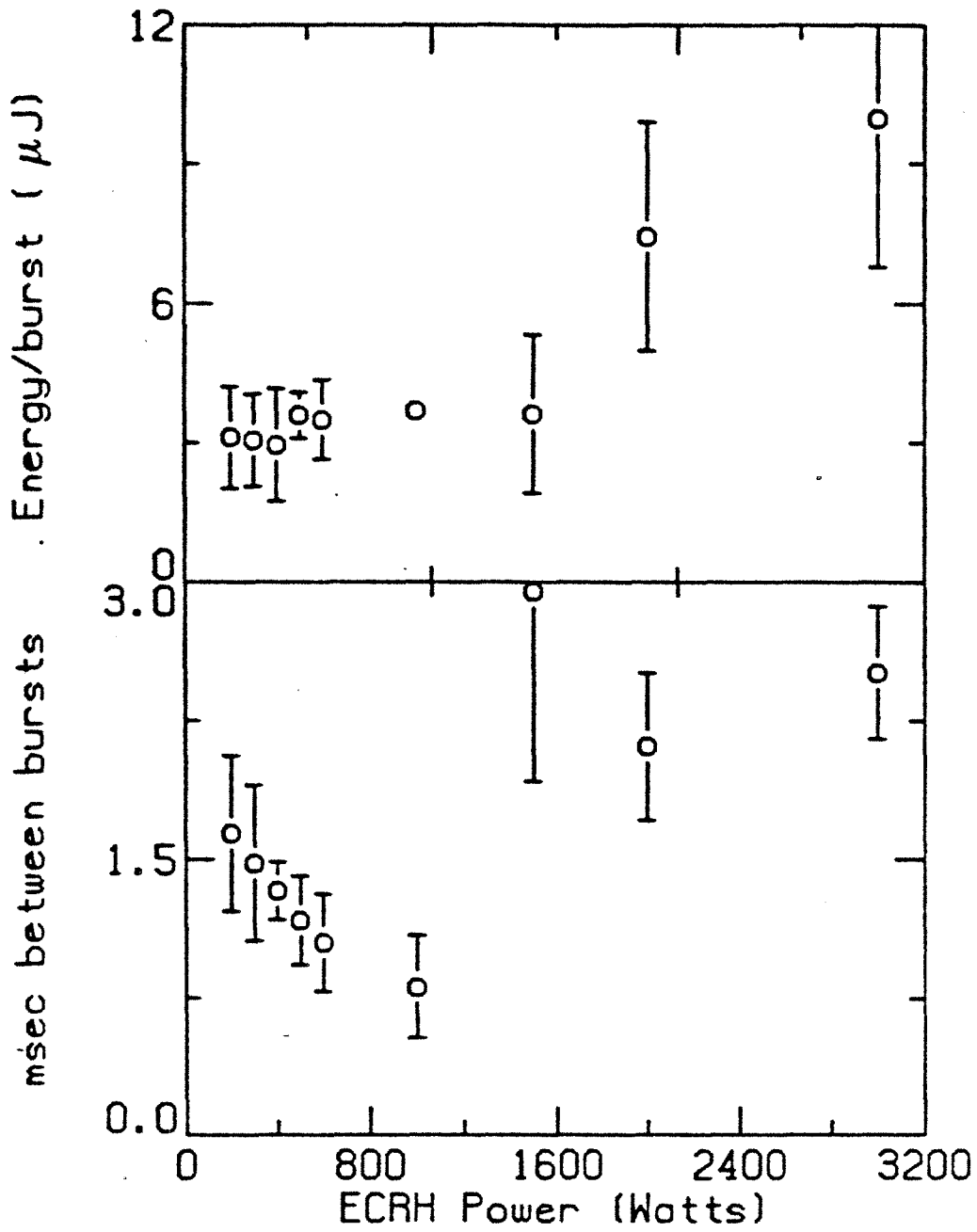
Figure 3.34: Axial endloss burst rate and charge per burst versus ECRH power for a magnetic field of 3 kG and a pressure of 2×10^{-7} torr.
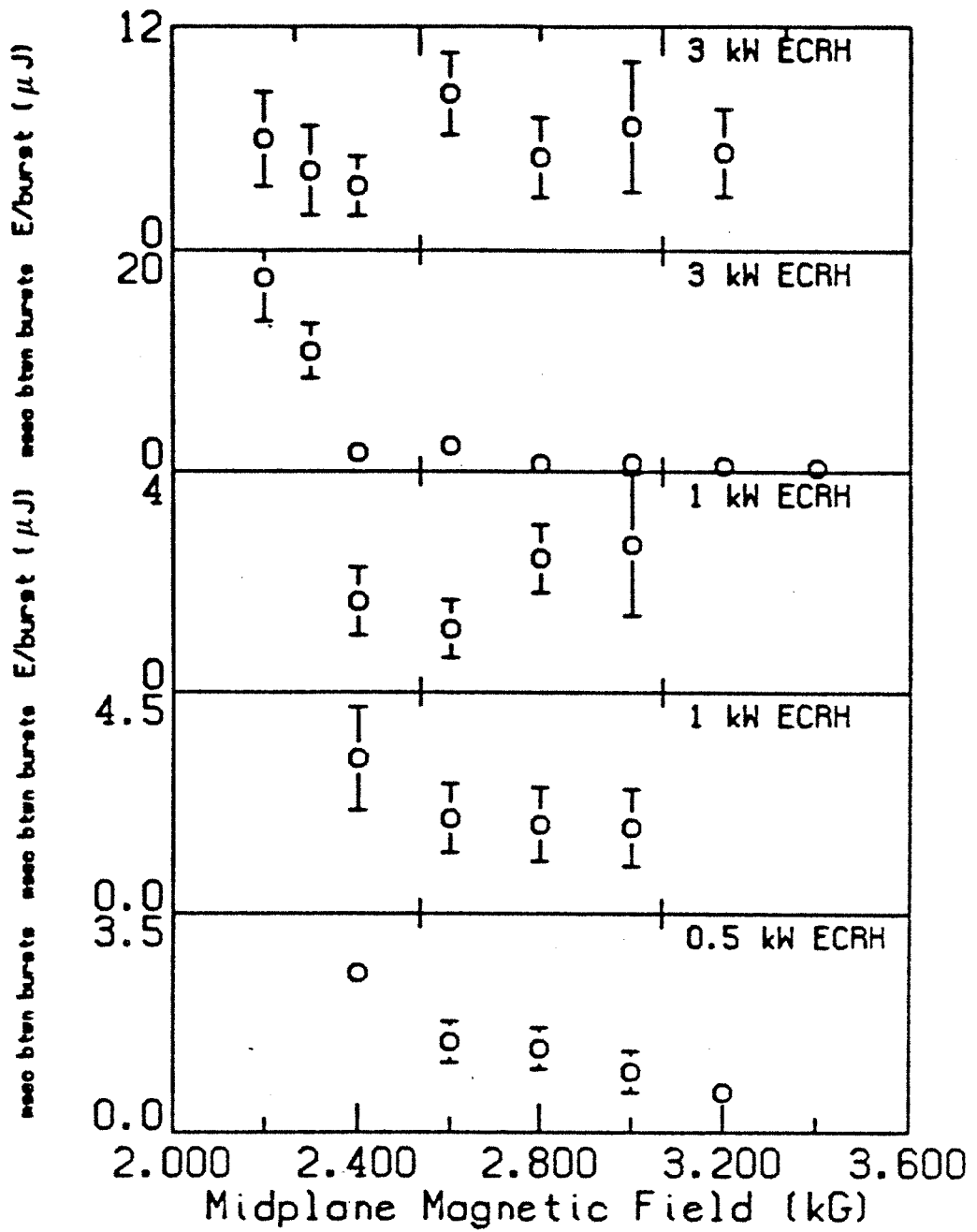
Figure 3.35: Axial endloss burst rate and charge per burst versus magnetic field for an ECRH power of 1 kW and a pressure of 2×10^{-7} torr.
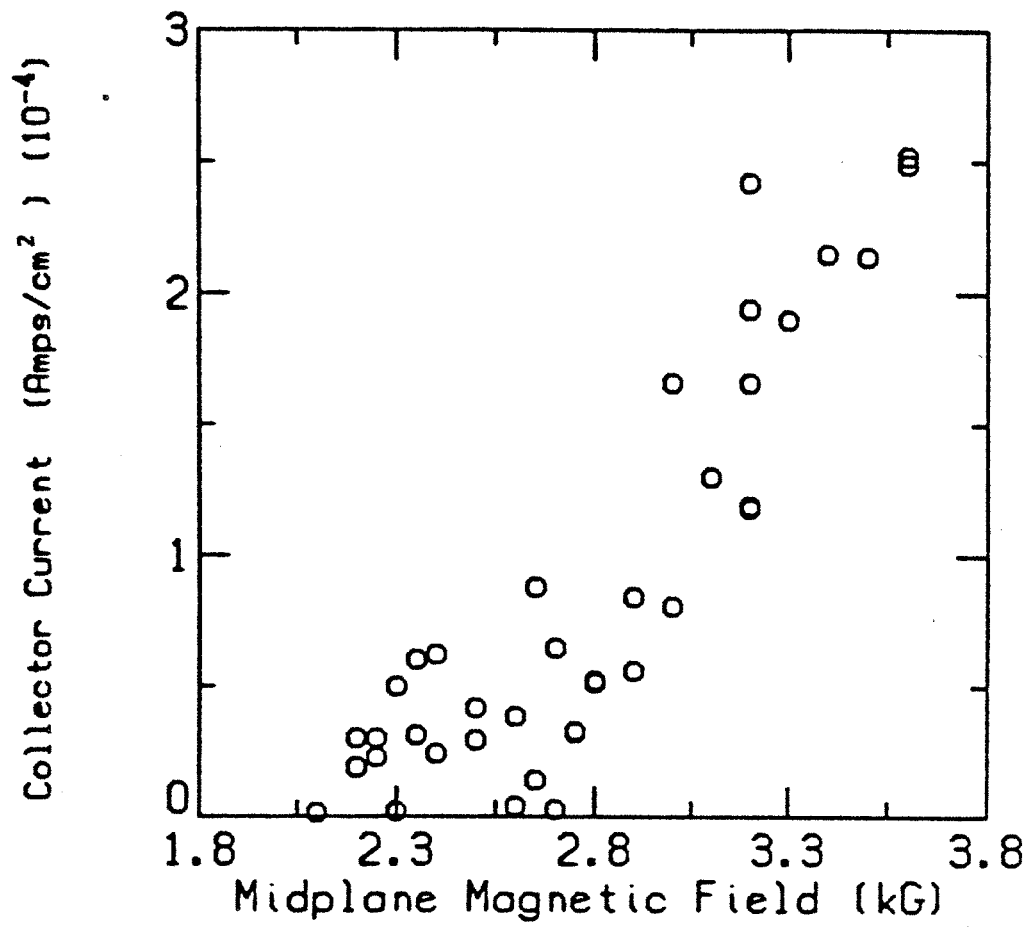
Figure 3.36: Axial endloss current for electrons greater than 500 eV versus magnetic field for an ECRH power of 1 kW and a pressure of 2×10^{-7} torr.

Figs. 3.31 to 3.33. Below 1×10^{-6} torr, the pressure at which both microinstability induced endloss and total unstable rf emission power are maximum, the burst rate and charge per burst increase with pressure, indicating a higher heating rate with a greater fueling density. Above 1×10^{-6} torr the increase in cold plasma density may reduce the instability growth rates so that the unstable waves are damped as they propogate out of the plasma.

The endloss analyzers detect bursts of ions which accompany bursts of electrons. Figure 3.37 shows an ion endloss burst at the south end of the machine on axis. the corresponding electron endloss burst at the north end of the machine on axis, and a corresponding potential fluctuation at the location of an emissive probe outside the plasma. Figure 3.38 shows a plot of the ion endloss charge per burst as a function of ion repeller grid voltage. Each point corresponds to the charge contained in a single burst. Figure 3.38 indicates that ions with energy as high as 400 eV exist in a burst. The amount of charge in an ion burst is, on the average, 3 times less than the amount of charge in an electron burst. The emissive probe for the shot depicted in Fig. 3.37 indicates a local potential fluctuation of approximately 100% during a burst.

For the shot depicted in Fig. 3.37 the south endloss analyzer, which was set up to detect ions of all energies. also detects electrons with energies greater than 5 keV. Since some electrons with this energy and greater exist during a burst. the time delay between the start of the electron burst and the start of the ion burst can be determined. Figure 3.37 indicates that the ion burst at the endwall begins 1 μsec after the electron burst. If the burst had originated at the midplane then an ion of 400 eV has a 7 μsec time of flight to the endwall (a distance of 200 cm); an ion of less energy has an even longer time of flight. This implies that the ion burst would have had to precede the electron burst *if it came from the midplane*. Therefore, it is concluded that the ion burst does not originate from the midplane and that the electrons of a burst drag some ions along with them as they move along the axis toward the endwall.
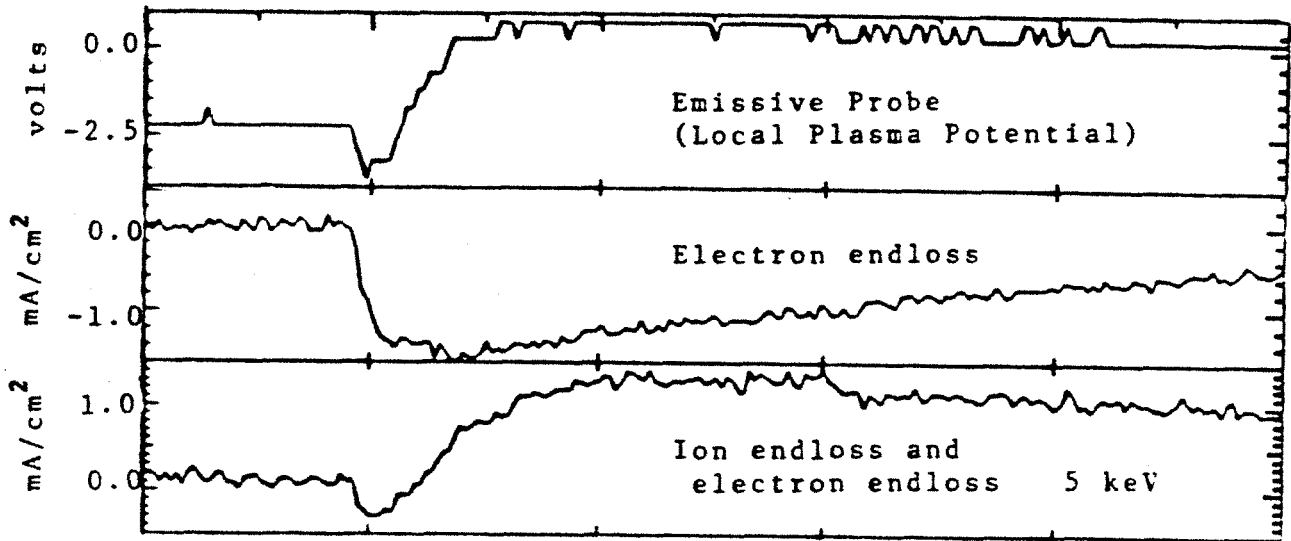
Figure 3.37: a) Ion burst. b) Electron burst. c) Potential fluctuation observed with an emissive probe outside the plasma.
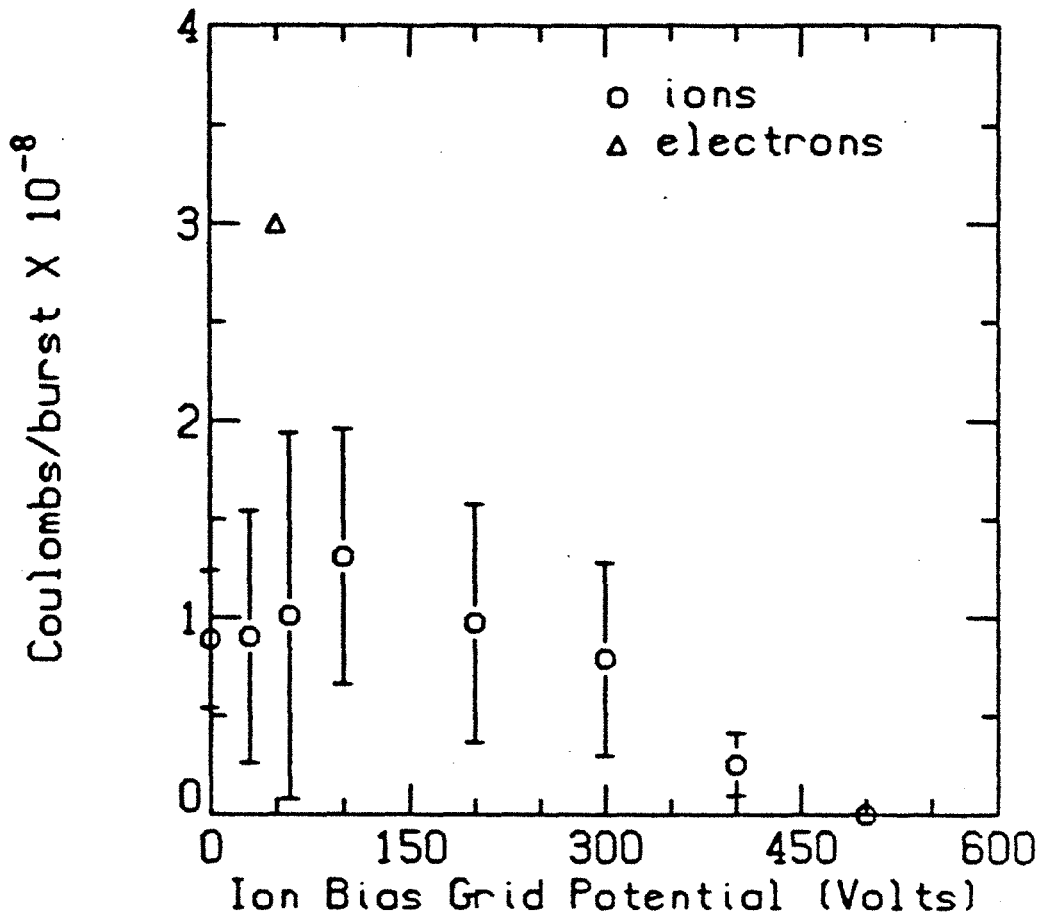
Figure 3.38: Ion endloss charge per burst on axis as a function of ion repeller grid voltage.

3.4.2 Warm Electron Endloss

The warm electron endloss is almost entirely due to microinstability. For the low pressure regime this is easy to determine since the bursts are so well-defined. Fig. 3.39(a) shows a plot of the charge per burst and Fig. 3.39(b) shows a plot of the current between bursts both as a function of endloss analyzer bias grid voltage for a series of low pressure shots in which the ECRH power was 1 kW and the magnetic field was 3 kG. During the bursts the effective endloss temperature is 1.5 keV and the total charge per burst, on axis, mapped to the midplane is 3×10^{-8} Coulombs/cm^2 for each end of the machine. Analysis of the endloss at both ends indicate that the on axis endloss is similar. Between the bursts the effective endloss temperature is 250 eV. There is no warm component detected between bursts in the low pressure regime. The warm component loss rate between bursts is determined by collisions and ECRH diffusion. Since a warm component is not detected then an upper limit can be placed on the warm endloss current between bursts. This upper limit is determined by the 2 mV resolution of the digitizers used to record the endloss analyzer signal. With the particular setup for these shots[6] the upper limit on the current density, on axis, mapped to the midplane is 6 μA/cm^2. The time averaged burst current is

$$\langle \text{charge per burst} \rangle \times \text{burst rate} = 2 \times 3 \times 10^{-8} \text{Coulombs/cm}^2 \times 1000 = .6 \, \mu\text{A/cm}^2$$

The difference between the density between and during a burst is not known, so it is assumed that they are the same. This will give a higher upper limit if the density during a burst is actually lower (because the electrons are depleted due to microinstability as well as collisions). An upper limit for the ratio between the loss rates due to collisions and ECRH and due to microinstability is then given by

$$\frac{\nu_{coll,ecrh}}{\nu_{inst}} = \frac{J_{coll,ecrh}}{J_{inst}} < \frac{.6}{6} = .1$$

---

[6]analyzer resistor: 51 kΩ, collector area: .18 cm^2, grid transmission: .21, field line mapping: 37:1, amplifier gain: 5
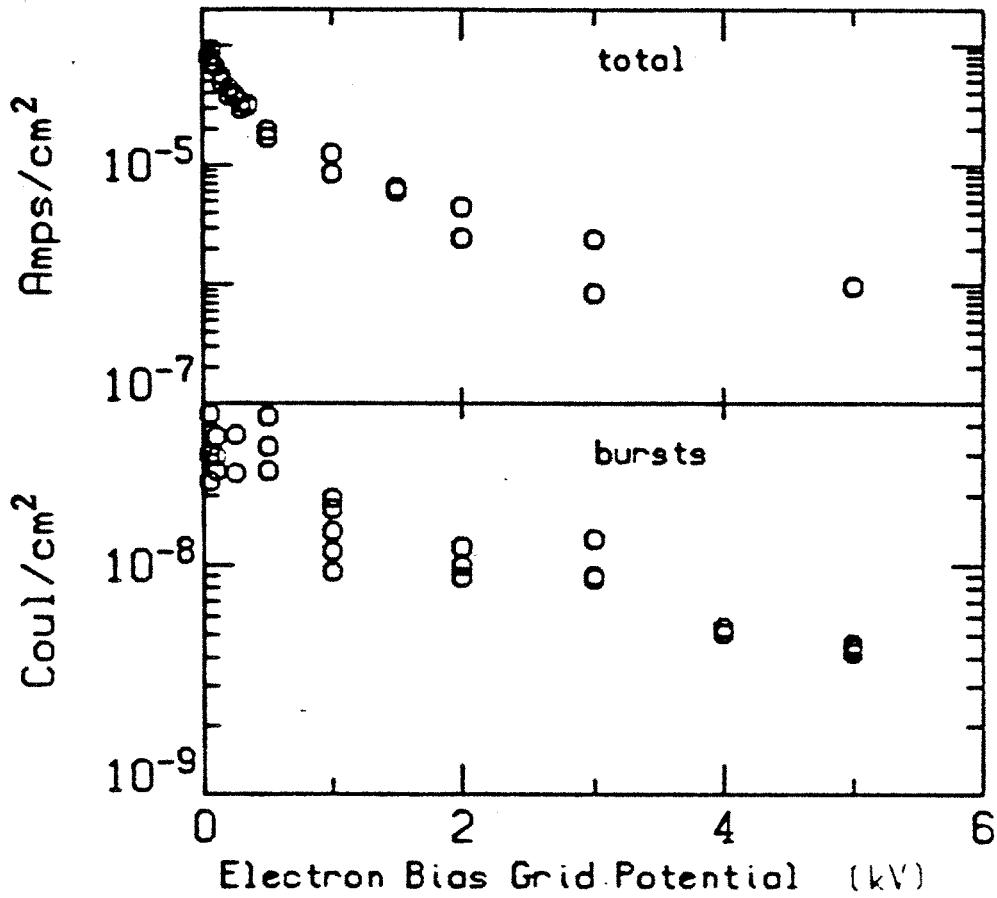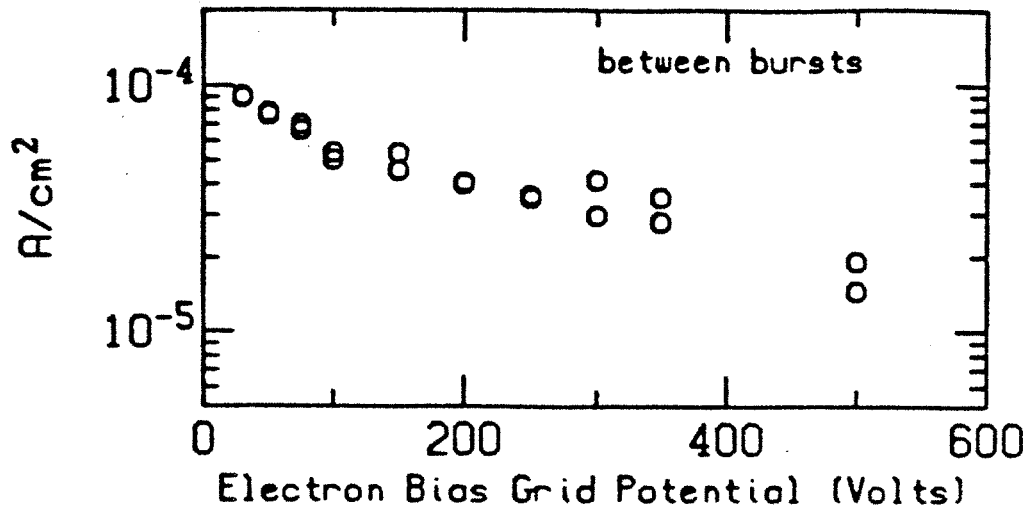
Figure 3.39: Top plot shows the average electron endloss current between bursts. Bottom plot shows the average charge per burst. Center plot shows the average current including both bursts and the current between bursts.

Figure 3.39(c) shows a plot of the data of Figs. 3.39(a) and 3.39(b) in another way. It displays the total electron endloss current. averaged over the 40 msec time span in which the bursts from Fig. 3.39(a) were analyzed. This figure shows the 1.5 keV component along with the 150 eV cold electron component. With a burst rate of 2 kHz the time averaged current of Fig. 3.39(a) then agrees with the average current of Fig. 3.39(b). Plots like those of Fig. 3.39(c) can be used for situations in which the bursts are not easily identified. The microinstability induced component of the endloss is then readily identified. For example, Fig. 3.40 is a plot of average endloss current as a function of endloss analyzer bias grid voltage for a shot in the medium pressure range. A 2 keV component corresponding to microinstability is evident, in addition to the 250 eV cold component. Such plots can be made for a variety of machine operating conditions and they always result in a warm temperature in the range of 1.5–2.5 keV at any time during ECRH approximately 20 msec after gas breakdown.

There is no apparent dependence of the average energy of the microinstability induced warm electron endloss to plasma parameters beginning approximately 20 msec after the gas breaks down. Endloss bursts begin to appear almost simultaneouly with the detection of endloss (to within a digitization period of 2.5 μsec). For the first 40 msec their average energy rises to the 1.5–2.5 keV temperature range that they will have for the rest of the heating phase of the shot. This is shown in Fig. 3.41, where the electron endloss energy spectrum is shown at various times after the interferometer first begins to detect a non-zero density. Figure 3.42 shows a plots of the warm electron endloss energy spectrum for different radial positions in the medium pressure regime for a magnetic field of 3 kG and an ECRH power of 1 kW. The figure indicates a similar endloss temperature on analyzers U1,C and D1. Analyzers U2 and D2 do not show microinstability induced endloss for this machine operating condition.

Plotting the warm electron endloss as a function of machine operating conditions further verifies its connection to the microinstability. when compared to similar plots
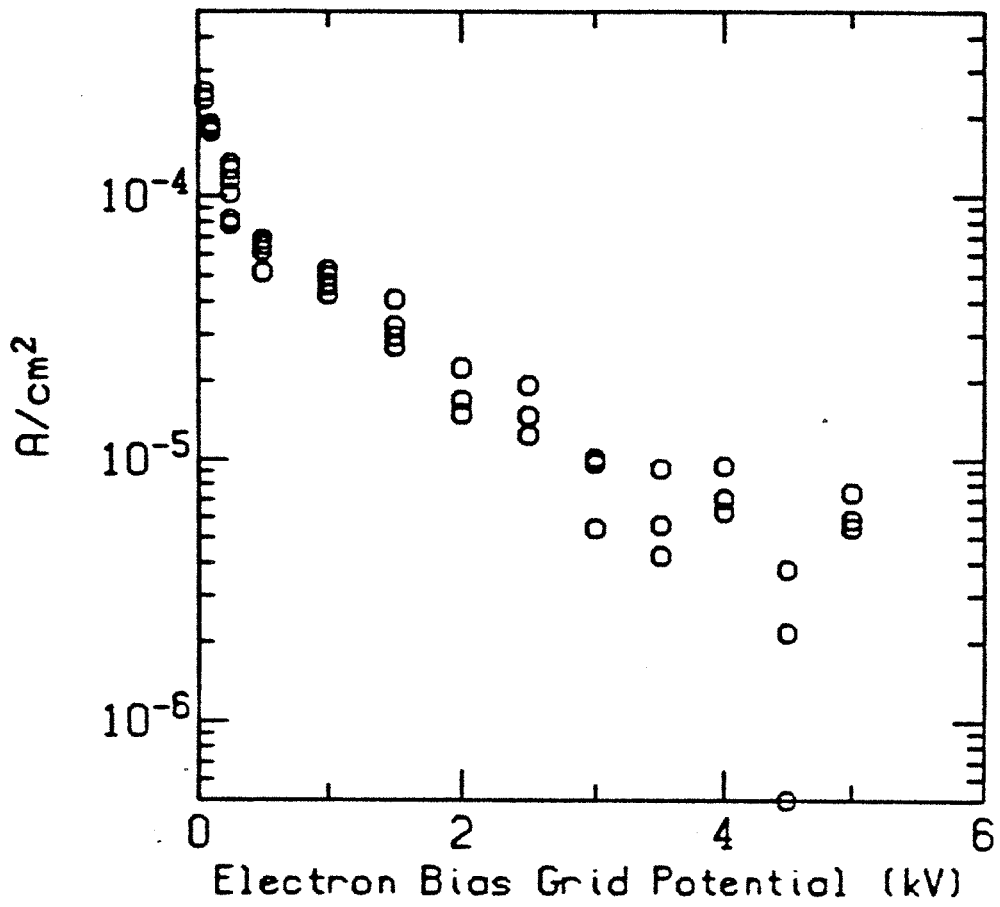
Figure 3.40: Average electron endloss current in the medium pressure regime.
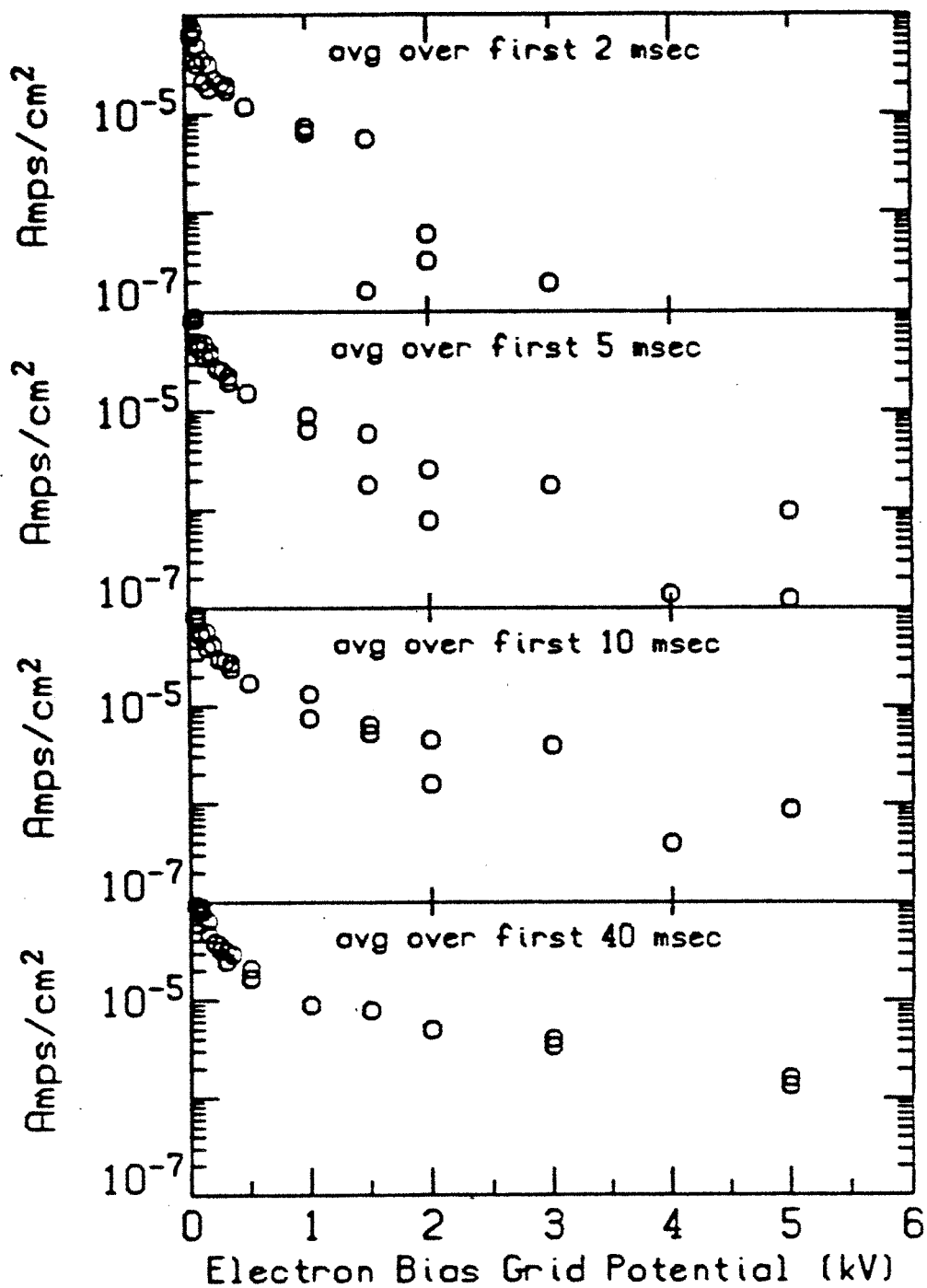
Figure 3.41: Electron endloss energy spectrum for the first (a) 2 msec, (b) 5 msec, (c) 10 msec, and (d) 40 msec after the interferometer indicates a non-zero density.
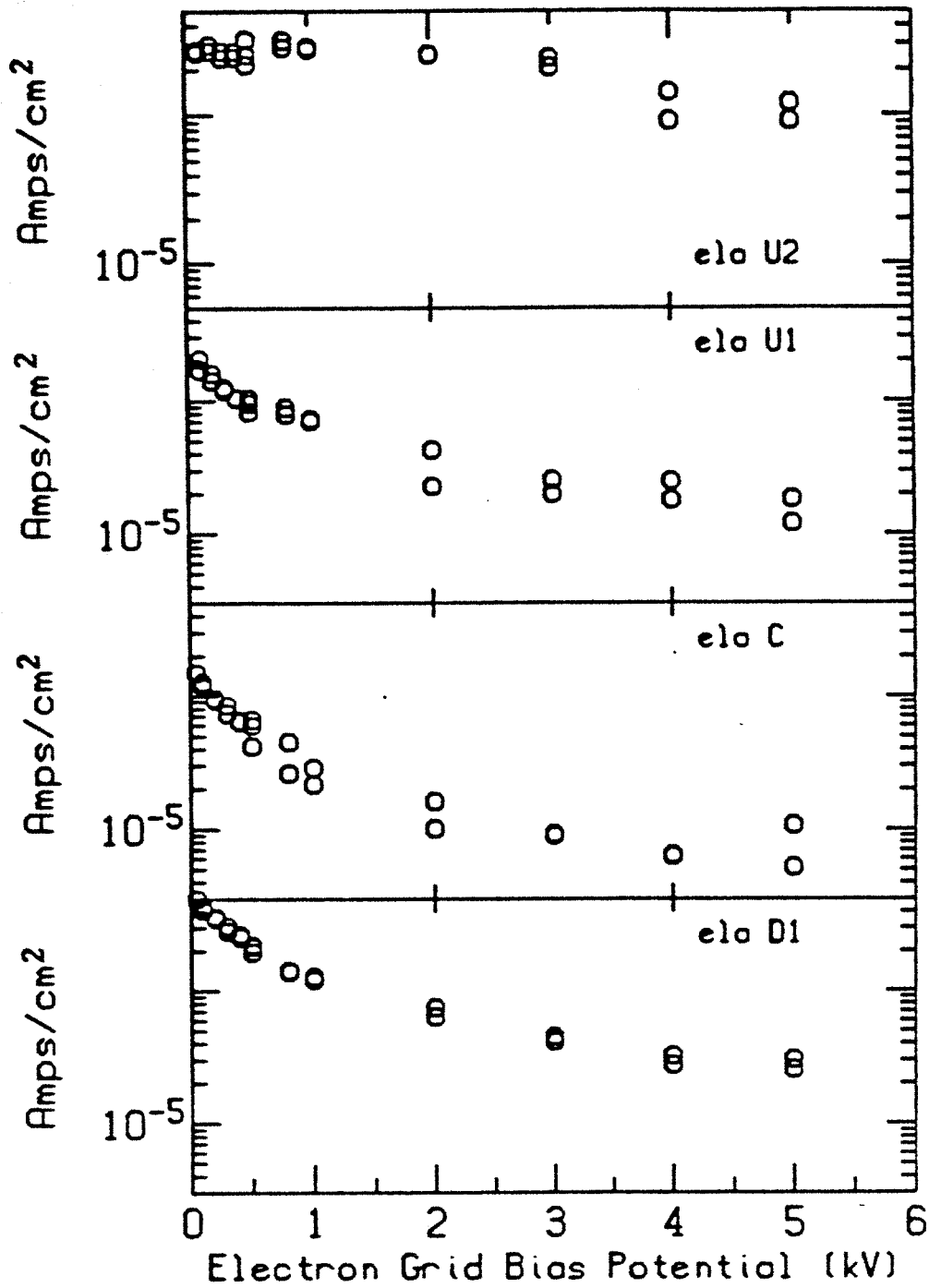
Figure 3.42: Electron endloss versus energy for different radial positions.

of the rf emission. Fig. 3.43 shows a plot of the endloss with with energies greater than 500 eV as a function of pressure. This can be compared to Fig. 3.22 which shows the same dependence of the rf emission on pressure.

The total energy loss due to microinstability induced warm electron endloss is the total number of such electrons multiplied by their average energy. Since the effective temperature is approximately the same, 2 keV on the average, then the relative currents for the various machine operating conditions give the relative energy losses as well. The worst case is when the pressure is 1×10^{-6} Torr. For 1 kW ECRH and 3 kG magnetic field the total energy loss across the loss cone boundary from the plasma is estimated to be

$$\left(4 \times 10^{-4} \text{ amps}\right) \times (2000 \text{ eV}) \times \underbrace{\pi(6 \text{ cm})^2}_{area} = 90 \text{ Watts}$$

where the cross sectional area of bursting has been taken to be circular with a radius of 6 cm, as determined by the endloss analyzers.

The energy loss due to microinstability induced endloss in the low pressure regime is considerably less. In this situation the individual bursts can be considered. Figure 3.39 indicates a charge per burst of 3×10^{-8} Coulombs/cm^2 for each end and a burst rate of approximately 1500 sec^{-1}. With an average burst energy of 2 keV the power loss is given by

$$6 \times 10^{-8} \text{ Coulombs/cm}^2 \times 2000 \text{ eV} \times 1500 \text{ sec}^{-1} = .18 \text{ Watts/cm}^2 \tag{3.1}$$

The bursts exist over the same cross sectional area but the charge per burst is lower by a factor of 10 at 6 cm. Assuming a parabolic cross section which is a factor of 10 less than its maximum at 6 cm gives an effective cross sectional area of 62 cm^2 and a total power loss for the low pressure regime of 11 W.
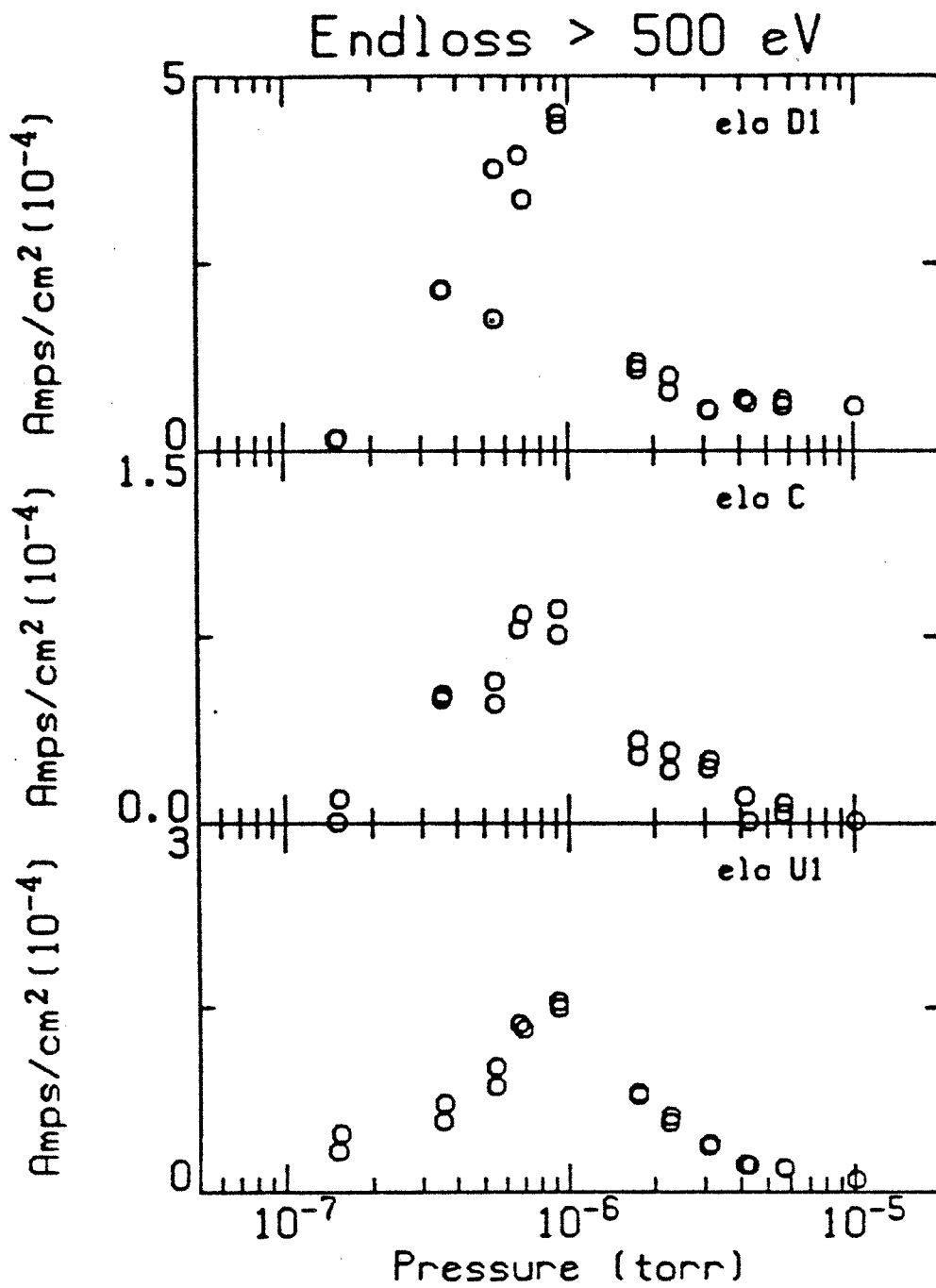
Endloss > 500 eV

Figure 3.43: Electron endloss with energy greater than 500 eV versus pressure.
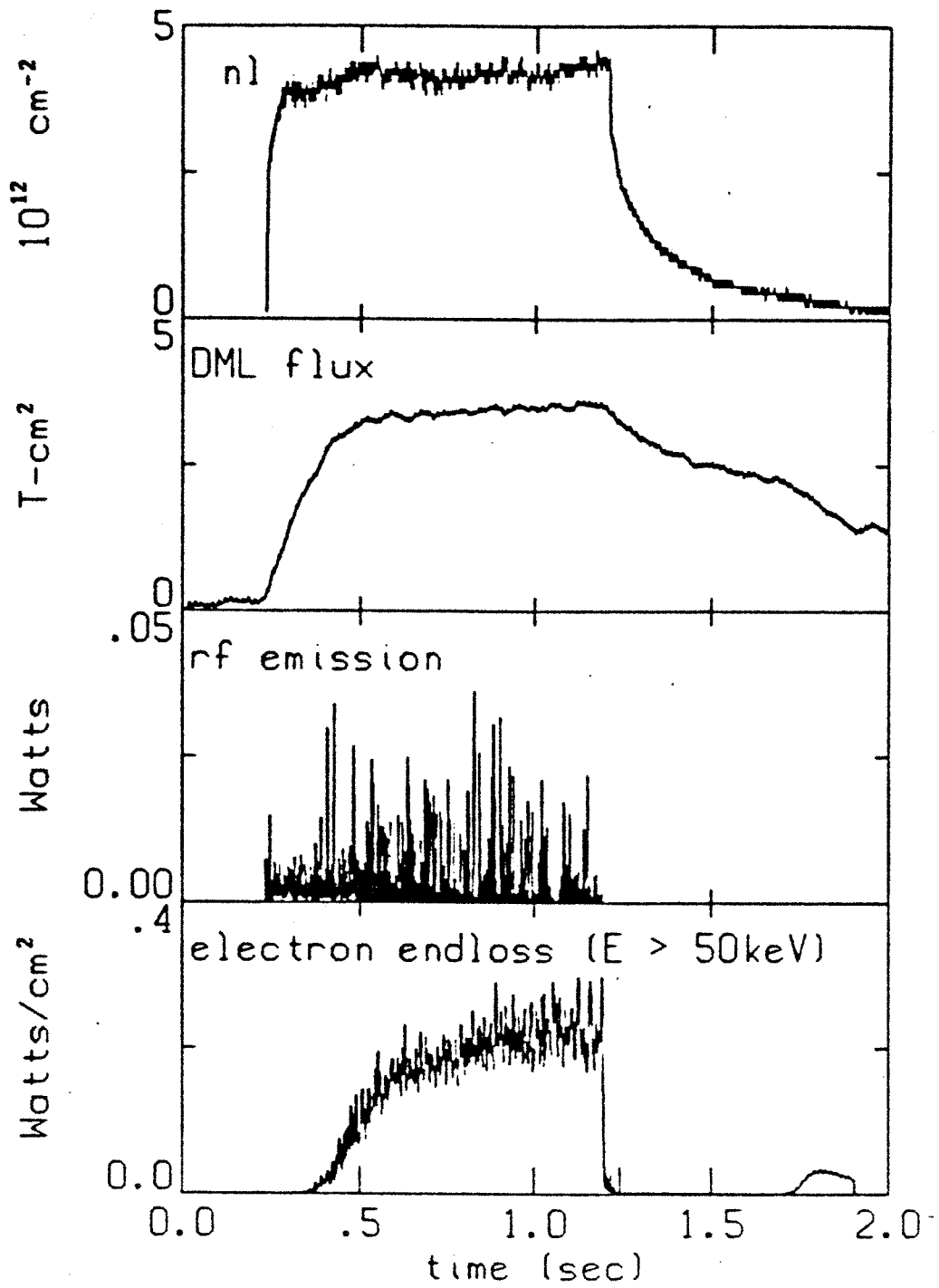
Figure 3.44: Two pulse ECRH shot. No gas on the second pulse.

3.4.3 Hot Electron Endloss

The microinstability induced hot electron endloss (E $\approx$ 100 keV) can be directly compared to the ECRH induced and the collisionally induced hot electron endloss by taking shots similar to the one depicted in Fig. 3.44. This shot is is composed of three parts. The first part is like any typical plasma shot, with constant gas and constant ECRH power. The hot electron endloss is caused by all three processes. For the second part the ECRH and gas are turned off. With no ECRH the microinstability stops and with no gas the cold and warm components decay in a few milliseconds, leaving only a hot component which collisionally decays over a longer time period. The hot electron endloss is then due solely to collisions. The third part has a second ECRH pulse with no gas so that a hot electron plasma exists alone. The hot electron component is stable and therefore the hot electron endloss is due to ECRH and collisions.

From these shots it is possible to find the relative importance of the three processes to the hot electron endloss. Collisional endloss is found to be 100 times smaller than rf induced endloss, including both ECRH and unstable waves. It is therefore neglected. Fig. 3.45 shows a plot of the power of the microinstability induced and ECRH induced hot electron endloss as a function of pressure. The scintillator probe was used to collect this data and the the theoretical calibration factor to obtain a power was discussed in Section 2.2. It is recalled that the calibration factor indicates a lower bound on the hot electron power to within a factor of 2. Figure 3.45 is accurate in providing the ratio of the powers of the microinstability induced and ECRH induced hot electron endloss. For this data the scintillator probe was located on axis 27 inches from the midplane, corresponding to a mirror ratio of 0.8 with respect to the midplane. The cross sectional area of the resonance zone at the midplane is approximately 315 cm^2 for a magnetic field of 3.2 kG. Assuming the entire volume within the resonance zone contributes to the hot electron endloss a total hot electron endloss power can be determined with this area and the
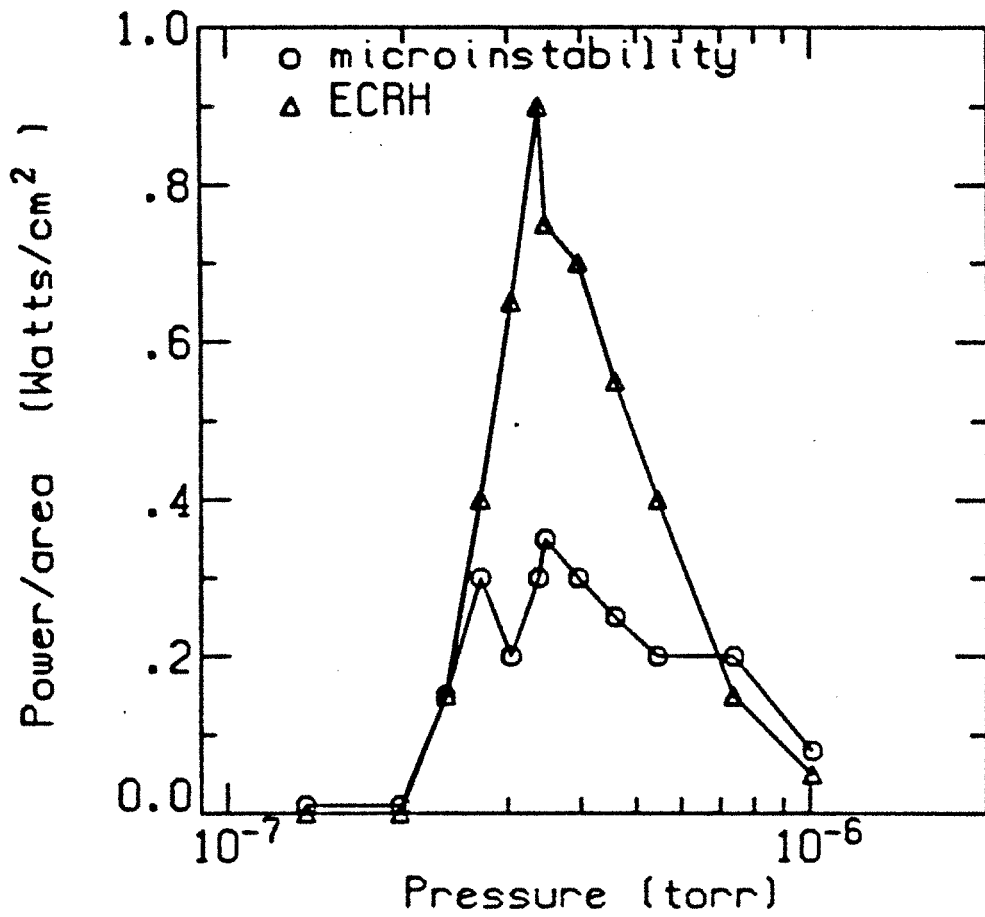
Figure 3.45: Microinstability induced endloss and ECRH induced endloss versus pressure for an ECRH power of 2 kW and a magnetic field of 3.2 kG.

ECRH input power:	1 kW
cold electron endloss:	24 W
warm electron endloss (microinstability):	80 W
hot electron endloss (microinstability):	90 W
hot electron endloss (ECRH)	280 W
unstable rf emission:	40 W

Table 3.1: Summary of power losses due to microinstability.

data of Fig. 3.45. At a pressure of 3×10^{-7} torr, where microinstability induced and ECRH induced endloss are maximum, the total microinstability induced hot electron endloss power is 180 Watts and the ECRH induced hot electron endloss power is 560 Watts (includes both ends of the plasma). The ECRH power for the data of Fig. 3.45 was 2 kW.

Figure 3.45 does not show the same pressure dependence of the microinstability induced hot electron endloss as the microinstability induced warm electron endloss and the unstable rf emission. The hot endloss peaks at approximately the same pressure that the diamagnetism peaks. This might be expected since the hot electrons do not drive the microinstability but are only scattered out when microunstable waves exist.

Table 3.1 is a summary of the microinstability induced power losses from the Constance B plasma. Hot electron endloss powers in the table are one half of the corresponding endloss powers mentioned above, which were for an ECRH power of 2 kW.

Chapter 4

Theoretical Analysis of Microinstability

This Chapter identifies the microinstability of Constance B as the whistler instability. It calculates the growth rates of unstable waves using an infinite, homogeneous, linearized, Vlasov-Maxwell model, considering only the effects from resonant particles. The results *a priori* justify the use of such a model, as will be shown. Section 4.1 introduces the formalism. It derives an expression for the growth rate ω_i by linearization of the relativistic Vlasov equation together with Maxwell's equations. For $\omega_i \ll \omega_r$ growth or damping is determined by the anti-Hermitian part of the dispersion tensor, while the natural modes of the plasma are determined by the Hermitian part of the dispersion tensor. The Hermitian part is approximated by the cold, fluid dispersion tensor. Section 4.2 gives a geometric interpretation for the final form of the expression for ω_i. Section 4.3 briefly describes the nonrelativistic theory so that comparisons could be made later. The equilibrium electron velocity space distribution function is a free parameter in this model. Section 4.5 models the Constance B experiment analytically using the experimental results as a guide. A new distribution function, the ECRH distribution, is introduced to model the warm electrons. It describes a population of electrons that have undergone diffusion due to ECRH waves. Section 4.6 presents the results of calculations which use this distribution. These results are compared to the experimental results, the whistler

instability is identified, and speculations on the microstability of the hot component are made.

4.1 Relativistic Vlasov-Maxwell Theory

4.1.1 Basic Formalism

The Vlasov equation describes the dynamics of each species of particles of a collisionless plasma in response to electric and magnetic fields. For plasmas where the particles may achieve even mildly relativistic velocities the relativistic Vlasov equation is needed:

$$\frac{\partial f_\alpha}{\partial t} + \mathbf{u} \cdot \frac{\partial f_\alpha}{\partial \mathbf{r}} + \frac{q_\alpha}{m_\alpha} \left(\mathbf{E} + \frac{\mathbf{v} \times \mathbf{B}}{c} \right) \cdot \frac{\partial f_\alpha}{\partial \mathbf{u}} = 0 \qquad (4.1)$$

where $\mathbf{u} = \mathbf{p}/m_\alpha = \mathbf{v}\gamma$ is the relativistic velocity, $\gamma = (1 + |\mathbf{u}|^2/c^2)^{1/2}$, and $f_\alpha(\mathbf{r}, \mathbf{u}, t)$ is the distribution function for species α, normalized to 1. Each of the electron components discussed in Section 2.5.1 is considered a separate species and each will be described by a distribution function obeying Eq. 4.1. Since the waves of interest have frequencies near the electron cyclotron frequency the ion dynamics are neglected. The ions are assumed to form a stationary background of positive charge which neutralizes the charge of the electrons.

Maxwell's equations describe the dynamics of the electric and magnetic fields in the presence of plasma charges and currents:

$$\nabla \cdot \mathbf{E} = 4\pi\rho \qquad (4.2)$$

$$\nabla \times \mathbf{B} - \frac{1}{c} \frac{\partial \mathbf{E}}{\partial t} = \frac{4\pi}{c} \mathbf{J} \qquad (4.3)$$

$$\nabla \times \mathbf{E} + \frac{1}{c} \frac{\partial \mathbf{B}}{\partial t} = 0 \qquad (4.4)$$

$$\nabla \cdot \mathbf{B} = 0 \qquad (4.5)$$

where

$$\mathbf{J} \;=\; -\sum_\alpha n_\alpha \epsilon \int \mathbf{u} f_\alpha d^3\mathbf{u} \tag{4.6}$$

$$\rho \;=\; -\sum_\alpha n_\alpha \epsilon \int f_\alpha d^3\mathbf{u} \tag{4.7}$$

The system of Eqs. 4.1 to 4.7 forms a complete set of nonlinear differential equations with the unknowns $\mathbf{E}(\mathbf{r},t)$, $\mathbf{B}(\mathbf{r},t)$, and f_α. The solution, however, is rather intractable and many simplifications will be made before performing calculations.

4.1.2 Linear, Homogeneous, and Infinite

The unstable rf emission from the plasma has a particular frequency signature (see Section 3.2.1) which can be compared to the frequencies of the unstable waves predicted by this analysis.[1] These unstable frequencies are determined by analyzing the behavior of small perturbations about some equilibrium configuration of the system (i.e by linearizing the equations). Each unknown is written as the the sum of a time independent equilibrium quantity and a time dependent. perturbed quantity:

$$\mathbf{B}(\mathbf{r},t) \;=\; \mathbf{B}_0(\mathbf{r}) + \mathbf{B}_1(\mathbf{r},t) \tag{4.8}$$

$$\mathbf{E}(\mathbf{r},t) \;=\; \mathbf{E}_1(\mathbf{r}.t) \tag{4.9}$$

$$f_\alpha(\mathbf{r},\mathbf{u},t) \;=\; f_{\alpha 0}(\mathbf{u}) + f_{\alpha 1}(\mathbf{r},\mathbf{u},t) \tag{4.10}$$

where the perturbed quantities of subscript 1 are much smaller than their corresponding equilibrium quantities of subscript 0. The absence of an equilibrium electric field is assumed because the 100 volt plasma potential of Constance B does not effect the behavior of the magnetically trapped particles which drive the microinstability. The solution of the linearized equations ceases to be valid when the

---

[1]The frequencies of the unstable (stable) waves will be referred to as the unstable (stable) frequencies.

perturbed quantities come to be on the order of the equilibrium quantities. There-fore, if the theory predicts the existence of instability there is a limited time during which it accurately describes the growth of an unstable wave.

Substituting Eqs. 4.8 to 4.10 into Eqs. 4.1 to 4.7 and separating the zero order terms and the first order terms produces an equilibrium set and a perturbed set of equations. The equilibrium set is

$$\nabla \cdot \mathbf{B}_0 = 0 \tag{4.11}$$

$$\nabla \times \mathbf{B}_0 = \mu_o \mathbf{J}_0 \tag{4.12}$$

$$\mathbf{u} \cdot \frac{\partial f_{\alpha 0}}{\partial \mathbf{r}} - \frac{\epsilon}{mc} (\mathbf{v} \times \mathbf{B}_0) \cdot \frac{\partial f_{\alpha 0}}{\partial \mathbf{u}} = 0 \tag{4.13}$$

where

$$\mathbf{J}_0 = -\sum_{\alpha} n_{\alpha} \epsilon \int \mathbf{u} f_{\alpha 0} d^3 \mathbf{u} \tag{4.14}$$

The plasma has many possible equilibrium configurations allowed by these equa-tions. These equations are not solved, but are used as a guide in choosing an allowable and physically meaningful equilibrium configuration of the plasma.

The solution of Eqs. 4.11 to 4.14 is also rather intractable, especially considering the complicated Constance B magnetic geometry, and some simplifying assumptions are made. Eqs. 4.11 and 4.12 describe the imposed magnetic field from the Con-stance B baseball magnet, altered by the equilibrium currents of the plasma. These equations are disregarded and the equilibrium magnetic field is considered homo-geneous. With the addtional assumption that $f_{\alpha 0}$ is homogeneous the first term of Eq. 4.13 can be eliminated. These assumptions limit the validity of the theory to situations in which wavelengths are short compared to scale lengths of change of plasma parameters. This assumption is justified when results of calculations are presented in Section 4.6.3.

Because of the homogenous magnetic field a cylindrical velocity space coordinate system is chosen with $u_z \equiv u_\parallel$ in the direction of $\mathbf{B}$. Eq. 4.13 can be rewritten as

$$\omega_{ce} \frac{\partial f_{\alpha 0}}{\partial \phi} = 0 \tag{4.15}$$

where $\omega_{ce} = \epsilon B / mc$ is the nonrelativistic cyclotron frequency. The gyrophase φ is defined by the relations $u_x = u_\perp \cos \phi$ and $u_y = u_\perp \sin \varphi$, where $u_\perp$ is the component of the velocity perpendicular to $\mathbf{B_0}$. Equation 4.15 admits any equilibrium distribution function that is independent of gyrophase. More generally, for inhomogeneous systems, the equilibrium Vlasov equation allows for equilibrium velocity space distributions which are arbitrary functions of the particle constants of motion. For particles in a magnetic mirror total energy is constant, and the magnetic moment μ and the longitudinal adiabatic invariant J are adiabatic invariants. Section 4.5 will model the warm electron component of Constance B with the ECRH distribution, a function of μ and E.

The perturbed set of equations is

$$\nabla \cdot \mathbf{E}_1 = 4\pi \rho_1 \tag{4.16}$$

$$\nabla \times \mathbf{B}_1 - \frac{1}{c} \frac{\partial \mathbf{E}_1}{\partial t} = \frac{4\pi}{c} \mathbf{J}_1 \tag{4.17}$$

$$\nabla \times \mathbf{E}_1 + \frac{1}{c} \frac{\partial \mathbf{B}_1}{\partial t} = 0 \tag{4.18}$$

$$\nabla \cdot \mathbf{B}_1 = 0 \tag{4.19}$$

$$\frac{\partial f_{\alpha 1}}{\partial t} - \mathbf{u} \cdot \frac{\partial f_{\alpha 1}}{\partial \mathbf{r}} - \frac{\epsilon}{mc} (\mathbf{v} \times \mathbf{B}_0) \cdot \frac{\partial f_{\alpha 1}}{\partial \mathbf{u}} = \frac{\epsilon}{m} \left(\frac{\mathbf{v} \times \mathbf{B}_1}{c} - \mathbf{E}_1 \right) \cdot \frac{\partial f_{\alpha 0}}{\partial \mathbf{u}} \tag{4.20}$$

where

$$\mathbf{J}_1 = -\sum_\alpha n_\alpha \epsilon \int \mathbf{u} f_{\alpha 1} d^3 u \tag{4.21}$$

$$\rho_1 = -\sum_\alpha n_\alpha \epsilon \int f_{\alpha 1} d^3 u \tag{4.22}$$

134

A dispersion relation can be derived from the perturbed equations. The details of this have been reported elsewhere (Baldwin *et al.*, 1969) and will not be reproduced here. The general technique is to write $f_{\alpha 1}$ in terms of $\mathbf{E}_1$ using the perturbed Vlasov equation (4.20), eliminating $\mathbf{B}_1$ with Eq. 4.18. The result is inserted into Eqs. 4.21 and 4.22 which then give the plasma charges and currents in terms of $\mathbf{E}_1$. These are inserted into Maxwell's equations (4.16 to 4.19) which then only contain the unknown $\mathbf{E}_1$.

Several assumptions are made in performing these steps:

1) Each perturbed quantity is assumed to be of the form

$$A(\mathbf{k}, \omega) e^{i(\mathbf{k} \cdot \mathbf{r} - \omega t)}$$

Therefore, the perturbation grows if $\omega_i = \mathrm{Im}(\omega) > 0$.

2) The plasma is assumed infinite so that boundary conditions do not impose a discrete spectrum of values on the free parameters $\mathbf{k}$ and ω. If the short wavelength condition that is needed for the homogeneity condition is satified, then this condition will also be satisfied (since scale lengths of change of the plasma are less than the plasma size).

3) $\mathbf{k}$ is a real quantity. This assumption will be useful later.

4) ω is allowed to be complex. Furthermore, $\omega_i > 0$ is a necessary condition for the convergence of a particular time integral performed over the unperturbed particle orbits, starting at $t = -\infty$. Positive values of ω_i are necessary for a causal theory and negative values would be necessary for an anti-causal theory. If negative values of ω_i are to be considered later then analytical continuation must be done with this condition in mind. This will happen later in the present section.

5) The theory describes a steady state plasma. The same integral that causes ω to be complex with $\omega_i > 0$ also removes all memory of initial conditions, since the integral over unperturbed particle orbits is done from $t = -\infty$ and since it is assume that $f_{\alpha 1}(\mathbf{r}, \mathbf{u}, 0) = 0$.

6) A consequence of imposing $\mathbf{k}$ real is that if this analysis predicts instability (natural modes with $\omega_i > 0$). it will not be able to determine whether such instabilities are of the convective or of the absolute type. This is only determined by locating pinch points in the complex $\mathbf{k}$ and complex ω planes. The occurence of $\omega_i > 0$, however, is sufficient for determining whether instability exists.

The result of the above analysis is

$$\mathbf{D}(\mathbf{k},\omega) \cdot \mathbf{E}(\mathbf{k},\omega) = 0. \tag{4.23}$$

where $\mathbf{D}$ is the dispersion tensor and $\mathbf{E}$ now refers to the amplitude of the perturbed electric field. For nontrivial solutions of $\mathbf{E}$ this equation implies $|\mathbf{D}| = 0$. the dispersion relation. The dispersion tensor is given by (Wong *et al.*, 1982)

$$\mathbf{D}(\mathbf{k},\omega) = \left(1 - \frac{c^2 k^2}{\omega^2}\right)\mathbf{I} + \frac{c^2}{\omega^2}\mathbf{kk} + \sum_\alpha \mathbf{Q}_\alpha(\mathbf{k},\omega) \tag{4.24}$$

The first two terms on the right hand side of Eq. 4.24 represent the vacuum effects while the last term represents the plasma effects. $\mathbf{Q} = \sum_\alpha \mathbf{Q}_\alpha$. which can be written in terms of the more familiar conductivity or dielectric tensors as $\mathbf{Q} = \frac{4\pi i}{\omega}\sigma = \epsilon - \mathbf{I}$. is given by

$$\begin{aligned}
\mathbf{Q}(\mathbf{k},\omega) =\ & 2\pi\frac{\omega_p^2}{\omega^2}\int_{-\infty}^{\infty} du_\parallel \int_0^\infty du_\perp \frac{u_\perp}{\gamma}\left(u_\perp\frac{\partial}{\partial u_\parallel} - u_\parallel\frac{\partial}{\partial u_\perp}\right) f_0 \hat{\mathbf{e}}_\parallel \hat{\mathbf{e}}_\parallel \\
& + 2\pi\frac{\omega_p^2}{\omega^2}\int_{-\infty}^{\infty} du_\parallel \int_0^\infty du_\perp \left[\left(\omega - \frac{k_\parallel u_\parallel}{\gamma}\right)\frac{\partial}{\partial u_\perp} + \frac{k_\parallel u_\perp}{\gamma}\frac{\partial}{\partial u_\parallel}\right] f_0 \\
& \times \sum_{n=-\infty}^{\infty} \frac{\mathbf{T}_n}{\gamma\omega - n\omega_{ce} - k_\parallel u_\parallel}
\end{aligned} \tag{4.25}$$

where

$$\omega_p^2 f_0 = \sum_\alpha \omega_{p\alpha}^2 f_{\alpha 0} \tag{4.26}$$

Because of the linearity of $\mathbf{Q}_\alpha$ in the term $\omega_{p\alpha}^2 f_{\alpha 0}$. the the distributions of each component of electrons, weighted by their plasma respective frequencies. can be

136

added, as in Eq. 4.26, to become one distribution function. The tensor $\mathbf{T}_n$, in the (E_x, E_y, E_z) basis, is given by

$$\mathbf{T}_n = \begin{pmatrix} \frac{n^2\omega_{ce}^2}{k_\perp^2}J_n^2 & -i\frac{n\omega_{ce}}{k_\perp}u_\perp J_n J_n' & \frac{n\omega_{ce}}{k_\perp}u_\parallel J_n^2 \\ i\frac{n\omega_{ce}}{k_\perp}u_\perp J_n J_n' & u_\perp^2 J_n'^2 & iu_\parallel u_\perp J_n J_n' \\ \frac{n\omega_{ce}}{k_\perp}u_\parallel J_n^2 & -iu_\parallel u_\perp J_n J_n' & u_\parallel^2 J_n^2 \end{pmatrix} \qquad (4.27)$$

where $J_n = J_n(k_\perp u_\perp/\omega_{ce})$ is the ordinary Bessel function of order n, and the prime indicates differentiation with respect to the argument.

With a choice of distribution function Eq. 4.23 determines the modes of the plasma and indicates whether they are growing (unstable, $\omega_i > 0$) or decaying (stable, $\omega_i < 0$). With $\mathbf{D}$ given by Eqs. 4.24 to 4.27 solving the dispersion relation is still a difficult task. It has been done for certain choices of distribution function, and for certain special cases and additional approximations. In this thesis the intention is to determine the unstable modes using a distribution function which models the ECRH of Constance B. Additional simplifications will be made before this is done.

4.1.3 Small Growth Rate Expansion

Equation 4.23 is simplified by assuming $\omega_i \ll \omega_r$, where $\omega = \omega_r - i\omega_i$. Separating the dispersion tensor into an Hermitian part ($\mathbf{D}^h$) and an anti-Hermitian part ($\mathbf{D}^a$), and Taylor-expanding about ω_r gives

$$\begin{aligned} \mathbf{D}(\mathbf{k},\omega) &= \mathbf{D}^h(\mathbf{k},\omega) + i\mathbf{D}^a(\mathbf{k},\omega) \\ &\approx \mathbf{D}^h(\mathbf{k},\omega_r) + i\omega_i\frac{\partial \mathbf{D}^h}{\partial \omega_r} + i\mathbf{D}^a(\mathbf{k},\omega_r) \end{aligned} \qquad (4.28)$$

Multiplying Eq. 4.23 on the left by $\mathbf{E}^*$, (the complex conjugate of $\mathbf{E}$), replacing $\mathbf{D}$ there with the expression from Eq. 4.28, and separating the real terms and imaginary terms gives

$$\mathbf{E}^* \cdot \mathbf{D}^h(\mathbf{k},\omega_r) \cdot \mathbf{E} = 0 \qquad (4.29)$$

$$\omega_i = -\frac{\mathbf{E}^* \cdot \mathbf{D}^a \cdot \mathbf{E}}{\mathbf{E}^* \cdot \frac{\partial \mathbf{D}^h}{\partial \omega_r} \cdot \mathbf{E}} \tag{4.30}$$

Equation 4.29 gives the modified dispersion relation $|\mathbf{D}^h(\mathbf{k}, \omega_r)| = 0$. This dispersion relation implies that the normal modes can be determined by the Hermitian part of the dispersion tensor with $\omega = \omega_r$ when $\omega_i \ll \omega_r$. Growth or damping of these normal modes is then determined by the anti-Hermitian part of the dispersion tensor as indicated by Eq. 4.30. The denominator of Eq. 4.29 is recognized (from analysis not done here) as the perturbed energy density (i.e. the difference from the equilibrium energy density) of a small amplitude, slowly varying wave in an infinite, homogeneous linear medium (Bers, 1972).

4.1.4 $\mathbf{D}^a$ and $\mathbf{D}^h$

The final step before choosing a distribution function to model the Constance B plasma is to determine $\mathbf{D}^a$ and $\mathbf{D}^h$. These are formed in the following manner:

$$\mathbf{D}^h = \frac{1}{2}(\mathbf{D} + \mathbf{D}^\dagger) \tag{4.31}$$

$$\mathbf{D}^a = \frac{1}{2i}(\mathbf{D} - \mathbf{D}^\dagger) \tag{4.32}$$

where $\mathbf{D}^\dagger$ is the Hermitian conjugate of $\mathbf{D}$ and can be written as $\mathbf{D}^\dagger = \mathbf{D}^h - i\mathbf{D}^a$.

Before applying this prescription to Eqs. 4.24 to 4.27 the following normalizations are made:

$$
\begin{array}{ccc}
\frac{\omega_r}{\omega_{ce}}, \frac{\omega_i}{\omega_{ce}}, \frac{\omega_p}{\omega_{ce}} & \longrightarrow & \omega_r, \omega_i, \omega_p \\
\frac{u_\perp}{c}, \frac{u_\parallel}{c} & \longrightarrow & u_\perp, u_\parallel \\
\frac{ck_\perp}{\omega_{ce}}, \frac{ck_\parallel}{\omega_{ce}} & \longrightarrow & k_\perp, k_\parallel \\
c^3 f_0 & \longrightarrow & f_0
\end{array} \tag{4.33}
$$

In addition, a change of variables is made from $(u_\perp, u_\parallel)$ to $(\gamma, u_\parallel)$. The transformation equations are

$$
\begin{aligned}
\gamma &= \sqrt{1 + u_\perp^2 + u_\parallel^2} \\
u_\parallel &= u_\parallel
\end{aligned} \tag{4.34}
$$

which has the Jacobian

$$\left| \frac{\partial(u_{\parallel}, u_{\perp})}{\partial(u_{\parallel}, \gamma)} \right| = \frac{\gamma}{u_{\perp}} \tag{4.35}$$

This is a convenient transformation because the singularities of $\mathbf{Q}$ occur for $\gamma\omega - n\omega_{ce} - k_{\parallel}u_{\parallel} = 0$, which is a simple pole with respect to γ. The usefulness of this transformation shows up later.

The $\mathbf{Q}$ tensor of Eq. 4.25 then becomes

$$\mathbf{Q} = 2\pi\frac{\omega_p^2}{\omega^2}\int_{-\infty}^{\infty} du_{\parallel}\int_0^{\infty} du_{\perp}\frac{u_{\parallel}}{\gamma}\left(u_{\perp}\frac{\partial}{\partial u_{\parallel}} - u_{\parallel}\frac{\partial}{\partial u_{\perp}}\right) f_0\hat{\mathbf{e}}_{\parallel}\hat{\mathbf{e}}_{\parallel}$$

$$-2\pi\frac{\omega_p^2}{\omega^2}\int_{-\infty}^{\infty} du_{\parallel}\int_{\sqrt{1+u_{\parallel}^2}}^{\infty} d\gamma\left(\frac{\partial}{\partial\gamma} + \frac{k_{\parallel}}{\omega}\frac{\partial}{\partial u_{\perp}}\right) f_0$$

$$\times \sum_{n=-\infty}^{\infty} \frac{\mathbf{T}_n}{\gamma - \frac{k_{\parallel}u_{\parallel}+n}{\omega}} \tag{4.36}$$

The γ integral is now written as the sum (or difference) of the principle part and $i\pi$ times the integrand evaluated at the simple pole. The sum is taken if the contour goes below the pole and the difference is taken if the contour goes above the pole. The assumption of $\omega_i > 0$, made while deriving the dispersion relation, predetermines that the contour should go *above* the pole. Since the pole occurs at

$$\gamma = \frac{k_{\parallel}u_{\parallel} + n}{\omega} = \frac{k_{\parallel}u_{\parallel} + n}{|\omega|^2}(\omega_r - i\omega_i) \tag{4.37}$$

then the original condition of $\omega_i > 0$ (and $\mathbf{k}$ real, a simplification which shows its usefulness here!) places the pole below the real γ axis. If the domain of definition of ω_i is to be extended to regions where $\omega_i < 0$ by analytical continuation, then the integration path in γ space must remain above the pole as the pole is moved upward. Equation 4.36 becomes

$$\mathbf{Q} = 2\pi\frac{\omega_p^2}{\omega^2}\int_{-\infty}^{\infty} du_{\parallel}\int_0^{\infty} du_{\perp}\frac{u_{\parallel}}{\gamma}\left(u_{\perp}\frac{\partial}{\partial u_{\parallel}} - u_{\parallel}\frac{\partial}{\partial u_{\perp}}\right) f_0\hat{\mathbf{e}}_{\parallel}\hat{\mathbf{e}}_{\parallel}$$

139

$$-2\pi \frac{\omega_p^2}{\omega^2} \mathbf{P} \int_{-\infty}^{\infty} du_{\parallel} \int_{\sqrt{1+u_{\parallel}^2}}^{\infty} d\gamma \left(\frac{\partial}{\partial \gamma} + \frac{k_{\parallel}}{\omega} \frac{\partial}{\partial u_{\parallel}} \right) f_0 \sum_{n=-\infty}^{\infty} \frac{\mathbf{T}_n}{\gamma - \frac{k_{\parallel} u_{\parallel} + n}{\omega}}$$

$$-2\pi^2 i \frac{\omega_p^2}{\omega^2} \int_{L1}^{L2} du_{\parallel} \left[\left(\frac{\partial}{\partial \gamma} + \frac{k_{\parallel}}{\omega} \frac{\partial}{\partial u_{\parallel}} \right) f_0 \times \sum_{n=-\infty}^{\infty} \mathbf{T}_n \right]_{\gamma = \frac{k_{\parallel} u_{\parallel} + n}{\omega}} \tag{4.38}$$

where the limits $L1$ and $L2$ of the $u_{\parallel}$ integral are the positive solutions to

$$\left(\frac{k_{\parallel}^2}{\omega^2} - 1 \right) u_{\parallel}^2 + \frac{2nk_{\parallel}}{\omega^2} u_{\parallel} + \left(\frac{n^2}{\omega^2} - 1 \right) = 0 \tag{4.39}$$

arranged such that $L1 < L2$. If $L1$ and $L2$ are complex then the third term of Eq. 4.38 is zero. If only one solution is positive then $L1$ is the positive solution and $L2 = \infty$. $L1$ and $L2$ are the intersections of the resonant particle line and the boundary that separates the physical region from the unphysical region of $\gamma - u_{\parallel}$ space.

The tensor $\mathbf{T}_n$ is Hermitian and the tensor $i\mathbf{T}_n$ is anti-Hermitian. Also, the first two terms of $\mathbf{D}$ in Eq. 4.24 (the vacuum terms) are Hermitian. Therefore, $i\mathbf{D}^a$ is given by the last term of Eq. 4.38 while $\mathbf{D}^h$ is given by the sum of the vacuum terms and the first two terms of Eq. 4.38.

The final simplification is to approximate $\mathbf{D}^h$ by the nonrelativistic cold, fluid dispersion tensor, $\mathbf{D}_{fluid}$ (which is Hermitian). This dispersion tensor results by considering the the Vlasov dispersion tensor with a Maxwellian distribution in the limit $v_{th} \ll \omega/k$. This simplification is somewhat justified because the cold plasma of Constance B contributes approximately half of the total line density and is even a greater fraction if only considering the cold and warm components without the hot component. Of course, it is reasonable to expect that the hot plasma alters the cold plasma modes, especially near resonances, which may be shifted and broadened in frequency. Although this simplification places limits on the theory's validity, the theory is still useful for identifying unstable parameter regimes, which are dependent on the sign of $\mathbf{D}^a$. The theory is also useful in comparing the relativistic and nonrelativistic formulations.

In summary, the growth rate ω_i of a wave of frequency $\omega_r \gg \omega_i$ in a plasma characteristized by an equilibrium electron distribution f_0 is calculated in the following manner:

$$\omega_i = -\frac{\mathbf{E}^* \cdot \mathbf{D}^a \cdot \mathbf{E}}{\mathbf{E}^* \cdot \frac{\partial \mathbf{D}^h}{\partial \omega_r} \cdot \mathbf{E}} \tag{4.40}$$

where $\mathbf{k}$ and $\mathbf{E}$ are determined by solving $\mathbf{D}^h \cdot \mathbf{E} \approx \mathbf{D}_{fluid} \cdot \mathbf{E} = 0$. $\mathbf{D}_{fluid}$ is the sum of fluid dispersion tensors from each component of the plasma: $\mathbf{D}_{fluid} = \sum_\alpha \mathbf{D}_{fluid,\alpha}$, where each term is characterized by the plasma frequency characteristic of that component. Nonrelativistically these terms would add to form one term with $\omega_p^2 = \sum_\alpha \omega_{p\alpha}^2$. Relativistically the plasma frequency and cyclotron frequency are reduced by a factor of $(\langle 1/\gamma \rangle)^{1/2}$ and $\langle 1/\gamma \rangle$ respectively, so that the fluid dispersion tensor must be calculated separately for each component and then added. For convenience calculations are done in the $(E_r, E_l, E_{\|})$ basis, where

$$E_r = E_x - iE_y$$

$$E_l = E_x + iE_y$$

The cold fluid dispersion tensor $\mathbf{D}_{fluid}$ is then given by[2]

$$\begin{pmatrix} 1 - \frac{\omega_p^2}{\omega(\omega-\xi)} - \frac{1}{2}\frac{k^2}{\omega^2}(1+\cos^2\theta) & \frac{1}{2}\frac{k^2}{\omega^2}\sin^2\theta & \frac{1}{\sqrt{2}}\frac{k^2}{\omega^2}\sin\theta\cos\theta \\ \frac{1}{2}\frac{k^2}{\omega^2}\sin^2\theta & 1 - \frac{\omega_p^2}{\omega(\omega+\xi)} - \frac{1}{2}\frac{k^2}{\omega^2}(1+\cos^2\theta) & \frac{1}{\sqrt{2}}\frac{k^2}{\omega^2}\sin\theta\cos\theta \\ \frac{1}{\sqrt{2}}\frac{k^2}{\omega^2}\sin\theta\cos\theta & \frac{1}{\sqrt{2}}\frac{k^2}{\omega^2}\sin\theta\cos\theta & 1 - \frac{\omega_p^2}{\omega^2} - \frac{k^2}{\omega^2}\sin^2\theta \end{pmatrix}$$

$$\tag{4.41}$$

where $\xi = \langle 1/\gamma \rangle^{1/2}$ and ω_p here is the relativistically correct plasma frequency.

$$\mathbf{D}^a = -2\pi^2 \frac{\omega_p^2}{\omega^2} \int_{L1}^{L2} du_\perp \left[\left(\frac{\partial}{\partial\gamma} + \frac{k_\|}{\omega}\frac{\partial}{\partial u_\|} \right) f_0 \times \sum_{n=-\infty}^{\infty} \mathbf{T}_n \right]_{\gamma = \frac{k_\| u_\| + n}{\omega}} \tag{4.42}$$

The tensor $\mathbf{T}_n$ contains $u_\perp$, which is written as $(\gamma^2 - u_\|^2 - 1)^{1/2}$. γ obeys the resonance condition so that Eq. 4.42 contains just a one dimensional integral. The one dimensional integral is done numerically using the DCADRE integration routine of the IMSL math package[3] implemented on a VAX 11/750.

---

[2]The cold plasma dispersion tensor in the (E_x, E_y, E_z) basis is given by Stix (1962).

[3]See *The IMSL Library User's Manual*, IMSL, Inc., Houston (edition 9.2: 1984).

4.2   Geometric Intrepetation

A geometric interpretation of the above equations provides an understanding of why instability might exist. The sign of ω_i is determined by the net slope that the distribution function has, in the direction of characteristic paths, along the resonant particle line. The characteristic paths are the diffusion paths which are obtained from a quasilinear formulation of the interaction of a plasma with an rf wave. Only the resonant particles, those which are in synchronism with the wave, contribute to the sign. The resonant particles are defined by $\omega\gamma - n\omega_{ce} - k_\parallel u_\parallel = 0$.

The geometric interpretation is obtained by noting the properties of $\mathbf{D}^a$ in Eq. 4.42. For simplicity, the explanation which follows below applies to the right hand circularly polarized mode, for which D^a_{rr} is the only non-zero component. and $[\mathbf{T}_n]_{rr} = \frac{1}{2}u_\perp^2 > 0$. The sign of ω_i is opposite to the sign of D^a_{rr} because the energy density of a wave in a cold, fluid plasma (the denominator of Eq. 4.40) is always positive. The derivative operator in parenthesis in Eq. 4.42 can be reinterpreted as the derivative along some path χ:

$$\frac{\partial}{\partial\gamma} + \frac{k_\parallel}{\omega}\frac{\partial}{\partial u_\parallel} \longrightarrow \frac{\partial}{\partial\chi} \tag{4.43}$$

which implies

$$\frac{d\gamma}{d\chi} = 1$$

$$\frac{du_\parallel}{d\chi} = \frac{k_\parallel}{\omega} \tag{4.44}$$

A differential equation for the path is then determined:

$$\frac{d\gamma}{du_\parallel} = \frac{\omega}{k_\parallel} \tag{4.45}$$

Since this is only of interest along the resonant particle line. $k_\parallel$ can be eliminated by using the resonance condition. The following result then applies to the resonant particles:

$$\frac{d\gamma}{du_\parallel} = \frac{\omega u_\parallel}{\gamma\omega - n} \tag{4.46}$$

142

This has the solution

$$\left(\gamma - \frac{n}{\omega}\right)^2 - u_\parallel^2 = constant \qquad (4.47)$$

Eq. 4.47 represents a family of hyperbolas which indicate the direction in which the derivative of f_0 is taken. These curves are also the diffusion paths from a quasilinear formulation of the Vlasov-Maxwell equations. Particles which interact with a wave of frequency ω diffuse in the direction of the gradients of f_0, along these paths.

Figure 4.1 shows the $\gamma - u_\parallel$ plane and the diffusion paths for $\omega > 1$ and $\omega < 1$, and for $n = 1$. The unphysical region is defined by $\gamma^2 < 1 + u_\parallel^2$. The prescription given by equation Eq. 4.42 is to integrate the slope of f_0 in the direction of the diffusion paths, along the resonant particle line, in the physical region (there are cases when there are no resonant particles). This is done for every harmonic of the wave, each of which has a different set of diffusion paths. The result is the sum of the contributions from each harmonic. If the result is negative (positive) then the wave with frequency ω is unstable (stable). Quasilinear theory, which includes a conservation of energy principle (Krall and Trivelpiece, 1973), adds to this description the fact that resonant particles, as they diffuse, exchange energy with the wave. Then, if more particles lose energy than gain energy during this diffusion (with each particle weighted by some factor dependent on velocity space location) then the wave, which acquires this energy, is unstable.

Two types of microinstabilities are not predicted by the present theory:
1) *Negative energy wave instabilities.* These were briefly mentioned in Section 1.2.1. If a negative energy wave exists in the plasma then any mechanism which takes energy from this wave causes the wave to grow. Such a mechanism could either be resonant particles which diffuse to higher energies due to interaction with the wave, or a positive energy wave with the same phase velocity (so the two waves can couple to each other). Both of these mechanisms may exist simultaneously and, in a more general theory, may not be separable. Negative energy wave instabilities are not predicted by the theory presented in this thesis because the fluid dispersion

143
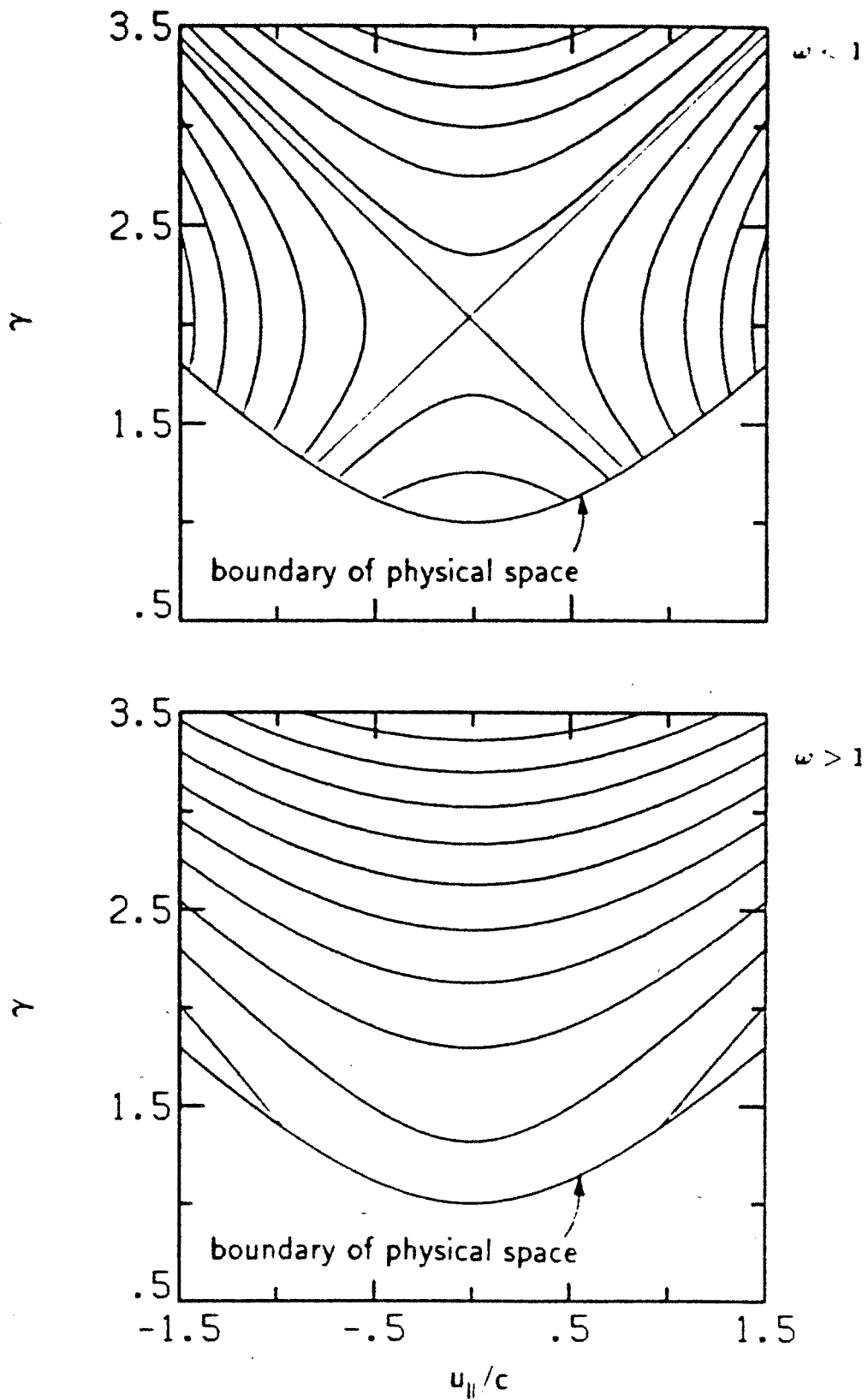
Figure 4.1: Diffusion paths in the $\gamma - u_\parallel$ plane. (a) $\omega < 1$ (b) $\omega > 1$.

tensor for a stationary plasma ($\langle v \rangle = 0$) only predicts positive energy waves.[4] The coupling of a positive and negative energy wave is not predicted for the additional reason that the theory only describes instabilities driven by resonant particles.

2) *Electrostatic instabilities.* Electrostatic instabilities occur for electrostatic modes of the plasma where $k \times E = 0$. Either the reactive part of the Vlasov dispersion relation or, more simply, a dispersion relation derived from the Vlasov equation together with Poisson's equation is necessary to predict electrostatic instabilities. An example of an electrostatic instability is the upper hybrid loss cone instability (UHLCI), which occurs for $k_\perp \gg k_\parallel$ and has frequencies near the upper hybrid frequency, $\omega_{uh} = (\omega_p^2 + \omega_{ce}^2)^{1/2}$ (Porkolab, 1984). The UHLCI is ruled out for the Constance B microinstabilities. The whistler C emission would be the only candidate for the UHLCI. However, for high magnetic fields (see **Fig. 3.11**) the whistler C emission is observed for frequencies below the midplane cyclotron frequency, which means that it does not occur at, or near, the upper hybrid frequency for any location in the plasma.

4.3 Nonrelativistic Theory

The nonrelativistic theory is introduced here so that the relativistic theory can be compared to it. The nonrelativistic formulation is based on Maxwell's equations and the nonrelativistic Vlasov equation:

$$\frac{\partial f}{\partial t} + v \cdot \frac{\partial f}{\partial r} + \frac{q}{m}\left(E + \frac{v \times B}{c}\right) \cdot \frac{\partial f}{\partial v} = 0 \tag{4.48}$$

A similar procedure is followed in deriving a dispersion relation. It turns out, by going through the procedure formally (Krall and Trivelpiece, 1973), that the relativistic form of D is the same as the nonrelativistic form if u/γ is replaced by v (and $\omega/\gamma \longrightarrow \omega$ in the resonance condition). Equation 4.40 is still used to calculate

---

[4]In general, a negative energy wave can only occur in a medium which is not in thermodynamic equilibrium and in which there is a source of free energy (Bers, 1972).

ω_i and $\mathbf{D}^h$ is taken to be the cold plasma dispersion tensor. It is desirable to express $\mathbf{D}^a_{nr}$, the nonrelativistic version of $\mathbf{D}^a$, with respect to an $energy - v_\parallel$ space so that comparisons can be made with the relativistic theory, which was cast in terms of $\gamma - u_\parallel$ space. If the energy variable is $\gamma' = 1 + \frac{1}{2}v^2$, then $\mathbf{D}^a_{nr}$ is given by

$$\mathbf{D}^a_{nr} = -2\pi^2 \frac{\omega_p^2}{\omega^2} \int_{L1}^{\infty} d\gamma' \left[\left(\frac{\omega}{k_\parallel} \frac{\partial}{\partial \gamma'} + \frac{\partial}{\partial u_\parallel} \right) f_0 \times \sum_{n=-\infty}^{\infty} \mathbf{T}_n \right]_{v_\parallel = \frac{\omega-1}{k_\parallel}} \tag{4.49}$$

where $L1 = 1 + \frac{1}{2}v_\perp^2$, and the same normalizations given in Eq. 4.33 have been used with $u_\parallel$ and $u_\perp$ replaced by $v_\parallel$ and $v_\perp$. Unlike the relativistic theory, in which the γ integral is performed first, in the nonrelativistic theory the $v_\parallel$ integral is performed first because there is no pole associated with γ'. In actual implementation the one dimensional integral of Eq. 4.49 is solved, as in the relativistic case, with the DCADRE integration routine of the IMSL math package implemented on a VAX 11/750 computer.

Figure 4.2 shows the $\gamma' - v_\parallel$ plane and the diffusion paths for $\omega < 1$ and $\omega > 1$, and for $n = 1$. The unphysical region is defined by $\gamma' < 1 + v_\parallel^2$. The resonant particle line, defined by $v_\parallel = \frac{\omega-1}{k_\parallel}$, always overlaps the physical region. The diffusion paths are a family of parabolas described by the equation

$$\gamma' = \frac{1}{2} \left(\frac{\omega}{\omega - 1} \right) v_\parallel^2 + constant \tag{4.50}$$

These are concave downward for $\omega < 1$ and concave upward if $\omega > 1$.

4.4 Identification of Instabilities[4]

4.4.1 Whistler and Fast Wave Instabilities

Instabilities are identified according to their location in $\omega - \mathbf{k}$ space and according to the branch of the dispersion relation on which they occur. Since the theory presented here uses the cold plasma dispersion tensor, it is useful to use the CMA
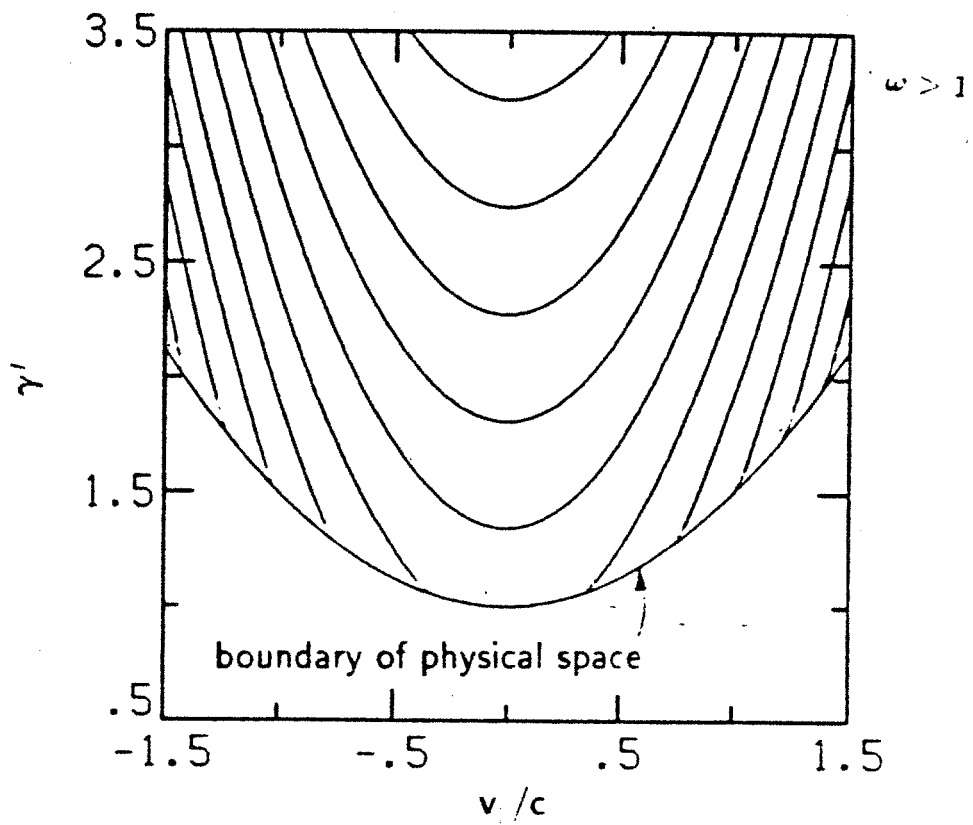
146
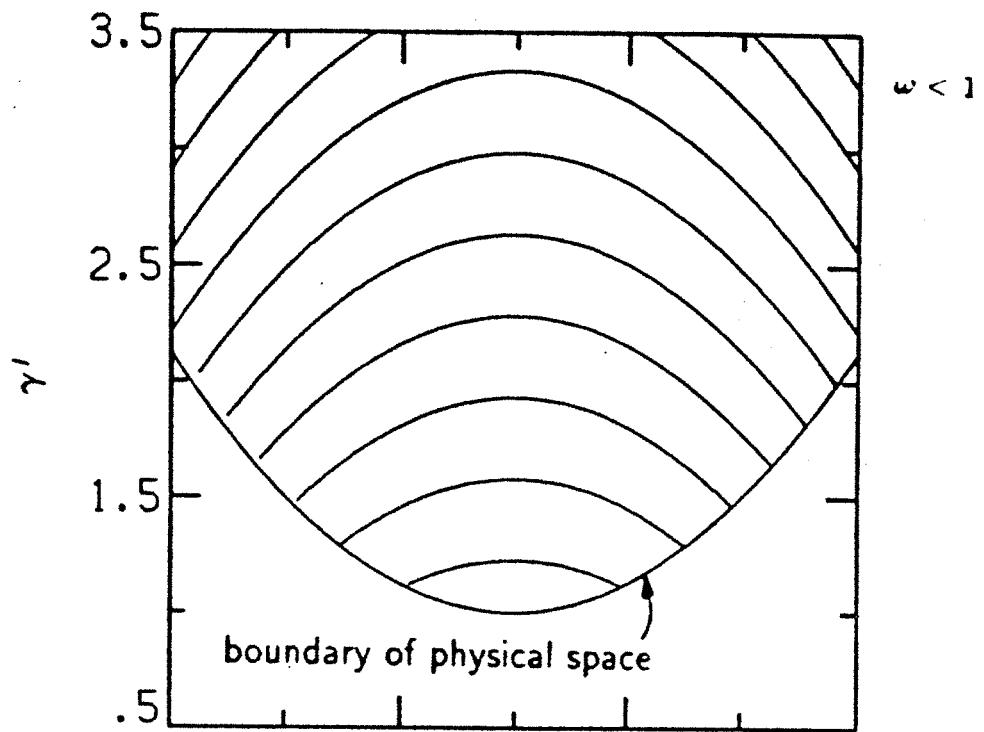
Figure 4.2: Diffusion paths in the $\gamma' - v$ plane. (a) $\omega < 1$ (b) $\omega > 1$.
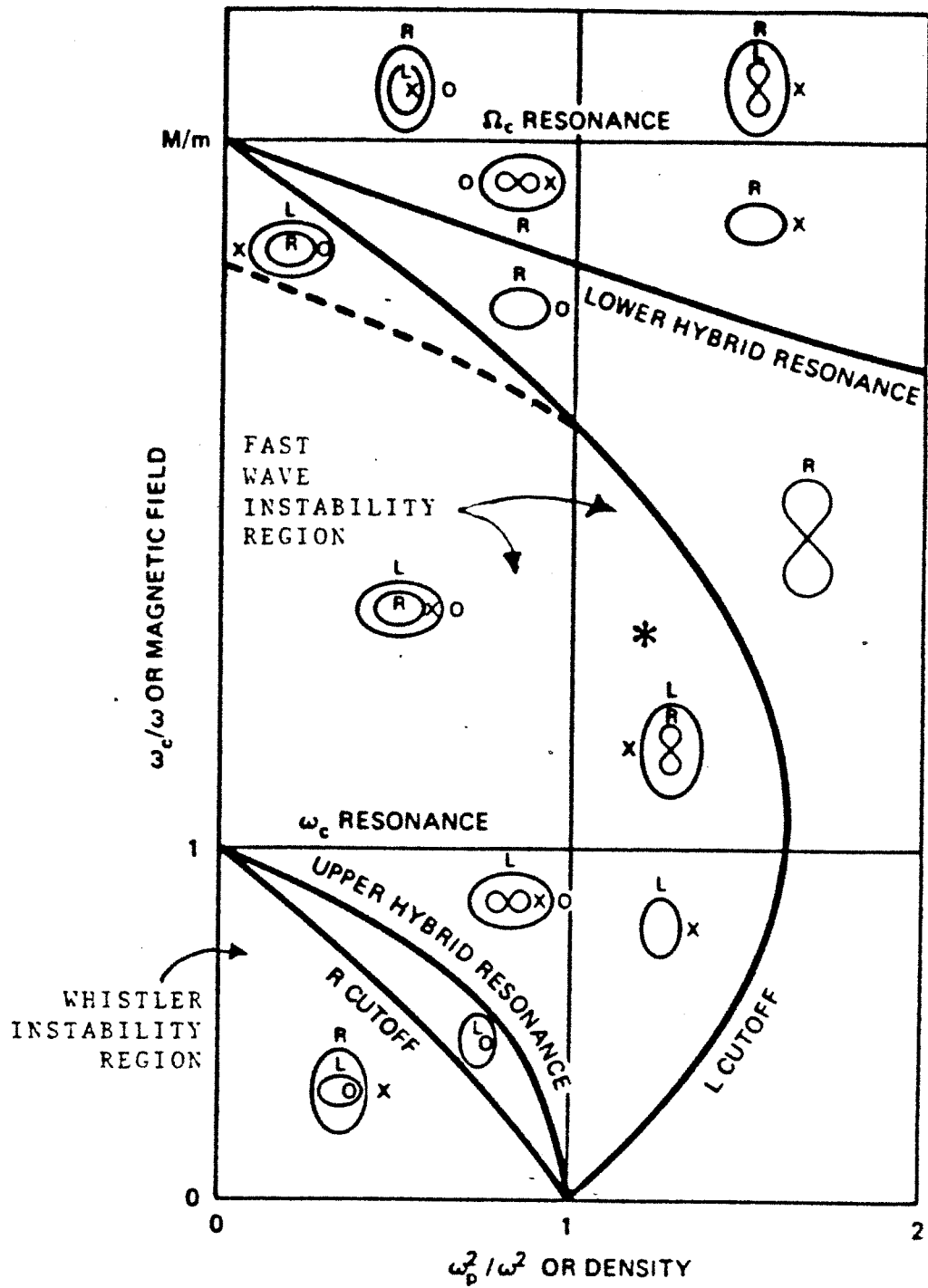
Figure 4.3: The CMA diagram (Chen. 1974).

diagram as a map in locating the various types of instabilities (see Fig. 4.3). Two basic types of instabilities predicted by the present theory are the whistler (slow wave) instability and fast wave instabilities. The cyclotron maser instability is a special type of fast wave instability.

The whistler instability occurs on the whistler branch of the dispersion relation, which is characterized by $k_\perp = 0$, $\omega < \omega_{ce}$ and right hand circular polarization. Whistler waves have phase velocities less than the speed of light which give them the additional name of slow wave. Because they are slow waves, it is easy for particles to resonant with them, exchange energy and cause instability. Waves which are on the same branch of the dispersion relation as the whistler waves (the R-X branch) but which have $k_\perp \neq 0$ may also be unstable, although their growth rates tend to be less than the growth rates for pure whistler waves, as will be shown below. The branch of the dispersion relation which compliments the R-X is the L-O branch (when $\omega_p < \omega_{ce}$). These waves may be unstable for $k_\perp \neq 0$, although their growth rates are smaller than the corresponding growth rates of the R-X branch (as will be shown below). For $k_\perp = 0$ these waves are left hand circularly polarized and do not couple to the electron cyclotron motion.

The two branches of fast wave (for $\omega_p < \omega_{ce}$) are the R-X branch and the L-O branch and are characterized by $\omega > \omega_{ce}$. The cyclotron maser instability occurs on the fast wave portion of the R-X branch of the dispersion relation. When $k_- = 0$ these waves are the fast wave version of the whistler waves—they are right hand circularly polarized but have phase velocities greater than the speed of light. When $k_- = 0$ these waves cannot be unstable in a nonrelativistic formulation via the interaction with resonant particles ($\mathbf{D}_{nr}$ has no pole which implies $\mathbf{D}_{nr}^a = 0$). For this situation a relativistic formulation is necessary. The fast waves on the L-O branch of the dispersion relation have been studied (Lee and Wu, 1980) but have

---

[5]For the rest of this chapter the variables refer to their unnormalized versions, before appication of Eq. 4.33, unless specified otherwise.

not been given a name. In the context of the theory presented here instabilities on this branch would be similar to the cyclotron maser instability.

The geometric picture of Section 4.2 provides a qualitative understanding of the whistler and cyclotron maser instabilities. It is recalled that Fig. 4.1 shows $\gamma - u_{\parallel}$ space and a set of diffusion paths for the relativistic formulation and that Fig. 4.2 shows $\gamma' - v_{\parallel}$ space and a set of diffusion paths for the nonrelativistic formulation. Both figures show the two cases of $\omega < \omega_{ce}$ and $\omega > \omega_{ce}$ (in those figures $\omega/\omega_{ce} \longrightarrow \omega$). In the relativistic formulation the basic shape of the hyperbolic diffusion paths remains the same for all values of ω; as ω is varied only the location of the center of the hyperboloas changes, although it is always on the γ axis. For $\omega < \omega_{ce}$ the center is at $\gamma > 1$ and for $\omega < \omega_{ce}$ the center is at $\gamma < 1$. This is the reason why slow and fast waves have different instability properties. When $\omega < \omega_{ce}$ the concave downward diffusion paths exist in the physical region of velocity space and a sufficient anisotropy in the distribution function may lead to instability. When $\omega > \omega_{ce}$ the concave downward diffusion paths do not exist in the physical region of velocity space and anisotropy alone can never lead to instability. For this situation instability can only occur if there are gradients of f_0 in the direction of lower energy (i.e. a population inversion).

The situation is similar for the nonrelativistic formulation, although the hyperbolas are replaced with parabolas. For $\omega < \omega_{ce}$ all the parabolic diffusion paths are concave downward and, as in the relativistic case, a suitable anisotropy in the distribution function may lead to instability. For $\omega > \omega_{ce}$ all the diffusion paths are concave upward and a population inversion is necessary for instability to exist.

These pictures also qualitatively suggest that the relativistic growth rates should be lower than the corresponding nonrelativistic growth rates. For example, if a distribution function has a suitable anisotropy which leads to whistler instability. the nonrelativistic picture would indicate that all parts of the distribution function up to arbitrarily high energies contribute to instability (i.e. contribute a negative amount in the integral of Eq. 4.42). However, in the relativistic picture the diffusion

150

paths at high energies become concave upward. This would have a stabilizing effect on a wave if anisotropy were the only nonthermal feature of the distribution function. In fact, an unstable situation in the nonrelativistic formuation may be a stable situation in the relativistic formulation.

The above arguments indicate necessary conditions for the existence of the two types of instabilities. They indicate the conditions for which there exist resonant particles which can give their energy to a wave. There are also resonant particles which take energy from the wave, so that the full integral of Eq. 4.42 over all the resonant particles must be done to determine the actual answer.

4.4.2 Example: Bi-Maxwellian

The bi-Maxwellian distribution function is considered as an example because of its widespread usage in the past and because the integrals in Eqs. 4.42 and 4.49 can be performed analytically for $k_\perp = 0$. It is therefore useful as a check of the numerical integration.

The bi-Maxwellian distribution is given, either relativistically or nonrelativistically, in dimensionless variables, by:

$$f_{bM}(u_\perp, u_\parallel) = \left(\frac{\rho_\perp^2 \rho_\parallel}{8\pi^3}\right)^{\frac{1}{2}} exp\left[-\frac{1}{2}\rho_- u_\perp^2 - \frac{1}{2}\rho_\parallel u_\parallel^2\right] \qquad (4.51)$$

where $\rho_\perp = E_o/T_\perp$, $\rho_\parallel = E_o/T_\parallel$, and E_o is the rest mass energy of the electron (for the nonrelativistic situation replace $u_\parallel$ with $v_\parallel$). Inserting the nonrelativistic version of Eq. 4.51 into Eq. 4.49 and setting $k_\perp = 0$ gives

$$[\mathbf{D}_{nr}^a]_{rr} = 2\pi^2 \frac{\omega_p^2}{\omega^2} \frac{1}{k_\parallel \rho_\perp^2} \left(\frac{\rho_\perp^2 \rho_\parallel}{8\pi^3}\right)^{1/2} \left\{\omega_{ce}\left(\rho_\perp - \rho_\parallel\right) + \rho_\parallel \omega\right\} exp\left[-\frac{1}{2}\rho_\parallel \left(\frac{\omega - \omega_{ce}}{k}\right)^2\right]$$

$$(4.52)$$

(the corresponding relativistic expression is long and complicated and will not be shown). Instability occurs if $\omega_i > 0$ or $[D^a]_{rr} < 0$. Therefore, the nonrelativistic result shows that instability occurs if and only if the term in braces in Eq. 4.52 is

151

less than zero. This leads to the well-known *sufficient* condition for instability for a nonrelativistic bi-Maxwellian

$$\frac{\omega}{\omega_{ce}} < 1 - \frac{T_{\parallel}}{T_{\perp}} \qquad (4.53)$$

Only the whistler instability can occur, as was determined above using the geometric picture. Equation 4.53 is straightforward to obtain from the geometric picture because the contours of nonrelativistic bi-Maxwellian in $\gamma' - v_{\parallel}$ space are concave downward parabolas when $T_{\perp} > T_{\parallel}$, similar to the diffusion paths for $\omega < \omega_{ce}$. A sufficient condition for instability does **not** exist for the relativistic formulation, although it is asserted here, without proof, that Eq. 4.53 is a necessary condition for instability relativistically.

Fig. 4.4 shows plots of ω_i versus ω_r for the relativistic and nonrelativistic formulations using the bi-Maxwellian distribution. The same temperatures are used in each case. It is seen that the condition of Eq. 4.53 is upheld, and that the growth rates are smaller for the relativistic formulation, as was determined above qualitatively.

4.5 Model for Constance B

Local growth rates are calculated for the Constance plasma at every point along a single magnetic field. This is done by choosing a suitable distribution function for the midplane and mapping it along the field line using the unperturbed particle orbits as the transformation. Doing this for different radial positions then generates a map of local growth rates for every position in the plasma.
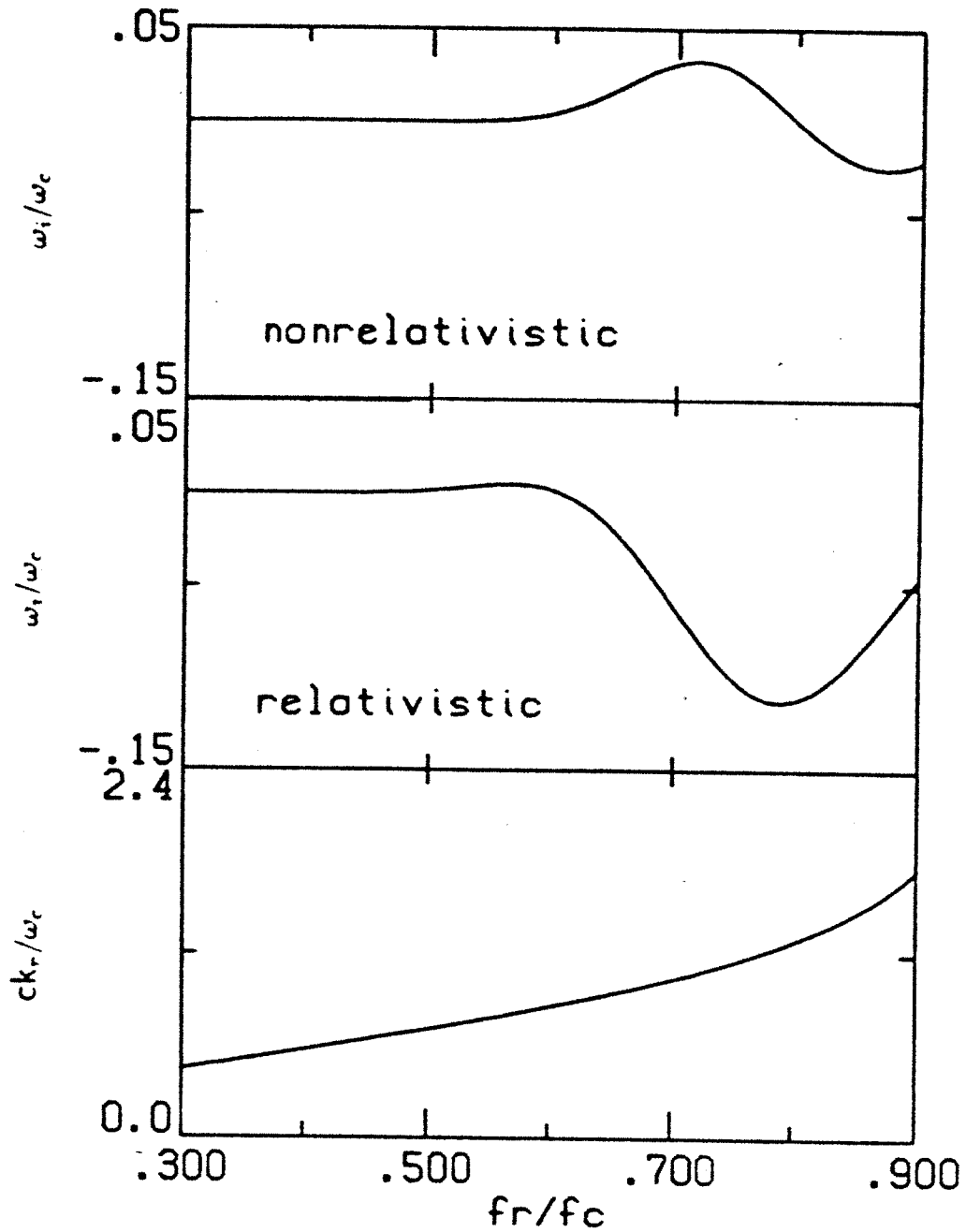
Figure 4.4: ω_i versus ω_r for the bi-Maxwellian (a) nonrelativistically and (b) relativistically. (c) k from the cold plasma dispersion relation.

4.5.1 Constance B Distribution Function

Section 2.5.1 discusses three electron components observed in Constance B. Section 3.3 concludes, based on the experimental analysis, that the warm electrons (with an average energy of approximately 2 keV) drive the microinstability, while the hot electrons (with a temperature of approximately 400 keV) are microstable. In this section the warm electrons are modeled with a distribution function which is motivated by Fokker-Planck calculations of an ECRH, mirror-confined plasma. The results of calculations using this distribution will be shown in Section 4.6 and used to interpret the experimental results. It is not understood why the hot electrons are microstable because the theoretical calculations will show them to be microunstable. Speculations as to why the hot electrons are microstable will be presented in Section 4.6.3. The calculations of Section 4.6 will treat the two components independent of each other.

The cold, electrostatically confined component is modeled with a Maxwellian distribution. As mentioned in Section 2.5.2, these electrons are highly collisional and have no loss cone.

Motivation of the Choice for the Warm Electron Distribution

The choice of distribution function for the warm electrons is motivated by quasilinear theory in which electron heating is described as a diffusion process in velocity space (Lieberman and Lichtenberg, 1973). Quasilinear diffusion is a valid description only if the gyrophase of an electron is random with respect to the phase of the heating wave each time the electron passes through the region in which it is in resonance with the wave. Such a situation occurs if the effective time an electron spends in resonance is short compared to the time spent between resonances because the gyrophase then has a chance to decorrelate with the wave phase.[6] When this happens an electron gets a random kick every time it passes through resonance.

---

[6]Multiple frequency heating and non-zero $k_\parallel$ will also randomize the gyrophase. These effects may lead to higher energy boundaries for the stochastic heating regime than are arrived at below.

The random kick is however confined to a certain line in velocity space, since the kick at resonance is only in μ. A distribution of electrons will then tend to spread out in velocity space along this characteristic line. This is the diffusion mechanism of quasilinear theory. As the energy of an electron increases, while holding the electric field of the wave constant, the effective time an electron spends in resonance becomes longer. Therefore, at high enough energies (with respect to the electric field of the wave) the electron gyrophase is always "locked" to the wave phase and the electron can only undergo small oscillatory excursions in velocity space as it forever oscillates with the wave. The regime in which the gyrophase is random at each resonance crossing is called the stochastic regime. When a particle's gyrophase is not random at each resonance crossing the particle is called superadiabitic, even though its motion is referred to as adiabatic motion. There is a region between the stochastic regime and the superadiabatic regime in which there are isolated islands in velocity space which are stochastic.

Jaeger *et al.* (1972) have determined a nonrelativistic condition for stochasticity assuming a monochromatic heating wave

$$W_{\perp,res} < 3.65 g^{2/3} \left(\frac{\hat{t}}{\tau_{eff}} \right)^{2/3} \epsilon E_k L \qquad (4.54)$$

where $W_{\perp,res}$ is the perpendicular particle energy at resonance, E_k is the electric field strength of the wave, τ_{eff} is the time it takes a particle's phase to slip π out of phase relative to the wave's phase at resonance (i.e. the effective time spent in resonance), g is a constant which is approximately equal to $1/2$, and

$$\hat{t} = \left[\frac{mL}{\epsilon E_k} \left(1 + \frac{z_{res}^2}{L^2} \right) \right]^{1/2} \qquad (4.55)$$

for a magnetic field which is approximated by a parabolic well, and for $\omega_b \tau_{eff} \ll 1$. Also, for a parabolic well magnetic field of length L

$$\tau_{eff} \approx \frac{4\pi L^2}{\omega_{co} z_{res}^2} \qquad (4.56)$$

155

where z_{res} is the resonance position. Equation. 4.54 indicates that a particle that is heated by stochastic diffusion eventually gets to an energy where its motion is superadiabatic and it is no longer heated.

An upper limit on $W_{\perp,res}$ can be estimated for Constance B by considering E_k to be the value at the mouth of the ECRH waveguide (rectangular XL band). The value in the plasma must be less than this. The average transmitted power of a $TE_{1,0}$ mode in a low loss rectangular waveguide in mks units is given by (Lorrain and Corson, 1970)

$$ P = \frac{E_k^2 ab}{4c\mu_o} \left[1 - \left(\frac{c}{2fb} \right)^2 \right]^{1/2} \tag{4.57} $$

where $a = 1.25$ cm and $b = 2.8$ cm are the width and length of the cross section of the waveguide respectively, and f is the wave frequency. For $P = 1$ kW, Eq. 4.57 gives $E_k = 700$ V/cm. Then, taking $z_{res} = 5$ cm and $L = 40$ cm gives $W_{\perp,res} < 150$ keV for stochastic heating to take place. A more realistic value for E_k would be the electric field value determined with a diode which measures total rf power at some location on the vacuum chamber wall.[7] The value of E_k from this is approximately 30 V/cm. Noting that $W_{\perp,res}$ scales as $E_k^{2/3}$ this value of E_k gives $W_{\perp,res} < 19$ keV. In reality E_k in the plasma is probably even less than the 30 V/cm cavity field because of plasma shielding effects. These calculations indicate that the warm electron component of Constance B (~ 2 keV) heats by stochastic diffusion while the hot component (~ 400 keV) does not.

The ECRH Distribution Function

The following function, referred to as the ECRH distribution, has been chosen[8] as a model for the warm electrons because of its similarity to distribution functions

---

[7] See Section 2.2 for a discussion of this diagnostic and Section 2.3 for an interpretation of its signal.

[8] The original idea for the ECRH distribution function was from Mike Mauel (1984a).

predicted by Fokker-Planck simulations of ECRH, mirror-confined plasmas (Mauel, 1984b), which models the heating mechanism as quasilinear diffusion:

$$f_{w0}(\mu, E) = \frac{N}{c^3} \exp\left[-\frac{\chi}{T_\chi} - \theta(\eta)\frac{\eta}{T_{\eta_+}} + \theta(-\eta)\frac{\eta}{T_{\eta_-}}\right] \qquad (4.58)$$

where $\chi = \frac{1}{2}(E + \mu B_h)$, $\eta = \frac{1}{2}(E - \mu B_h)$, E is the particle kinetic energy, $B_h = mc\omega_h/e$, ω_h is the applied heating frequency, θ is the unit step function, m is the rest mass energy of the electron, and T_χ, T_{η_-}, and T_{η_+} are three constants. N is the normalization coefficient which has been determined for the nonrelativistic case:

$$N = \begin{cases} \frac{1}{\sqrt{4\pi^3}}\left[\sqrt{\frac{2}{\rho_{\perp_+}^2 \rho_{\parallel_+}}} - \sqrt{\frac{R_h-1}{\rho_\chi \rho_{\perp_-}^2 R_h}} + \sqrt{\frac{R_h-1}{\rho_{\parallel_-}^2 \rho_\chi R_h}}\right]^{-1} & \text{if } R_h > 1 \\ \sqrt{\frac{\rho_{\parallel_+} \rho_{\perp_\pm}^2}{8\pi^3}} & \text{if } R_h \leq 1 \end{cases} \qquad (4.59)$$

where $\rho_\chi = E_o/T_\chi$ and

$$\rho_{\perp_+} = \frac{1}{2}\rho_\chi(1 + R_h) + \frac{1}{2}\rho_{\eta_+}(1 - R_h)$$

$$\rho_{\perp_-} = \frac{1}{2}\rho_\chi(1 + R_h) - \frac{1}{2}\rho_{\eta_-}(1 - R_h)$$

$$\rho_{\parallel_+} = \frac{1}{2}\left(\rho_\chi + \rho_{\eta_+}\right)$$

$$R_h = \frac{B_h}{B_{local}}$$

and $\rho_{\eta_-} = E_o/T_{\eta_-}$ and $\rho_{\eta_+} = E_o/T_{\eta_-}$. When $R_h < 1$ the ECRH distribution is a bi-Maxwellian.

Velocity space contours of the ECRH distribution are plotted in Fig. 4.5(a) for a particular choice of the parameters: $T_\chi = 5$ keV, $T_{\eta_-} = 0.5$ keV, $T_{\eta_-} = 0.25$ keV, and $R_h = 1.25$. Velocity space contours of a distribution function from a Fokker-Planck simulation (Garner and Mauel, 1983) are plotted in Fig. 4.5(b). (A positive plasma potential was included in the Fokker-Planck simulation which caused cold electrostatically confined Maxwellian distribution to develop.) The similarity in
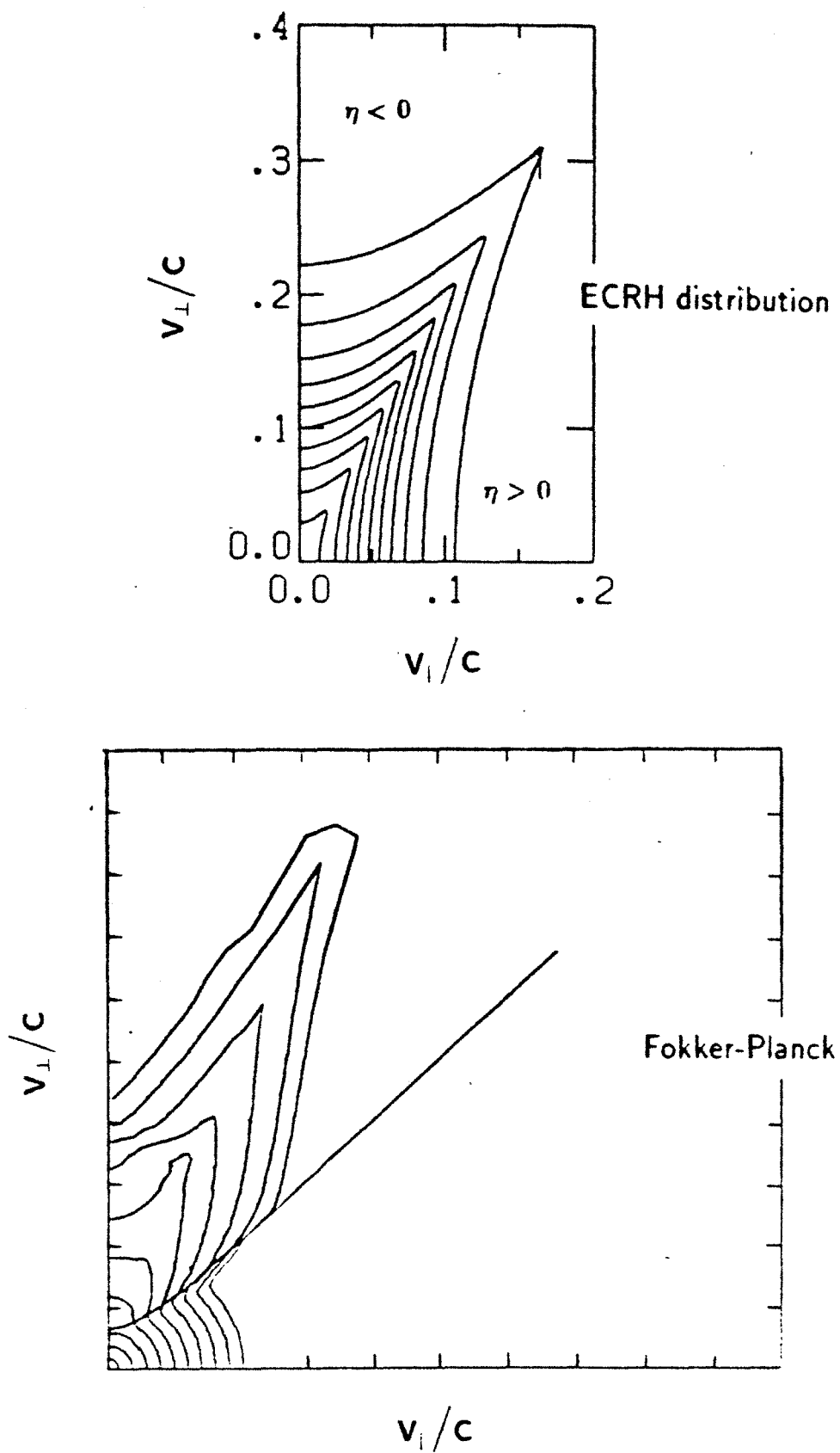
Figure 4.5: (a) Contours of the ECRH distribution. (b) Contours of a distribution generated by a Fokker-Planck simulation.

appearance of these two sets of contours is partly the motivation for chosing the ECRH distribution.

The ECRH distribution function is not an analytic fit to a Fokker-Planck generated distribution, nor is it an expression, approximate or otherwise, which solves the quasilinear diffusion equation. It is a merely a useful model because of its intuitive appeal and because of its simplicity to handle analytically.

The Hot Electron Distribution Function

The hot electron component is modeled with a bi-Maxwellian distribution modified with a loss cone (BMLC distribution), similar to the one used by Lee and Wu (1980) (first suggested by Dory *et al.* (1965)). In dimensionless variables, it is given by:

$$f_{h0}(u_\perp, u_\parallel) = \frac{1}{m!} \left(\frac{\rho_\perp^2 \rho_\parallel}{8\pi^3} \right)^{\frac{1}{2}} \left(\frac{1}{2}\rho_\perp u_\perp^2 \right)^m exp\left[-\frac{1}{2}\rho_\perp u_\perp^2 - \frac{1}{2}\rho_\parallel u_\parallel^2 \right] \qquad (4.60)$$

where m is the loss cone parameter. This choice is motivated experimentally by the fact that the experimentally determined x-ray spectrum as a function of axial position is predicted well using a BMLC distribution with $T_\perp/T_\parallel = 5$ (Hokin *et al.*, 1985). There is no theoretical motivation for the choice of hot electron distribution since there has been no theory done on the ECRH of a population of relativistic electrons where stochasticity, as described above, breaks down.

4.5.2 Properties of the ECRH distribution

The contours of the ECRH distribution function approach the ECRH diffusion paths as T_χ/T_{η_-} and T_χ/T_{η_-} both approach infinity. This is readily seen by considering $\mu - E$ space, where the contours of the ECRH distribution and the ECRH diffusion paths are both families of straight lines for the relativistic and the nonrelativistic formulations (nonrelativistic: $\mu = mu_\perp^2/2B$; relativistic: $\mu = mv_\perp^2/2B$). This is shown in Figure 4.6. The equation for the ECRH diffusion paths is

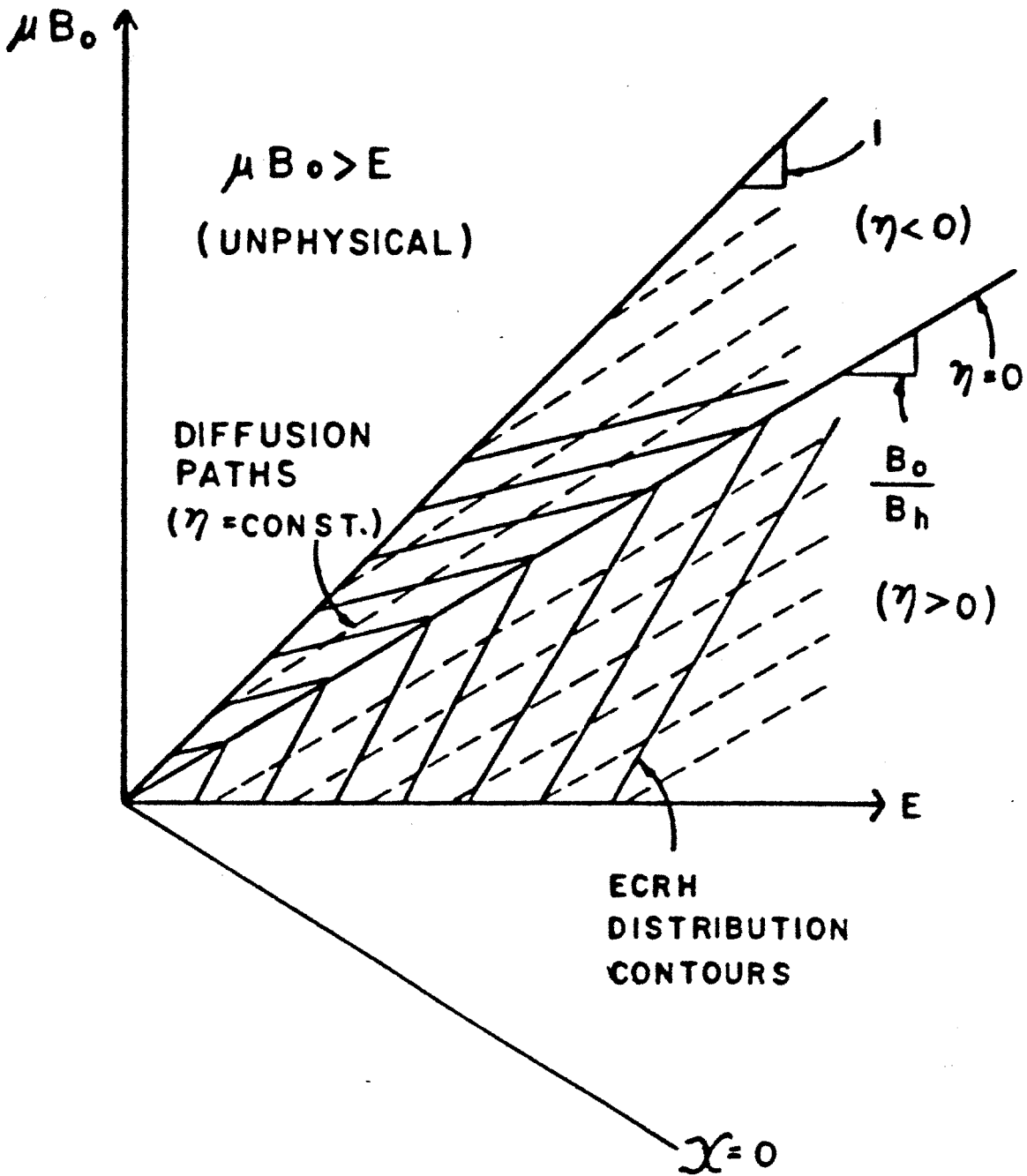Figure 4.6: Contours of the ECRH distribution in $\mu - E$ space along with the ECRH diffusion paths.

$$\mu = \frac{1}{B_h} E + constant \qquad (4.61)$$

Therefore, the lines of constant $\eta = \frac{1}{2}(E + \mu B_h)$ are simply the ECRH diffusion paths and $\chi = \frac{1}{2}(E - \mu B_h)$ can be interpreted as a coordinate along the diffusion paths. The parameters T_χ/T_{η_+} and T_χ/T_{η_-} are the slopes of the ECRH distribution contours with respect to the $\chi - \eta$ axes for $\eta > 0$ and $\eta < 0$ respectively. These parameters are an indication of the strength of the diffusion which has taken place. As they increase, the ECRH distribution contours approach the ECRH diffusion paths.

The region defined by $\eta < 0$ is stabilizing to a wave while the region defined by $\eta > 0$ is unstabilizing to a wave. The diffusion paths corresponding to a wave of arbitrary frequency ω are also straight lines in $\mu - E$ space and the equation which describes them is the same as Eq. 4.61 except with B_h replaced with $B = mc\omega/\epsilon$. Figure 4.6 can be used to visualize the situation for the case of $\omega < \omega_h$. The diffusion paths for ω should be steeper than the ones for ω_h. As ω decreases, the diffusion paths become steeper, and the ratio T_χ/T_{η_+} can then be smaller for instability to occur. If T_χ/T_{η_+} were infinite, then an unstable wave could have frequency up to the applied ECRH frequency. The ECRH distribution does not allow for instability greater than the ECRH frequency. For a sufficiently high T_χ/T_{η_+} it is therefore possible for both the whistler and cyclotron maser instabilities to exist.

The well-known condition of Eq. 4.53 for the bi-Maxwellian distribution is replaced with a new condition for the ECRH distribution. A necessary condition for instability can be ascertained for the case of $k_\perp = 0$. Plugging the $\eta > 0$ part of the distribution function into Eqs. 4.49 or 4.42 indicates that $\omega_i > 0$ only if

$$\frac{\omega}{\omega_h} < \frac{T_\chi - T_{\eta_-}}{T_\chi + T_{\eta_-}} \qquad (4.62)$$

This is only a necessary condition because the region $\eta < 0$ may provide enough stability to completely stabilize the wave.

4.5.3 Magnetic Geometry

A way of connecting the local velocity space theory at different spatial locations along a single field line is to pick the distribution function at a reference location and to map it along the field line using the unperturbed particle orbits and the fact that phase space density is conserved for a collisonless plasma (implied by the Vlasov equation). In calculating the growth rate at some location s, the integral in Eq. 4.42 is performed such that $u_{\parallel}$, f, and ω_p all pertain to the local velocity space. Since phase space density is conserved then

$$
\begin{aligned}
f(\gamma, u_{\parallel}, s) &= g(\gamma, u_{\parallel o}, s_o) \\
&= f_o(\gamma, u_{\parallel o}(\gamma, u_{\parallel}), s_o)
\end{aligned}
\tag{4.63}
$$

where the subscript o refers to the midplane, the chosen reference location, f_o is the distribution function at the midplane, and

$$
u_{\parallel o}^2 = u_{\parallel}^2 + \left(1 + \frac{1}{R}\right) u_{\perp}^2
\tag{4.64}
$$

R is the local mirror ratio with respect to the midplane. Eq. 4.63 is the same for the nonrelativistic and relativistic formulations. The difference between the two cases enters in the way $u_{\perp}$ is written with respect to $u_{\parallel}$ and γ.

For the ECRH, BMLC, and bi-Maxwellian distributions this transformation has the effect of changing the temperatures and densities but leaving the functional dependence on γ and $u_{\parallel}$ the same at different locations. In addition, the density is multiplied by R to take into account its increase due to the compression of magnetic flux as the magnetic field increases. The temperatures and densities of the ECRH. BMLC and bi-Maxwellian distributions change with location in the following way:

ECRH distribution:

$$
\begin{aligned}
\rho_{\lambda} &= \rho_{\lambda o} \\
\rho_{\eta_{\pm}} &= \rho_{\eta_{\pm} o} \\
\frac{\omega_p^2}{\omega_{po}^2} &= R^2 \left| \frac{B}{A} \right|
\end{aligned}
\tag{4.65}
$$

where for $R_h > R$

$$
\begin{aligned}
A &= -h(y_1, 1, \rho_{\eta_-}, -1) \\
&\quad + h(y_1, 1, \rho_{\eta_+}, 1) \\
&\quad - h(1, 1, \rho_{\eta_+}, -1)
\end{aligned}
$$

$$
\begin{aligned}
B &= -h(y_r, R, \rho_{\eta_-}, -1) \\
&\quad - h(y_r, R, \rho_{\eta_+}, 1) \\
&\quad - h(1, R, \rho_{\eta_+}, 1)
\end{aligned}
$$

and for $R_h < R$

$$
\begin{aligned}
A &= -h(1, 1, \rho_{\eta_+}, 1) \\
B &= -h(1, R, \rho_{\eta_+}, 1)
\end{aligned}
$$

where

$$
h(y, R', \rho_\eta, \alpha) = \frac{y \cdot w}{\rho_\lambda \left(1 - \frac{R_h}{R'}\right) + \alpha \rho_\eta \left(1 - \frac{R_h}{R'}\right)}
$$

$$
y_1 = \sqrt{1 - \frac{1}{R_h}}
$$

$$
y_r = \sqrt{1 - \frac{R}{R_h}}
$$

$$
w = \begin{cases} \sqrt{2\rho_\lambda} & \text{if } y \neq 1 \\ \sqrt{\rho_\lambda + \rho_\eta} & \text{if } y = 1 \end{cases}
$$

BMLC distribution:

$$
\begin{aligned}
\rho_\perp &= \frac{\rho_{\perp o}}{R} + \rho_{\| o}\left(1 - \frac{1}{R}\right) \\
\rho_\| &= \rho_{\| o} \\
\frac{\omega_p^2}{\omega_{po}^2} &= R^2 \left[\frac{\rho_{\perp o}}{\rho_{\perp o} - \rho_{\| o}(R - 1)}\right]^{m+1}
\end{aligned}
\tag{4.66}
$$

Bi-Maxwellian distribution:

$$\rho_\perp = \frac{\rho_{\perp o}}{R} + \rho_{\|o}\left(1 - \frac{1}{R}\right)$$

$$\rho_\| = \rho_{\|o} \tag{4.67}$$

$$\frac{\omega_p^2}{\omega_{po}^2} = R^2\left[\frac{\rho_{\perp o}}{\rho_{\perp o} + \rho_{\|o}(R-1)}\right]$$

Figure 4.7 shows plots of ω_{ps}/ω_{po} along a magnetic field for the ECRH, the BMLC, the bi-Maxwellian, and the Maxwellian distribution functions.

As an aside, the particular way that the temperatures change for the bi-Maxwellian distribution leads to a generalization of the sufficient condition for instability given by Eq. 4.53. Plugging $T_\perp$ from Eq. 4.68 into Eq. 4.53 indicates that $\omega_i > 0$ for a nonrelativistic bi-Maxwellian if and only if

$$\frac{\omega}{\omega_{co}} < 1 - \frac{T_{\|o}}{T_{\perp o}} \tag{4.68}$$

That is, the whistler instability only occurs for frequencies below the midplane cyclotron frequency and it is determined by the midplane temperature anisotropy.

4.6 Growth Rate Calculations for Constance B

Growth rate calculations pertaining to the Constance B experiment are made using the ECRH distribution for the warm electrons and a Maxwellian distribution for the cold electrons. The two distributions are mapped to different locations on a single field line according to the method described in Section 4.5.3. The total density pertaining to both distribution functions is used to calculate the cold plasma dispersion relation. Both distribution functions are used separately in a calculation of $\mathbf{D}^a$ in Eq. 4.42, and the two results are added to give a total $\mathbf{D}^a$. Results of calculations using the BMLC distribution to model the hot electrons will be presented separately.
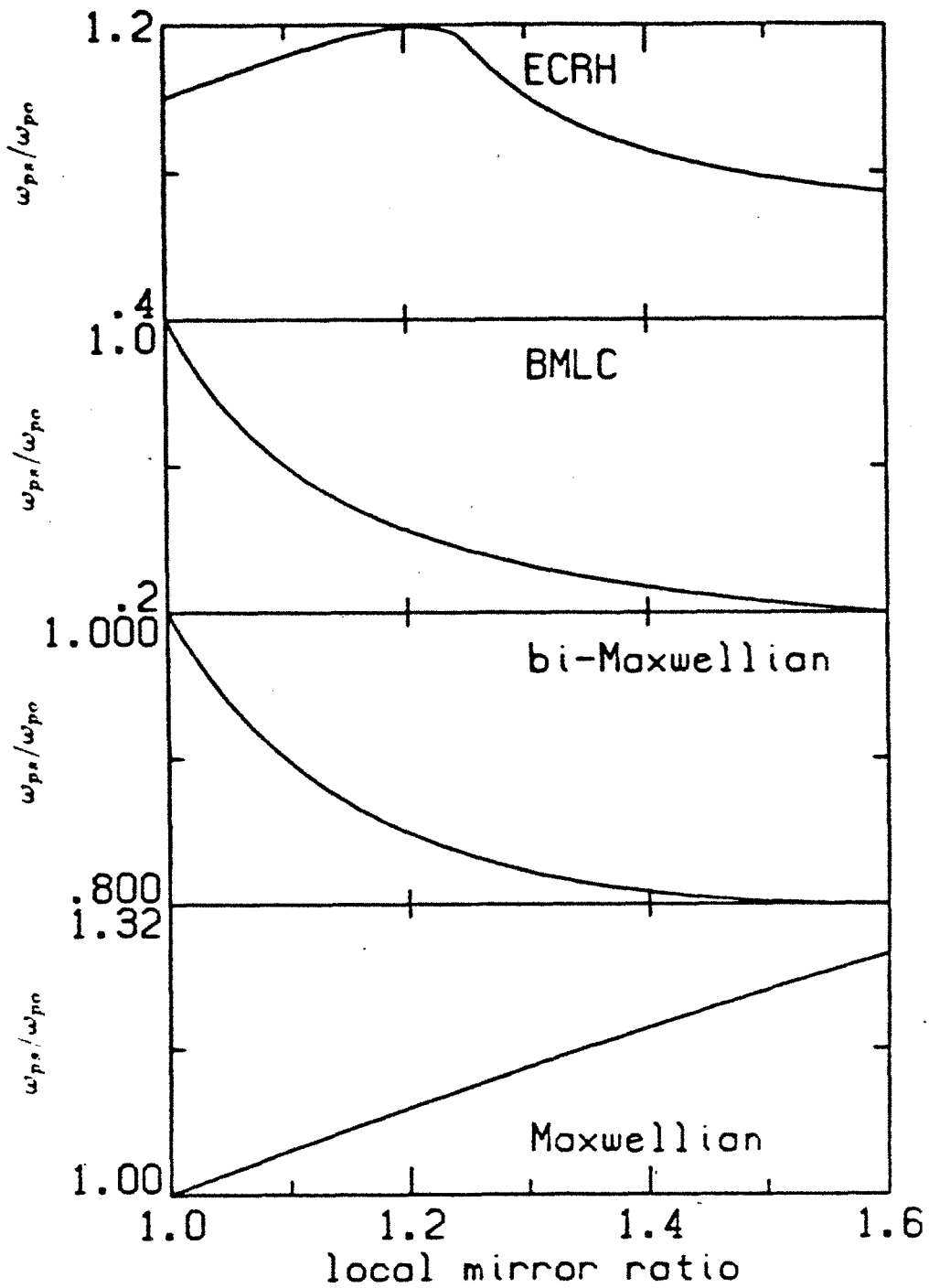
Figure 4.7: ω_{ps}/ω_{po} as a function of local cyclotron frequency for (a) ECRH. (b) BMLC, (c) bi-Maxwellian, and (d) Maxwellian distribution functions.

The ECRH distribution is successful in describing the microinstability of Constance B for two reasons: 1) the theoretically predicted frequencies of the unstable whistler waves agree well with the experimentally observed frequencies of the unstable rf emission from Constance B and 2) the frequencies of the theoretically predicted unstable whistler waves are not sensitive to changes in midplane magnetic field, changes in the temperature parameters T_χ, T_{η_-}, and T_{η_-}, or changes in the density parameters. They are sensitive to changes in the ECRH frequency. As discussed in Chapter 3 the frequency spectrum of the observed unstable rf emission is similar for a wide variety of operating conditions, including changes in midplane magnetic field. Therefore, in addition to supporting experimental observations, this second point indicates that the ECRH distribution is fairly robust in describing microinstability. The parameters are not limited to a small regime which must be determined experimentally. This is a useful quality since the distribution function is never actually measured and the temperature parameters are not known.

4.6.1 Results: ECRH Distribution

Typical results for the ECRH distribution function in a relativistic calculation for the growth rate are shown in Fig. 4.8. In this figure contours of $f_i = \omega_i/2\pi$ are plotted as a function of the local cyclotron frequency (vertical axis) and the wave frequency (horizontal axis). The vertical axis corresponds to the position along a magnetic field line, with the lowest value corresponding to the lowest point of the magnetic well for that field line (which will be referred to as the midplane). The ratio of warm density to total density n_{ew}/n_e for Fig. 4.8 is 0.1. Since ω_p^2 only enters in the calculation of $\mathbf{D}^a$ as an overall multiplicative factor, f_i is approximately proportional to n_{ew}/n_e, for constant n_e. This is a good approximation because the cold Maxwellian subtracts a negligible amount from f_i. This will be verified below. For comparison, results for the ECRH distribution in a nonrelativistic calculation, with the same parameters as above, are shown in Fig. 4.9. The nonrelativistic

Figure 4.8: Contours of f_i for the ECRH distribution. Relativistic calculation with $k_- = 0$. $T_\lambda = 5$ keV. $T_{\eta_-} = 0.5$ keV. $T_{\eta_-} = 0.25$ keV. $f_{i,max} = 0.04$ nsec^{-1}.
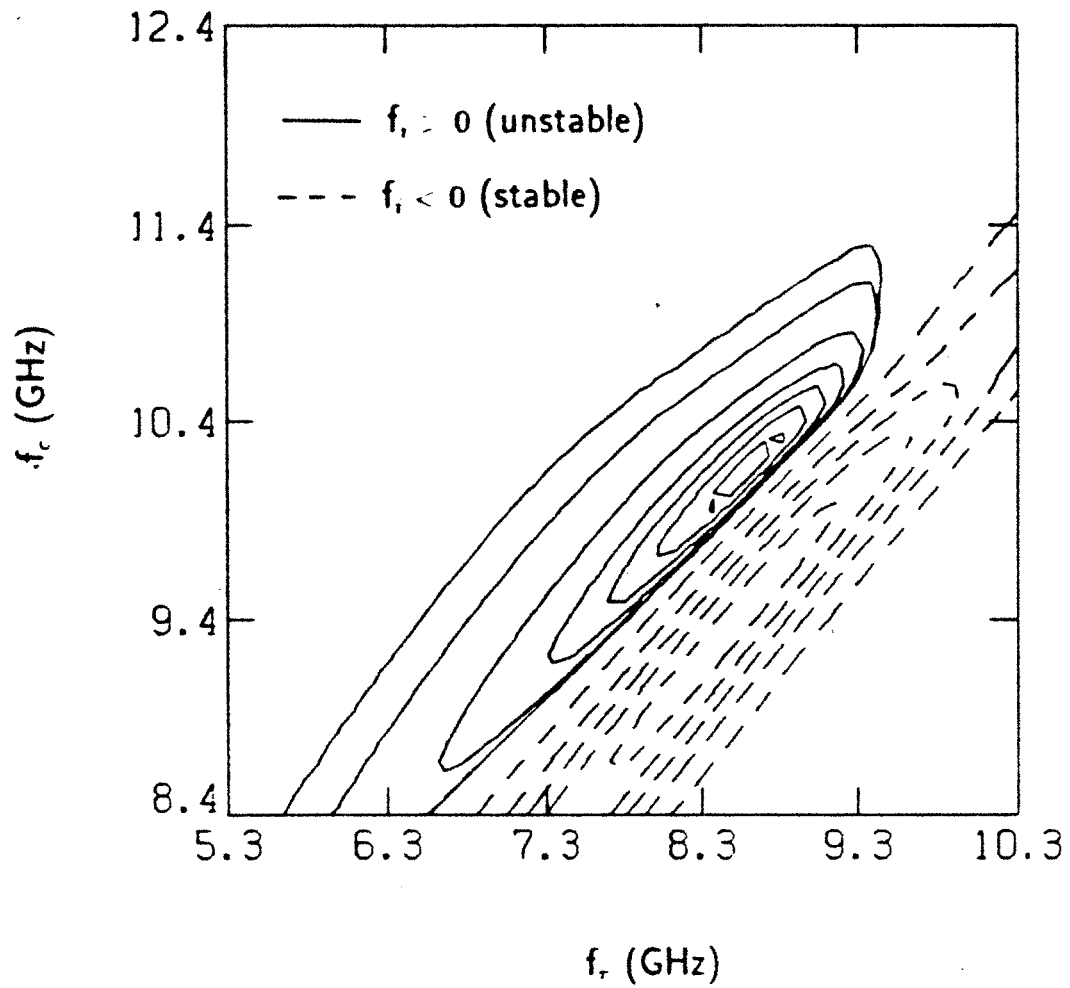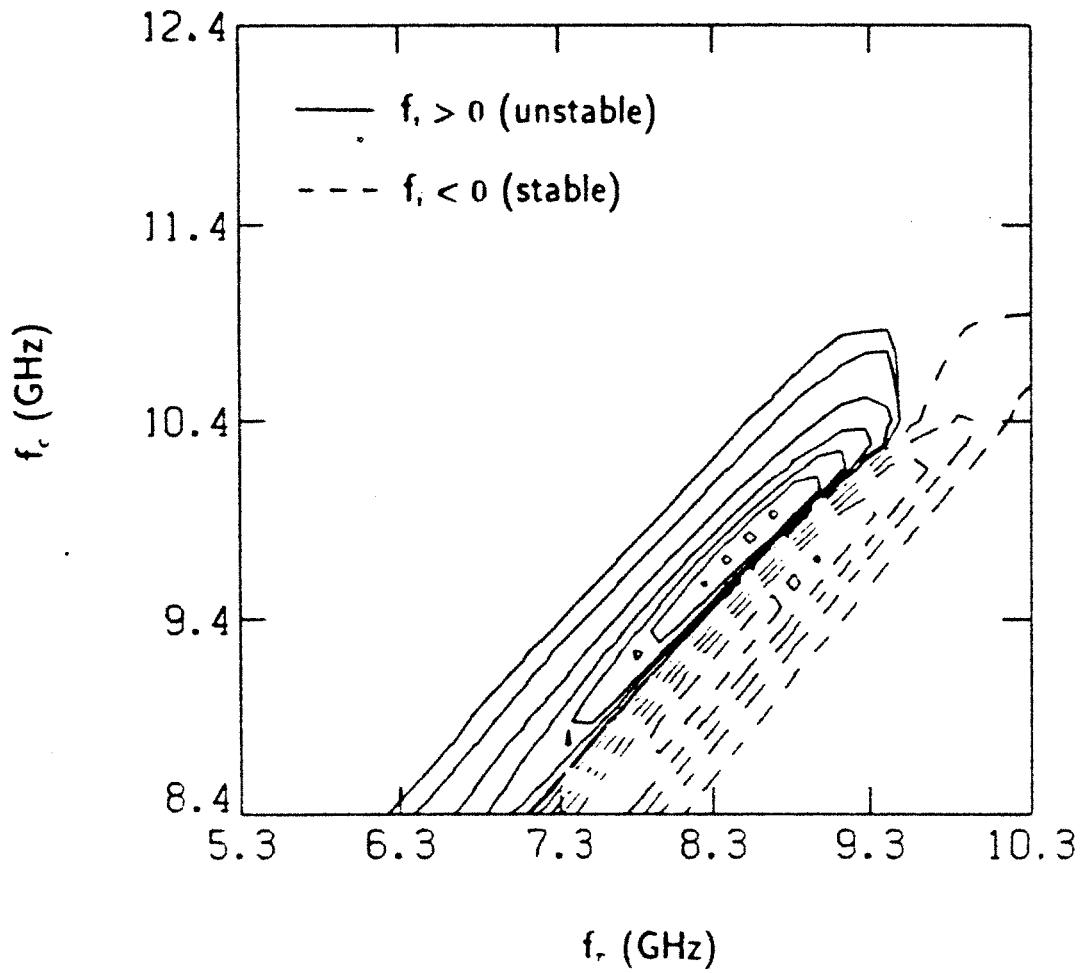
Figure 4.9: Contours of f_i for the ECRH distribution. Nonrelativistic calculation with $k_- = 0$. $T_\lambda = 5$ keV, $T_{\eta_-} = 0.5$ keV. $T_{\eta_-} = 0.25$ keV. $f_{i,max} = 0.56$ nsec^{-1}.

contours of f_i are similar to the relativistic ones except the values are higher. This was predicted using qualitative arguments in Section 4.4.1.

For comparison, results for the BMLC distribution and the bi-Maxwellian distribution in relativistic calculations are shown in Figs. 4.10 and 4.11 respectively. The temperatures were chosen so that the average energies of these distributions are near the average energy of the ECRH distribution used above. The frequencies of the most unstable waves for these distributions are usually approximately 20% lower than what is observed experimentally. The above plots in Figs. 4.8 to 4.11, in conjunction with the theoretical discussion of Section 4.5.1 suggest that the ECRH distribution is a feasible model for the Constance B plasma.

Figures 4.12 and 4.13 show the contours of f_i as a function of wave frequency and θ_k, the angle between $\mathbf{k}$ and the magnetic field, for a fixed location using the ECRH distribution. Figure 4.12 is for the slow wave R-X mode and Fig 4.13 is for the slow wave L-O mode. For these two figures $n_{ew}/n_t = 1$. These figures show that the pure whistler wave (R-X mode, $\theta_k = 0$) has the highest growth rates. Therefore, the pure whistler wave will be considered for calculations below. It is recalled that Section 3.2.1 concluded that fast wave instabilities are not observed in Constance B; fast waves will therefore not be considered here. The theory predicts the existence of fast wave instabilities, however their growth rates are typically an order of magnitude less than the maximum whistler wave growth rates.

Figures 4.14 to 4.22 give the results of relativistic (and some corresponding nonrelativistic) whistler wave growth rate calculations using the ECRH distribution, together with a cold stabilizing Maxwellian, for different choices of the density, temperature, and midplane cyclotron frequencies. Each figure contains a plot of $f_{i,max}$ and the corresponding $f_{r,max}$, $f_{c,max}$, $k_{r,max}$, and $k_{i,max}$ as a function of one parameter, while the others are held constant. $f_{i,max}$ is the maximum growth rate to occur in a contour plot like the one shown in Fig. 4.8 and the other four quantities are the corresponding values of wave frequency, local cyclotron frequency, real $\mathbf{k}$, and imaginary $|\mathbf{k}|$ respectively. $f_{i,max}$ is therefore the maximum growth rate to occur
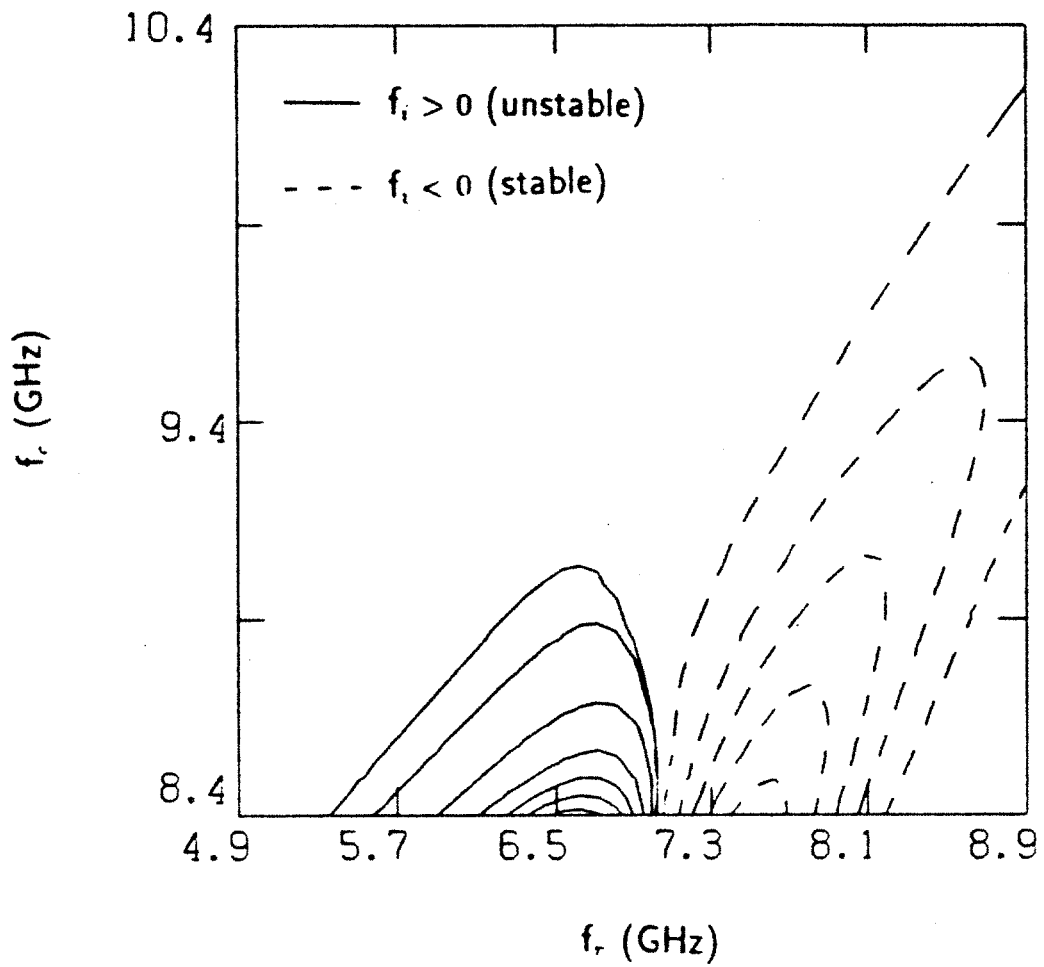
Figure 4.10: Contours of f_i for the BMLC distribution. Relativistic calculation with $k_- = 0$. $T_- = 2.5$ keV. $T_i = 0.5$ keV. m=2. $f_{i.max} = 0.03$ nsec^{-1}.
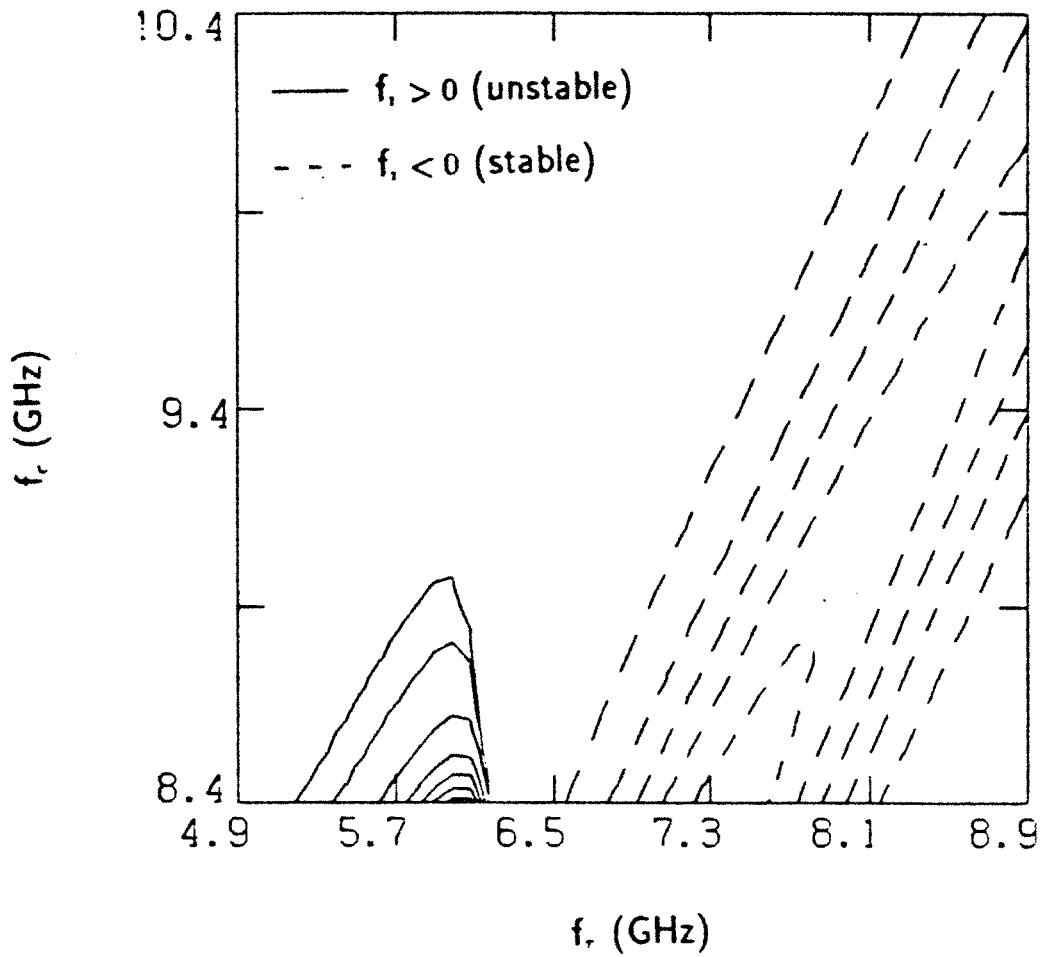
Figure 4.11: Contours of f_i for the bi-Maxwellian distribution. Relativistic calculation with $k_\perp = 0$. $T_\perp = 2.5$ keV, $T_i = 0.5$ keV, $f_{i,max} = 0.01$ nsec^{-1}.

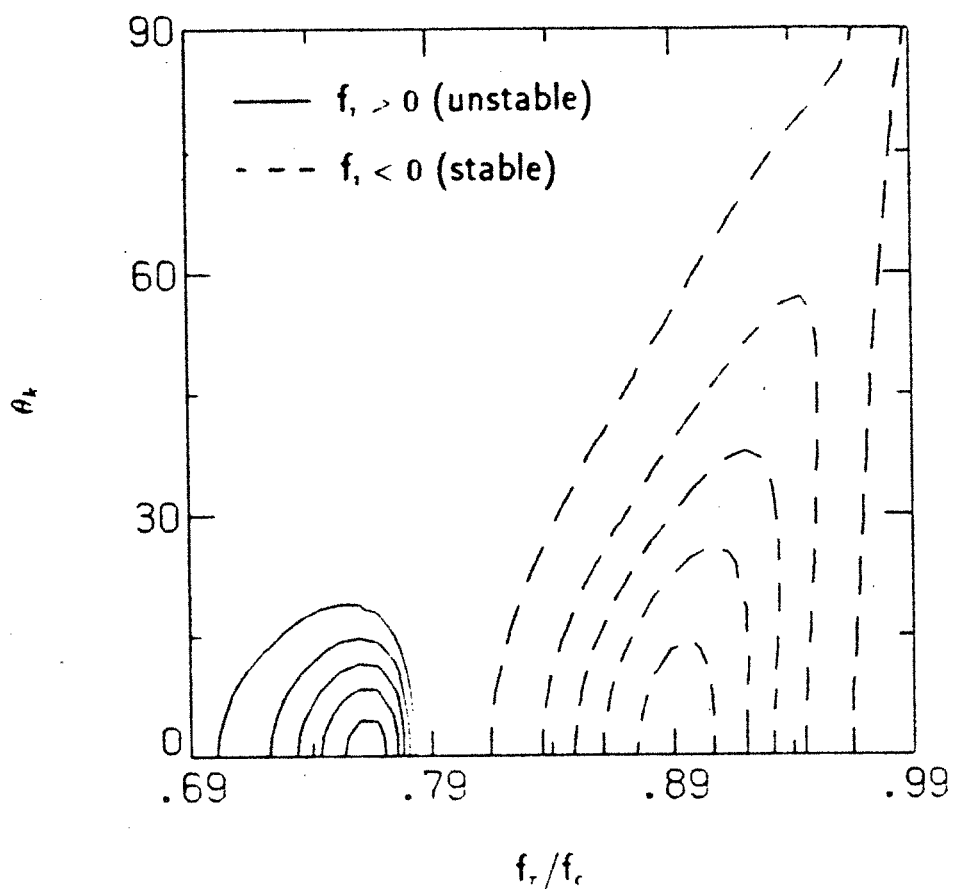Figure 4.12: Contours of f_i as a function of wave frequency and θ_k. R-X branch. $f_{i,max} = 0.06$ nsec^{-1}.
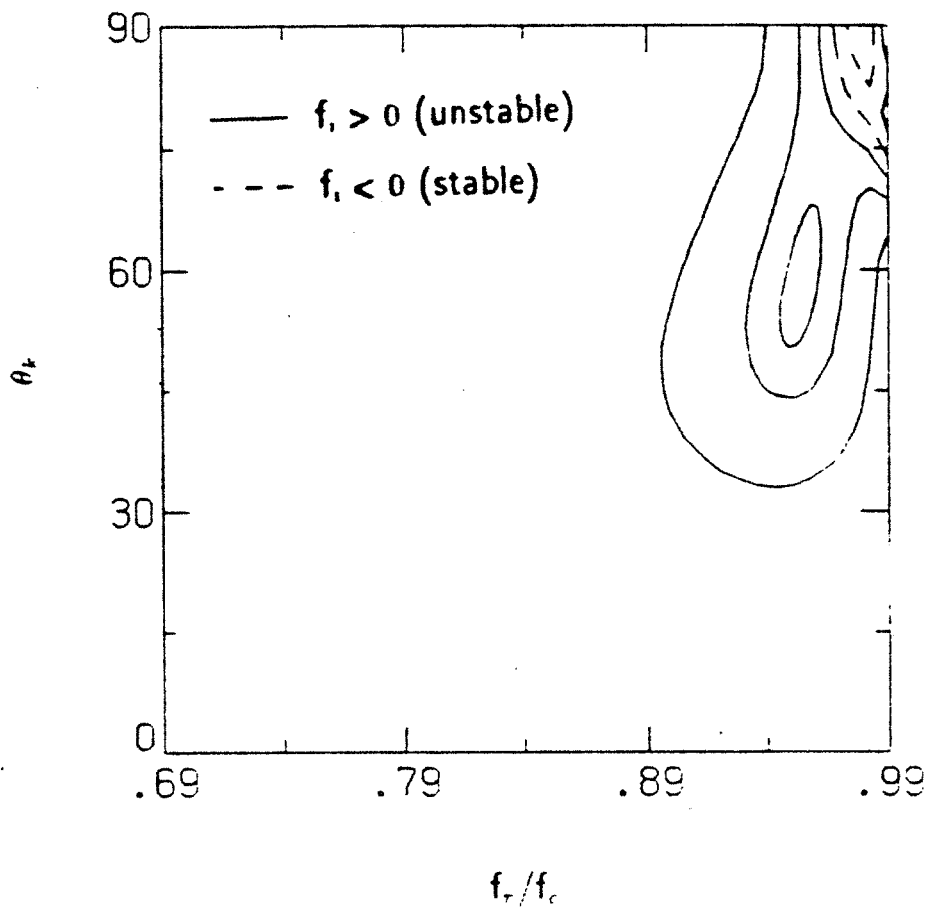
Figure 4.13: Contours of f_i as a function of wave frequency and θ_k. L-O branch. $f_{i,max} = 0.01$ nsec^{-1}.

along a single field line for a given set of parameters. Unless specified otherwise, the constant parameters have the standard values as given in Fig. 4.8. The plots of $f_{r,max}$ in addition show the real frequencies corresponding to growth rates that are half of the maximum growth rate. These plots indicate the frequency range of the most unstable waves for the particular parameters.

4.6.2 Results: BMLC Distribution

Figure 4.23 shows a plot of the contours of f_i as a function of the local cyclotron frequency and the wave frequency in a relativistic and nonrelativistic calculation using the BMLC distribution with temperature parameters chosen to model the hot electron component of Constance B and with $k_\perp = 0$. Figure 4.24 shows a plot of $f_{i,max}$ and the corresponding $f_{r,max}$, $f_{c,max}$, $k_{r,max}$, and $k_{i,max}$ as a function of $T_\perp$, holding $T_\perp / T_\parallel$ constant. For the high temperatures characteristic of the hot electron component the frequencies of the most unstable waves shift to low frequency and the growth rates increase as temperature increases. Thus, the model does not explain the microstability of the hot electrons. Speculations as to why the hot electrons are microstable and why the theoretical model breaks down are made in Section 4.6.3.

Figure 4.25 shows a plot of the contours of f_i as a function of local cyclotron frequency and wave frequency for the three component distribution function made up of the sum of a cold Maxwellian distribution, a warm ECRH distribution, and a hot BMLC distribuion. These contours are simply the sum of the contours of Fig. 4.8 and the contours of Fig. 4.23. This plot is illuminating because it shows that the stabilizing effects of the BMLC distribution at high frequencies (the emission frequencies observed in Constance B in the neighborhood of 8 GHz) are not great enough to stabilize the instabilities of the ECRH distribution at these frequencies. The instability of the BMLC distribution at low frequencies still exists also. Waves with these frequencies are not observed experimentally.

174
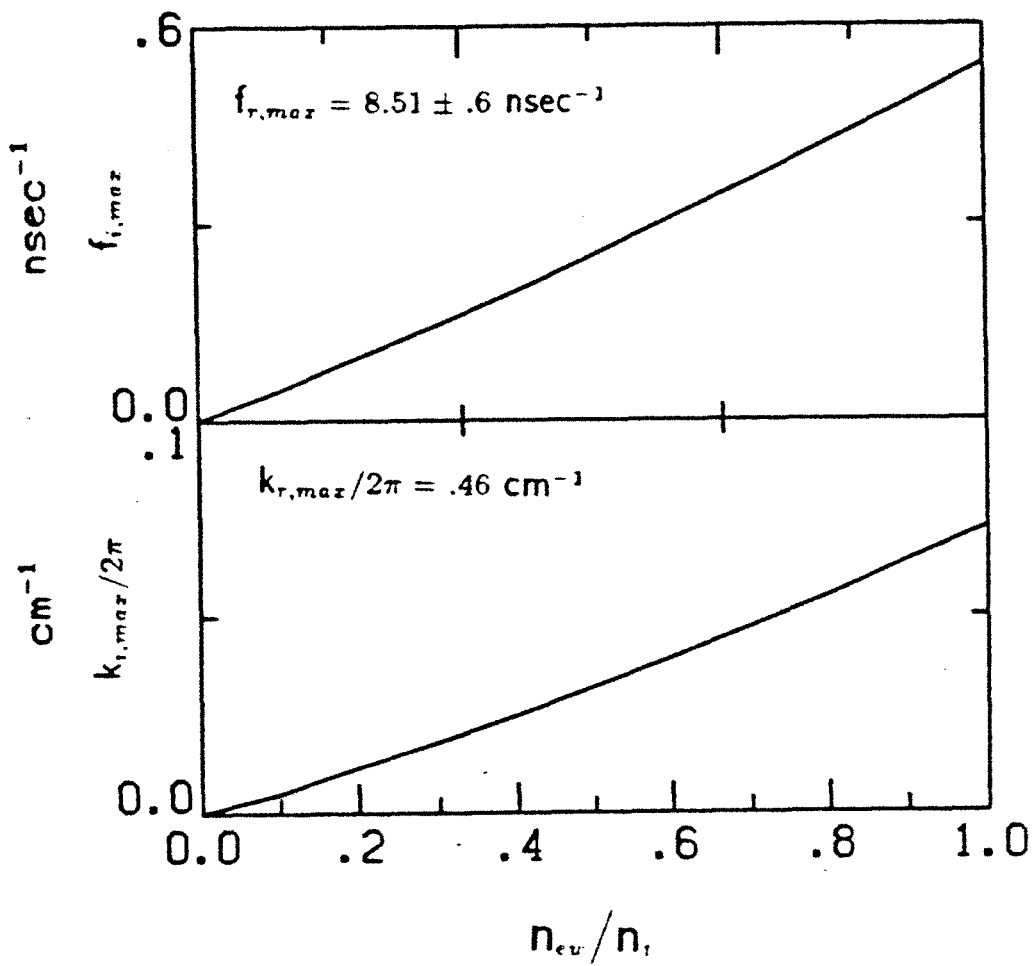
Figure 4.14: $f_{i,max}$ and $k_{i,max}$ as a function of n_{eu}/n_i, holding n_i constant.
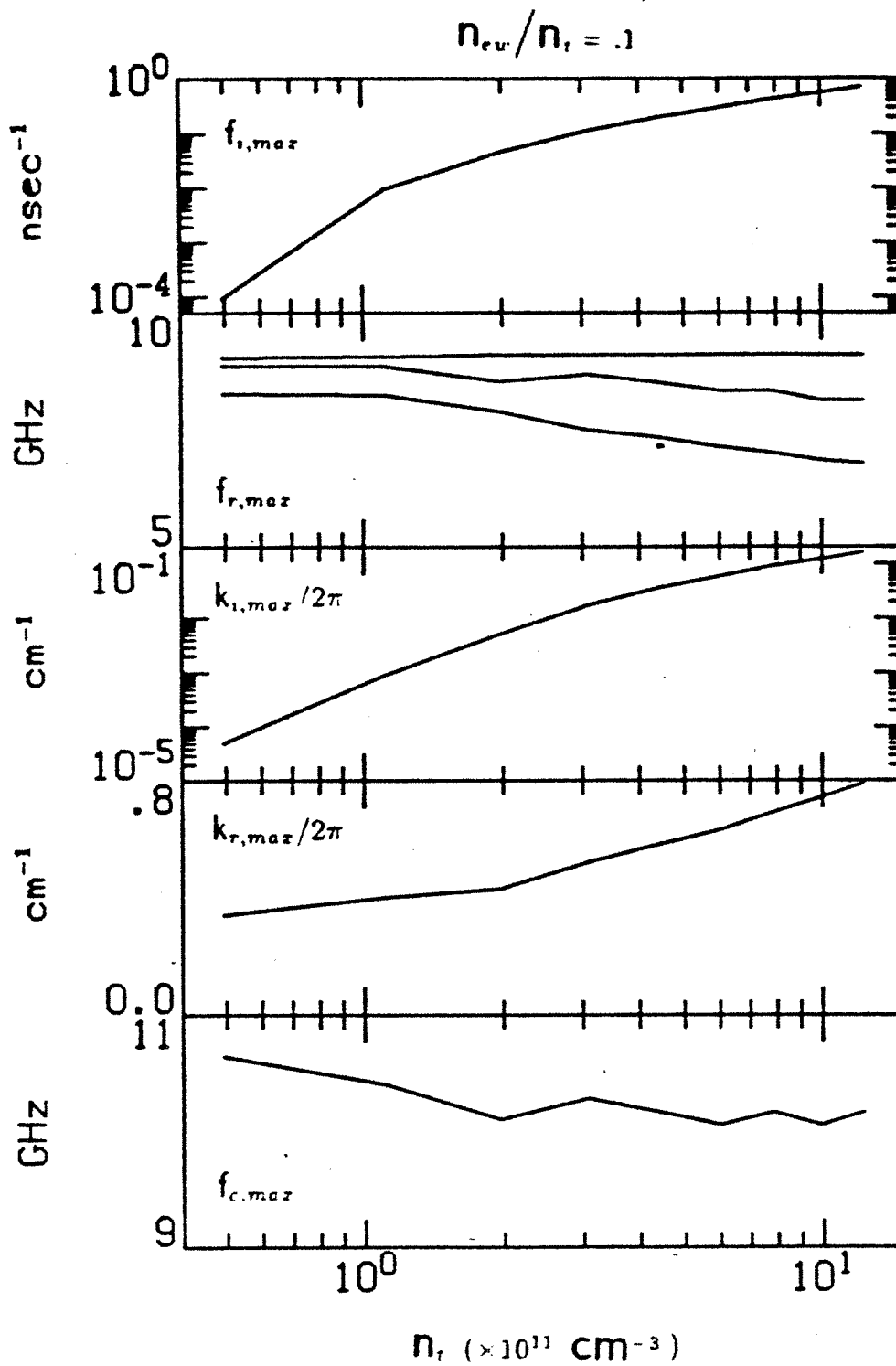
Figure 4.15: $f_{i,max}$, $f_{r,max}$, $k_{i,max}$, $k_{r,max}$ and $f_{c,max}$ as a function of n_e, holding n_{eu}/n_e constant.

Figure 4.16: $f_{i,max}$, $f_{r,max}$, $k_{i,max}$, $k_{r,max}$, and $f_{c,max}$ as a function of T_x, holding T_x/T_{η_+} and T_x/T_{η_-} constant. *Relativistic.*

Figure 4.17: $f_{i,max}$, $f_{r,max}$, $k_{i,max}$, $k_{r,max}$ and $f_{c,max}$ as a function of T_λ, holding T_λ/T_{η_-} and T_λ/T_{η_-} constant. *Nonrelativistic*
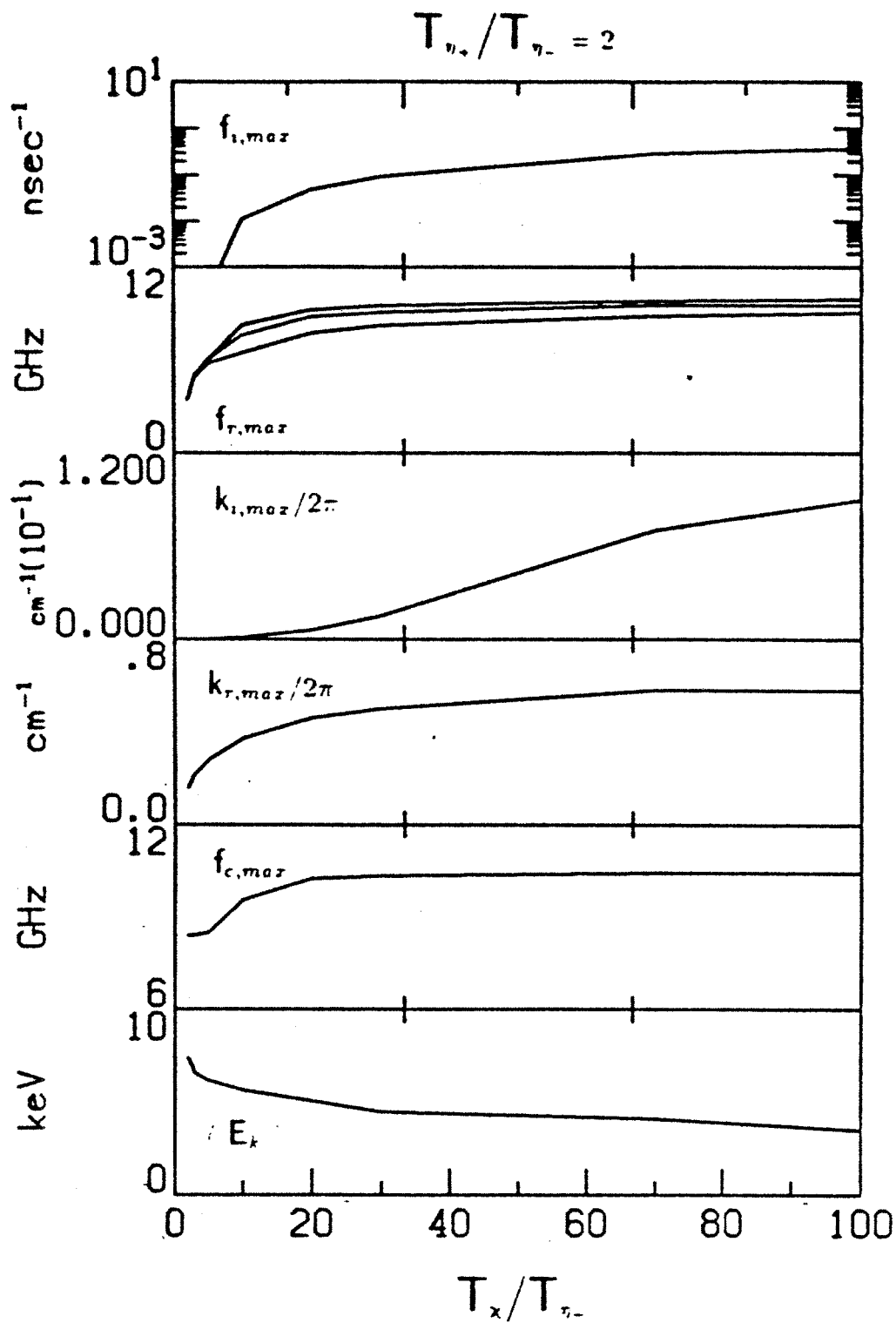
Figure 4.18: $f_{i,max}$, $f_{r,max}$, $k_{i,max}$, $k_{r,max}$, and $f_{c,max}$ as a function of T_λ/T_{η_-}, holding T_λ and T_{η_-}/T_{η_-} constant. *Relativistic.*

Figure 4.19: $f_{i,max}$, $f_{r,max}$, $k_{i,max}$, $k_{r,max}$, and $f_{c,max}$ as a function of T_λ/T_{η_-}, holding T_λ and T_{η_-}/T_{η_-} constant. *Relativistic.*
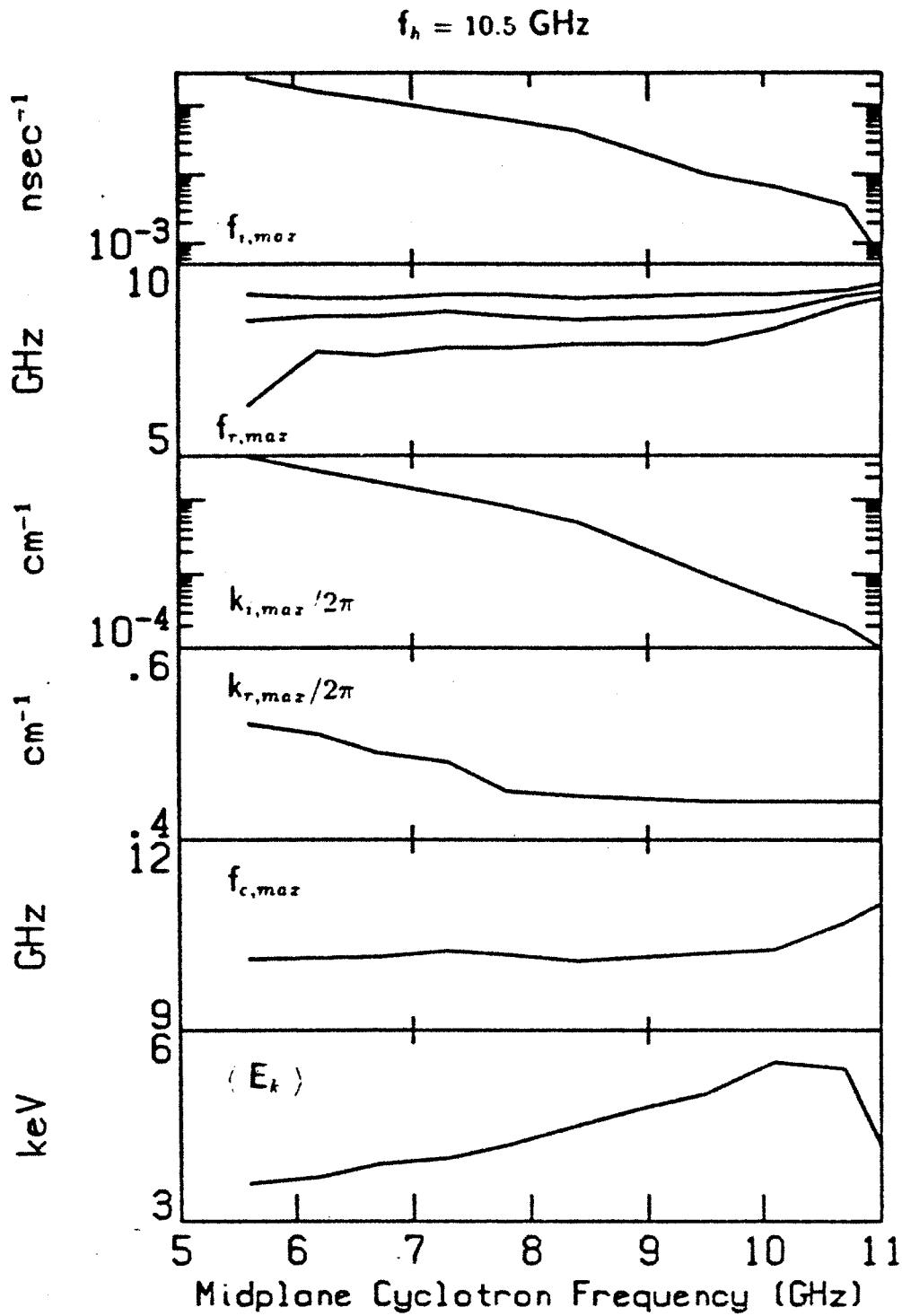
Figure 4.20: $f_{i,max}$, $f_{r,max}$, $k_{i,max}$, $k_{r,max}$ and $f_{c,max}$ as a function of midplane cyclotron frequency f_{co}.
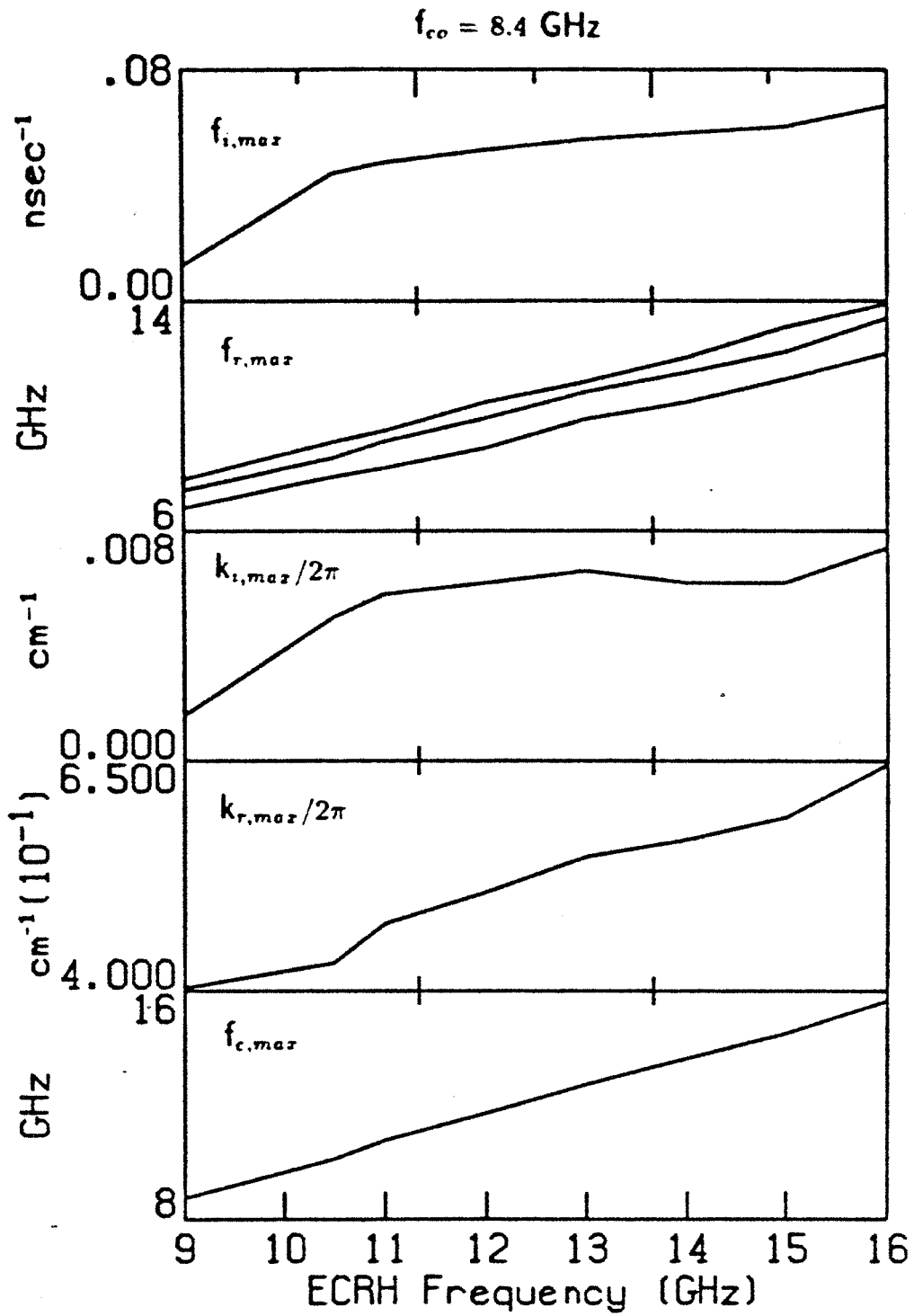
Figure 4.21: $f_{i,max}$, $f_{r,max}$, $k_{i,max}$, $k_{r,max}$, and $f_{c,max}$ as a function of heating frequency f_h, holding midplane cyclotron frequency f_{co} constant.

$$f_h/f_{co} = 1.25$$

Figure 4.22: $f_{i,max}$, $f_{r,max}$, $k_{i,max}$, $k_{r,max}$ and $f_{c,max}$ as a function of heating frequency f_h, holding f_h/f_{co} constant.

Figure 4.23: Contours of f_i for the BMLC distribution with hot electron parameters and for $k_- = 0$. $T_- = 500$ keV. $T = 100$ keV.
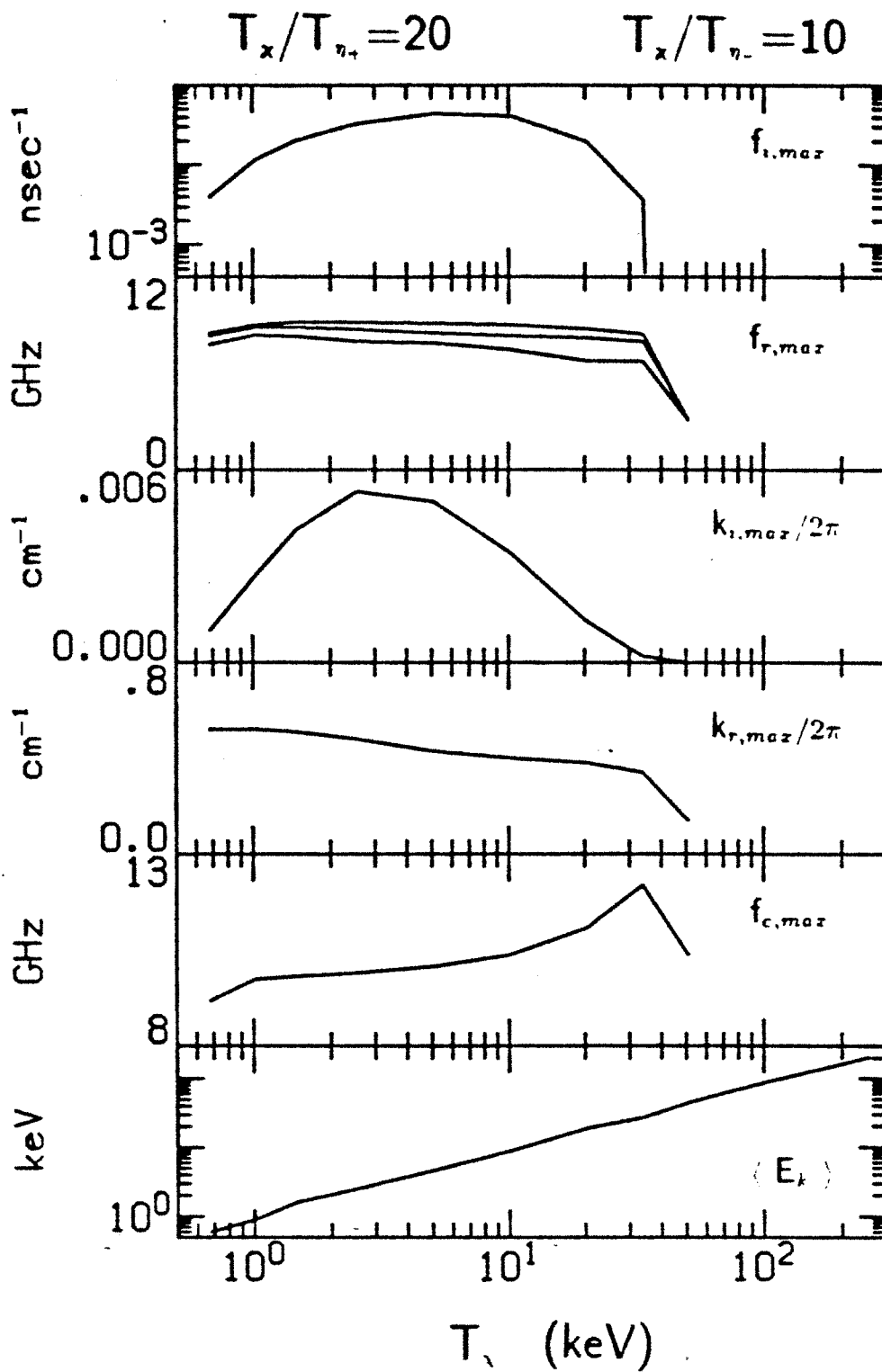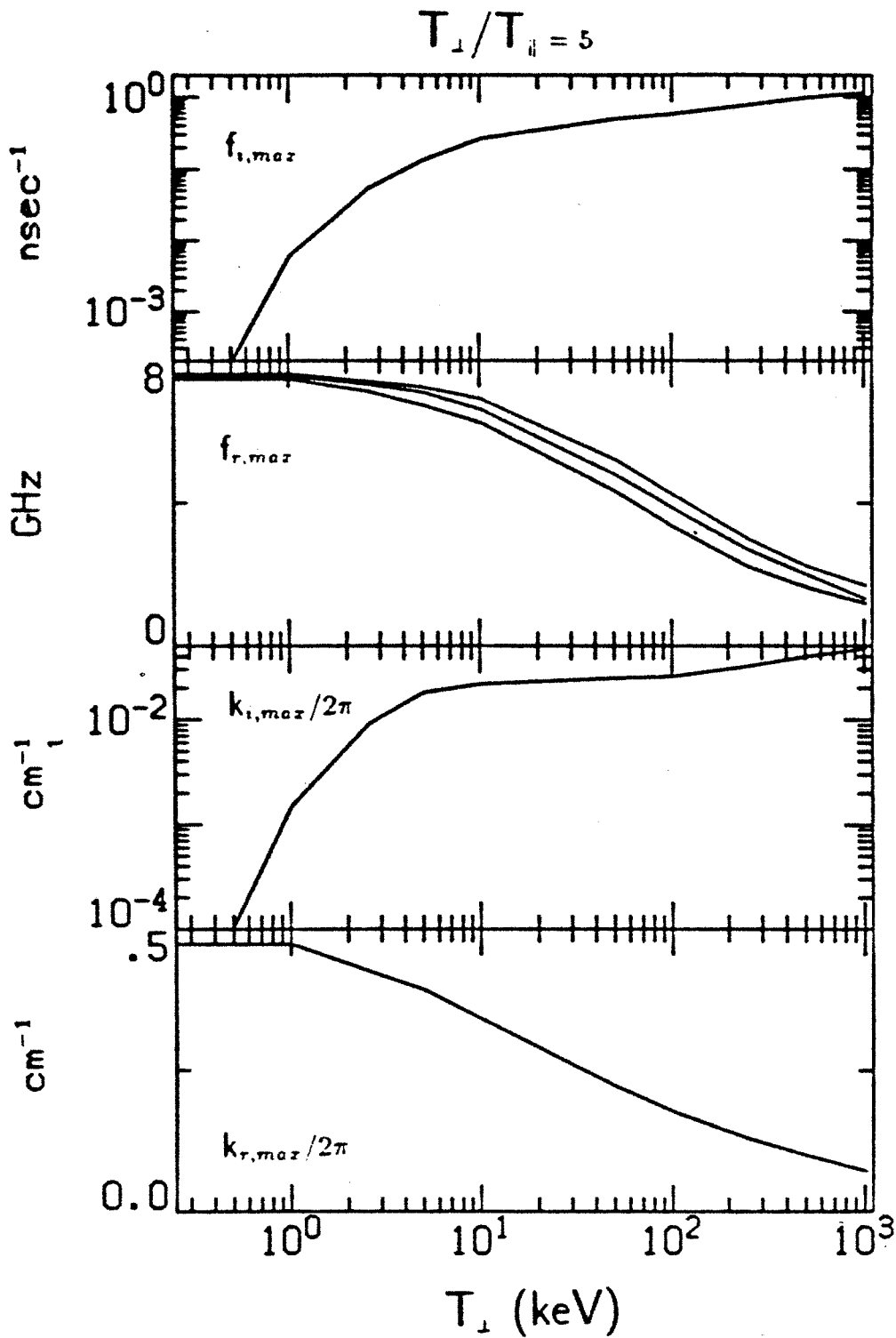
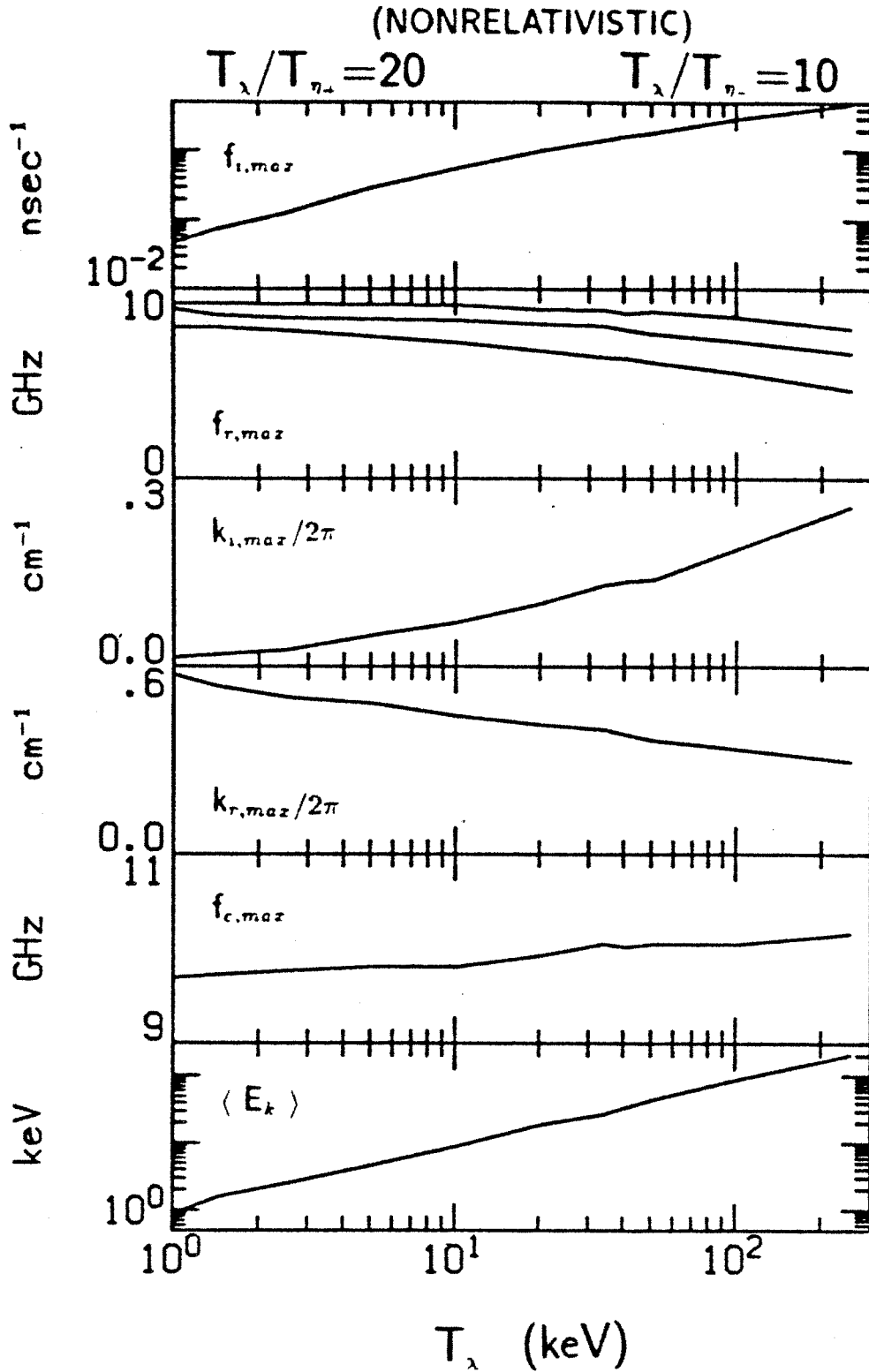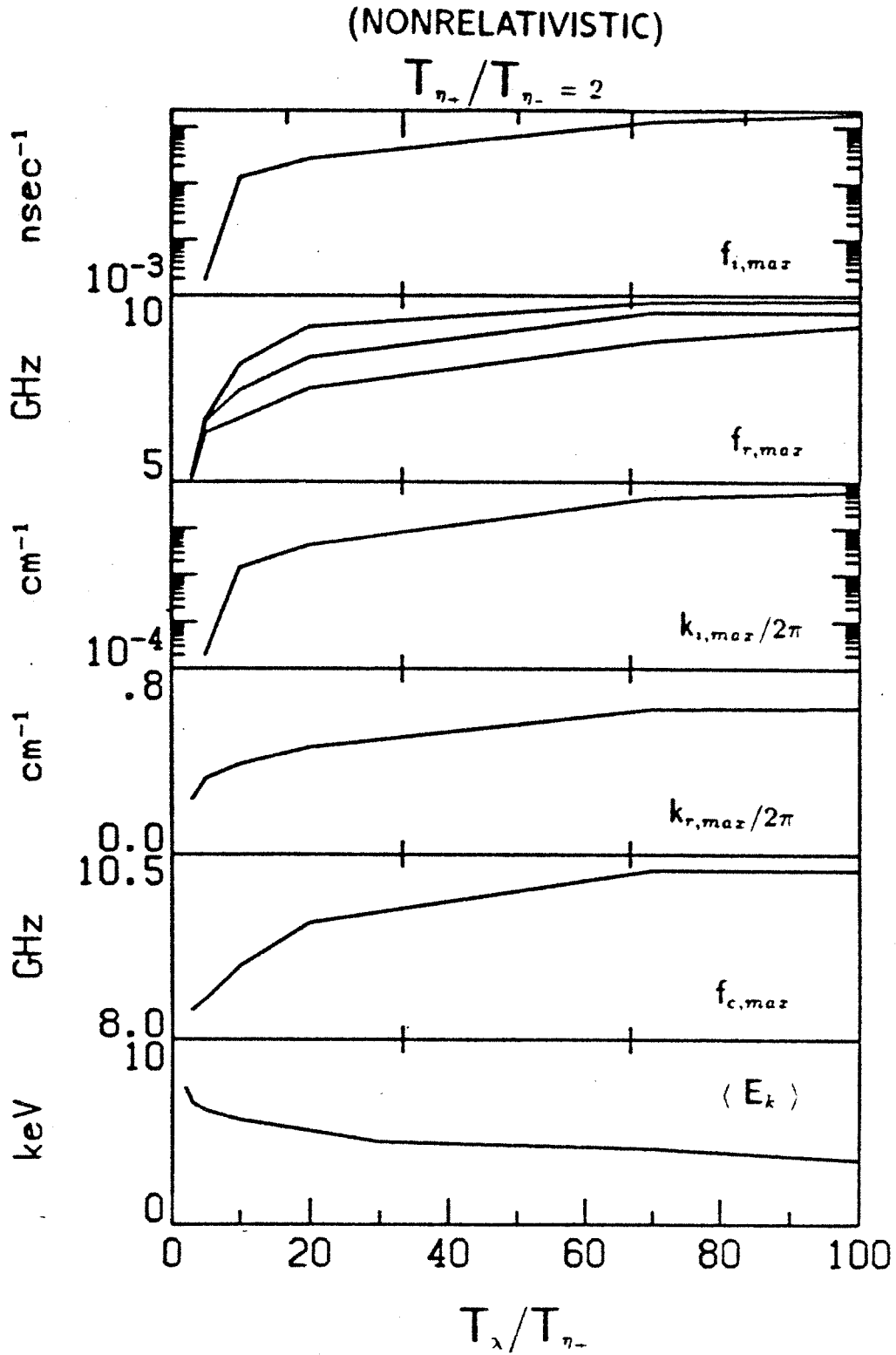Figure 4.24: $f_{i,max}$, $f_{r,max}$, $k_{i,max}$, $k_{r,max}$ and $f_{c,max}$ as a function of T_-, holding T_-/T_i constant, for the BMLC distribution.
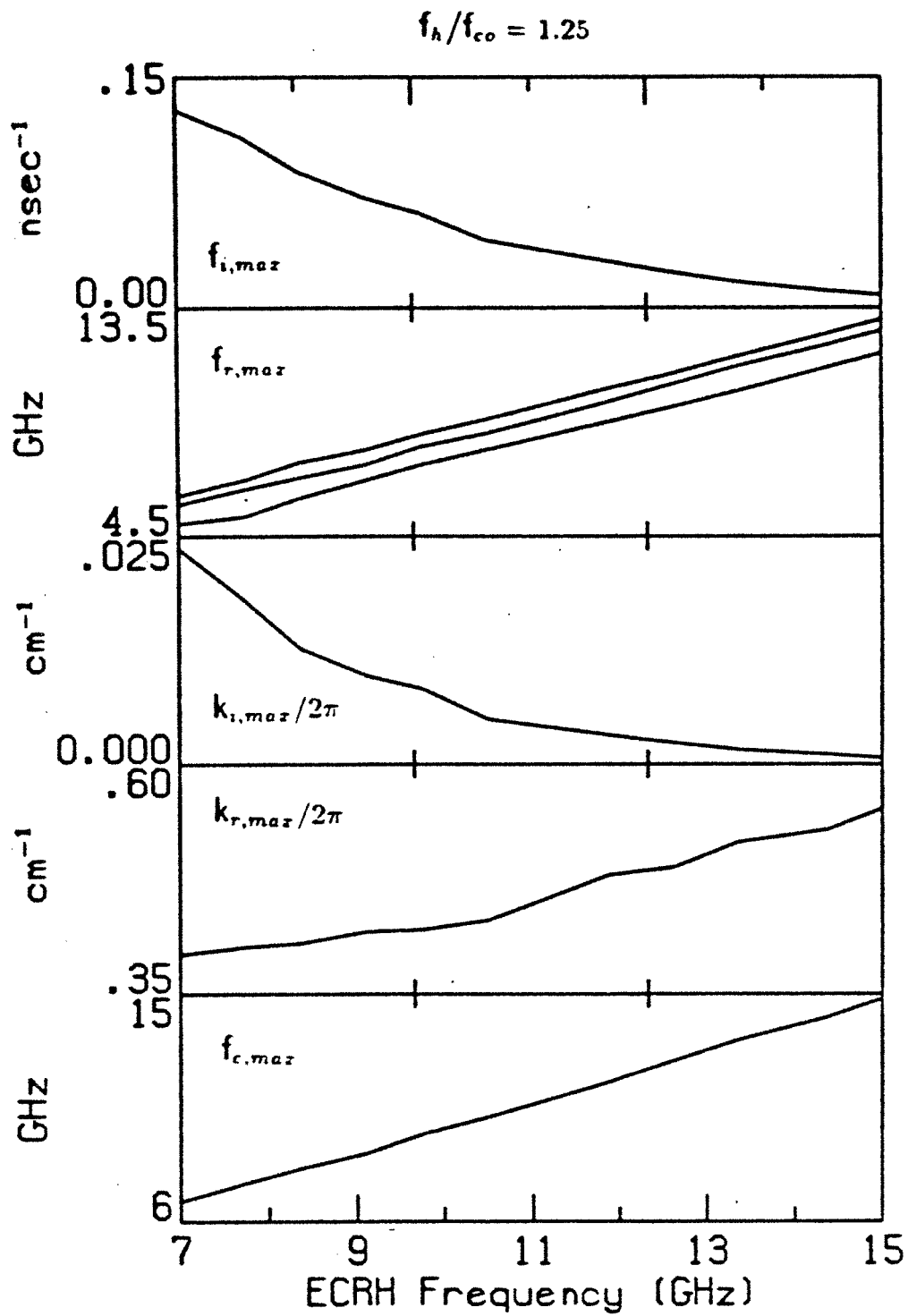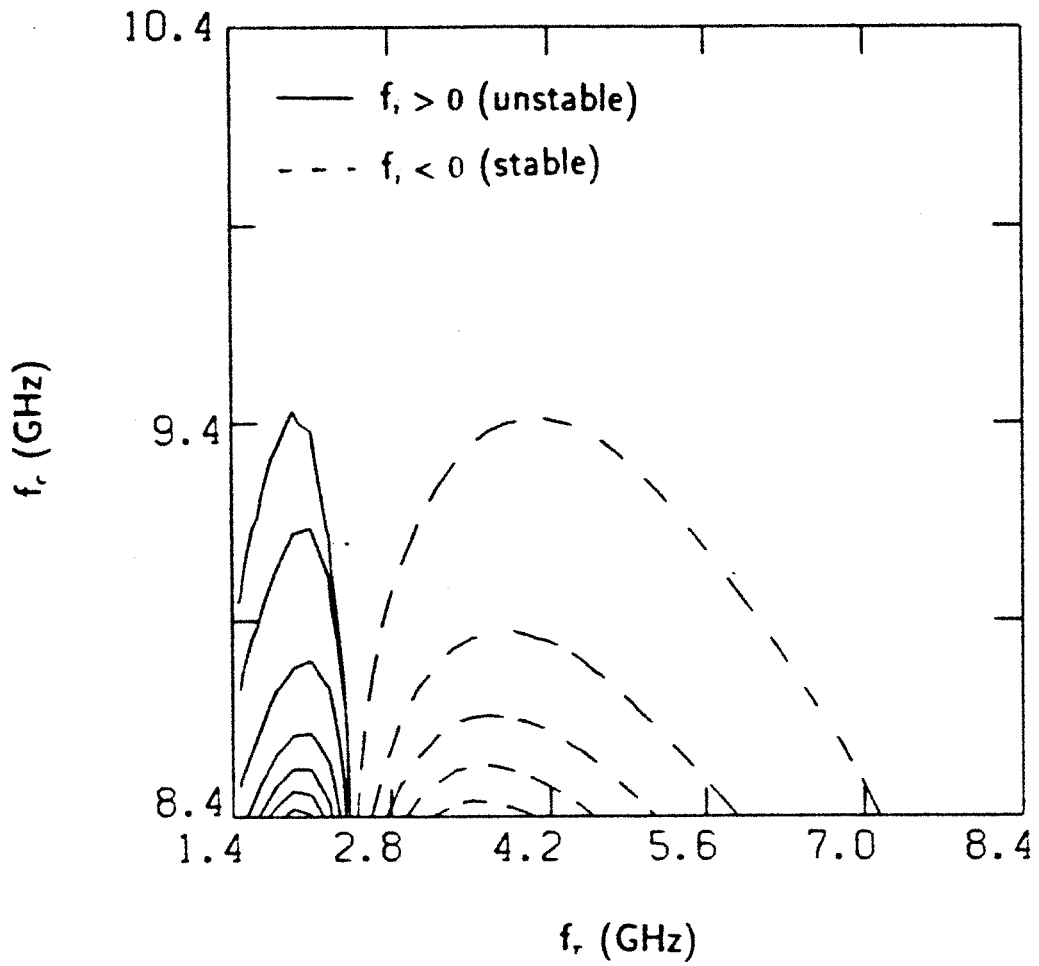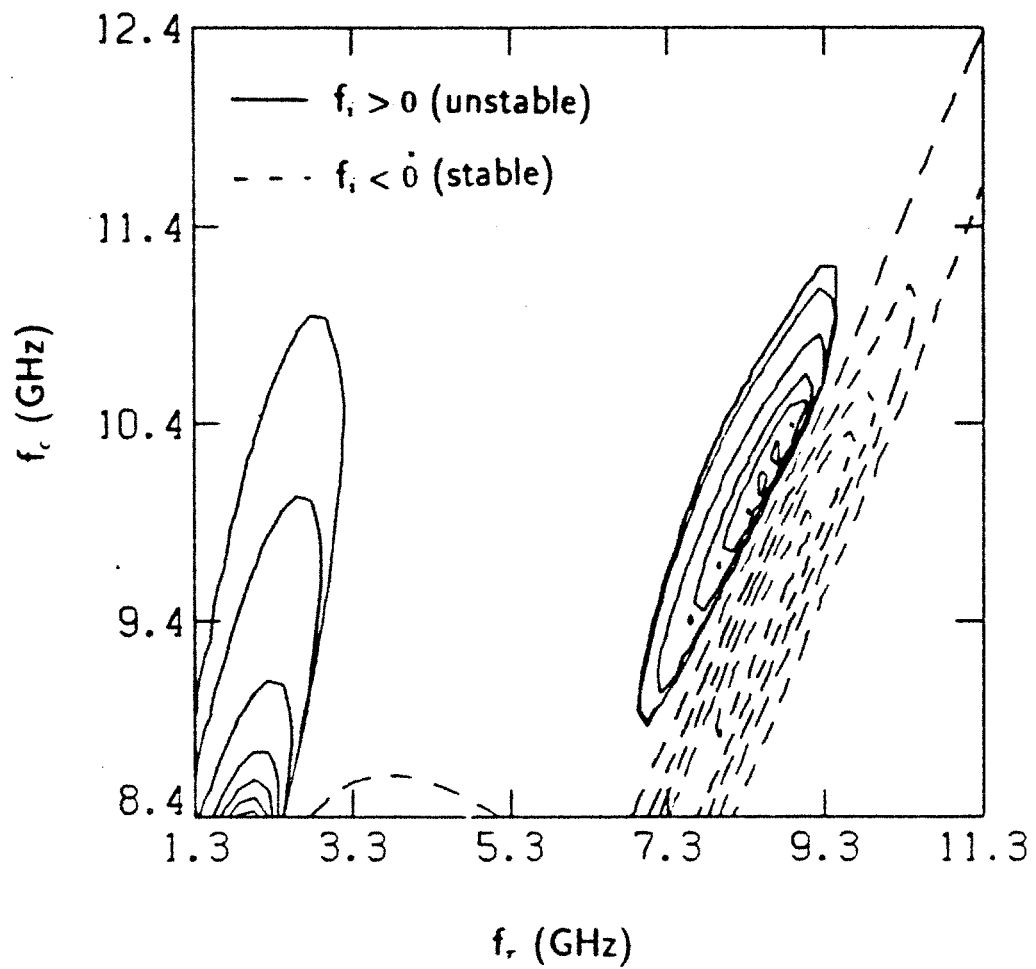
Figure 4.25: Contours of f_i for the three-component distribution function which models Constance B. $n_{ec} : n_{eu} : n_{eh} = 0.5 : 0.1 : 0.4$ and $\omega_p = 4$ nsec^{-1}.

4.6.3 Interpretation of Theoretical Results

Justification of Model

The results of the Section 4.6 justify the assumptions made in Sections 4.1.2 of an infinite, homogeneous plasma and the assumption of $\omega_i \ll \omega_r$ made in Section 4.1.3 A survey of the information plotted in Figs. 4.8 to 4.24 shows this. The calculated wavelengths of the maximally unstable waves are typically less than 1 cm. The length and radius of the approximately ellipsoidal Constance plasma is 30 cm and 10 cm respectively. Since the theoretically predicted waves are whistler waves with $k_\perp = 0$, they travel primarily parallel to the field lines. so that the 30 cm length is the more relevant parameter for comparison. The magnetic field changes by a factor of 1.25 over 15 cm of length at the magnetic well, which gives an average $B/\frac{dB}{dl} = 60$ cm. The density along the magnetic field line for an ECRH distribution function is shown in Fig. 4.7 not to change appreciably within the resonance zone, which is where the theoretically predicted instabilities always occur.

For the infinite and homogeneous medium assumptions to be valid the growth rates must be much greater than the bounce frequency so that an electron does not sample a large portion of space during a growth time. The bounce frequency in a magnetic field approximated by a parabolic well is $f_b = v_{\perp o}/2\pi L$. where $v_{\perp o}$ is the midplane perpendicular velocity and L is the mirror length. chosen here to be 30 cm so that the resonance zone is in the correct location corresponding to Constance B. For a 2 keV particle $f_b = 14$ MHz, which is much less than a typical calculated growth rate. For a 400 kev particle $f_b = 130$ MHz. assuming the perpendicular energy is the total energy. This is only moderately less than the calculated f_i of approximately 0.4 nsec^{-1} for the BMLC distribution.

Warm Electron Microinstability

Chapter 3 described the two types of unstable rf emission observed in the Constance B experiment. The whistler B emission has frequencies in the range of 6.7–8.7 GHz when the magnetic field is 3 kG, although the range does not change too much as the midplane magnetic field is varied (see Fig. 3.4). The whistler C emission has frequencies in a range with a lower bound near the upper bound of the whistler B emission, and an upper bound at the ECRH frequency. This range is also insensitive to changes in magnetic field. The burst rate of the whistler C emission is much higher than the burst rate of the whistler B emission and is continous in many cases. The whistler C emission was found to be associated with plasma located off the axis (6 cm off axis at the midplane for a magnetic field of 3 kG).

The results of calculations using the ECRH distribution identify the whistler B emission and the whistler C emission as whistler instability. The frequencies of the whistler B emission fall in the range of the theoretically predicted, maximally unstable frequencies for almost all choices of the density and temperature parameters, as long as the ECRH frequency is taken as 10.5 GHz. The theoretical frequencies only deviate in extreme parameter regimes which do not model the experiment well anyway. For example, Fig. 4.16 shows that the frequencies deviate for values of T_χ above approximately 50 keV, which is much greater than the 2 keV average endloss temperature of the warm electrons. (For the parameters chosen in Fig. 4.16 the average particle energy is $1.05T_\chi$.) As another example, Fig. 4.20 shows that the frequencies deviate when the midplane magnetic field is greater than the ECRH frequency (because the ECRH distribution becomes a bi-Maxwellian). A plasma cannot be produced in such a situation.

The whistler C emission is identified as whistler instability and exists at higher frequencies than the whistler because of higher total density of the off-axis plasma. The frequencies of the whistler C emission fall in a range of frequencies which are theoretically predicted to be whistler unstable, although their growth rates are

usually less than half of the maximum unstable growth rates.[9] However, Fig. 4.15 shows that the maximum growth rates increase as total density increases. If an unstable wave is to be emitted from the plasma (before it is absorbed by other portions of the plasma) it must have a growth rate greater than some threshold value. But that threshold will occur at higher frequencies for higher total density because the overall level of the f_i contours is then higher. The whistler C emission is associated with off-axis field lines where the density is believed to be higher (than field lines closer to the axis, because the density profile has been measured to be hollow). The higher density makes it possible for the higher frequencies corresponding to the whistler C emission to be emitted, and they come out with a higher burst rate because the heating rate on these field lines is greater. The lower frequencies, corresponding to the whistler B emission, should also be emitted at these higher densities.

4.6.4 Speculations on the microstability of the Hot Electrons

The possible explanations for why the hot electrons are microinstable fall into two categories: those that described within the context of the theory presented in this chapter and those that require a different theory or at least less stringent assumptions than were made in deriving the present theory. Both types of explanations are presented below.

Assuming the theory to be valid for the hot electrons two speculations are made, within the context of the theory, which may explain the stability of the hot electrons: 1) The theory predicts that the most unstable waves for the hot electrons, as modelled by the BMLC distribution, occur at the midplane. For the warm electrons they occur up the magnetic well relatively far from the midplane (see Fig. 4.8 for the ECRH distribution and Fig.4.23 for the BMLC distribution). Therefore, the

---

[9]As shown in Fig. 4.15, the exception to this is for low total densities of $\lesssim 5 \times 10^{10}$ cm^{-3}, which is too low to be believed for Constance B. In addition, the growth rates become very small for these densities.

unstable, low frequency, waves corresponding to the hot electrons may require much higher growth rates to escape from the plasma.

2) The hot electron distribution function may actually be more like a high temperature ECRH distribution function instead of a BMLC distribution function. This might be the case if superadiabaticity of the hot electrons does not set in as discussed in Section 4.5. This might occur if the stochastic regime actually covers a wider region of velocity space due to the existence of a broad k spectrum of the ECRH waves, or due to two frequency heating (fundamental and first harmonic due to the relativistic shift of the resonance). At high temperatures Fig. 4.16 shows that the growth rates for the ECRH distribution are reduced drastically, and complete stabilization occurs at $T_\chi \approx 400$ keV (the average particle energy is $1.05T_\chi$ for parameters chosen there). Of course, the axial x-ray measurements were the motivation for the choice of the BMLC distribution for the hot electrons; the ECRH distribution predicts an axial x-ray spectrum that is significantly different from the experimentally measured one. Therefore, the assumption that the hot electrons be modelled with the ECRH distribution would imply that the axial x-ray measurements or interpretation are wrong.

The assumption which lead to the use of the cold plasma dispersion relation to calculate the modes is severely violated. The infinite and homogeneous assumptions is moderately violated (or moderately not violated, depending on your point of view) due to the relatively high hot electron bounce frequencies:

1) The underlying assumption that lead to the use of the cold plasma dispersion relation was that the cold electrons contribute the most to the total density. The hot electrons contribute approximately half of the total line density, as determined by the interferometer. Therefore, the modes may be altered significantly if the correct Hermitian part of the dispersion tensor had been used. Of course, this would also alter the results of the warm electron calculations, which work out so well that it is difficult to disregard them.

2) The assumptions of an infinite and homogeneous medium may be violated because of the relatively high bounce frequencies of the hot electrons. As indicated in the last section, a 400 keV electron has a bounce frequency f_b of 130 Mhz. This is to be compared to a calculated maximum growth rate of 0.4 nsec^{-1} using the BMLC distribution (see Fig. 4.23). Put another way, in the 0.4 nsec^{-1} that it takes a wave to grow by a factor of e, a particle makes approximately one half of a bounce, which means it traverses the length of the mirror. The infinite theory predicts that the growth rates decrease by more than a factor of 10 between the midplane and the ECRH resonance zone. Therefore, a bounce-averaged theory, or some other theory which includes information of the inhomogeneities along the field line, may predict much lower growth rates than the present theory.

Chapter 5

Conclusions

5.1 Summary of Results

1) Unstable rf emission is observed in the Constance B plasma and is identified as whistler instability. The rf emission has both a bursting behavior (whistler B emission) and a continuous behavior (whistler C emission). The instability is identified by dispersion relation calculations in conjunction with the experimentally measured frequency spectrum for different magnetic fields. The dispersion relation calculations use a new distribution function (the ECRH distribution) that models a population of ECRH electrons confined in a magnetic mirror. The ECRH distribution agrees with experiment much better than previously used distribution functions.

2) The whistler B emission has frequencies in the range of approximately 6.7–8.7 GHz for a midplane magnetic field of 3 kG. The range is fairly insensitive to changes in the magnetic field. The whistler C emission has frequencies in a range which has a lower bound at approximately the upper bound of the whistler B emission, and an upper bound at the ECRH frequency. Correlating the electron endloss current at different radii with the two types of rf emission shows that the whistler C emission is associated with off-axis field lines and the whistler B emission is associated with all field lines (within a radius at the midplane of approximately 6 cm when the midplane magnetic field is 3 kG, or when the resonance zone is at a radius of 10 cm). The whistler C emission has higher frequencies because of the higher densities

of the outer field lines. The theory predicts higher overall growth rates with higher densities for both the whistler C frequencies and the whistler B frequencies. The whistler C emission burst rate is much greater than the whistler B emission burst rate because the heating rates increase for increasing radial distance from the axis (within the resonance zone). This is due to the decrease in gradients of the magnetic field at the resonance zone, or an increase in the effective time a particle spends in resonance.

3) The whistler instability is driven by a warm electron component which has an average energy of approximately of 2 keV. The 400 keV hot electron component is microstable. The infinite, homogeneous, linear theory describes the microinstability of the warm electrons well, using the ECRH distribution as a model. The theory is only moderately valid for the hot electrons. The high bounce frequencies associated with hot electrons ($\sim$ 100 MHz) are near the predicted wave growth rates ($\sim$ 800 MHz) which leads to a violation of the assumptions of an infinite and homogeneous medium. Speculations as to the reasons for the microinstability of the hot electrons can be made if it is assumed that the theory is valid. For example, if the ECRH distribution were an accurate model for the hot electron component then the theory would predict stability since this distribution is stable for temperatures above a few hundred keV (if a relativistic forumlation is used).

4) Microinstability degrades particle confinement significantly with respect to the classically expected particle confinement calculated on the basis of collisions. The warm electrons drive the microinstability by diffusing in velocity space in response to a wave. More energy is lost in the process than is gained, and the result is an unstable wave. Some of the warm electrons diffuse into the loss cone and leave the plasma. The warm component particle loss rate is at least 10 times greater than the classical loss rate when the instability is at its maximum intensity (determined by the power of unstable rf emission).

When an unstable wave is present due to the warm electrons, it interacts with the hot electrons by causing them to diffuse in velocity space. Since these particles

are by themselves microstable, there is a net transfer of energy from the wave to the hot electrons (i.e. the unstable waves heat the hot electrons). However, the hot electrons which diffuse down in energy have a chance to move into the loss cone and carry all of their energy out of the plasma, thus amplifying the overall particle and power loss due to microinstability. The hot electron component loss rate due to microinstability is 25–50 times greater than the classical loss rate.[1]

5) The total power loss due to microinstability is in the form of rf emission and induced particle endloss. The power loss is a function of the machine operating condition and the maximum is approximately 10% of the ECRH input power (just considering the loss due rf emission and warm electron endloss). This maximum does not occur for those parameters which provide maximum plasma diamagnetism. The maximum power loss due to microinstability induced hot electron endloss is approximately 180 Watts when the ECRH power is 2 kW. This maximum occurs for the same pressure as the maximum in diamagnetism and ECRH induced hot electron endloss. This is not the same pressure at which the unstable rf emission is maximum.

5.2   Implications for Tandem Mirrors

The primary purpose of the Constance B experiment is to study the physics issues relevant to the endplugs of tandem mirrors. The particle and power balance issues of electron microinstability are perhaps most critical with respect to the creation of thermal barriers in these endplugs.

The original tandem mirror scheme of operation was called Boltzmann operaton (Kesner *et al.*, 1983), in which a single-temperature electron species exists throughout the tandem mirror, and the plug potential, needed for electrostatically confining the central cell ions, is created by producing higher endplug densities. In such an operating mode the potential throughout the entire machine obeys a Boltzmann

---

[1]The major loss mechanism for the hot electrons for certain conditions is diffusion into the loss cone due to ECRH waves (Hokin *et al.*, 1986).

law, whereby the potential difference between the the central cell and the endplugs is a logarithmic function of the density ratio between the two regimes. This logarithmic dependence for Boltzmann operation makes it necessary to achieve very high densities for only moderate plug potentials. This, of course, affects the overall feasibility of a tandem mirror as a useful reactor.

In the current scheme a thermal barrier is created in each endplug. A thermal barrier is a potential depression which thermally isolates the cooler electrons of the central cell from the hotter electrons of the endplugs. A plug potential is then created through the combination of sloshing ions from injected neutral beams and off-midplane ECRH. In such an operating mode high plug to central cell potential differences can be achieved with much lower endplug densities than in the Boltzmann operation.

A thermal barrier is created by ECRH at the midplane of the mirror plasma of the endplug. This creates a population of hot electrons which causes a potential depression at the midplane—i.e. the thermal barrier. The electron microinstability of an ECRH, mirror-confined plasma is therefore an important issue to consider for the creation of a thermal barrier.[2] In particular, it is useful to know how microinstability affects the particle loss rate of the hot electrons, since this determines the hot electron density which, in turn, determines the the extent of the potential depression. If a particular mechanism such as microinstability causes an increase in the loss rate by some factor over the classical loss rate then the steady state density would be higher by that same factor if that mechanism were not present, and with all other mechanisms the same.[3] It has been shown directly (i.e. with no derived quantities based on theory) that the hot electron loss rate due to microinstability is

---

[2] Electron microinstability has been observed in the endplug of the TMX-U tandem mirror (James et al., 1984).

[3] If microinstability were somehow prevented from occuring it is possible that some other nonclassical loss mechanism would cause an additional amount of loss so that the loss rate, and hence the density, were the same as for the situation in which microinstability were present. It is not known whether this would happen in the present case.

approximately 1/3 of the loss rate due to ECRH. Both of these processes together are 100 times the collisional loss rate.

The power loss due to microinstability is also an important issue since the majority of the power input to a tandem mirror is the microwave heating power in the endplugs. The power loss due to microinstabitity induced hot electron endloss has shown to be approximately 10% of the ECRH input power (a low estimate to within a factor of 2).

Although the numbers may be different, the results here would seem to apply to the endplugs of such tandem mirrors as TMX-U and MFTF-B, both of which employ minimum-B endplug configurations similar to the Constance B experiment. The minimum-B aspect of the field is not a critical issue for the existence of microinstability and therefore the axisymmetric endplugs of the Tara tandem mirror is expected to be microunstable as well.

5.3   Suggestions for Future Work

Several questions remain unanswered:

1) Why are the hot electrons microstable? This is a critical issue to resolve in connecting the work of this thesis to other mirror devices, such as the endplugs of tandem mirrors. It is not known if the different plasma parameters of different devices also leads to the microstability of hot electrons. Theoretical work must be done in order to answer this question. It might involve alteration of the theory presented in this thesis to include effects of the inhomogeneity of the plasma, or it might involve consideration of an entirely different physical mechanism.

2) What is the warm electron density? The answer to this question will lead to a knowledge of the enhancement of the warm electron loss rate due to microinstability with respect to the classical loss rate. In this thesis only a lower limit of this enhancement has been detemined. An answer to this question will also show a direct connection between the microinstability and the warm electron component.

In this thesis an indirect connection was made by showing that the hot electrons do not drive microinstability. Additional x-ray measurements with a detector better suited for low energies (< 2 keV regime) must be performed to answer this question. 3) What is the total power loss due microinstability induced hot electron endloss? This is a critical issue for understanding the power and particle balance of Constance B-like devices since it probably respresents a significant portion of the losses. The production of a thermal barrier is directly related to this issue. More detailed scintillator probe measurements (e.g. radial measurements) of the hot electron endloss is needed to answer this question. Also, another diagnostic to directly measure hot electron endloss current would be useful as a reference point for the scintillator probe.

4) How are the theoretical results changed with the use of the correct Hermitian part of the dispersion tensor? The success of the theoretical analysis of this thesis is due to the choice of the ECRH distribution to model the warm electrons. The major limitations of the model are due to the use of the cold electron dispersion relation to determine the modes. This is a fairly good approximation since the density of the warm electrons is much less than the density of the cold electrons although the question remains as to how good of an approimation it is. The presence of a significant fraction of hot electrons also affects the plasma modes that exist.

5) What is the saturation mechanism of the instability and what about the bursting? The theory of Bespalov (1982), discussed briefly in Chapter 1 on page 20 relates the particle source function to the saturation and bursting mechanism of the whistler instability. For an ECRH plasma the ultimate driving source of the whistler is the ECRH. which affects the source function. An extension to Bespalov's work should therefore include ECRH diffusion. This would turn the one dimensional theory into a two dimensional theory since the ECRH diffusion and the whistler diffusion have different sets of diffusion paths.

Bibliography

[1] Baldwin D. E., Bernstein I. B. and Weenink M. P. H. (1969), *Advances in Plasma Physics, Vol 3.*, edited by W. B. Thompson and A. Simon, Wiley, New York.

[2] Bers A. (1972) *Plasma Physics–Les Houches 1972*, Gordon and Breach Science Publishers, New York.

[3] Bers A. and Ram A. K. (1982) "Relativistic Pulse Shape of Absolute and Convective Instabilities," *Bulletin of the American Physical Society* **28**, 919.

[4] Bers A., Ram A. K. and Francis G. E. (1983) "Relativistic Stability Analysis–Electromagnetic Waves Across a Magnetic Field," *Bulletin of the American Physical Society* **28**, 1158.

[5] Bespalov P. A. (1982) "Self–Excitation of Periodic Cyclotron Instability Regimes in a Plasma Magnetic Trap," *Physica Scripta* **12**, 576.

[6] Blanken R. A. and Lazar N. H. (1971) "Low Density Cyclotron Instability in a Two–Component Electron Plasma," *Phys. Fluids* **13**, 2752.

[7] Booske J. H., Getty W. D., Gilgenbach R. M. and Jong R. A. (1985) "Experiments on Whistler Mode Electron–Cyclotron Resonance Plasma Startup and Heating in an Axisymmetric Magnetic Mirror," *Phys. Fluids* **28**, 3116.

[8] Calvert W. (1971) "The Signature of Auroral Kilometric Radiation on Isis 1 Ionograms," *Journal of Geophysical Research* **86**, 76.

[9] Chen F. F. (1971) *Introduction to Plasma Physics*, Plenum Press, New York.

[10] Chen X. (1986) "Hollow Baseball-Seam Hot-Electron Plasma Equilibrium in the Constance B Mirror Experiment," *Bulletin of the American Physical Society*, to be published.

[11] Chu K. R. and Hirshfield J. L. (1978) "Comparative Study of the Axial and Azimuthal Bunching Mechanisms in Electromagnetic Cyclotron Instabilities," *Phys. Fluids* **21**, 461.

[12] Cohen R. H., Resnick M. E., Cutler T. A. and Mirin A. A. (1978) "Collisional Loss of Electrostatically Confined Species in a Magnetic Mirror," *Nuclear Fusion* **18**, 1229.

[13] Dory R. A., Guest G. E., and Harris E. G. (1965) "Unstable Electrostatic Plasma Waves Propagating Perpendicular to a Magnetic Field," *Phys. Rev. Lett.* **14**. 131.

[14] Freeman R. L. and Jones E. M. (1977) "Analytic Expressions for Selected Cross–Sections and Maxwellian Rate Coefficients," Culham Laboratory Report CLM-R-175, Abington, Berkshire, U. K.

[15] Garner R. C. and Mauel M. E. (1983) "Fokker–Planck Studies of the Constance B Plasma," *Bulletin of the American Physical Society* **28**. 1182.

[16] Gladd N. T. (1983) "The Whistler Instability at Relativistic Energies," *Phys. Fluids* **26**, 974.

[17] Goodman D. L.. Post R. S., Smatlak D. L. and Smith D. K. (1986) "Ion Heating and Transport in the Constance B Mirror Experiment," *Bulletin of the American Physical Society*, to be published.

[18] Gurnett D. A. and Green J. L. (1978) "On the Polarization and Origin of Auroral Kilometric Radiation." *Journal of Geophysical Research* **83**, 689.

[19] Heitler W. (1954) *The Quantum Theory of Radiation*. Oxford University Press, London.

[20] Hokin S. A., Post R. S. and Smatlak D. L. (1985) "Hot Electron Velocity–Space Diffusion in Constance B," *Bulletin of the American Physical Society* **30**, 1489.

[21] Hokin S. A., Post R. S. and Smatlak D. L. (1986) "Velocity–Space Diffusion of Super–Adiabatic Electrons," *Bulletin of the American Physical Society*, to be published.

[22] Ikegami H., Ikezi H., Hosokawa M., Takayama K. and Tanaka S. (1968) "Microwave Burst Triggered Instability in a Hot Electron Plasma," *Phys. Fluids* **11**, 1061.

[23] Jaeger F., Lichtenberg A. J. and Lieberman M. A. (1972) "Theory of Electron Cyclotron Resonance Heating–I. Short Time and Adiabatic Effects," *Plasma Physics* **14**, 1073.

[24] James R. A., Ellis R. F. and Lasnier C. J. (1984) "Electron–Cyclotron Instability Emission From Hot Electrons in TMX-U," *Bulletin of the American Physical Society* **29**, 1187.

[25] Kesner J., Gerver M. J., Lane B. G., McVey B. D., Aamodt R. E., Catto P. J., D'Ippolito D. A. and Myra J. R. (1983) *Introduction to Tandem Mirror Physics*. Plasma Fusion Center Report PFC/RR-83-35. M.I.T., Cambridge, Massachusetts.

[26] Klinkowstein R. E., Irby J. H., Sullivan J. and Post R. S. (1983) "Tara Base Case Diagnostic Set," *Bulletin of the American Physical Society* **28**, 1180.

[27] Krall N. A. and Trivelpiece A. W. (1973) *Principles of Plasma Physics*, McGraw Hill, New York.

[28] Landau L. (1946) "On the Vibrations of the Electronic Plasma," *Journal of Physics* **10**, 25.

[29] Lau Y. Y. and Chu K. R. (1983) "Electron–Cyclotron Maser Instability Driven by a Loss–Cone Distribution," *Phys. Rev. Lett.* **5**, 243.

[30] Lee L. C. and Wu C. S. (1980) "Amplification of Radiation Near Cyclotron Frequency Due to Electron Population Inversion," *Phys. Fluids* **23**, 1348.

[31] Lieberman M. A. and Lichtenberg A. J. (1973) "Theory of Electron Cyclotron Resonance Heating–II. Long Time and Stochastic Effects," *Plasma Physics* **15**, 125.

[32] Lorrain P. and Corson D. R. (1970) *Electromagnetic Fields and Waves*, W. H. Freeman and Company, San Fransisco.

[33] Mauel M. E. (1982) *Electron Cyclotron Heating in the Constance 2 Mirror Experiment*, Ph.D. Thesis, Massachusetts Institute of Technology, Cambridge, Massachusetts.

[34] Mauel M. E. (1984a) Private Communication.

[35] Mauel M. E. (1984b) "Electron–Cyclotron Heating in a Pulsed Mirror Experiment," *Phys. Fluids* **27**, 2899.

[36] Mauel M. E. (1985) Internal Laboratory Memorandum.

[37] Omidi N. and Gurnett D. A. (1982) "Growth Rate Calculations of Auroral Kilometric Radiation Using the Relativistic Resonance Condition," *Journal of Geophysical Research* **87**, 2377.

[38] Pastukhov V. P. (1974) "Collisional Losses of Electrons from an Adiabatic Trap in a Plasma with a Positive Potential," *Nuclear Fusion* **14**, 3.

[39] Perkins W. A. and Barr W. L. (1968) "Cyclotron Instability in a Hot Electron Plasma with a Double–Humped Velocity Distribution," *Phys. Fluids* **11**, 388.

[40] Porkolab M. (1984) "Upper Hybrid Loss–Cone Instability in Tandem Mirror Thermal Barriers," *Phys. Fluids* **27**, 162.

[41] Schmidt G. (1979) *Physics of High Temperature Plasmas*, Academic Press, New York.

[42] Schwartz M. J. and Lichtenberg A. J. (1972) "Velocity Space Instabilities in a Hot Electron Plasma," *Phys. Fluids* **15**, 470.

[43] Smatlak D. L., Chen X., Garner R. C., Goodman D. L. and Hokin S. A. (1986) Plasma Fusion Center Report PFC/RR-86-15, Massachusetts Institute of Technology, Cambridge, Massachusetts.

[44] Smatlak D. L. (1986) Private Communication.

[45] Smith G. R.. Chen Yu-Juan and Nevins W. M. (1983) "Parallel–Propogating Microinstabilities of Relativistic–Electron Plasmas." *Bulletin of the American Physical Society* **28**. 1194.

[46] Stix T. H. (1962) *The Theory of Plasma Waves*, McGraw Hill, New York.

[47] Sudan R. N. (1963) *Phys. Fluids* **6**, 57.

[48] Sudan R. N. (1965) "Electromagnetic Instabilities in the Nonthermal Relativistic Plasma," *Phys. Fluids* **8**, 153.

[49] Tsang K. T. (1984) "Electron–Cyclotron Maser and Whistler Instabilities in a Relativistic Electron Plasma with Loss Cone Distribution," *Phys. Fluids* **27**, 1659.

[50] Wong H. K., Wu C. S., Ke F. J., Schneider R. S. and Zieball L. F. (1982) "Electromagnetic Cyclotron–Loss–Cone Instability Associated with Weakly Relativistic Electron," *Plasma Physics* **28**, 503.